

NSF Grant ATM-9015485
National Science Foundation

Non-Inductive Charging of Tropical Convection in High and Low Cape Environments

by
Scot C. Randell

Department of Atmospheric Science
Colorado State University
Fort Collins, Colorado

Steven A. Rutledge, P.I.

**Colorado
State
University**

**Department of
Atmospheric Science**

Paper No. 499

**NON-INDUCTIVE CHARGING OF TROPICAL CONVECTION
IN HIGH AND LOW CAPE ENVIRONMENTS**

by

Scot C. Randell

Department of Atmospheric Science

Colorado State University

Fort Collins, CO 80523

Research Supported by

National Science Foundation

under Grant ATM-9015485

May 29, 1992

Atmospheric Science Paper No. 499

ABSTRACT OF THESIS

NON-INDUCTIVE CHARGING OF TROPICAL CONVECTION IN HIGH AND LOW CAPE ENVIRONMENTS

Numerical modelling studies of continental tropical and maritime tropical convection were conducted using a two-dimensional, nonhydrostatic, cloud electrification model, developed at the South Dakota School of Mines and Technology. The model contains six classes of water (water vapor, cloud water, cloud ice, rain, snow, graupel/hail) and a full set of ion equations. All the hydrometeors are permitted to exchange charge. Charge transfer between microphysical species is accomplished through a non-inductive charging parameterization.

In the broadest sense, the goal of the numerical experiments was to explain the electrical differences between the different convective regimes observed during the DUNDEE (Down Under Doppler and Electricity Experiment). This was accomplished by modelling a case (19 January 1990) that was characteristic of continental convection, also termed "break period" convection, and then a case representative of maritime or monsoon convection (12 January 1989). A more specific goal was to test the validity of the hypothesis that the mass of ice and convective vigor in the mixed phase region is a dominant controlling factor in determining the intensity of electrical activity. This hypothesis developed out of the realization that there was a significant correlation between the CAPE (Convective Available Potential Energy) and lightning event rates observed during the DUNDEE. The modelling studies were also intended to test the ability of the non-inductive charging mechanism to produce the charge structures that have been reported in previous studies as well the those observed during the DUNDEE.

Results of the storm electrification simulations indicate that the high CAPE continental tropical storm develops a deep mixed phase region at temperatures well below the non-inductive charge reversal temperature, thereby effectively producing a normal polarity dipole (consistent with high observed lightning flash rates). The maritime tropical case also produced a deep mixed phase region, but it is centered near the charge reversal temperature. This prevents ice particles from acquiring and accumulating charge of one sign, and no organized charge structure develops (consistent with the low observed flash rates). Currently, it is hypothesized that the low CAPE storms, although they have deep mixed phase regions, lack the energy to carry the ice mass to cold enough temperatures to produce a dipole structure as in the case of the high CAPE continental tropical storms.

Scot C. Randell
Atmospheric Science Department
Colorado State University
Fort Collins, CO 80523
Spring 1992

ACKNOWLEDGEMENTS

I would like to express my sincere appreciation and gratitude to my advisor, Dr. Steven Rutledge, for his guidance and support while I was undertaking this research. Additional thanks goes to Dr. Richard Farley and Dr. John Helsdon for their cooperation and help in the modelling studies. I also wish to thank my committee members Dr. Richard Johnson and Dr. Reza Zoughi for their helpful criticism. Cindy Carrick has been incredibly helpful in every way and deserves a sincere thank you. I would also like to extend my appreciation to my office companions, who besides providing enlightening conversations on my research, endured my obstreperous office activities. Finally, I would like to recognize my family and friends for their support and encouragement.

In dedication to my grandparents, Sol and Zelda Rafkin, who have given me never ending love and support, and without whose encouragement my accomplishments would be only dreams.

TABLE OF CONTENTS

CHAPTER I INTRODUCTION		1
1.1	Electrification Mechanisms.....	1
1.2	The Distribution of Thunderstorms Over Land and Ocean.....	2
1.3	Scientific Objectives.....	4
CHAPTER II CHARGE STRUCTURE AND CHARGING MECHANISMS OF THUNDERSTORM		6
2.1	Observations of Thunderstorm Charge Structures.....	6
2.2	The Convective Charging Mechanism.....	9
2.3	The Non-inductive Charging Mechanism.....	12
2.4	Previous Numerical Modelling Using Non-inductive Charging.....	17
CHAPTER III CHARACTERISTICS OF WET SEASON CONVECTION AND SELECTED CASE STUDIES		23
3.1	Break Period Case Study: 19 January, 1990.....	31
3.2	Monsoon Case Study: 12 January, 1990	48
CHAPTER IV MODEL DESCRIPTION		62
4.1	Dynamics	62
4.2	Microphysics Without Electrification.....	64
4.2.1	Conservation of Water Substance and Parameterization of Precipitation Fields....	64
4.2.2	Source and Sink Terms for P_s	67
4.2.3	Production Terms for Graupel	71
4.2.4	Production Terms for Rain.....	74
4.2.5	Production Terms for Non-precipitating Fields.....	75
4.3	Electrification Microphysics	76
4.3.1	Contribution of Non-inductive Charging in the Hydrometeor Charge Interaction Term.....	77
4.3.2	Ion Physics.....	78
4.4	Representation and Determination of Electricity Fields	79
CHAPTER V BREAK PERIOD MODELLING RESULTS		81
5.1	Non-Electrical Characteristics of the Simulated Cloud.....	84
5.1.1	Microphysics and Dynamics of the Initial Development Stage.....	84
5.1.2	Microphysics and Dynamics of the Rapid Development Stage.....	88
5.1.3	Microphysics and Dynamics of the Mature Stage.....	103
5.2	Electrical Evolution of the 19 January Simulation.....	110
5.3	Comparison Of Model Predicted Radar Reflectivity with Observation.....	123
5.2.2		
CHAPTER VI MONSOON MODELLING RESULTS		133
6.1	Non-Electrical Characteristics of the Simulation.....	133
6.2	Electrical Evolution of the 12 January Simulation.....	146
6.3	Comparison of Model Predicted Reflectivity with Observation.....	159

CHAPTER VII CONCLUSION	166
7.1 Relationship Between CAPE and the Level of Storm Electrification	166
7.2 Effectiveness of the Non-inductive Charging Mechanism	173
7.3 Lightning and the Degree of Storm Electrification	174
7.4 Future Studies	174
REFERENCES	176
APPENDIX A LIST OF SYMBOLS	187

CHAPTER I

INTRODUCTION

Meteorological records show that tropical regions are the most favored regions for the development of highly electrified clouds (Livingston and Krider, 1978; Lhermitte and Krehbiel, 1979; Williams, 1985). Satellite observations of lightning (Orville and Spencer, 1979; Orville and Henderson, 1986) reveal that close to half of all lightning occurs within 10° of the equator (about 20% of the total surface area of the earth). These observations suggest that tropical convection is a good place to begin when studying cloud electrification mechanisms. Interestingly, few modelling studies have been done that investigate the role of non-inductive charging in tropical convection. This study will partly fill that gap in the literature.

1.1 Electrification Mechanisms

There are three principle mechanisms which have been proposed to explain the electrification of clouds: the convective mechanism, the inductive mechanism, and the non-inductive mechanism. The convective mechanism (Grenet, 1947; Vonnegut, 1953) relies upon convective motions to transport ions. Both the inductive and non-inductive mechanism involve hydrometeor interactions, but as the names imply, the inductive mechanism also requires the presence of an electric field whereas the non-inductive mechanism does not.

According to the convective mechanism, negative ions drifting towards the surface of the earth become attached to the hydrometeors in the upper portions of a cloud.

Negative charge accumulates on the edges of the updraft and is transported downward due to convective motions, finally developing a pocket of negative charge. The negative charge induces positive ions into the updraft where they are transported by convective motions high into the cloud. The positive ions then attract more negative ions to the cloud edges and the process feeds back upon itself.

The inductive mechanism relies upon the presence of an electric field strong enough to polarize hydrometeors. As the hydrometeors collide with each other in a rebounding collision, the charged end of one of the interacting particles cancels with the oppositely charged end of the other interacting particle, and the two particles rebound carrying a net charge of equal magnitude, but of opposite sign. Over time, the lighter particles will be carried high into the cloud and produce a pocket of charge, and the heavier particles will produce a pocket of charge lower in the cloud.

The non-inductive mechanism is currently the most popular mechanism, and is the one that is specifically addressed in this study. Based on laboratory studies (Reynolds *et al.*, 1957; Takahashi, 1978) it has been discovered that when graupel collides with cloud ice in the presence of supercooled liquid water that the graupel and cloud ice can rebound carrying opposite charges. The magnitude and sign of the resulting charge transfer is dependent upon the temperature and liquid water content.

1.2 The Distribution of Thunderstorms Over Land and Ocean

Satellite observations reveal that lightning is an order of magnitude more common over land than water (Turman and Edgar, 1982; Orville and Spencer, 1979). A one year composite of midnight lightning events taken from satellite emphasizes the contrast: The continents and their coasts are well defined by a dense number of events, while the oceans are virtually void of lightning activity (Fig 1.1). The evidence that lightning occurs primarily over land masses was a primary motivation for the modelling studies.

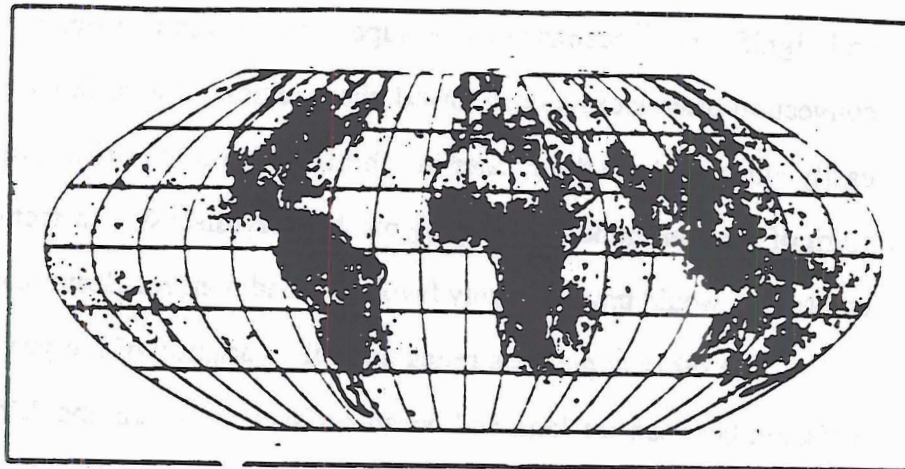


Fig. 1.1: One year of midnight lightning locations for the period September, 1977 through August, 1978 (adapted from Orville and Henderson, 1986).

Two explanations have been forwarded to account for the land/ocean lightning discrepancies. The first hypothesis relates the differences in electrical activity to differences in the vertical development of continental and oceanic convection (Williams, 1991). Generally, vertical velocities in continental convection are greater than in the oceanic cases, and radar reflectivities are correspondingly greater in the subfreezing levels, presumably from greater concentrations of precipitation sized hydrometeors (Szoke *et al.*, 1986). In contrast to land-based thunderstorms which frequently contain small ice crystals, graupel, and significant concentrations of super cooled liquid water in coexistence, maritime convection often lacks a deep mixed phase region. The difference in convective vigor is easily attributable to the greater instability which often exists over land surfaces. In the spirit of the non-inductive charging mechanism (discussed in section 2.3), the continental convection would provide highly favorable conditions for electrification.

The other hypothesis relies upon the variation of ion production through corona emission between the land and ocean surfaces to explain the differences in oceanic and continental lightning rates (Vonnegut, 1982). The rough land is expected to more easily produce free ions than a relatively flat ocean under equal electric fields. In the spirit of the convective charging mechanism, the continental convection would be the preferred storm for electrification. As will be discussed in section 2.2, there are several problems with the convective charging mechanism which disqualify this hypothesis as a reasonable explanation for the observed differences between continental and maritime lightning production rates.

1.3 Scientific Objectives

This modelling study will primarily address the non-inductive charging differences of continental tropical and maritime tropical convection. In particular, the role of ice mass within the mixed phase region of the cloud, and the ability of the storm dynamics to

produce and distribute hydrometeors will be investigated and used to explain the dissimilar charging rates and lightning events that were observed during the Down Under Doppler and Electricity Experiment (DUNDEE) conducted in Darwin, Australia during two consecutive winter monsoon seasons in 1989 and 1990. To accomplish this, thermodynamic profiles considered to be representative of the continental and maritime convective environments observed during DUNDEE were used to initialize a two dimensional, time dependent, bulk parameterized electricity model (Helsdon and Farley, 1987a,b). The results of these two case studies are presented herein.

CHAPTER II

CHARGE STRUCTURE AND CHARGING MECHANISMS OF THUNDERSTORMS

Nearly all charged convective clouds have an electric dipole structure with a large pocket of negative charge centered near -10°C , and a large pocket of positive charge centered at -25°C or colder. In some cases a tripole structure has been observed. In this instance a thin band of positive charge at the base of the cloud is observed in addition to the dipole structure (Simpson and Scrase, 1937; Reynolds, 1954; Takahashi, 1965; Magono, 1977; Byrne *et al.*, 1987). The main charge centers contain roughly equal, but opposite charge on the order of tens of Coulombs. The positive charge at the base of the clouds with a tripole structure is often an order of magnitude less (Uman, 1969). Williams (1989) points out that at a distance, a tripole structure might appear as dipole. Also, he provides an excellent summary of previous investigations on the polarity of thunderstorms.

2.1 Observations of Thunderstorm Charge Structures

In addition to simply measuring the electrical structure of thunderstorms, a few investigators have made simultaneous electrical and microphysical measurements. These studies are of particular interest because they link the electrification to the microphysical processes that are operating within the cloud. Dye *et al.* (1988), conducted *in situ* aircraft measurements in two small thunderstorms in New Mexico. The clouds were in the early stages of electrification. In the first case a negative region of charge was detected near the -12°C isotherm. The total charge estimated at this altitude was only -0.01C assuming spherical symmetry. In the other case, a positive charge center was located near the -20°C

isotherm and the charge was estimated to be 0.01C. In both cases the horizontal extent of the charged regions was about 500m. A summary of the electric field, the liquid water content, the ice concentration, and an overlay of the aircraft flight path on the radar reflectivity is presented in Fig. 2.1. Both clouds exhibited the strongest charging where the liquid water content and ice concentration were at a maximum. Not surprisingly, the collision rate between graupel, ice, and liquid water was calculated to be a relative maximum as well. The center of charge correspond well to the regions of strongest reflectivity in both cases.

A flight through a thunderstorm in Flagstaff, Arizona (Latham and Stow, 1969) and in France (Laroche *et al.*, 1986) revealed microphysical and electrical characteristics similar to those presented by Dye *et al.* The electrification was greatest where aggregates coexisted with small ice crystals and liquid water, and where radar reflectivities were at a relative maximum.

Observations have made a strong case that the presence of a mixed phase region is necessary to generate significant charge within a thundercloud. This is consistent with the non-inductive charging hypothesis, although a minority of the community remains unconvinced that this is the primary mechanism operating. Strong updrafts are generally required to produce deep mixed phase regions, so it is not unexpected that reflectivity maxima are often coincident with the centers of charge.

Few, if any *in situ* electrical observations have been made in deep tropical systems. Investigations of subtropical storms in or around the Gulf of Mexico (Krehbiel *et al.*, 1983; Blakeslee *et al.*, 1989; Williams *et al.*, 1989), Japan (Magono, 1977; Takahashi, 1965), and Africa (Barnard, 1951; Hacking, 1954; Ette *et al.*, 1977) are the closest to tropical thunderstorms, and of these, most are continental. Surface measurements of the electric field during DUNDEE and other tropical experiments seem to suggest that the electrical structure of tropical storms is not significantly different than their middle latitude and subtropical cousins (Takeuchi *et al.*, 1978; Brode *et al.*, 1982; Ogawa and Sakaguchi,

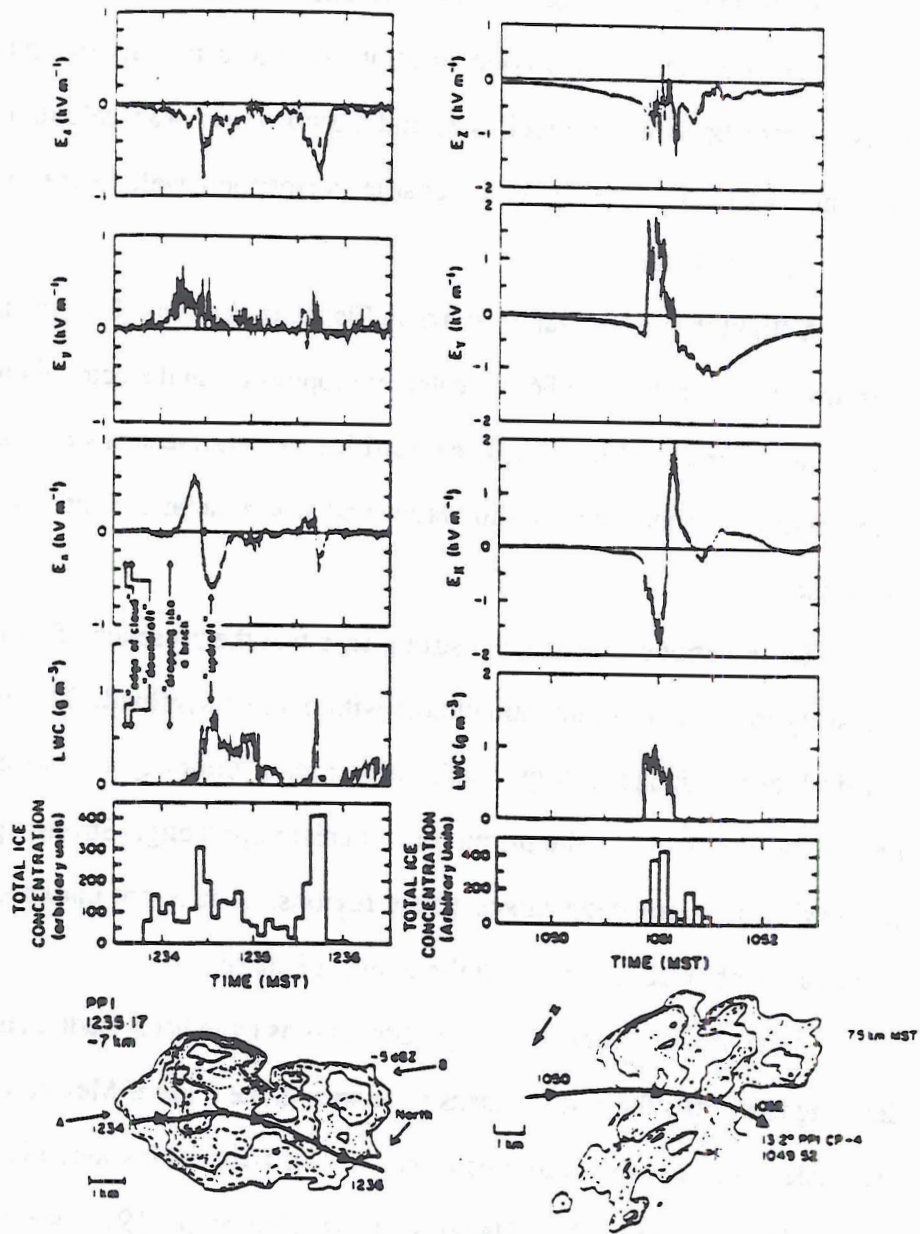


Fig. 2.1: A summary of the electric field, liquid water content, ice concentration and radar reflectivity with the aircraft path for two flights through developing New Mexico thunderstorms (from Dye *et al.*, 1988).

1983; Mogono *et al.*, 1983). If this is the case, then it is reasonable to extend the observations to the tropics.

2.2 The Convective Charging Mechanism

Although the manner by which clouds electrify is a subject with some controversy, of the charging hypotheses that have been forwarded over the last two centuries, besides the non-inductive charging mechanism, two have remained alive: the convective mechanism and the inductive mechanism.

In 1947, Grenet proposed cloud charging by convective motions of cloudy air, later described by Vonnegut (1953). According to this mechanism, negative ions, drifting towards the surface of the earth as part of the Wilson current, become attached to the hydrometeors in the upper portions of a cloud. The conductivity of cloudy air is for all practical purposes zero compared to the conductivity of cloud free air, and negative charge accumulates on the edges of the updraft. Overturning convective motions in a growing turret are then relied upon to transport the negative charge downward, opposite to the fair weather potential gradient, finally developing a pocket of negative charge. As the negative charge nears the surface it begins to induce positive point discharge from objects on the surface. The positive ions are then carried up into the convective updraft to produce a pocket of positive charge in the upper levels of the cloud and also serve to attract more negative ions. The process feeds back upon itself. The convective charging mechanism is shown schematically in Fig. 2.2.

The problems with the convective charging mechanism are well known. Here is a short list:

- Not all clouds electrify. Strong electrification usually occurs only in clouds with ice and precipitation sized particles.

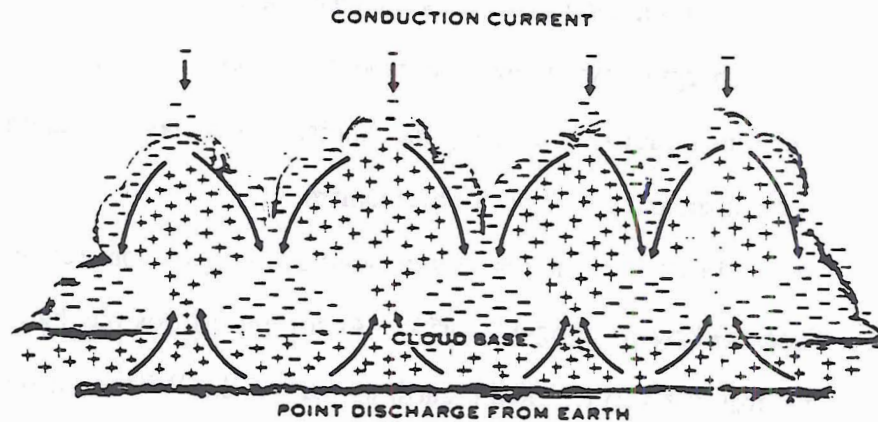


Fig. 2.2: An idealized sketch illustrating the convection theory of thundercloud electrification (after Vonnegut, 1963). In this mechanism, external charges drawn to the cloud are caught in the convective overturn and carried by the motions of the air against the local electric fields to increase the cloud's electrical potential energy. The ions carrying the Wilson current at the cloud top become attached to cloud particles and are carried downward by the compensating downdrafts. Point-discharge ions beneath the cloud are carried toward the cloud top by updrafts, and attract more negative ions to the cloud top from the conductive clear air around thus causing positive feedback in the cloud electrification.

- The strongest electrification occurs in mixed phase regions and in areas with a maximum in radar reflectivity. The convective mechanism offers no explanation for this.
- In the early development of the cloud, there should be a positively charged base and core. This is contradictory to observations (Colgate and Romero, 1970; Krasnogorskaya, 1969).
- Simple calculations and numerical modeling studies show that the upward conduction of negative charge (down gradient) should counteract or dominate over the upward convection current (Pruppacher and Klett, 1978; Ruhnke, 1970, 1972; Chiu and Klett, 1976).

In all fairness to the convective charging mechanism and its proponents it should be noted that no argument is being made to deny the existence of the process. Rather, the point is made that the convective charging mechanism cannot be the *dominant* process responsible for the electrical structure of thunderstorms. Vonnegut *et al.* (1962a,b) and Moore *et al.* (1986, 1989) have shown that the polarity of thunderstorms can be reversed by releasing anonymously high (orders of magnitude) concentrations of free ions into the convective updrafts of clouds. This shows that convective motions do transport ions, and that if ions were produced naturally in such concentrations that convective charging would be feasible.

The attachment of free ions to cloud hydrometeors is also known to occur and produces the screening layers which are often observed (Chauzy and Raisonville, 1983). The formation of screening layers seems to be the limit to which the convective charging mechanism operates. In any case, because the numerical model used in this study contains ion equations, any convective charging will be inherently accounted for (Chiu, 1978).

The inductive mechanism probably does operate in thunderstorms, but only after electric fields have become strong enough to significantly polarize hydrometeors. The fair weather electric field is far too weak to produce this effect. Therefore, an inductive mechanism can not be responsible for the initial charge separation.

2.3 The Non-inductive Charging Mechanism

Non-inductive charging (NIC) rests on very poorly understood physics; the underlying process that transfers charge when graupel collides with ice crystals in the presence of supercooled liquid water is unknown. This is perhaps the primary reason why it has taken so long for the non-inductive charging mechanism to gain acceptance. For the purposes of numerical modelling (at least in this study) it is more important to know the variables upon which the sign and magnitude of the charge transfer depends and not on how it happens. Since there is no formal theory describing the physics of the process, laboratory studies have provided the only information as to what the dependent variables are. Currently, the charge transferred in the non-inductive process seems to be dependent on temperature, cloud liquid water content, impact velocity, and ice crystal size. Of these, only temperature and cloud water have received appreciable attention, and none of the other parameters as of yet have been adequately addressed.

The first study on NIC simply noted that "a graupel pellet growing by the accretion of supercooled droplets, acquires negative charge as a result of collisions with ice crystals" (Reynolds *et al.*, 1957). In this experiment, spheres coated with ice (simulating hail or graupel) were drawn through a cloud of supercooled liquid water and ice. Neither the temperature, the cloud liquid water, nor size of the ice crystals were well controlled. The charge transferred per collision (between graupel and ice) was measured to be as high as 150 fC in magnitude. Further calculations showed that this was sufficient to produce the charges observed in the main thunderstorm dipole.

Little attention was given to the work of Reynolds *et al.* until 1978. This was most likely due to the abundance of other proposed charging mechanisms that rested on a firmer physical basis. Prior to 1978, only two studies were conducted that were concerned directly with non-inductive charging. Magono and Takahashi (1963a, 1963b) investigated NIC within the space of temperature and liquid water content. The results from these

studies were primarily qualitative: "positive electrification was observed at warmer temperatures, and a change in the electric sign, depending on the cloud water content at lower temperatures."

In 1978, Takahashi (Takahashi, 1978) published the first (and still probably the most complete) results on the dependence of the charge separated per collision on both temperature and cloud water content. The apparatus used in the experiment consisted of a riming rod (simulating a graupel particle) which was whirled within a cloud chamber. Peripheral instruments were used to measure ice concentrations and sizes, cloud liquid water, temperature, and electrification. The results are summarized in Fig. 2.3 and the following information should be gleaned.

- Positive charging of the rod occurred, regardless of cloud water content (cwc) when the temperature was greater than -10°C .
- At temperatures colder than about -10°C , positive charging occurred at low and high cwc.
- Negative charging occurred between regions of low and high cwc when the temperature was less than about -10°C , but the boundary between the positive and negative charging depends on temperature.
- The temperature at which charging switches from the lower positive region to the negative, called the charge reversal temperature, decreases as cwc decreases.

The following information which is not obvious from Fig. 2.3 should also be noted:

- No charging occurred when the riming rod stopped rotating.
- No charging occurred when the rod rotated in an environment containing only ice crystals or only supercooled liquid water.
- Strong electrification occurs when both ice crystals and supercooled droplets are present.

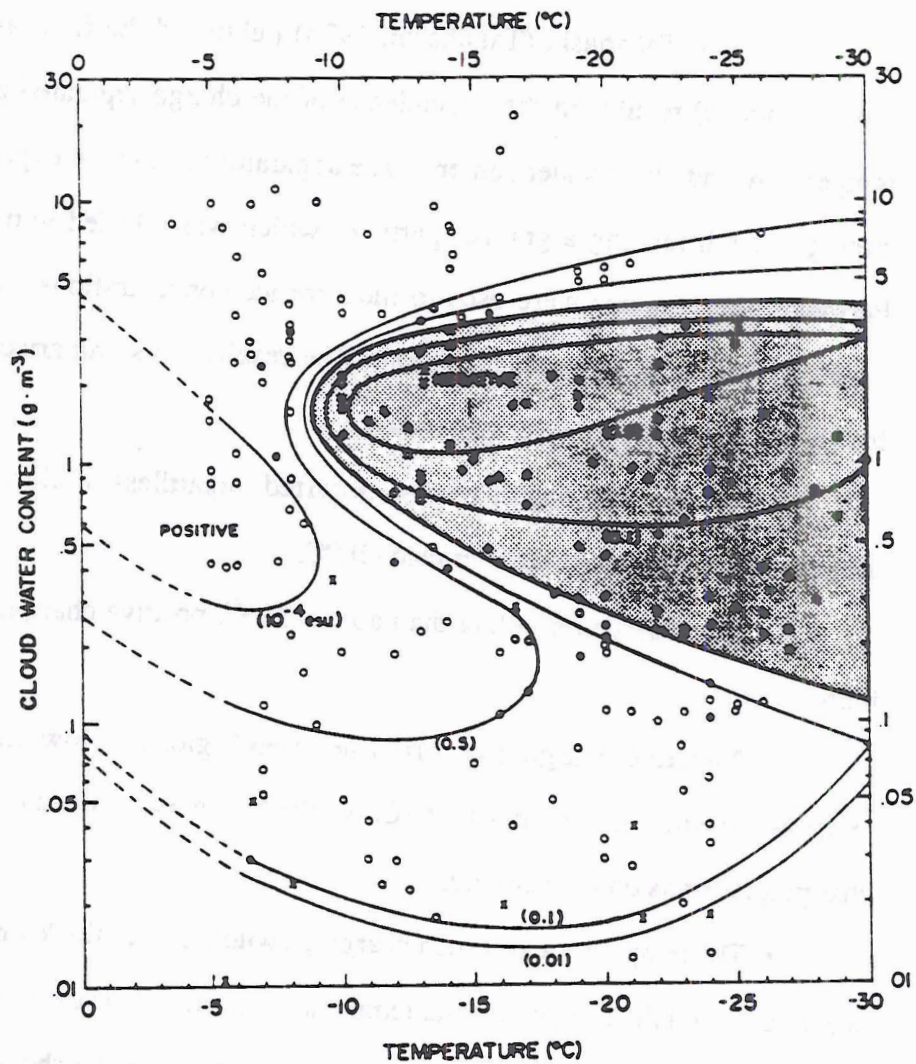


Fig. 2.3: Electrification of the riming rod. Open circles show positive charge, solid circles negative charge and crosses represent uncharged cases. The electric charge of the riming rod per ice crystal collision is shown in units of 10^{-4} esu (Takahashi, 1978)

Only the dependence on temperature and cloud water content was measured, but all the other parameters such as velocity and ice crystal size were kept reasonably constant so as to minimize extraneous effects.

Following the work of Takahashi, studies of NIC mechanism became more common, partly due to the failure of other charging mechanisms to account for observed thunderstorm charge structure. The dependence of the charge transfer on the impact velocity of the ice crystals was investigated by Gaskell and Illingworth (1980) and was found to have magnitude dependence proportional to the diameter of the ice crystal to the power 1.7. Also of significant importance, the role of thermal effects on the charge transfer was investigated. A hailstone which grew by deposition (by cooling below ambient temperature) acquired a positive charge. When a hailstone was cooled by the same amount but was maintained in a sublimating condition, the stone acquired negative charge. The conclusions from these observations were that thermal gradients between the hailstone/graupel and the ice crystals was not the driving force behind the charge transfer. Furthermore, the condition that supercooled liquid water be present for charging begins to make sense since the amount of water present can determine the state of growth of a hailstone through latent heat effects during accretion, or by acting as a vapor source for depositional growth. Baker *et al.* (1987) found similar results and proposed that the charge "is positive if the target surface is growing more rapidly from the vapour than the ice crystals and is negative for the opposite case".

Williams *et al.* (1990) investigated the validity of the above statement by dividing the temperature/cloud water diagram into three growth regions for graupel: wet growth (evaporation), dry growth (sublimation); and dry growth (deposition). The laboratory results of Takahashi (1978) and the theoretical boundaries were then compared (Fig. 2.4). In general, the lines separated events with different charge, especially at low temperatures. It would appear that knowing the temperature and cloud water content is sufficient to determine the sign of charge transfer without explicitly having to calculate the type of

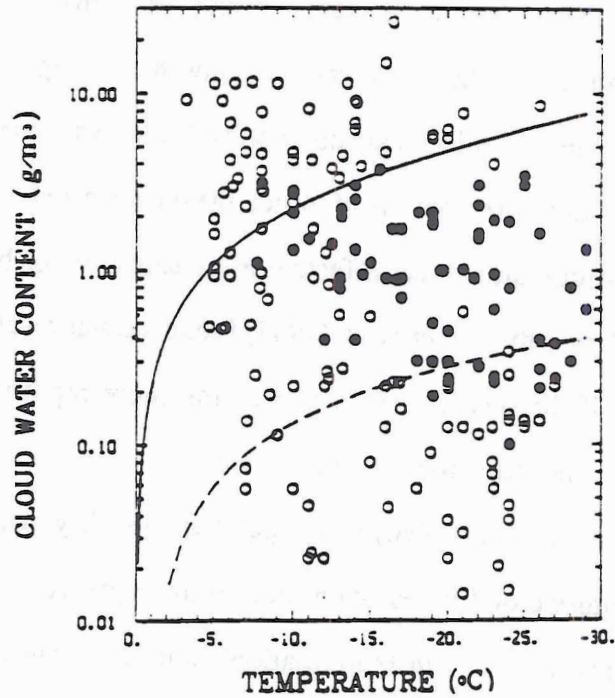
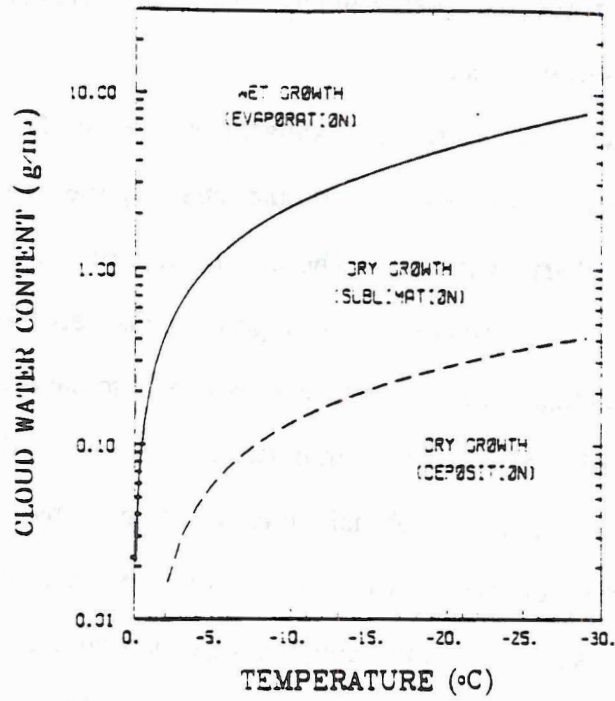


Fig. 2.4: Calculated boundaries between 'wet' and 'dry' growth and between sublimation and deposition for the rimer (graupel), applicable to the laboratory studies of Takahashi (1978). Black (white) dots denote negative (positive) charge transfer to the rimer (graupel)

growth the graupel is experiencing. This is particularly important for modelling, since any additional calculations add to the computation time and therefore cost of a model run.

A multitude of laboratory studies (Magono and Takahashi, 1963; Takahashi, 1978; Hallet and Saunders, 1979; Gaskell and Illingworth, 1980; Jayaratne *et al.*, 1983; Baker *et al.*, 1987; Avila *et al.*, 1988) have shown general agreement with the first experiments conducted by Reynolds, but there are still a few discrepancies. For example the charge reversal temperatures measured by Jayartne *et al.* (1983) and Baker *et al.* (1987) are much colder than those found by Takahashi (1978). The studies done by Reynolds (1957), Magono and Takahashi (1963a, 1963b), and Takahashi (1978) however are self consistent. A more careful analysis reveals that most of the inconsistent studies were conducted at the UMIST (University of Manchester Institute of Science and Technology) laboratories which suggests that there may be some systematic error.

The validity of Takahashi's results is supported by many observations of charge reversal near the -10°C isotherm, whereas UMIST studies generally have charge reversal temperatures near -20°C . Also, Takahashi (1978) has explored the largest range of temperatures and liquid water contents. The data presented by Jayartne *et al.* (1983) is the only other usable data set for the inclusion into a model. However, the data in this study uses effective liquid water content instead of liquid water content, and only explores relatively low values of effective liquid water content. This renders the results virtually useless for deep convection. For these reasons, the data acquired by Takahashi (1978) are used to parameterize the charging in the model.

2.4 Previous Numerical Modelling Using Non-inductive Charging

In a conceptual model it is easy to visualize how the non-inductive charging mechanism would produce a charge dipole. At temperatures colder than the charge reversal temperature, graupel will charge negatively and fall to establish a negative charge

center near the observed level of about -10°C . The crystals will acquire a positive charge and will be carried up in the updraft to form the positive charge center. At temperatures warmer than the charge reversal temperature, ice crystals will charge negatively and will be carried in the updraft to reinforce the negative charge center. The process is shown schematically in Fig. 2.5.

Only a dozen or so investigators have attempted to model storm electrification. Of these, only a handful have used non-inductive charging as a primary charging mechanism (Kuettner *et al.*, 1981; Tzur and Levin, 1981; Rawlins *et al.*, 1982; Takahashi, 1984; Helsdon and Farley, 1987; Rutledge *et al.*, 1990). Only the studies using non-inductive charging will be addressed since they are of direct interest to this study.

Kuettner *et al.* (1981), Tzur and Levin (1981), and Rawlins (1982) explored the relative importance of non-inductive and inductive charging. The first two investigations used a one dimensional model, and Kuettner *et al.* was steady-state. The results indicated that a combination of both mechanisms provided the most realistic simulation, but the non-inductive process was the primary initial electrification mechanism. Because of the simplicity and limitations of the models, however, specific results were difficult to interpret.

Rawlins (1982) used a three dimensional, time dependent model which incorporated a simple bulk ice parameterization. He concluded that both the inductive and non-inductive mechanisms were independently capable of producing electric field breakdown within a reasonable period of time, provided that in the case of inductive charging that "the hail size spectrum represents relatively small particles and that the effect of multiple collisions of any ice crystal with more than one particle is discounted, *i.e.*, when it is assumed that ice crystals are uncharged before impact", and in the case of non-inductive charging that the product of ice particle concentration and charge separation per collision is greater than 7 pC per liter. The assumption that the small end of the hail size spectrum is representative of the small ice particles is questionable. Both charging

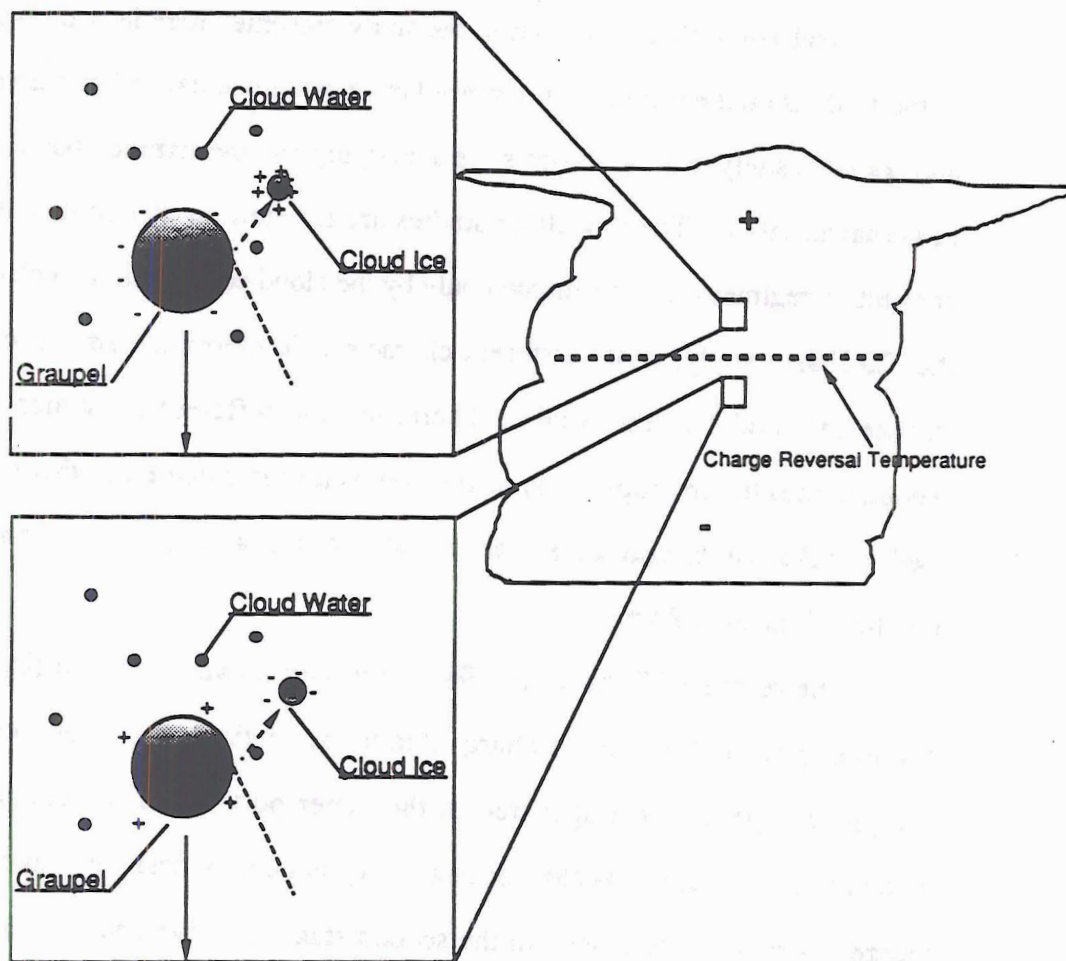


Fig. 2.5: The non-inductive charging mechanism. At temperatures colder than the charge reversal temperature, graupel charges negatively and falls to establish a negative charge center. Cloud ice acquires positive charge and is carried higher into the cloud to establish a region of positive charge. At warmer temperatures, cloud ice will charge negatively and will be carried in the updraft to reinforce the negative charge center.

parameterizations ignore multiple collisions of charged particles since no information is available from the laboratory on the results of such interactions. A combination of observations and laboratory work indicate that charge separation should be orders of magnitude greater than 7 pC per liter. Assuming an ice crystal concentration of 100 per liter and charge separation per collision of 10 to 100 pC, the product is on the order of 10^3 to 10^4 pC per liter.

Takahashi (1984) is similar to the study presented here in two respects. The focus of the study is on the electrical difference between continental and maritime thunderstorms, and both this study and Takahashi's use a charging parameterization based on the same data (Takahashi, 1978). The modelling studies are different in that continental and maritime convective regimes are differentiated only by the cloud condensation nuclei concentration in the Takahashi study, while different characteristic thermodynamic profiles are used to initiate the model in this study. Therefore, the different dynamics (and subsequent feedback into the microphysics) of the convection is captured in this study. The model used by Takahashi is also somewhat limited since it is axially symmetric and constrained to a vertical domain of 8 km.

The results of Takahashi (1984) indicated a two stage charging process. In the developing stage, large space charge due to gravitational separation of non-inductively charged graupel and ice appeared in the upper portions of the cloud, near the -30°C isotherm. The graupel was charged negatively and the ice positively, as expected below the charge reversal temperature. In the second stage, positive charging of graupel that had fallen from higher levels occurred near the -10°C isotherm. This is of course consistent with the charging expected above the charge reversal temperature. As the graupel near the -10°C isotherm falls, a large pocket of negative charge is left at that level. This is consistent with observations.

Another important study, primarily because it used the South Dakota Storm Electrification Model (the one used in this study) was conducted by Helsdon and Farley

(1987a,b). The non-inductive charging parameterization used in the model for the study was a simple one value representation; only the sign of the charge transfer changed as determined by the charge reversal temperature. Inductive charging was explicitly included while convective charging was contained inherently in ion equations. The model represented an advance over Takahashi (1984) because the model was not axisymmetric, and the domain was larger while the resolution remained the same or increased. The results were also compared to *in situ* aircraft measurements which provided excellent verification.

Many aspects of the storm were simulated favorably. The overall electrical structure was simulated very well. A positive electric dipole developed in the model with electric potentials becoming near the dielectric strength of air close to the time that the first lightning was detected in the actual storm. The charge centers were attributed to the gravitational separation of graupel and less dense ice. The non-inductive process was determined to be essential in the initial electrification of the storm. Inductive processes became active, but never surpassed the effectiveness of the non-inductive mechanism once a strong electric field had developed. A model run with only inductive charging failed to produce significant charging (the electric field remained below 3.2 kV m^{-1}). The general success of the Helsdon and Farley studies was the primary reason that the South Dakota model was chosen as the model for this study (with only a few modifications in the charging parameterization to be described later).

The role of non-inductive charging in the stratiform region of middle latitude mesoscale convective systems was investigated by Rutledge *et al.* (1990) using a one dimensional, kinematic (steady-state) and bulk parameterized microphysical model. The charging parameterization was based on the laboratory studies of Jayaratne *et al.* (1983) and Saunders and Jayartne (1986). The data of Takahashi (1978) was not used since almost no information was presented for the low liquid water contents that are typical in the stratiform regions of mesoscale convective systems. The results of this study indicated that the stratiform region is capable of producing charge densities on the order of 1 C km^{-1}

within about one hour. Interestingly, an inverted dipole, with positive charge underlying negative charge, was simulated. This was attributed to the relatively warm temperatures in the region of high particle interactions.

This thesis is significant for two reasons. First, this study represents only the second direct numerical model comparisons between continental and maritime convective regimes and electrification. Takahashi (1984) modeled continental and maritime convection, but attributed the differences to cloud condensation nuclei concentrations. Thus, this is the first direct numerical model comparisons which include the effects of the dynamic differences between maritime and continental convection. Furthermore, the South Dakota School of Mines and Technology Storm Electrification Model is better suited to study deep tropical convection. The model is not axisymmetric nor limited in the vertical dimension as was the case with Takahashi (1984).

Also, this is only the second modeling study which use a non-inductive charging mechanism that is based quantitatively, rather than qualitatively, upon laboratory studies of the non-inductive charging process. Previously, the South Dakota School of Mines and Technology Storm Electrification Model (Helsdon and Farley, 1987b) used only one value for the charge separated per collision and the sign was determined by the temperature.

CHAPTER III

CHARACTERISTICS OF WET SEASON CONVECTION AND SELECTED CASE STUDIES

Two distinct weather patterns, which depend on the location of the Intertropical Convergence Zone (ITCZ) occur in the vicinity of Darwin during the wet season. The location of the ITCZ may be controlled primarily by sea surface temperatures (Emanuel, 1988) and tends to migrate across the Darwin region several times during the course of a typical wet season. The onset of the Australian Monsoon has been linked to the 40-50 day oscillation (McBride, 1983, 1987; Holland, 1986; Keenan and Brody, 1988; Hendon and Liebmann, 1990). When the ITCZ is located to the south of Darwin, moist northwesterly flow prevails over Darwin (the winter monsoon). The Australian monsoon is characterized by persistent cloudy skies and wide spread convection with embedded deeper convection (Rutledge *et al.*, 1991). Generally, radar cloud top boundaries are below about 12 km during the monsoon. When the ITCZ is located to the north of Darwin, southeasterly winds flow off the continent toward the monsoon trough and place Darwin in a continental airmass. This weather regime is often referred to as the "break period" (*i.e.*, periods during which the monsoon trough retreats northward). During the break period, deep isolated thunderstorms and squall lines form over elevated terrain to the Southeast of Darwin. The convection is usually triggered by afternoon heating, or by the inland propagation of the sea breeze, and exhibits a strong diurnal cycle (Williams and Rutledge, 1990).

Composite (not smoothed) 0000 UTC soundings have been constructed for monsoon (17 soundings composited) and break period (197 soundings composited) environments to illustrate the general thermodynamic differences between the two (Fig.

3.1). The most striking difference is the moisture profile; the average monsoon sounding is nearly saturated through the depth of the troposphere while the break period is below water saturation at all levels. The lapse rate of both soundings exhibit three different regions of stability. In the lowest few hundred hectopascals, the lapse rate is conditionally unstable. Between about 700 hPa and 400 hPa, the lapse rate is moist adiabatic, and above 400 hPa the lapse rate is absolutely stable.

Because the composite is an average of morning soundings (local time), the effects of afternoon heating are not represented. In the break period cases, the boundary layer generally becomes well mixed and develops a nearly constant potential temperature layer. Usually the saturated (cloudy) conditions in the monsoon cases does not allow for nearly as much surface heating. Furthermore, any mixing of the saturated boundary layer produces clouds which results in a constant equivalent potential temperature profile instead of a constant potential temperature profile as in the case of the break period environments. The end result is that the monsoon convection has less energy available and is generally less vigorous than the break period convection. Statistics from the composite soundings reveal other differences (Table 3.1). Most notable among the differences are the mean relative humidity, CAPE, level of free convection, and precipitable water.

Besides the composited soundings, environmental differences between the monsoon and break period are well illustrated by time series plots of 850 hPa wind, 24 hour cumulative rainfall at Darwin, and CAPE for the two seasons of DUNDEE (Fig. 3.2). Following Holland (1986) the onset of the Australian Monsoon at Darwin is defined by the existence of westerlies at 850 hPa (Fig. 3.2a). A total of six monsoon periods were documented during DUNDEE--three in the first season and three in the second. CAPE was observed to be near minimum values during periods of westerlies at 850 hPa (Fig. 3.2a). In addition, heavy precipitation is well correlated with the monsoon except for the first westerly event during the second season of DUNDEE (Fig. 3.2b). Even though the monsoon environment shows a minimum in CAPE, it is a prolific producer of rain.

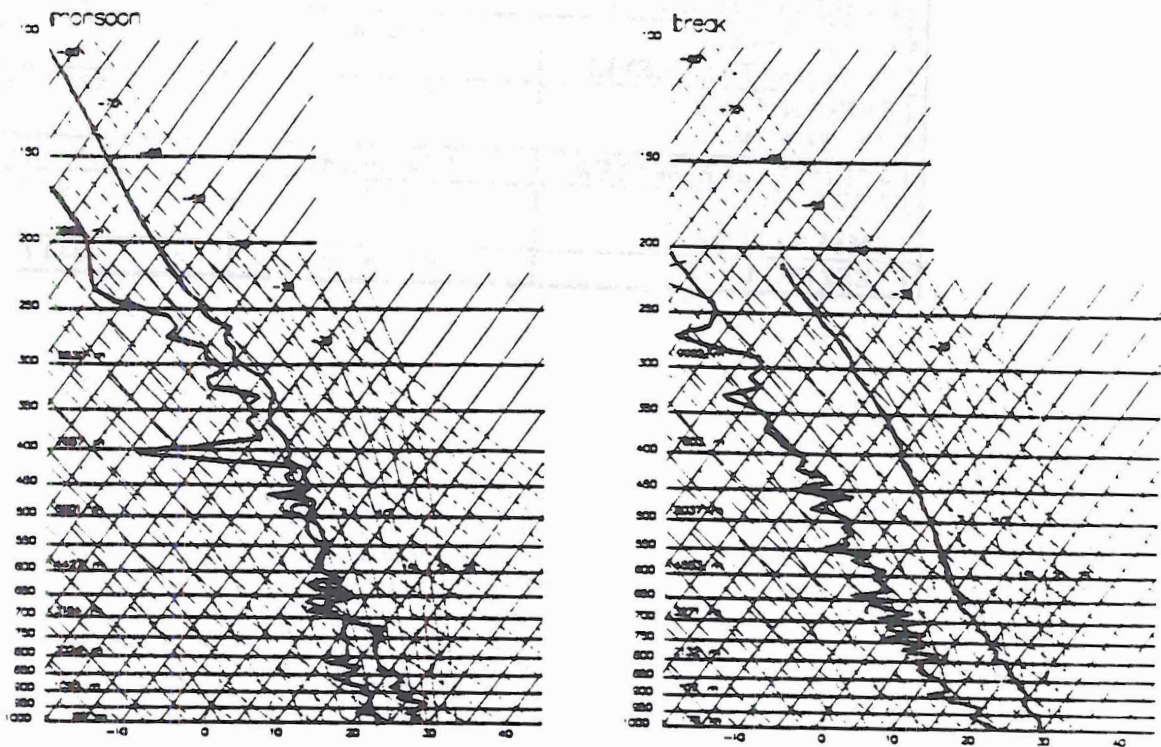


Fig. 3.1: Composite 0000 UTC soundings of the monsoon and break period.

Table 3.1: Statistics from the 0000 UTC composite monsoon and break period soundings.

	COMPOSITE BREAK	COMPOSITE MONSOON
CAPE	1193.7 Jkg ⁻¹	0.0 Jkg ⁻¹
ENERGY TO FORM MIXED LAYER	253.1 Jkg ⁻¹	35.0 Jkg ⁻¹
VERTICAL VELOCITY AT EQUILIBRIUM LEVEL	48.9 ms ⁻¹	0.0
CONVECTIVE CONDENSATION LEVEL	810.0 hPa	885.0 hPa
LEVEL OF FREE CONVECTION	810.0 hPa	885.0 hPa
PRECIPITABLE WATER	1.74 inches	2.40 inches
CONVECTIVE TEMPERATURE	36.4 °C	29.5 °C
FREEZING LEVEL	4973.5 m	4844.6 m

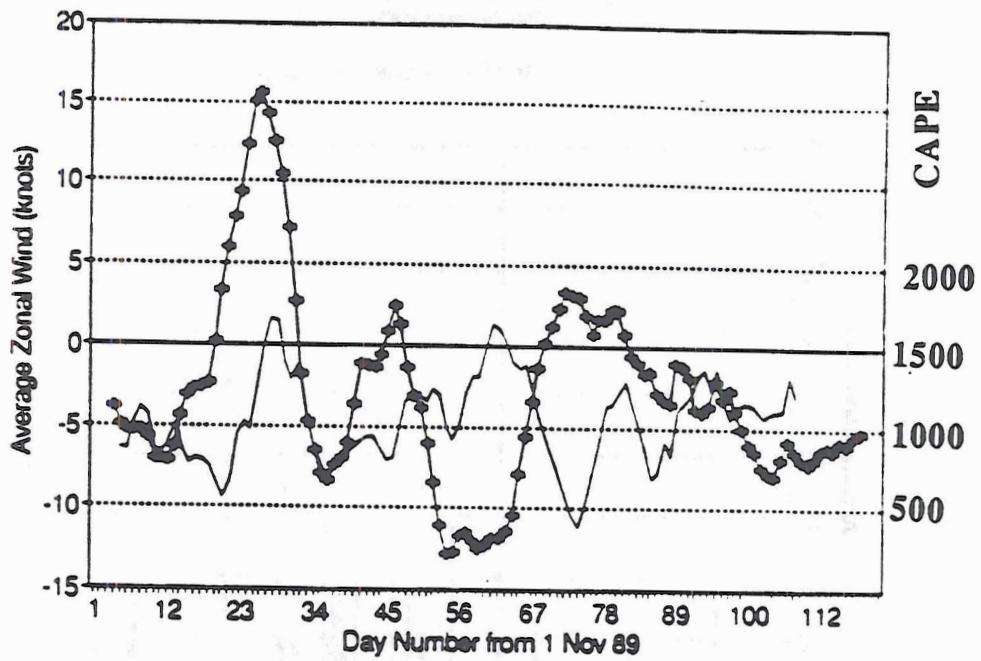
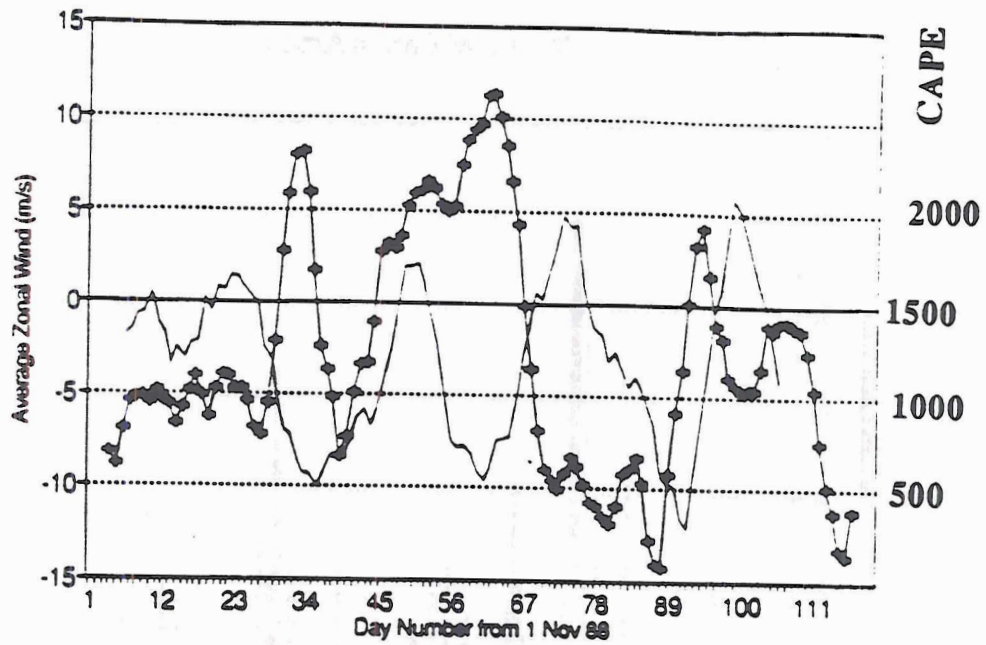
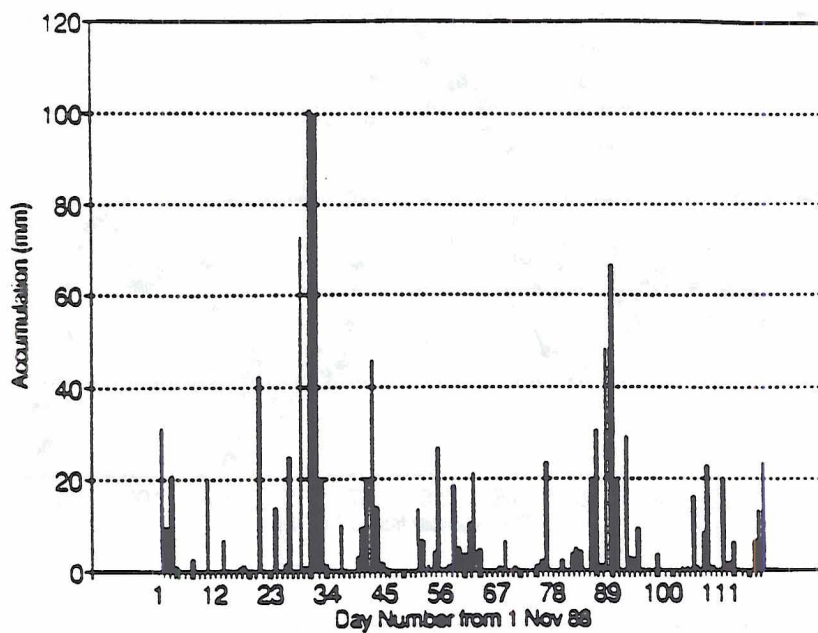


Fig 3.2a: Time series of the 850 hPa wind and Convective Available Potential Energy.

24h Rainfall Darwin Airport



24h Rainfall Darwin Airport

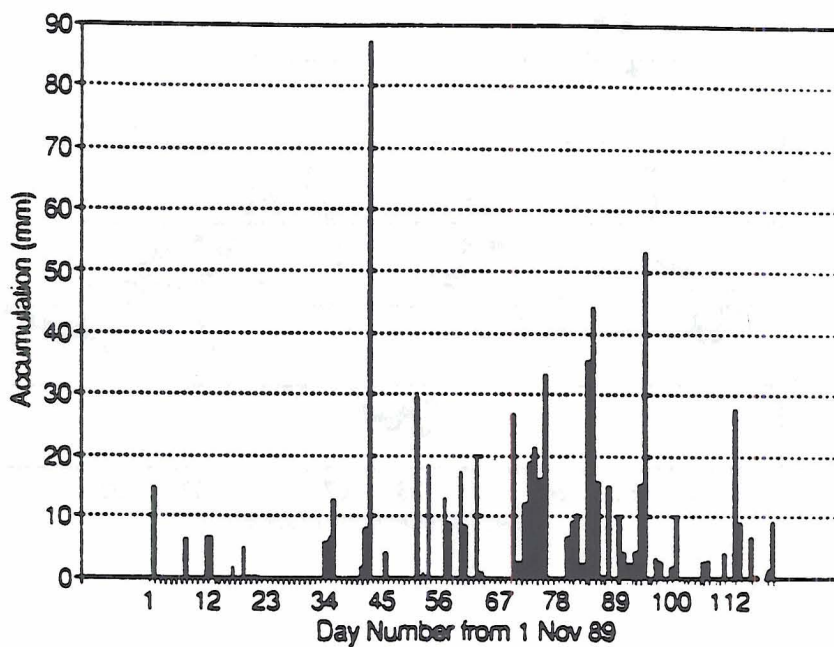


Fig. 3.2b: Time series of the 24 hour cumulative rainfall at Darwin Airport.

In contrast to the monsoon, break period convection is extremely vigorous, often reaching heights up to 18 km and containing updraft cores that may exceed 40 dBZ above 12 km (Williams *et al.*, 1990). The CAPE in the break period environment is comparatively high (commonly over 2000 J kg⁻¹). Soundings tend to be conditionally stable as a result of a very hot and moist boundary layer usually capped by the trade wind inversion that separates the boundary layer air from the dry air aloft. The break period convection also tends to be highly electrified with lightning flash rates that sometimes exceed 60 min⁻¹. Precipitation can be intense at times, but occurs over local areas and is ephemeral in nature. Convection is often organized in clusters of deep isolated convective cells or in squall lines which resemble the middle latitude systems.

Assuming a non-inductive charging mechanism, Williams and Rutledge (1990) presented a scaling analysis that attempts to explain the correlation between CAPE and lightning rates (Fig 3.3). The following assumptions go into the model:

- graupel is the dominant precipitation type in the cold part of the cloud.
- the terminal fall speed of graupel is proportional to the square root of its diameter.
- the graupel is spherical so that the mass is proportional to the cube of the diameter and the radar reflectivity is proportional to the sixth power of the diameter.
- the particle balance level (where the terminal fall speed is equivalent to the vertical velocity) is within the mixed phase region of the cloud.
- all the CAPE is converted into kinetic energy and all motion is vertical.

The above assumptions lead to the following scaling relations using the notation where W is vertical velocity, V_T is the terminal fall speed of graupel, D is the graupel diameter, Z is radar reflectivity, and M is the mass of ice:

$$V_T \sim D^{1/2} \quad (3.1)$$

$$Z \sim M^2 \sim D^6 \quad (3.2)$$

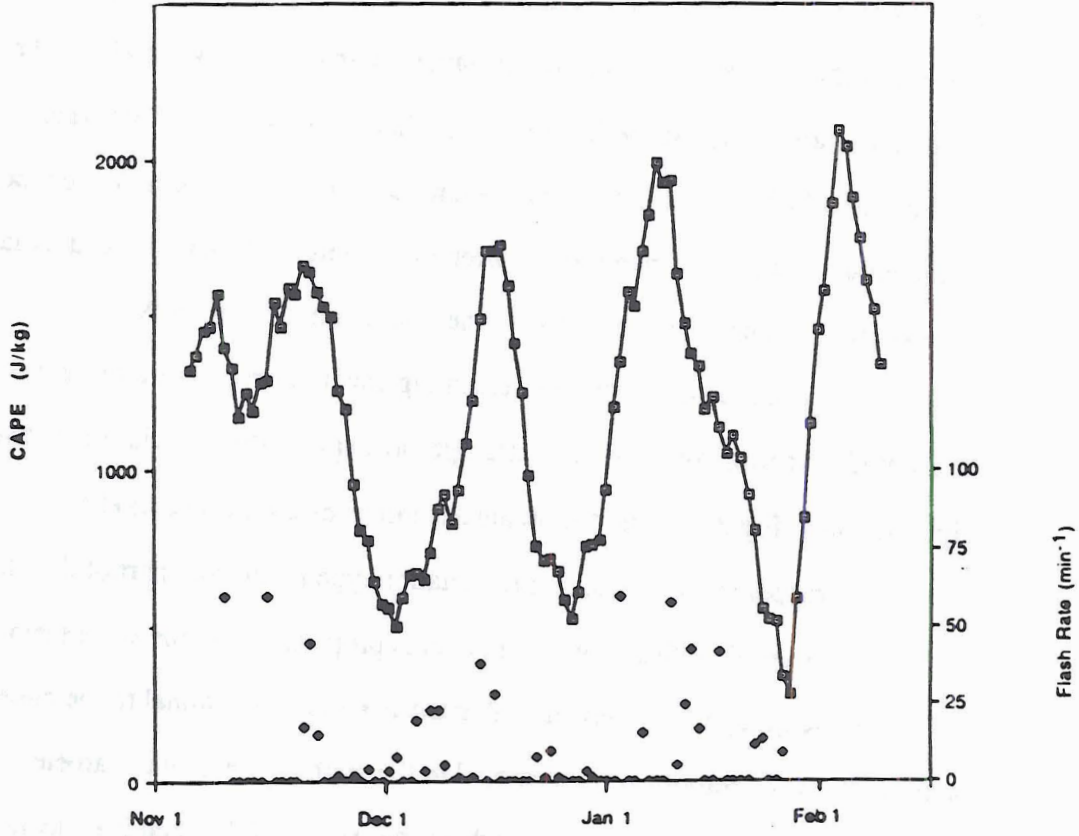


Fig. 3.3: Time series of Convective Available Potential Energy and lightning rates.

$$W = V_T \quad (3.3)$$

$$W \sim \text{CAPE}^{1/2} \quad (3.4)$$

Relations 3.1 through 3.4 may be combined to yield the final relationships:

$$Z \sim W^{12} \sim \text{CAPE}^6 \quad (3.5)$$

$$M \sim W^6 \sim \text{CAPE}^3 \quad (3.6)$$

The last two equations show that moderate changes in CAPE will produce large changes in cloud ice mass and even larger changes in radar reflectivity. The ice mass is critical in the non-inductive charging mechanism. An increase in ice mass can be interpreted as an increase in ice concentration and consequently an increase of ice-ice interactions. As the frequency of rebounding ice collisions increases, the electrification rate will proportionally increase. Electrification may be further enhanced in the high CAPE cases by an increased supply of supercooled water produced in the corresponding areas of high updraft velocities. The numerical modelling studies presented in the following chapters will be used to give quantitative estimates of the cloud ice mass, kinetic energy, and electrical charging rates.

3.1 Break Period Case Study: 19 January, 1990

The thermodynamic profile (Fig. 3.4) and corresponding statistics (Table 3.2) from the morning sounding (0000 UTC) taken at Darwin on 19 January, 1990 show that the environment was in a state characteristic of the break period. The CAPE of 1910 Jkg^{-1} is

Table 3.2: Statistics from the 0000 UTC 19 January, 1990 Darwin sounding.

	BREAK PERIOD: 19 JAN 90 0000 UTC SOUNDING
CAPE	1910.2 Jkg ⁻¹
ENERGY TO FORM MIXED LAYER	293.1 Jkg ⁻¹
VERTICAL VELOCITY AT EQUILIBRIUM LEVEL	61.8 ms ⁻¹
CONVECTIVE CONDENSATION LEVEL	812.0 hPa
LEVEL OF FREE CONVECTION	812.0 hPa
PRECIPITABLE WATER	2.15 inches
CONVECTIVE TEMPERATURE	37.6 °C
MEAN U-COMPONENT LOWEST 2 KM	0.9 ms ⁻¹
U-COMPONENT AT EQUILIBRIUM LEVEL	-19.6 ms ⁻¹
FREEZING LEVEL	5493.3 m

well above the average break period environment of 1194 Jkg^{-1} . The wind structure is also typical of the break period with easterlies at low levels and westerlies aloft.

Soundings were taken later in the day near Koolpinyah, where the MIT radar was located (Fig. 3.5) at 0330 UTC and shortly after 0600 UTC. The first of these soundings (Fig. 3.6) shows a much stronger cap than in the Darwin 0000 UTC sounding. The energy (971 Jkg^{-1}) required to mix out the lowest 100 hPa contributes to the extremely low CAPE value of 43.2 Jkg^{-1} . Additional sounding statistics for this sounding are shown in Table 3.3. The moisture profile is essentially identical to the Darwin sounding.

After a few more hours of heating, the 0600 UTC sounding indicates that the nocturnal inversion is virtually eliminated and the CAPE has increased to 879 Jkg^{-1} (Fig. 3.7 and Table 3.4). As the convective cape eroded away, weak convection began to form near 0552 UTC as indicated by MIT radar surveillance scans. This radar data is not presented since it is not of significant importance.

The MIT radar operators log entry at 0613 UTC reports visual confirmation of a small cell forming 10 km to the north. A sector scan taken at this time indicates that the convection is slightly more than a small cell. A 1.5 km CAPPI (Constant Altitude Plan Position Indicator) shows three regions or cores of reflectivity exceeding 40 dBZ (Fig. 3.8). The largest one located directly to the north of the radar is presumably the one mentioned in the observer's log. Because of the proximity of the cell to the radar, high elevation information is lost in a "cone of silence". However, a vertical cross section through the northern cell (0° azimuth from the radar) shows that the 40 dBZ echo extends at least to 6.5 km (Fig. 3.9).

An RHI (Range Height Indicator) was taken at 0° , and 10° azimuth at 0620 UTC (Fig. 3.10). By this time the 40 dBZ echo extended to near 8 km, well above the freezing level of 5.3 km. The echo tops are near 13 km. An entry in the MIT radar operators log at 0624 UTC is consistent with radar observations. Tops to 13 km and reflectivities of 30

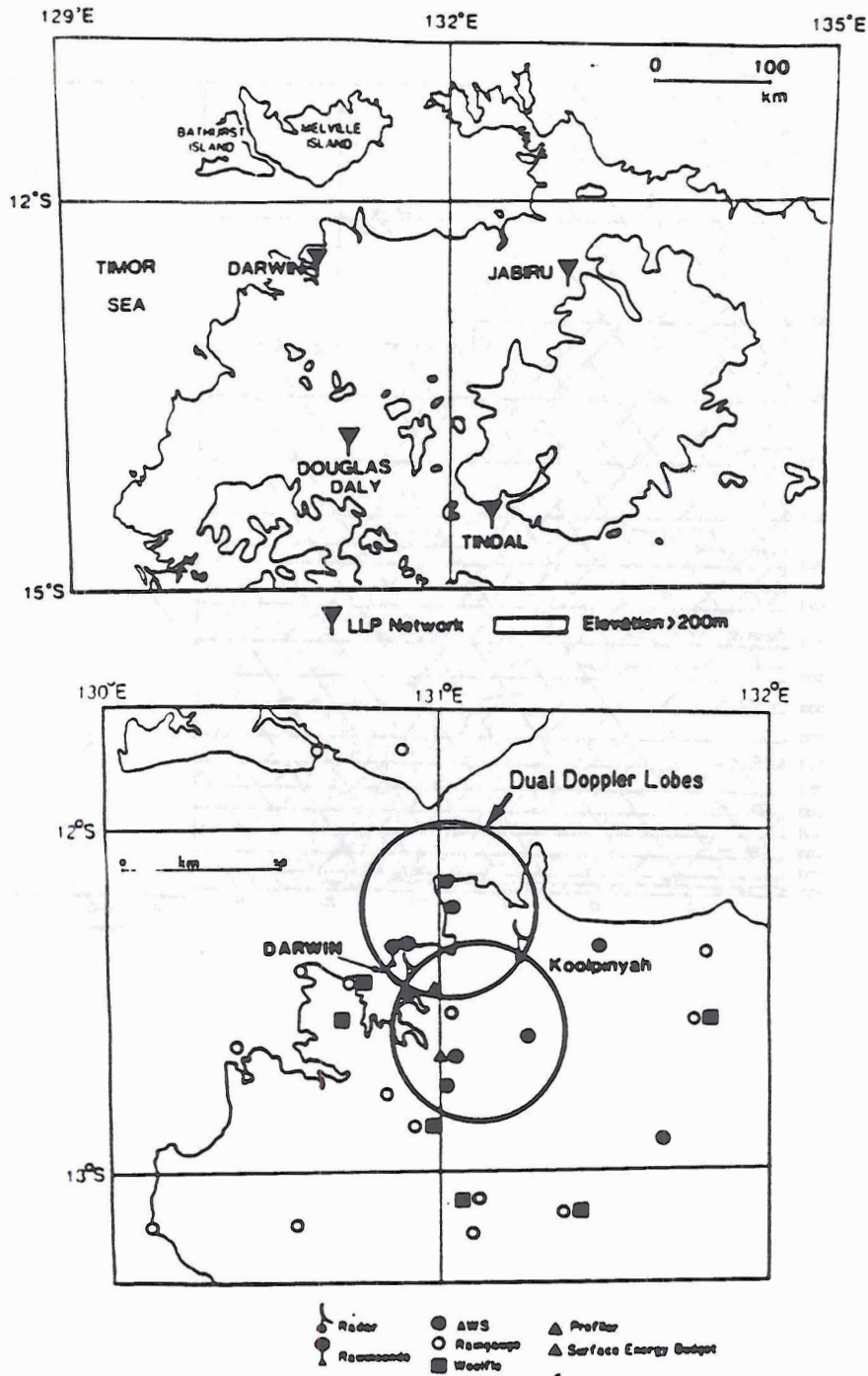


Fig. 3.5: Map of the DUNDEE region showing location of radars, sounding sites and other instrumentation.

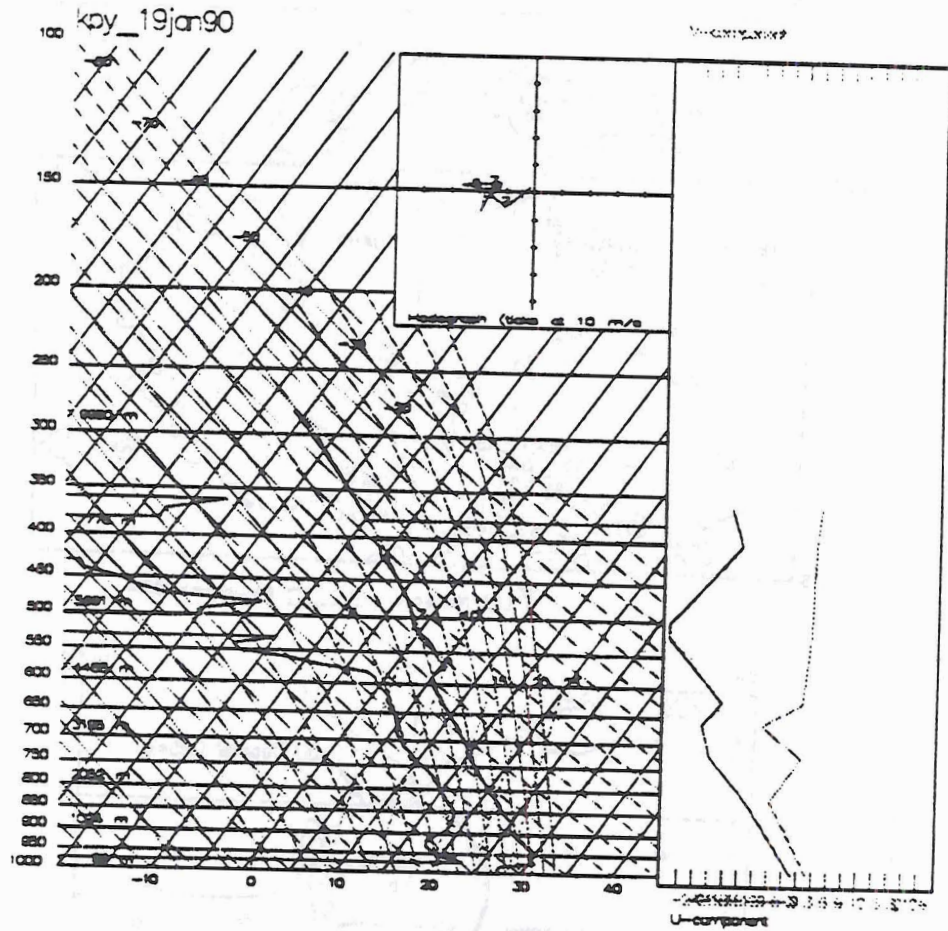


Fig. 3.6: Thermodynamic sounding taken 0330 UTC 19 January, 1990 at Koolpinyah.

Table 3.3: Statistics from the 0330 UTC 19 January, 1990 Koolpinyah sounding.

	BREAK PERIOD: 19 JAN 90 0330 UTC SOUNDING
CAPE	43.2 Jkg ⁻¹
ENERGY TO FORM MIXED LAYER	971.3 Jkg ⁻¹
VERTICAL VELOCITY AT EQUILIBRIUM LEVEL	9.3 ms ⁻¹
CONVECTIVE CONDENSATION LEVEL	650.7 hPa
LEVEL OF FREE CONVECTION	650.7 hPa
PRECIPITABLE WATER	NOT AVAILABLE
CONVECTIVE TEMPERATURE	45.3 °C
MEAN U-COMPONENT LOWEST 2 KM	-5.8 ms ⁻¹
U-COMPONENT AT EQUILIBRIUM LEVEL	-12.5 ms ⁻¹
FREEZING LEVEL	5515.8 m

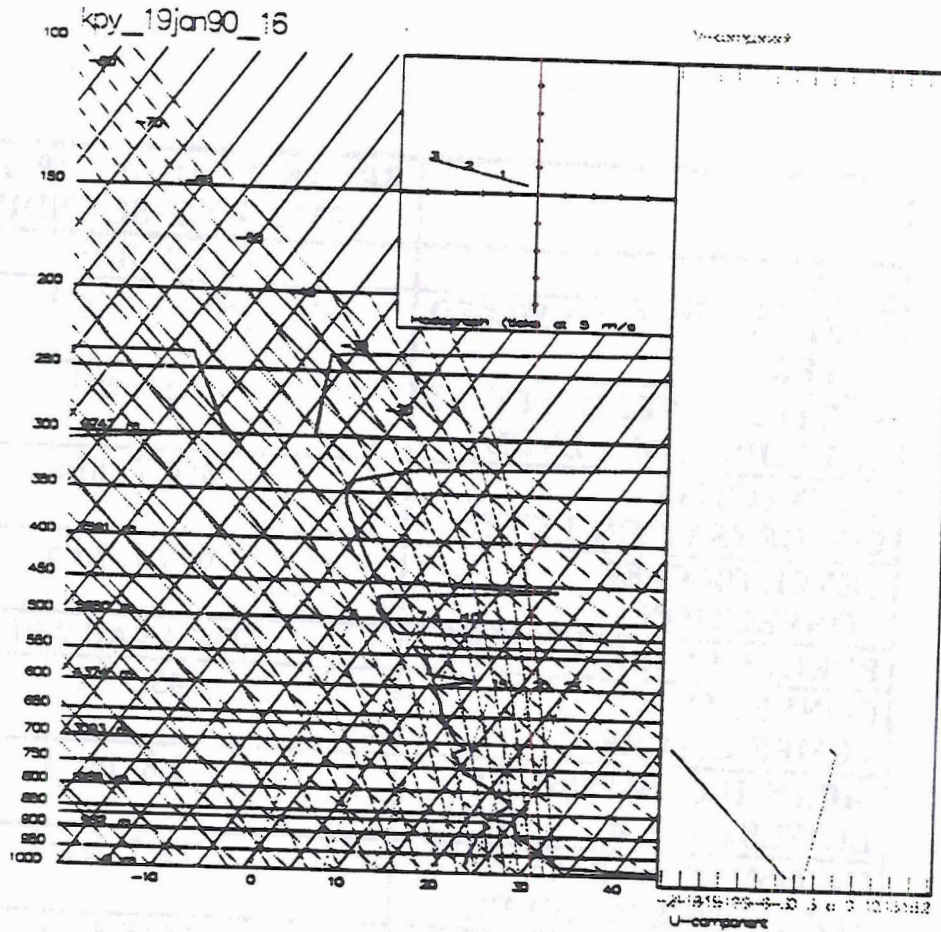


Fig. 3.7: Thermodynamic sounding taken 0630 UTC 19 January, 1990 at Koolpinyah.

Table 3.4: Statistics from the 0630 UTC 19 January, 1990 Koolpinyah sounding.

	BREAK PERIOD: 19 JAN 90 0630 UTC SOUNDING
CAPE	878.8 Jkg ⁻¹
ENERGY TO FORM MIXED LAYER	3.1 Jkg ⁻¹
VERTICAL VELOCITY AT EQUILIBRIUM LEVEL	41.9 ms ⁻¹
CONVECTIVE CONDENSATION LEVEL	908.8 hPa
LEVEL OF FREE CONVECTION	908.8 hPa
PRECIPITABLE WATER	NOT AVAILABLE
CONVECTIVE TEMPERATURE	32.2 °C
MEAN U-COMPONENT LOWEST 2 KM	-6.7 ms ⁻¹
U-COMPONENT AT EQUILIBRIUM LEVEL	NOT AVAILABLE
FREEZING LEVEL	5384.9 m

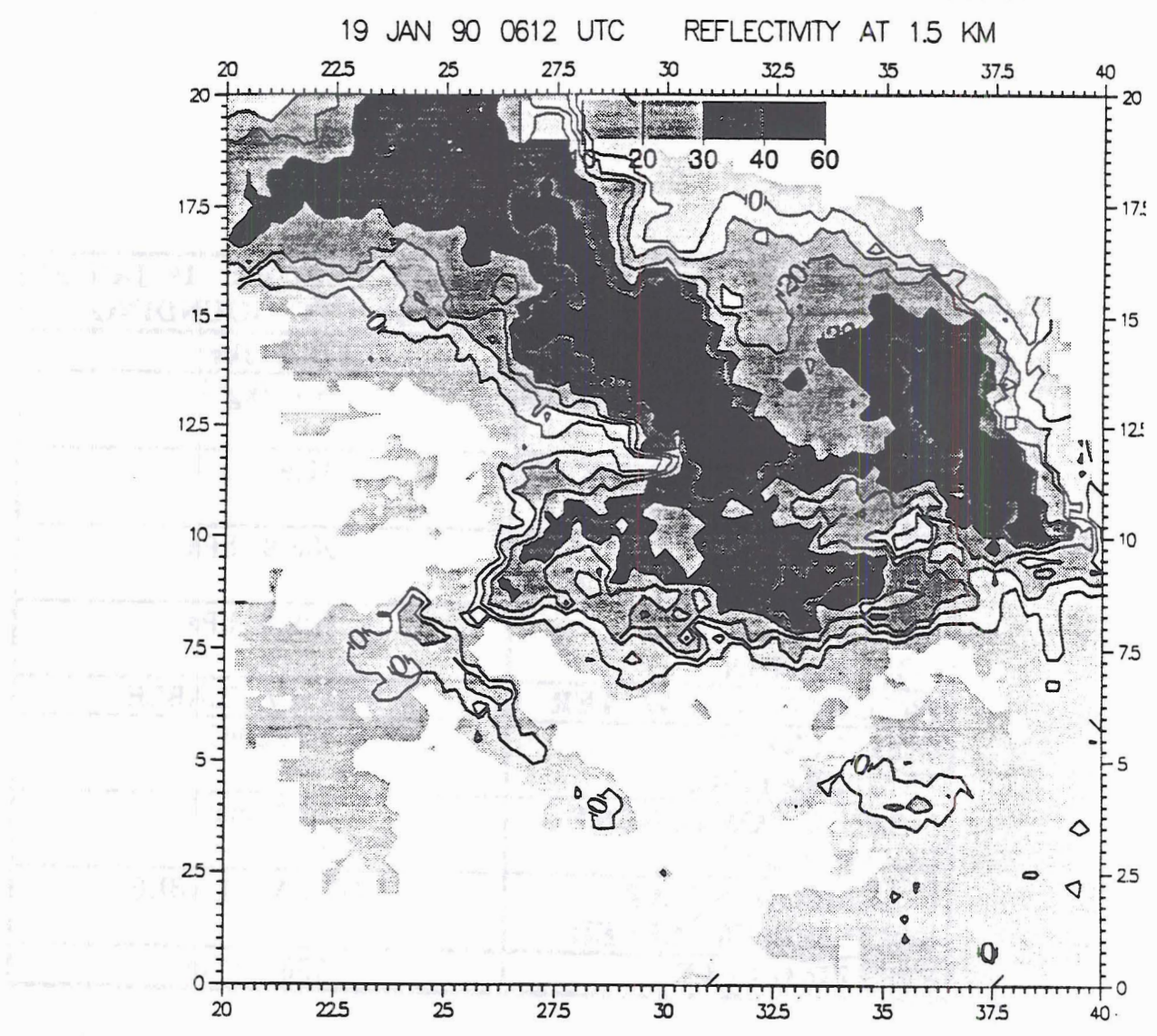


Fig. 3.8: A 1.5 km reflectivity CAPPI (Constant Altitude Plan Position Indicator) taken at 0613 UTC. The MIT radar is located at x=27 km, y=7 km).

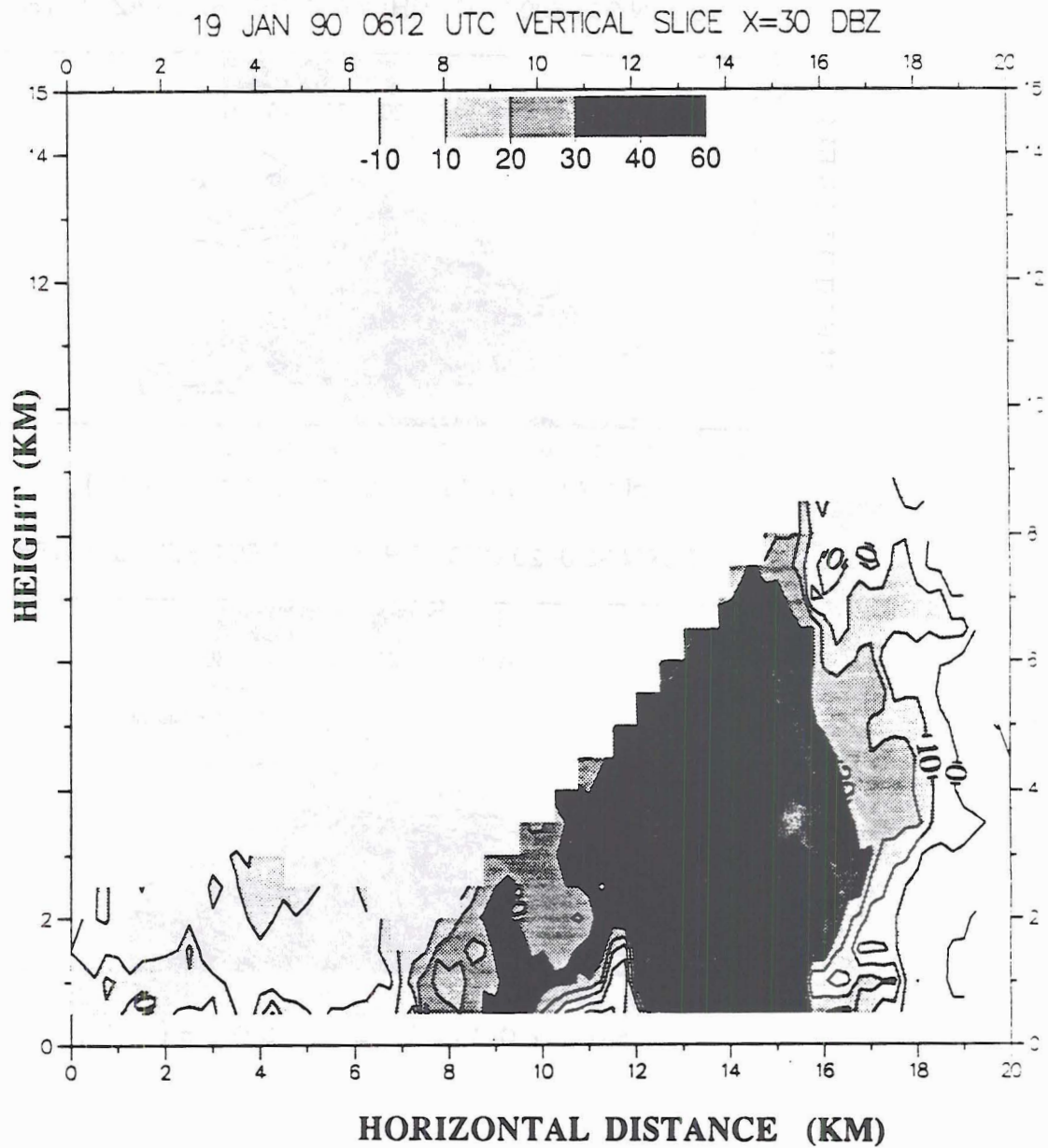


Fig. 3.9: A vertical slice of radar reflectivity through the 0613 volume scan (Fig. 3.8) taken at $x=30$ km.

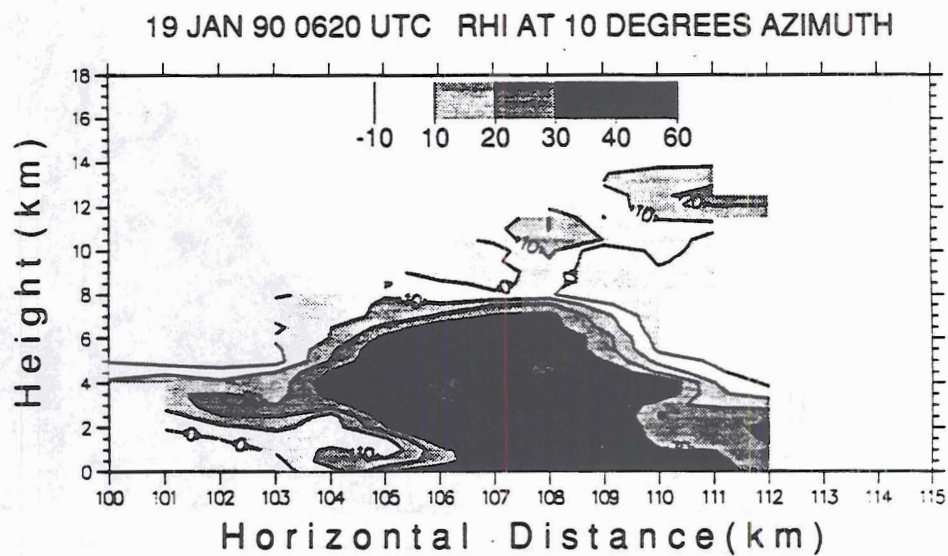
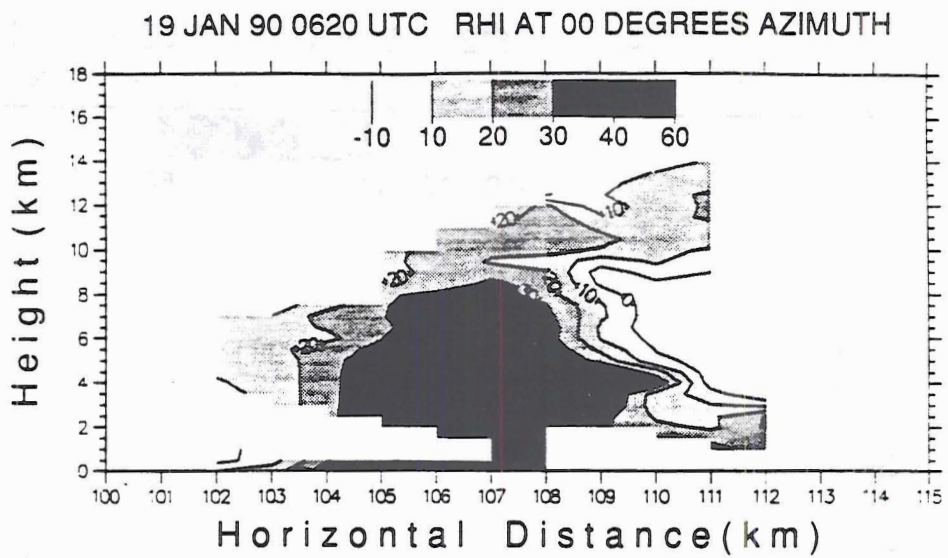


Fig. 3.10: RHI (Range Height Indicator) reflectivity scans taken at 0620 UTC at 0 and 10 degrees azimuth.

dBZ are noted as high as 10 km. Rain was also reported to begin falling at the radar site at this time.

Unfortunately there is gap in the radar and log data of approximately 15 minutes beginning after the RHIs were completed. A log entry at 0636 UTC reports 18 km tops, 20 dBZ echoes up to 17 km, and a lightning flash rate of at least 20 min^{-1} based on thunder. The flat plate antennae recording the vertical electric field at the MIT radar site indicates that electrical activity was intense at this time (Fig. 3.11). Also from Fig. 3.11, significant perturbation of the fair weather electric indicating the onset of significant cloud charging, and the first lighting event can be determined. These occurred at 0619 UTC and 0624 UTC respectively.

A volume scan was taken at 0637 UTC while the cell passed over the radar. A CAPPI at 1.5 km shows an extensive region of reflectivity greater than 40 dBZ, with some regions in excess of 50 dBZ (Fig. 3.12a). The cell to the west-southwest of the radar was triggered along the outflow boundary of the northern cell (Fig. 3.12b). Echoes in excess of 50 dBZ extending above 5 km are indicated (Fig. 3.13). Once again, because of the proximity of the storm to the radar, the data becomes scarce at the high elevation angles. However, the 20 dBZ echo mentioned in the log at an altitude of 17 km is apparent in the 17 km CAPPI (not shown).

Based on further log entries, the system weakens only slightly as it moves south, maintaining a 30 dBZ echo up to 16 km and an echo top of 17 km through 0650 UTC. After this time, the cell collapsed as rapidly as it formed: Tops fell to 14 or 15 km and the 30 dBZ echo dropped to only 6 km by 0658 UTC. The flash rate decreased to only 1 or 2 min^{-1} .

In summary, the chronological history of the storm is as follows and is also schematically shown in Fig 3.15:

- 0600: Convection begins. CAPE is near 880 Jkg^{-1} .

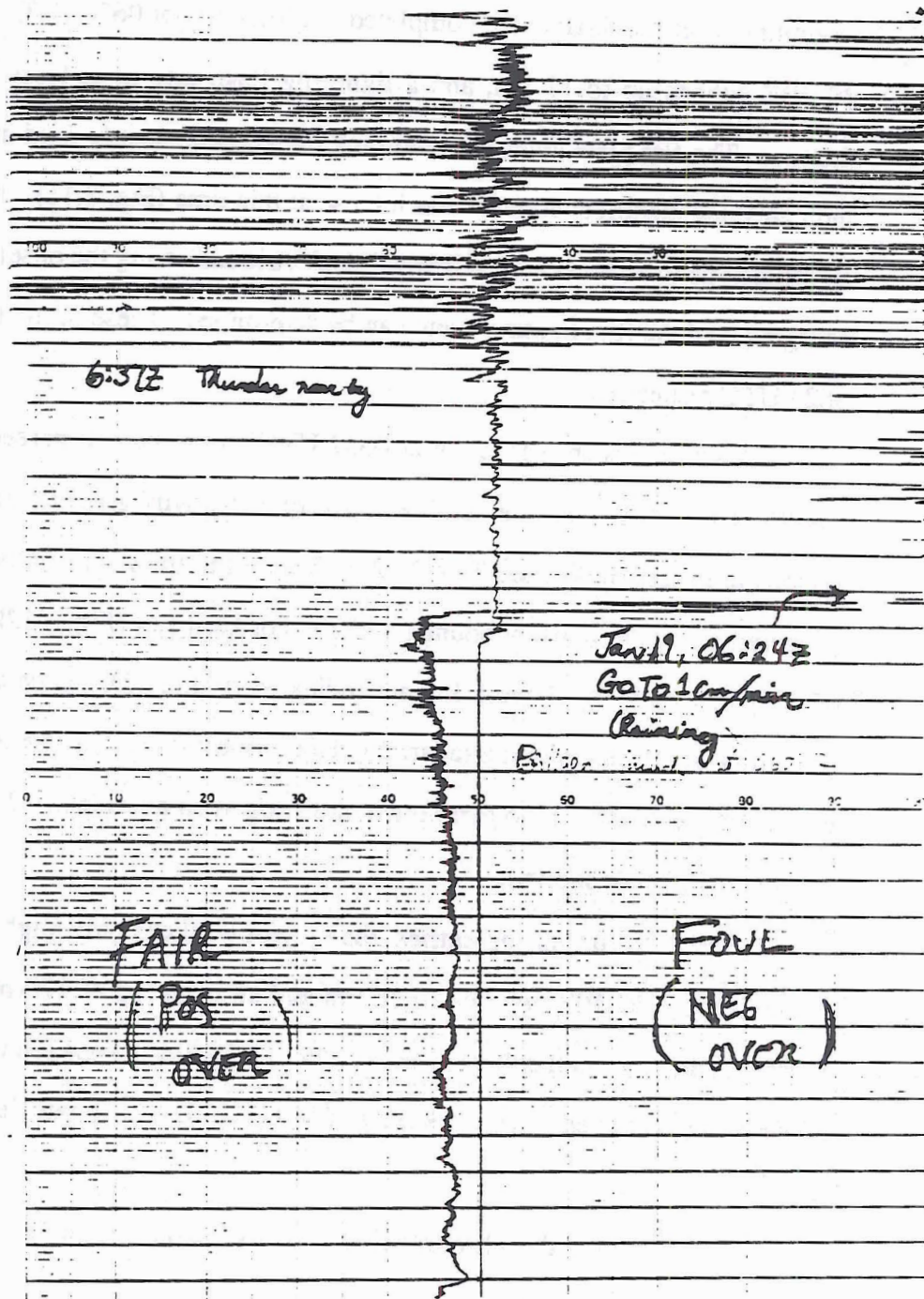


Fig. 3.11: Recording of the vertical electric field at the MIT radar site on 19 January, 1990.

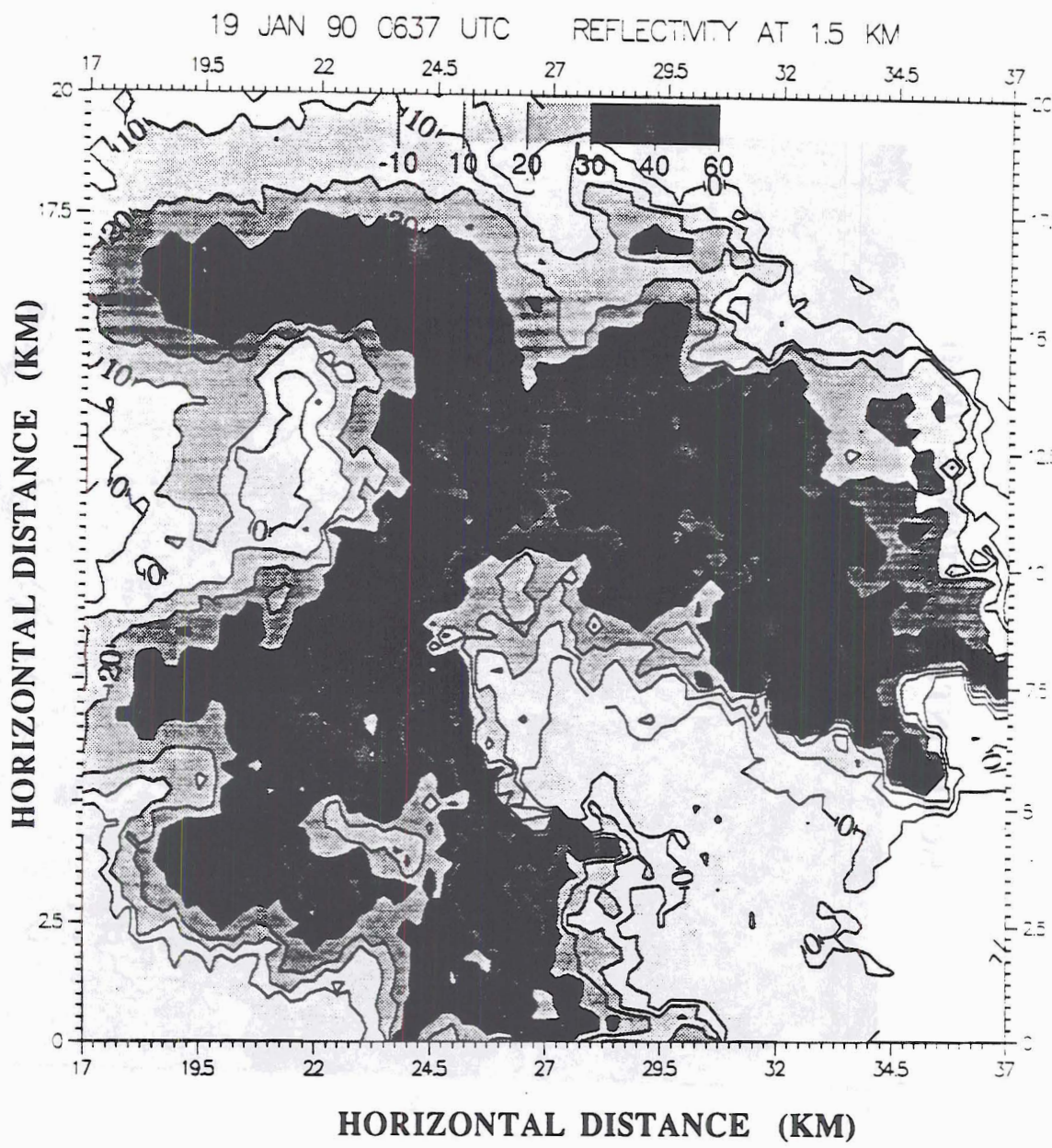


Fig. 3.12a: Same as Fig. 3.8, but at 0637 UTC.

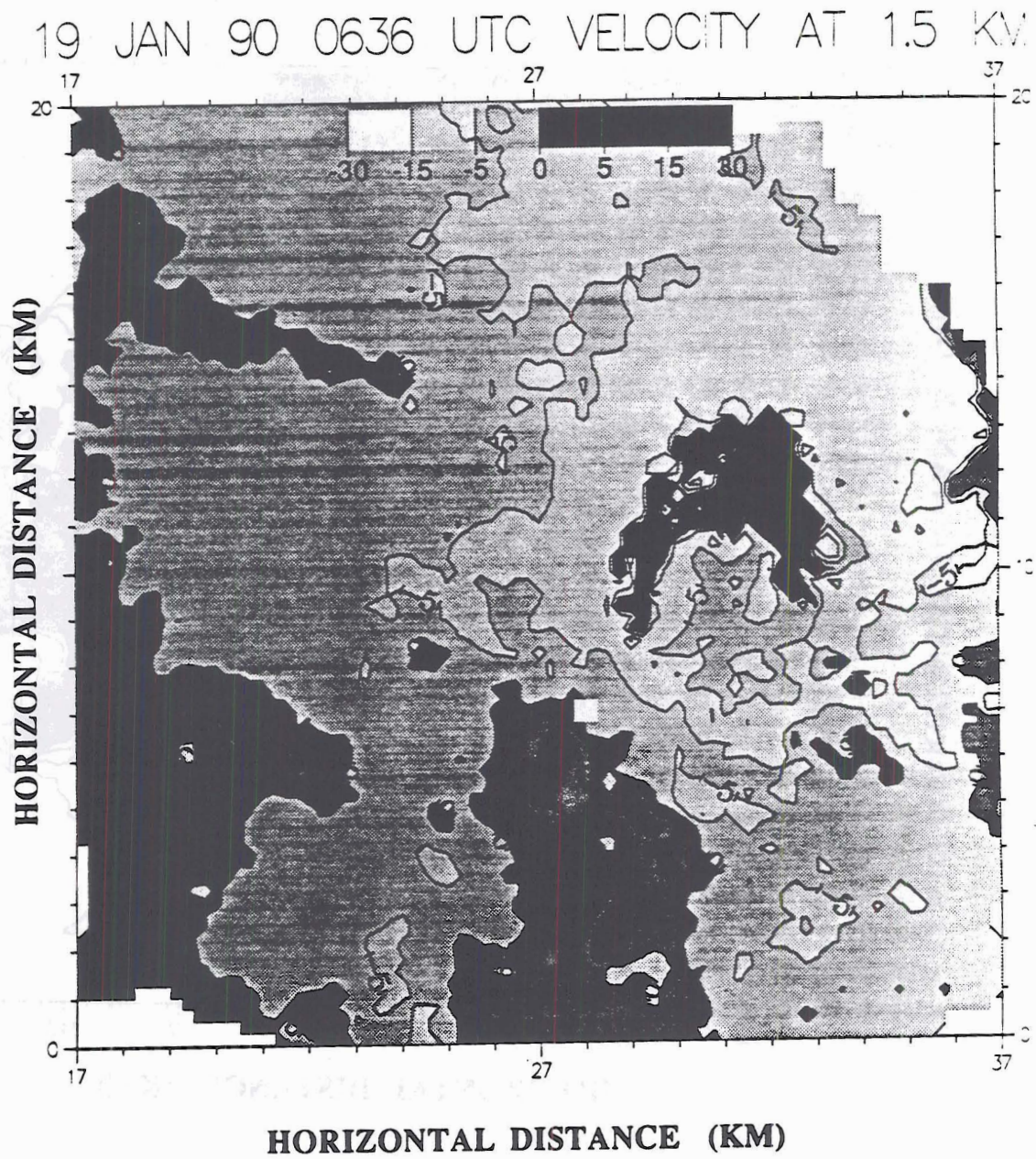


Fig. 3.12b: Same as Fig. 3.12a, but for velocity.

19 JAN 90 0636 UTC VERTICAL SLICE X=32 DBZ

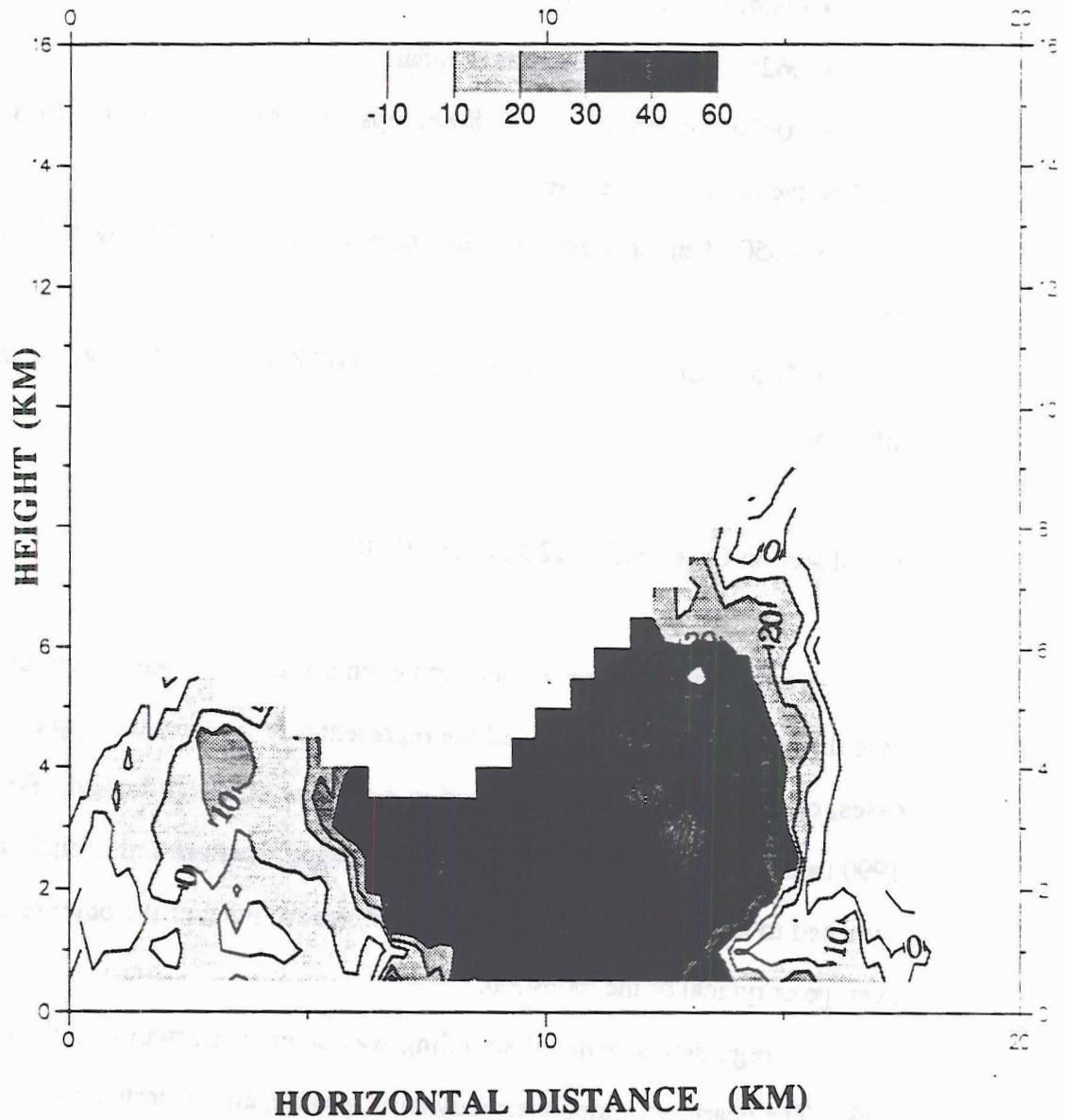


Fig. 3.13: A vertical slice of radar reflectivity through the 0636 volume scan taken at x=32 km.

- 0612: Convection is sighted visually 10 km to the north. Radar shows echoes in excess of 40 dBZ at low elevations.
- 0619: charging begins
- 0620: RHI shows 40 dBZ echo as high as 8 km and tops near 13 km.
- 0624: First lightning
- 0625: Rain begins falling at radar.
- 0636: Storm matures. 18 km tops, 20 dBZ up to 17 km. Flash rate 20 min⁻¹. based on the flat plate antennae.
- 0650: Cell changes very little through this time. 30 dBZ to 16 km. Tops to 17 km.
- 0658: Convection dies rapidly. 30 dBZ to 6 km. Tops at 14 km and flash rate only 1 or 2 min⁻¹.

3.2 Monsoon Case Study: 12 January, 1990

The limited number of monsoon events available made it very difficult to select a case that was "average" or had all the representative features of a typical monsoon. In all cases, one or more attributes seemed to be absent or compromised. For the 12 January, 1990 case that was selected, the tropospheric wind structure was initially atypical, but later switched to northwesterly flow. As will be shown, most of the other features were nearly average or typical of the monsoon.

A regularly scheduled sounding was taken at Darwin at 0000 UTC, 12 January, 1990. The nearly saturated thermodynamic profile, and easterlies aloft indicate conditions characteristic of the monsoon (Fig. 3.14). The monsoon trough (ITCZ) was located to north at this time resulting in the uncharacteristic easterly flow at low levels. The trough passed through Darwin later in the day and the lower tropospheric winds switched around to northwesterly, as evidenced by the sounding taken at 0330 UTC (Fig. 3.15).

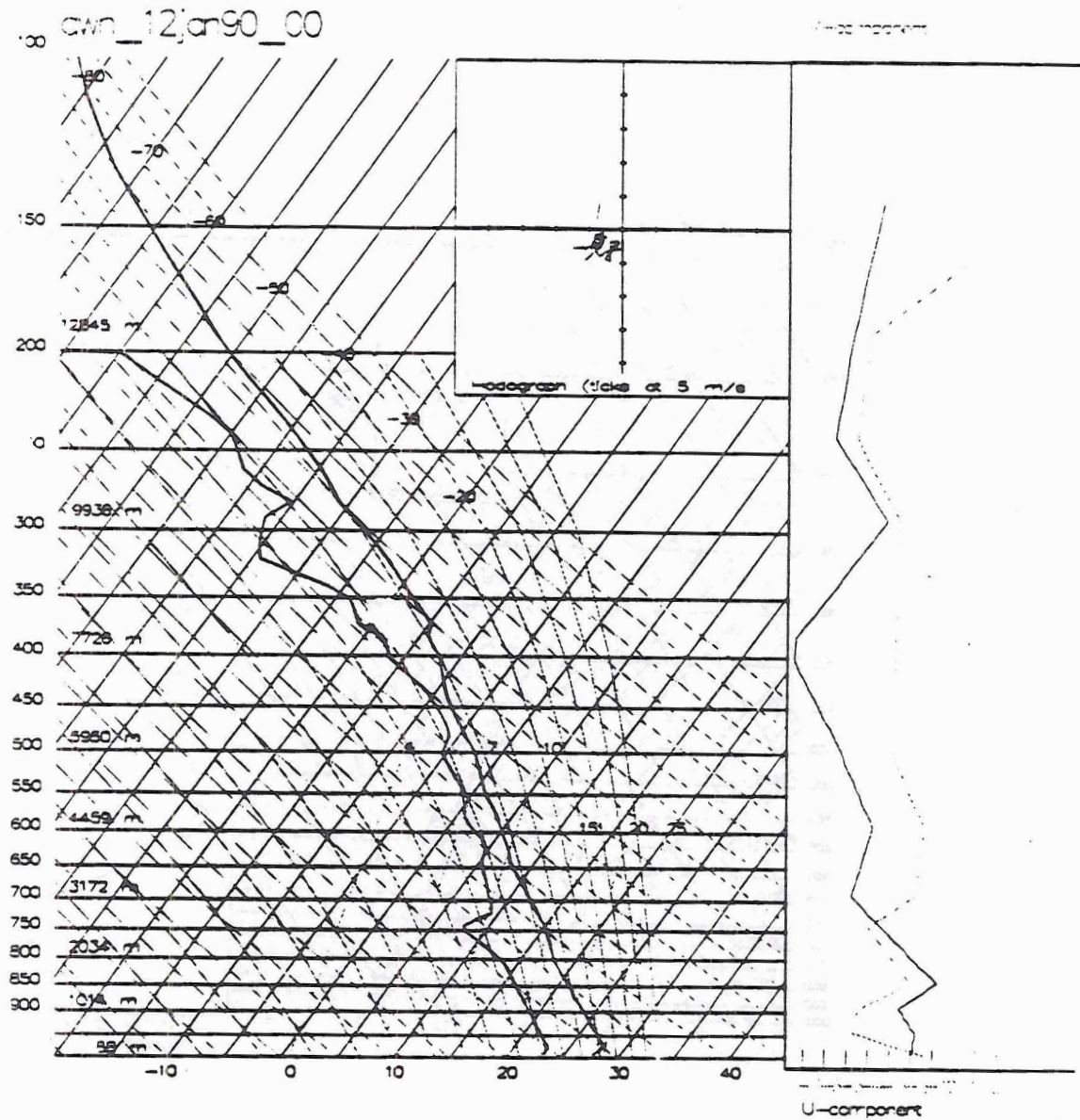


Fig. 3.14: Thermodynamic sounding taken 0000 UTC, 12 January, 1990 at Darwin.

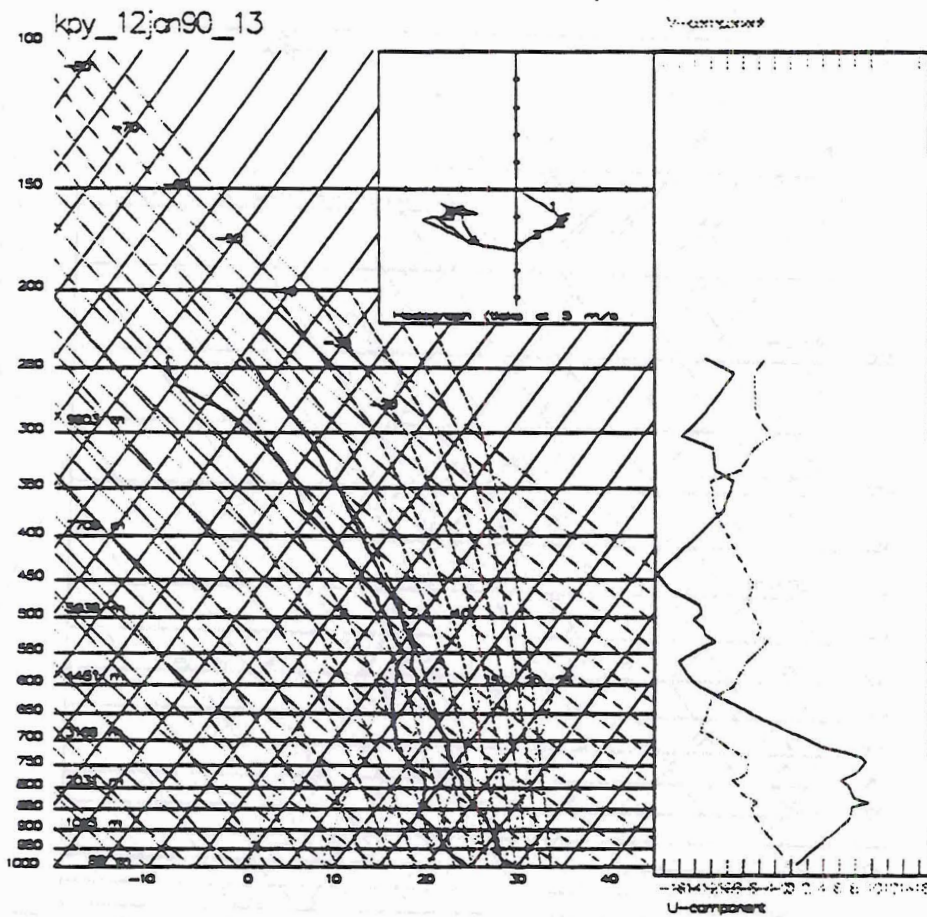


Fig. 3.15: Thermodynamic sounding taken at 0330 UTC, 12 January, 1990 at Koolpinyah.

The thermodynamic statistics and overall thermodynamic structure associated with the 0000 UTC sounding (Table 3.5) are very similar to those of the average monsoon cases (Table 3.1). The CAPE is noticeably larger (*i.e.*, 319 J kg^{-1} instead of zero), but is still small in absolute terms and certainly much less than the average break period CAPE (1194 J kg^{-1}). Below about 700 hPa, the sounding is conditionally unstable. Above this layer the sounding is approximately moist adiabatic up to about 400 hPa, and slightly stable above 400 hPa. This profile is characteristic of both the average monsoon and break period convection.

The MIT radar recorded two convective systems during the day. At 0340 UTC radar echo tops were near 10.5 km (Fig. 3.16a). The highest reflectivity values were near 40 dBZ and extended to a depth of only about 5.0 km and orientated in a northwest to southeast line (Fig. 3.16b). A sector scan taken at 0355 shows that the convection was moving southeast at about 10 ms^{-1} (Fig. 3.17a). The reflectivity structure remained similar to the previous time (Fig. 3.17b).

A more organized and vigorous squall line passed through the radar coverage area between 0730 UTC and 1010 UTC. This system was studied in detail by Keenan and Rutledge (1991). A 360° volume scan at 1010 UTC highlights a northeast to southwest line of convection with low level echoes (up to near 5 km) slightly in excess of 40 dBZ (Fig. 3.18). There are indications of a transition zone and trailing stratiform region similar to the structure seen in middle latitude mesoscale convective systems (Houze *et al.*, 1989). A bright band at 4.25 km is clearly evident. Another volume scan was taken at 1020 UTC (Fig. 3.19). The convection is still organized into a weak squall line and has propagated to the southeast.

The electric field trace for the day indicated very little electrical activity (not shown). There were no lightning flashes recorded by the flat plate antennae which is consistent with the amount of activity expected during the monsoon. Also, there were no cloud-to-ground

Table 3.5: Statistics from the 0000 UTC, 12 January, 1990 Darwin sounding.

	MONSOON: 12 JAN 90 0000 UTC SOUNDING
CAPE	313.8 Jkg ⁻¹
ENERGY TO FORM MIXED LAYER	90.2 Jkg ⁻¹
VERTICAL VELOCITY AT EQUILIBRIUM LEVEL	25.1 ms ⁻¹
CONVECTIVE CONDENSATION LEVEL	881.0 hPa
LEVEL OF FREE CONVECTION	881.0 hPa
PRECIPITABLE WATER	2.5 INCHES
CONVECTIVE TEMPERATURE	31.1
MEAN U-COMPONENT LOWEST 2 KM	-1.8 ms ⁻¹
U-COMPONENT AT EQUILIBRIUM LEVEL	-7.4 ms ⁻¹
FREEZING LEVEL	5174.5 m

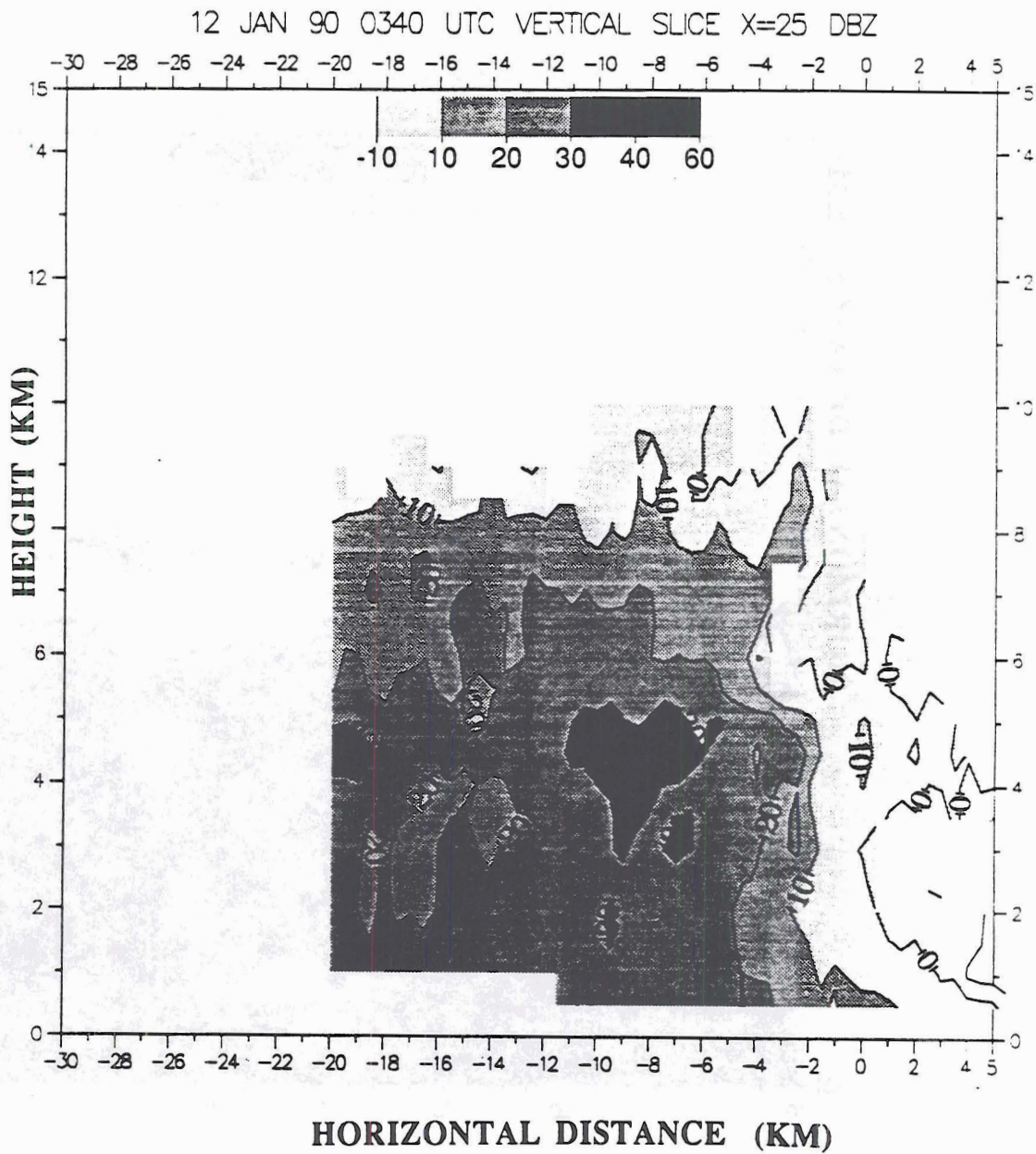


Fig. 3.16a: Vertical slice ($x=25$ km) through the volume scan taken 0340 UTC, 12 January, 1990.

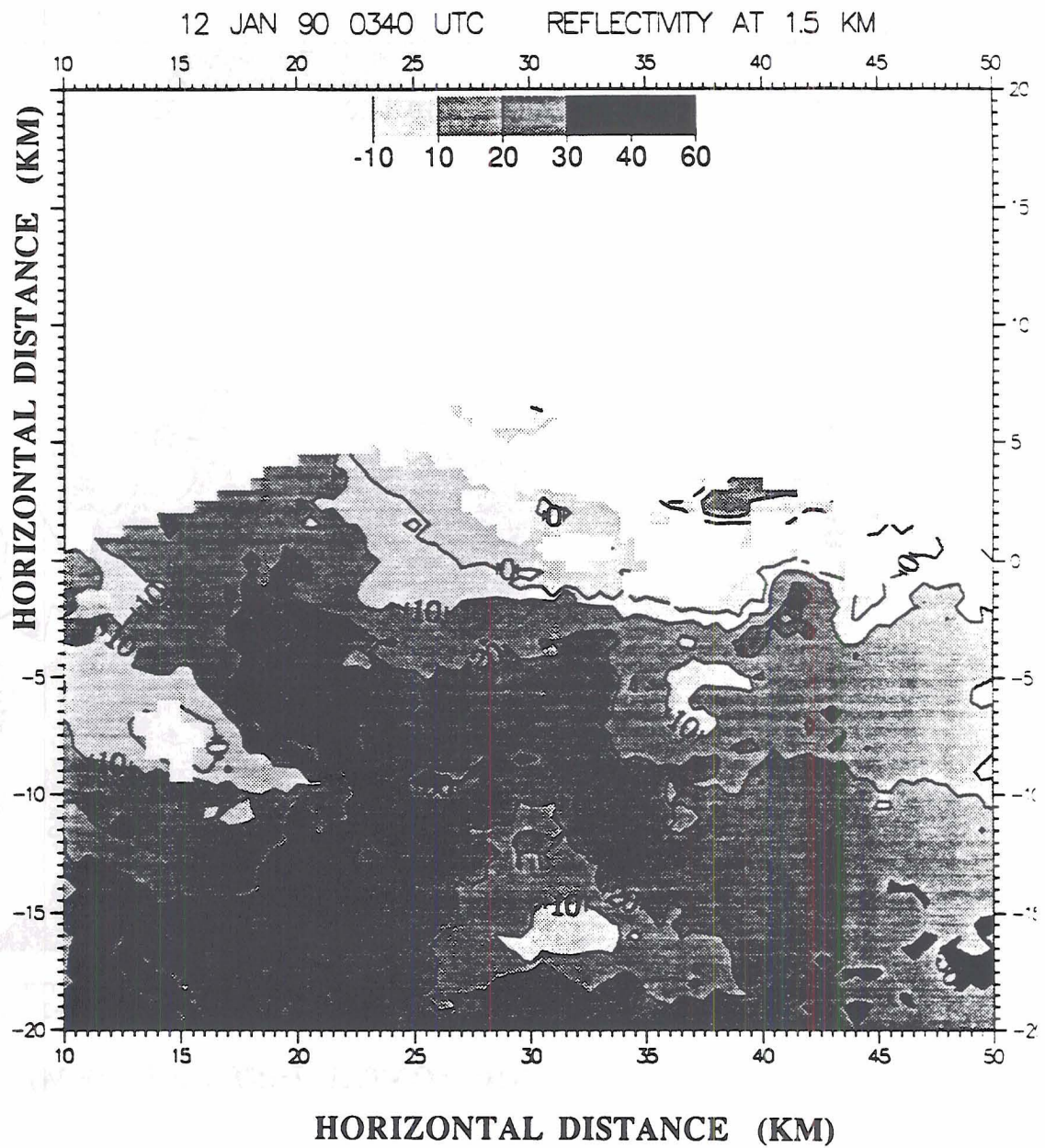


Fig. 3.16b: A 1.5 km CAPPI taken at 0340 UTC, 12 January, 1990. The MIT radar is located at $x=27$ km, $y=7$ km.

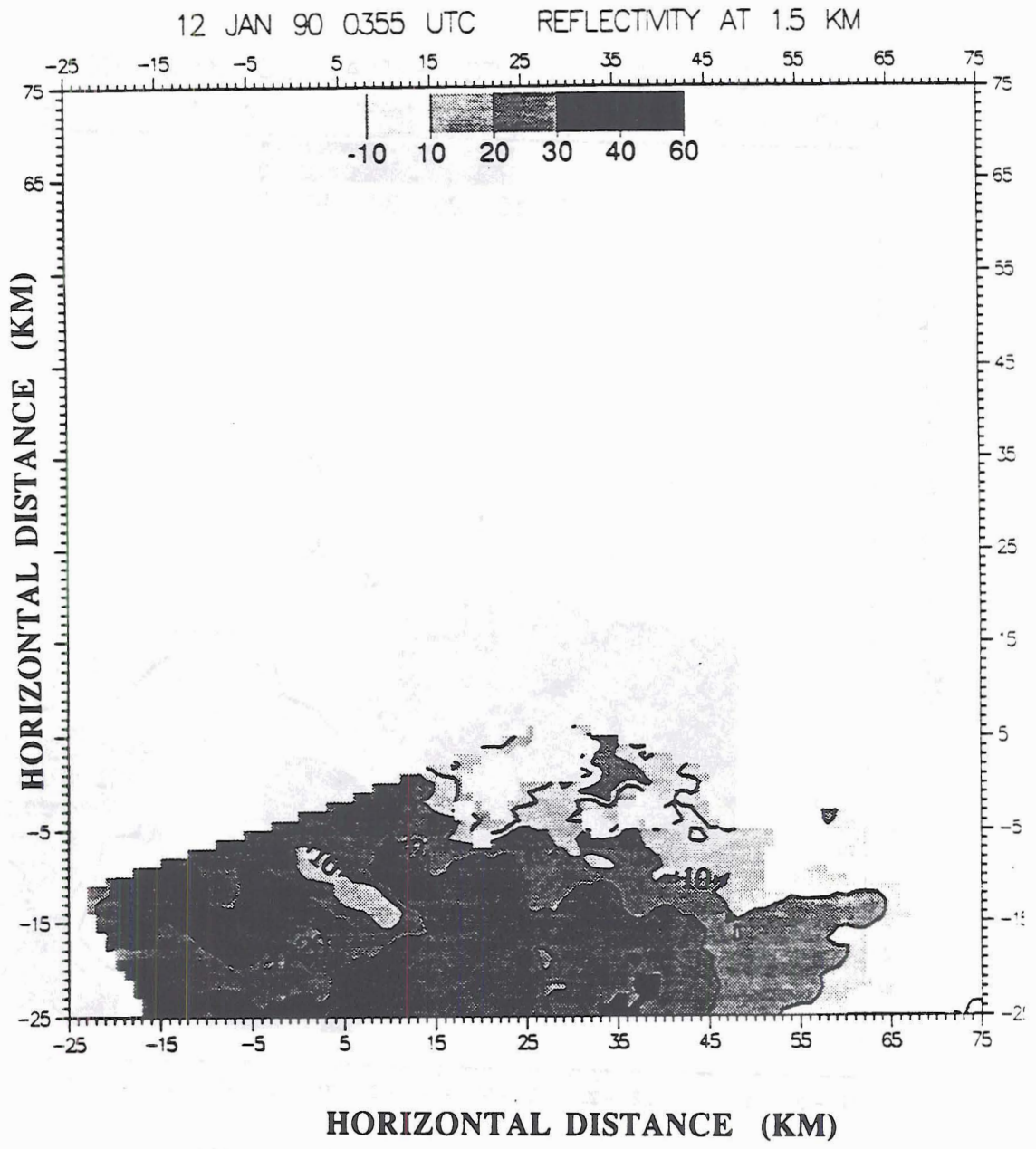


Fig. 3.17a: Same as Fig. 3.16b, except at 0355 UTC.

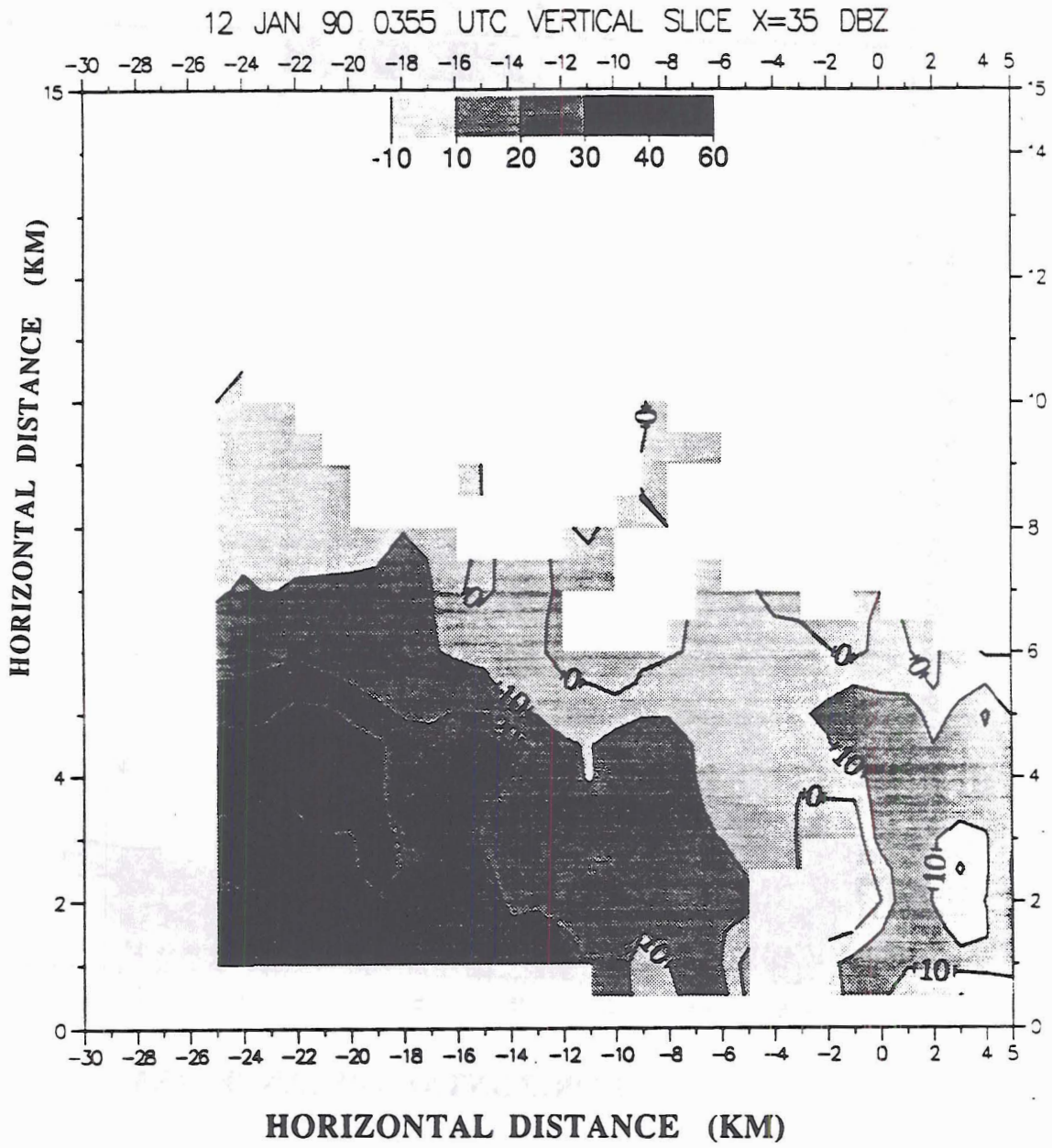


Fig. 3.17b: Same as Fig. 3.16a, except at 0355 UTC and at x=35 km.

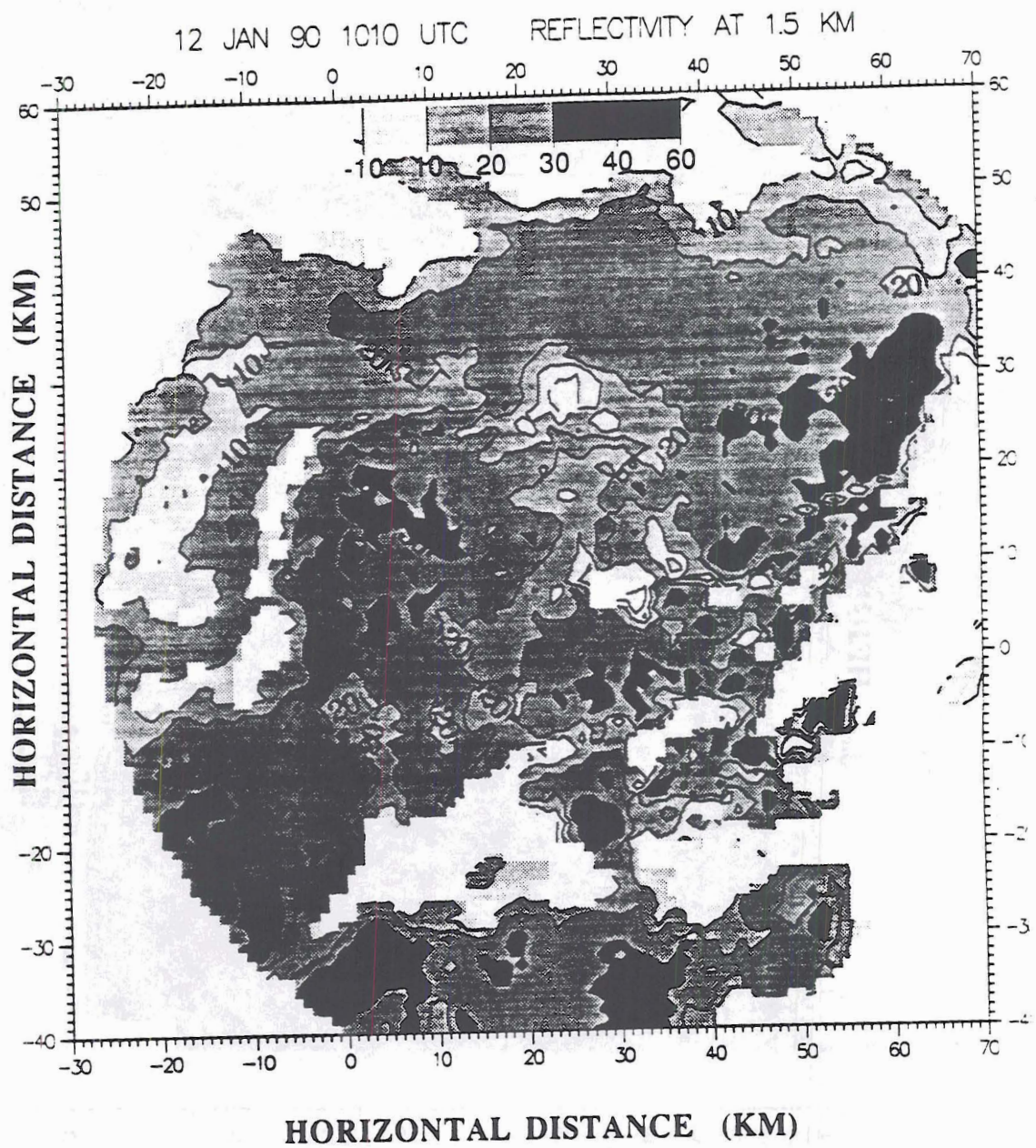


Fig. 3.18a: Same as Fig. 3.16b, except at 1010 UTC.

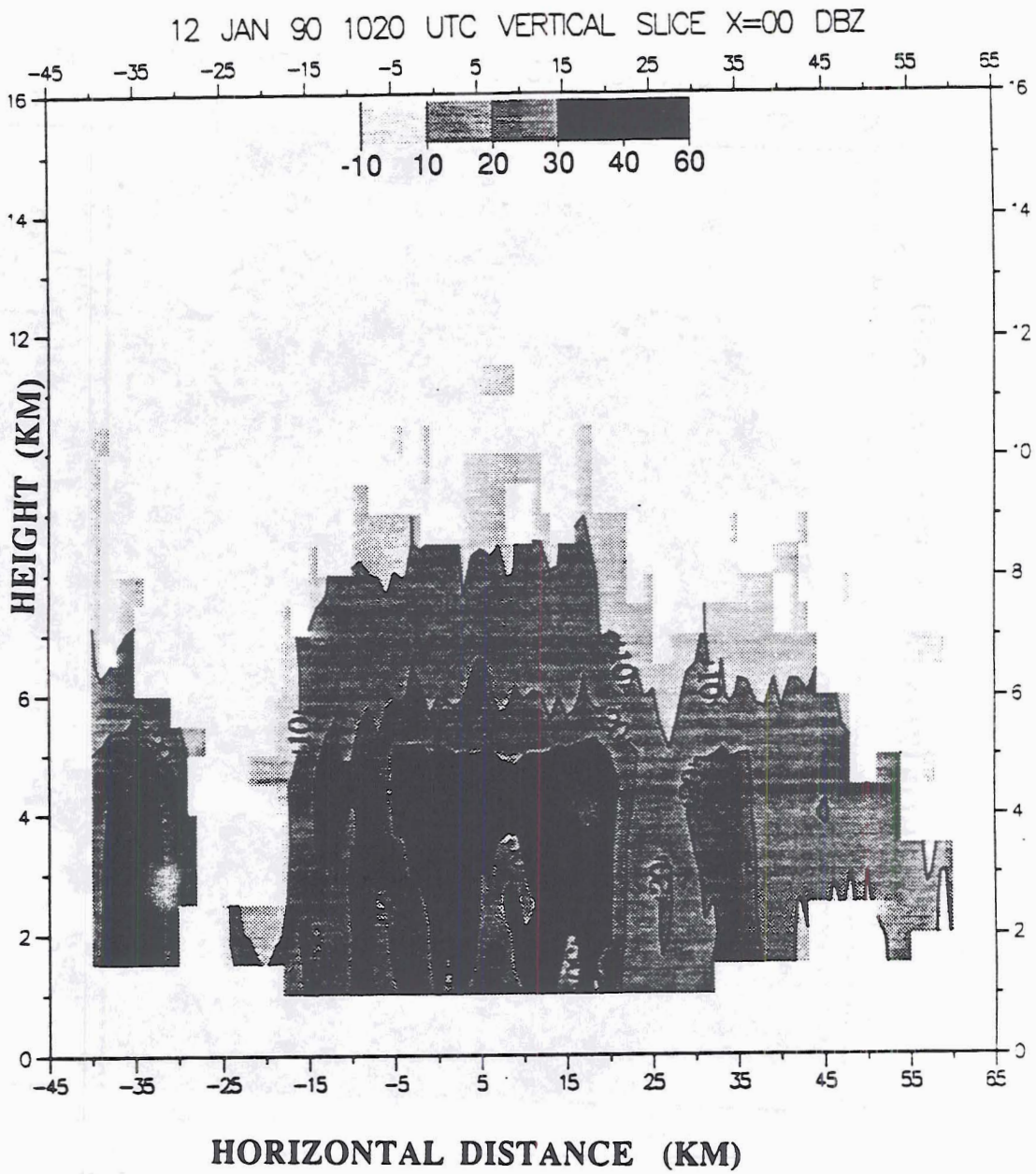


Fig. 3.19b: Same as Fig. 3.16a, except at 1020 UTC and at $x=0$ km.

flashes recorded by the LLP (Lightning Location and Protection, Inc) network within a 50 km radius of the MIT radar site from 0300 UTC to 1200 UTC.

No documentation of the complete life cycle of the systems was recorded on this day. Because of this, the generally poor organization of the convection, and limitations of the numerical model, a decision was made not to try and explicitly model the monsoon convection. Instead, using the 12 January, 1990 sounding, an attempt was made to simulate convection which resembled or had the characteristics of the convection that was observed on this day. This is in direct contrast to the break period case of 19 January, 1990 where the actual storm was simulated.

The important features to keep in mind for the monsoon case are:

- A nearly saturated thermodynamic profile typical of the "average" monsoon.
- Low CAPE (314 Jkg^{-1})
- An initial low level wind structure not usually associated with the monsoon (easterlies instead of westerlies).
- Reflectivity values seldom exceed 40 dBZ above about 5 km. Radar echo tops are generally less than 10 km.
- No lightning activity.

CHAPTER IV

MODEL DESCRIPTION

The numerical model used in this study has evolved over the last twenty-five years from the one constructed by Orville (1965) to study cumulus convection. The dynamics are represented by a vorticity equation and a density weighted stream function similar to those described by Takeda (1971), Schlesinger (1973a,b), and Hane (1975). Subgrid scale mixing is represented using nonlinear eddy coefficients as described by Drake et al (1974). The thermodynamics are not addressed here, but are coupled to the dynamics and microphysics. The dynamic coupling is addressed by Schlesinger (1973). The coupling of the thermodynamics and microphysics is presented by Lin *et al.*, (1983). The reader is referred to Appendix A: List of Symbols for an explanation of the notation used in the equations in this chapter.

4.1 Dynamics

The dynamical equations used in the model are based on a density weighted streamfunction and vorticity equation. These may be derived by first considering the following approximate forms of the momentum equation (in two dimensions) and the continuity equation:

$$\frac{\partial u}{\partial t} = -u \frac{\partial u}{\partial x} - w \frac{\partial u}{\partial z} - \frac{1}{\rho_0} \frac{\partial \hat{p}}{\partial x} + F_x \quad (4.1),$$

$$\frac{\partial w}{\partial t} = -u \frac{\partial w}{\partial x} - w \frac{\partial w}{\partial z} - \frac{1}{\rho_0} \frac{\partial \hat{p}}{\partial z} + g \left(\frac{\hat{T}_v}{T_{v0}} - \frac{\hat{p}}{p_0} - \frac{L}{p_0} \right) + F_z \quad (4.2),$$

$$\frac{\partial}{\partial x}(\rho_0 u) + \frac{\partial}{\partial z}(\rho_0 w) = 0 \quad (4.3).$$

Note that the effect of precipitation loading (L) on the buoyancy is accounted for in 4.2. A stream function will satisfy the continuity equation if it takes the form

$$u = \frac{1}{\rho_0} \frac{\partial \psi}{\partial z} \quad (4.4),$$

$$w = -\frac{1}{\rho_0} \frac{\partial \psi}{\partial x} \quad (4.5).$$

A density weighted vorticity is then defined by

$$\eta = \nabla^2 \psi \quad (4.6).$$

Through cross differentiation of 4.1 and 4.2, and using the continuity equation (4.3) and the definition of the stream function (4.4 and 4.5) a vorticity equation is obtained:

$$\frac{\partial \eta}{\partial t} = -u \frac{\partial \eta}{\partial x} - w \frac{\partial \eta}{\partial z} + g \rho_0 \left(\frac{1}{p_0} \frac{\partial \hat{p}}{\partial x} - \frac{1}{T_{v0}} \frac{\partial \hat{T}_v}{\partial x} \right) + g \frac{\partial L}{\partial x} \quad (4.7).$$

$$+ \frac{2w}{\rho_0} \frac{\partial \rho_0}{\partial z} \left(\eta - u \frac{\partial \rho_0}{\partial z} \right) + uw \frac{\partial^2 \rho_0}{\partial z^2} + \frac{\partial(\rho_0 F_x)}{\partial z} - \partial \left(\frac{\rho_0 F_z}{\partial x} \right)$$

The velocity fields are diagnosed by first integrating the vorticity equation (4.7). Then equation 4.6 is inverted to obtain the stream function. Finally, equations 4.4 and 4.5 are used to compute u and w . The horizontal pressure gradient is determined from the horizontal equation of motion.

4.2 Microphysics Without Electrification

The microphysical framework of the South Dakota cloud model manages cloud water, rain, cloud ice and precipitating cloud ice (graupel and hail will be used interchangeably) using standard bulk microphysical techniques. Water vapor, of course, provides the initial source of hydrometeors and constitutes the fifth class of water substance. Cloud water and cloud ice are assumed to have negligible terminal velocities compared to the vertical velocity of the air and the other hydrometeor classes. Fig. 4.1 provides a flow chart summary of the interactions which are represented.

4.2.1 Conservation of Water Substance and Parameterization of Precipitation Fields

Water substance must be conserved. In general this requires

$$\frac{\partial q}{\partial t} = -\mathbf{V} \cdot \nabla q + \nabla \cdot K_h \nabla q - P_G - P_R - P_S \quad (4.8),$$

$$\frac{\partial q_G}{\partial t} = -\mathbf{V} \cdot \nabla q_H + \nabla \cdot K_m \nabla q_G + P_G + \frac{1}{\rho} \frac{\partial}{\partial z} (V_G q_G \rho) \quad (4.9),$$

$$\frac{\partial q_R}{\partial t} = -\mathbf{V} \cdot \nabla q_R + \nabla \cdot K_m \nabla q_R + P_R + \frac{1}{\rho} \frac{\partial}{\partial z} (V_R q_R \rho) \quad (4.10),$$

$$\frac{\partial q_S}{\partial t} = -\mathbf{V} \cdot \nabla q_S + \nabla \cdot K_m \nabla q_S + P_S + \frac{1}{\rho} \frac{\partial}{\partial z} (V_S q_S \rho) \quad (4.11).$$

The terms on the right-hand side of the above equations represent the advection, subgrid scale mixing, production terms, and precipitation of hydrometeors in that order.

The three precipitating categories rain, hail, and snow are represented by Marshall-Palmer distributions,

$$n_{R,G,S}(D_{R,G,S}) = N_{0R,G,S} e^{-\Lambda_{R,G,S} D_{R,G,S}} \quad (4.12).$$

By integrating the third moment of these distributions with the density of the species, a diagnostic equation for the slope can be obtained as a function of the mixing ratio given by

$$\Lambda_{R,G,S} = \left(\frac{n_{0R,G,S} \pi \rho_{R,G,S}}{\rho q_{R,G,S}} \right)^{.25} \quad (4.13).$$

The mass weighted fall speeds of rain, graupel, and snow are computed following Srivastava (1967) where

$$V_{R,G,S} = \int_0^{\infty} V_D \frac{q(D)}{q} dD \quad (4.14),$$

and V_D is based on empirical relations determined by the laboratory studies of Gunn and Kinzer (1949), Wisner *et al.* (1969), and Locatelli and Hobbs (1974). After integration, the terminal velocities take the form:

$$V_R = \frac{a\Gamma(4+b)}{6\lambda_R^b} \left(\frac{\rho_0}{\rho} \right)^5 \quad (4.15),$$

$$V_S = \frac{c\Gamma(4+d)}{6\lambda_S^d} \left(\frac{\rho_0}{\rho} \right)^5 \quad (4.16),$$

$$V_G = \frac{\Gamma(4.5)}{6\lambda_G^{0.5}} \left(\frac{4g\rho_G}{3C_{DP}} \right)^5 \quad (4.17),$$

4.2.2 Source and Sink Terms for P_S

The continuity equation for P_S may be written

$$\begin{aligned} P_S = & P_{SAUT} + P_{SACI} + P_{SACW} + P_{SFW} + P_{SFI} + \delta_3(P_{RACI} + P_{LACR}) \\ & - P_{GACS} - P_{GAUT} - (1 - \delta_2)P_{RACS} + \delta_2 P_{SACR} + (1 - \delta_1)P_{SSUB} + \delta_1 P_{SDEP} \end{aligned} \quad (4.18)$$

if the temperature is below freezing. Equation 4.18 reduces to

$$P_S = P_{SMLT} - P_{GACS} \quad (4.19)$$

if the temperature is above freezing. Delta is nonzero for temperatures below freezing and is defined as follows:

$$\delta_1 = \begin{cases} 1, & \text{for } q_{cw} + q_{ci} > 0 \\ 0, & \text{otherwise} \end{cases}$$

$$\delta_2 = \begin{cases} 1, & \text{for } q_R \text{ and } q_S < 10^{-4} \text{ g g}^{-1} \\ 0, & \text{otherwise} \end{cases} \quad (4.20).$$

$$\delta_3 = \begin{cases} 1, & \text{for } q_R < 10^{-4} \text{ g g}^{-1} \\ 0, & \text{otherwise} \end{cases}$$

The following terms in the source/sink equation for snow (equation 4.18) are based on a continuous collection model and take the following forms:

$$P_{SACI} = \left(\frac{E_{SI} \pi n_{OS} c q_{CI} \Gamma(3+d)}{4 \lambda_S^{3+d}} \right) \left(\frac{\rho_0}{\rho} \right)^5 \quad (4.21),$$

$$P_{SACW} = \left(\frac{E_{SW} \pi n_{OS} c q_{CW} \Gamma(3+d)}{4 \lambda_S^{3+d}} \right) \left(\frac{\rho_0}{\rho} \right)^5 \quad (4.22),$$

$$P_{RACI} = \left(\frac{E_{RI} \pi n_{OR} a q_{CI} \Gamma(3+b)}{4 \lambda_R^{3+b}} \right) \left(\frac{\rho_0}{\rho} \right)^5 \quad (4.23),$$

$$P_{IACR} = \left(\frac{E_{RI} \pi^2 n_{OR} a q_{CI} \rho_w \Gamma(6+b)}{24 M_i \lambda_R^{6+b}} \right) \left(\frac{\rho_0}{\rho} \right)^5 \quad (4.24),$$

$$P_{RACS} = E_{SR} \pi^2 n_{OR} n_{OS} |V_R - V_S| \left(\frac{\rho_S}{\rho} \right) \left(\frac{5}{\lambda_S^6 \lambda_R} + \frac{2}{\lambda_S^5 \lambda_R^2} + \frac{0.5}{\lambda_S^4 \lambda_R^3} \right) \quad (4.25),$$

$$P_{SACR} = E_{SR} \pi^2 n_{OR} n_{OS} |V_R - V_S| \left(\frac{\rho_w}{\rho} \right) \left(\frac{5}{\lambda_R^6 \lambda_S} + \frac{2}{\lambda_R^5 \lambda_S^2} + \frac{0.5}{\lambda_R^4 \lambda_S^3} \right) \quad (4.26),$$

$$P_{GACS} = E_{GS} \pi^2 n_{OG} n_{OS} |V_G - V_S| \left(\frac{\rho_S}{\rho} \right) \left(\frac{5}{\lambda_S^6 \lambda_G} + \frac{2}{\lambda_S^5 \lambda_G^2} + \frac{0.5}{\lambda_S^4 \lambda_G^3} \right). \quad (4.27).$$

The collection efficiencies between snow and other ice species (E_{SI} and E_{GS}) are temperature dependent while all the other collection efficiencies involving snow are arbitrarily set to unity.

The terms P_{IACR} and P_{RACI} are peculiar in that they can be either sources for snow or graupel (but not both simultaneously). The mixing ratio of rain is the determining factor in placing the production terms appropriately. The reasoning is that if the mixing ratio of rain is below some threshold value (taken to be 10^{-4} g g^{-1}) then raindrops are most likely small enough to form particles of a density more closely related to snow. On the other hand, rain mixing ratios above the threshold value are assumed to form relatively high density particles with a closer resemblance to graupel than snow. An example of this is a large raindrop (*i.e.*, a rain drop in a region with a high mixing ratio) freezing due to contact nucleation to form a small hailstone.

The terms representing the accretion of cloud water and rain, P_{SACW} and P_{SACR} , although not explicitly appearing in the source/sink equation for snow above freezing (equation 4.19), contribute to changes in the snow concentration for temperatures above freezing. The processes appear as terms in P_{SMLT} where they represent the shedding of water to form rain and an increase in the melting rate by conduction of heat from the warmer water to the colder snow. The exact form for P_{SMLT} is:

$$P_{SMLT} = \frac{-2\pi}{\rho L_f} (K_a T_c - L_v \psi \rho \Delta r_s) n_{OS} \left[0.78 \lambda_S^{-2} + 0.31 S_C^{\frac{1}{3}} \Gamma \left(\frac{d+5}{2} \right) c^{\frac{1}{2}} \left(\frac{\rho_0}{\rho} \right)^{\frac{1}{4}} v^{-\frac{1}{2}} \lambda_S^{-\left(\frac{d+5}{2} \right)} \right] \quad (4.28).$$

$$-\frac{C_w T_c}{L_f} (P_{SACW} + P_{SACR})$$

The depositional growth rate of snow, P_{SDEP} bears close resemblance to the P_{SMLT} term since it also includes ventilation effects. The equations differ in that P_{SDEP} also includes the effect of supersaturation. The equation for P_{SDEP} is based on the work of Byers (1965) and is given by:

$$P_{SDEP} = \frac{2\pi(S_i - 1)}{\rho(A'' + B'')} n_{OS} \left[0.78 \lambda_S^{-2} + 0.31 S_C^{\frac{1}{3}} \Gamma \left(\frac{d+5}{2} \right) c^{\frac{1}{2}} \left(\frac{\rho_0}{\rho} \right)^{\frac{1}{4}} v^{-\frac{1}{2}} \lambda_S^{-\left(\frac{d+5}{2} \right)} \right] \quad (4.29),$$

where

$$A'' = \frac{L_S^2}{K_a R_w T^2} \quad (4.30).$$

$$B'' = \frac{1}{\rho r_{si} \psi}$$

It should be noted that P_{SSUB} is P_{SDEP} with the only difference being that P_{SDEP} operates in saturated air and P_{SSUB} operates outside the cloud boundary.

Of the remaining four source/sink snow terms two are based on the autoconversion ideas of Kessler (1969) for cloud drops colliding and coalescing to form rain. A fraction of cloud ice above a threshold value is assumed to aggregate to form snow, and a fraction of snow above a threshold value is assumed to aggregate to form graupel according to the following equations respectively:

$$P_{SAUT} = \alpha(q_{CI} - q_I^*) \quad (4.31),$$

$$P_{GAUT} = \alpha_2(q_S - q_S^*) \quad (4.32).$$

Finally the terms representing the Bergeron-Findeisen process are given by

$$P_{SFW} = N_{I50} (a_1 m_{I50}^{a_2} + \pi E_{TW} \rho q_{CW} R_{I50}^2 V_{I50}) \quad (4.33),$$

$$P_{SFI} = \frac{q_{CI}}{\Delta t_1} \quad (4.34),$$

and have been developed after the works of Orville and Kopp (1977) and Hsie *et al.* (1980).

4.2.3 Production Terms for Graupel

The graupel production rate is given by

$$P_G = P_{GAUT} + P_{GFR} + \text{MIN}(P_{GDRY}, P_{WET}) + (1 - \delta_2)(P_{SACR} + P_{RACS}) \\ + (1 - \delta_3)(P_{RACI} + P_{IACR}) + (1 - \delta_1)P_{GSUB} \quad (4.35)$$

for $T < T_0$, and

$$P_G = P_{GMLT} + P_{GACS} \quad (4.36)$$

for $T \geq T_0$.

The terms P_{GAUT} , P_{SACR} , P_{RACI} , P_{IACR} , and P_{GACS} have already been discussed in the context of snow production.

The growth rate of graupel by accretion of water substance is taken as the lesser of the two terms P_{GDRY} and P_{GWET} . Both terms are functions of P_{GACW} , P_{GACI} , and P_{GACR} . In the case of dry growth, P_{GDRY} is given by

$$P_{GDRY} = P_{GACW} + P_{GACI} + P_{GACR} + P_{GACS} \quad (4.37)$$

The terms on the right side of equation 4.37 are based on a continuous collection model and are given by

$$P_{GACW} = \left(\frac{E_{GW} \pi n_{0G} q_{CW} \Gamma(3.5)}{4 \lambda_G^{3.5}} \right) \left(\frac{4g\rho_G}{3C_{DP}} \right)^5 \quad (4.38),$$

$$P_{GACI} = \left(\frac{E_{GI} \pi n_{0G} q_{CI} \Gamma(3.5)}{4 \lambda_G^{3.5}} \right) \left(\frac{4g\rho_G}{3C_{DP}} \right)^5 \quad (4.39),$$

$$P_{GACR} = E_{GR} n_{0G} n_{0R} \pi^2 |V_G - V_R| \left(\frac{\rho_w}{\rho} \right) \left(\frac{5}{\lambda_R^6 \lambda_G} + \frac{2}{\lambda_R^5 \lambda_G^2} + \frac{0.5}{\lambda_R^4 \lambda_G^3} \right) \quad (4.40).$$

The term P_{GACS} has already been discussed and is described by equation 4.20.

The equation for wet growth of graupel includes thermal effects and is written

$$P_{GWET} = \frac{2\pi n_{0G} (\rho L_f \psi \Delta T_s - K_a T_c)}{\rho (L_f + C_w T_c)} \left[0.78 \lambda_G^{-2} + 0.31 S_c^{\frac{1}{3}} \Gamma(2.75) \left(\frac{4g\rho_G}{3C_D} \right)^{2.5} v^{\frac{1}{2}} \lambda_G^{-2.75} \right] \quad (4.41).$$

$$+ (P_{GACI} + P_{GACS}) \left(1 - \frac{C_i T_c}{L_f + C_w T_c} \right)$$

following the work of Musil (1970). As will be discussed in the section describing rain production, P_{GWET} can also be a source of rain by the shedding of water.

Immersion freezing of rain (Bigg freezing) is described by the equation

$$P_{GFR} = 20\pi^2 B' n_{OR} \left(\frac{\rho_w}{\rho} \right) \left\{ e^{[A'(T_0 - T)]} - 1 \right\} \lambda_R^{-7} \quad (4.42)$$

after Bigg (1953).

The sublimation of graupel is very similar to that of snow (equation 4.29). It may be written as

$$P_{GSUB} = \frac{2\pi(S_i - I)}{\rho(A'' + B'')} n_{OG} \left[0.78\lambda_G^{-2} + 0.31S_c^{\frac{1}{3}} \Gamma(2.75) \left(\frac{4g\rho_G}{3C_D} \right)^{.25} v^{\frac{1}{2}} \lambda_G^{-2.75} \right] \quad (4.43).$$

The melting of graupel is similar to that of snow and is based on a balance between latent heating and thermal conduction including the effects of ventilation. Like P_{SMLT} , P_{GMLT} can also serve as a source of rain through the shedding of water. P_{GMLT} is given by

$$P_{GMLT} = -\frac{2\pi}{\rho L_f} (K_a T_c - L_v \psi \rho \Delta r_s) n_{OG} \left[0.78\lambda_G^{-2} + 0.31S_c^{\frac{1}{3}} \Gamma(2.75) \left(\frac{4g\rho_G}{3C_D} \right)^{.25} v^{\frac{1}{2}} \lambda_G^{-2.75} \right] \quad (4.44).$$

$$-\frac{C_w T_c}{L_f} (P_{GACW} + P_{GACR})$$

4.2.4 Production Terms for Rain

Like snow and graupel the production of rain can be expressed as a summation of individual source/sink processes:

$$P_R = P_{RAUT} + P_{RACW} - P_{IACR} - P_{SACR} - P_{GACR} - P_{GFR} + (1 - \delta_I)P_{REVP}, T < T_0 \quad (4.45)$$

$$P_R = P_{RAUT} + P_{RACW} + P_{SACW} + P_{GACW} - P_{GMLT} - P_{SMLT} + (1 - \delta_I)P_{REVP}, T \geq T_0. \quad (4.46).$$

The autoconversion of cloud water to rain is as usual based on a threshold value. The expression is written

$$P_{RAUT} = \rho (q_{CW} - q_{CW}^*)^2 \left[1.2 \times 10^{-4} + \left\{ 1.569 \times 10^{-12} \frac{N_I}{D_0 (q_{CW} - q_{CW}^*)} \right\} \right]^{-1} \quad (4.47).$$

The accretion of cloud water by rain is determined by a continuous collection model so that

$$P_{RACW} = \frac{\pi E_{RW} n_{OR} a q_{CW} \Gamma(3+b)}{4 \lambda_R^{3+b}} \left(\frac{\rho_0}{\rho} \right)^5 \quad (4.48).$$

The evaporation rate of rain is governed by diffusional growth. This process is described by Byers (1965). The appropriate equation is

$$P_{REVP} = 2\pi(S-1)n_{OR} \left[0.78\lambda_R^{-2} + 0.31S_c^{\frac{1}{3}} \Gamma \left[\left(\frac{b+5}{2} \right) \right] a^{\frac{1}{2}} v^{-\frac{1}{2}} \left(\frac{\rho_0}{\rho} \right)^{\frac{1}{4}} \lambda_R^{-\left[\frac{b+5}{2} \right]} \right] \quad (4.49).$$

$$\times \left(\frac{1}{\rho} \right) \left(\frac{L_v^2}{K_a R_w T^2} + \frac{1}{\rho r_s \Psi} \right)^{-1}$$

As previously mentioned, the term P_{GWET} can also serve as a source of rain. The shedding of water to form rain is considered active if the collected water cannot be frozen. The actual amount of water shed is given by

$$P_{GACR} = P_{GWET} - P_{GACW} - P_{GACI} - P_{GACS} \quad (4.50)$$

with the values of E_{GI} and E_{GS} being set to 0.1 in P_{GACI} and P_{GACS} respectively. If the right hand side of equation 4.5 is negative, that amount is shed as rain water.

The remaining terms in equation have already been discussed in either the section describing the production of snow or graupel. A more complete discussion of all the production terms can be found in Lin *et al.* (1983).

4.2.5 Production Terms for Non-precipitating Fields

Using the conservation equation 4.8 for non-precipitating fields and expanding out the production terms for snow, graupel, and rain the effect of various P terms on water vapor, cloud water, and cloud ice can be seen.

Water vapor is depleted by the depositional growth of snow and graupel, and created by the sublimation of snow and graupel as well as the evaporation of rain. Cloud water is depleted by accretion on snow, graupel, and rain, through autoconversion to rain, and by the Bergeron-Findeisin process. Cloud water and cloud ice is created when

saturation conditions are exceeded (Ogura, 1963; Orville and Kopp, 1977) and in the case of cloud ice, when the temperature is simultaneously below freezing. Cloud ice is depleted by auto-conversion processes, accretion by rain, snow, and graupel, by the Bergeron-Findeisen process, and by instantaneous melting at temperatures above freezing. At temperatures below -40°C , all liquid water is frozen and becomes a source for ice through homogeneous nucleation (P_{IHOH}). At temperatures between 0°C and -40°C , ice is created in concentrations dictated by Fletcher's curve (Fletcher, 1962).

4.3 Electrification Microphysics

Graupel, rain, cloud ice, and cloud water can all carry charge. Free ions are also permitted in this model as described in the next section. Charge is transferred from one class of hydrometeors to another through any of the microphysical processes described in the previous section as well as through non-inductive and ion interactions. In general the charge conservation equation for a species i is

$$\frac{\partial Q}{\partial t} = \mathbf{v} \cdot \nabla Q + \frac{1}{r_i} \frac{\partial}{\partial z} (v_i Q r_i) + \nabla \cdot \mathbf{K}_m \nabla Q \pm \left(\frac{dQ}{dt} \right)_{\text{INTER}} \quad (4.51).$$

The terms on the right hand side of 4.51 are respectively, the horizontal and vertical advection of charge in or out of the grid cell, subgrid scale mixing by turbulence, and a term that represents interactions between different classes of hydrometeors or ions. The last term is the hydrometeor charge interaction term and is most significant in this study: The non-inductive charge parameterization is embodied in this term. For this reason, the next subsection will be devoted to a discussion of the non-inductive contribution to this term. The contribution of ionic diffusion will be discussed in subsection 4.3.2 Ion Physics.

4.3.1 Contribution of Non-inductive Charging in the Hydrometeor Charge Interaction Term

The charge transferred in a collision between two particles can be written as

$$\Delta\hat{q} = \Delta Q + A\hat{q}_{\text{LARGE}} - (1 - A)\hat{q}_{\text{SMALL}} \quad (4.52).$$

The variable A takes into account the effects of preexisting charge on the particles (*i.e.*, charge cancellation), and ΔQ represents the charge transfer due to non-inductive charging. In this study, ΔQ is based on the laboratory study by Takahashi (1978).

The values of ΔQ are dependent on liquid water content and temperature, and are determined from a table which was constructed by interpolating the data from Fig. 2.3 of Takahashi (1978) to a grid in liquid water content-temperature space. At temperatures colder than -35°C where no laboratory data was available, the values of charge transfer were taken as those at -35°C . This assumption should have only minor effects since no large values of liquid water content are expected at those cold temperatures. Furthermore, no water exists at temperatures colder than -40°C , and the charging goes to zero. The inclusion of a non-inductive charging “look up” table based on Takahashi (1978) represents an improvement over the previous parameterization where the magnitude of ΔQ was a constant and the sign changed at a constant temperature regardless of the liquid water content.

The value of charge transfer is integrated over the volume swept out per unit time to account for multiple interactions in a time step:

$$\frac{\partial\hat{q}_{\text{LARGE}}}{\partial t} = - \int E_f |V_{\text{SL}}| N_{\text{SMALL}} \Delta\hat{q} S(\alpha) dA \quad (4.53).$$

Essentially this amounts to multiplying the charge transfer by the number of collisions computed from a continuous collection model. The exact form is

$$\frac{d\hat{q}_{LARGE}}{dt} = E_f |V_{SL}| N_{SMALL} \pi r_{LARGE}^2 \langle S \rangle [-\Delta Q + (1 - A)\hat{q}_{SMALL} - A\hat{q}_{LARGE}] \quad (4.54).$$

There are two non-inductive interactions allowed: graupel and cloud ice, and graupel and snow. In both cases, graupel is considered to be the large particle and snow or cloud ice is the small hydrometeor.

4.3.2 Ion Physics

Interactions between free ions and hydrometeors are permitted in the model. These interactions are accounted for in the last term on the right hand side of equation 4.51. A complete description of the ion/hydrometeor interactions is described in Chiu (1978), but will be summarized here.

For small cloud droplets and cloud ice which have negligible terminal velocities, ions are assumed to attach through diffusional and Coulomb forces. In the case of ion attachment to raindrops and graupel, diffusional and Coulomb forces are considered, but the effects of terminal velocity are taken into account. This is necessary due to the hydrodynamic effects of the rain drop on the surrounding air.

Evaporation and sublimation of charged hydrometeors is a source of free ions. For rain and graupel, the process assumes that the surface charge density remains constant, and ions are discharged from the hydrometeor as the particle shrinks. In this way corona emission is simulated. Cloud water and ice release their charge when instantaneously evaporating or sublimating.

The prognostic equation for ion concentration is given by

$$\frac{\partial n_{\pm}}{\partial t} = -\nabla[n_{\pm} V \pm n_{\pm} m_{\pm} E - K_m \nabla n_{\pm}] + G - \alpha n_{+} n_{-} + \text{SOURCE} + \text{SINK} \quad (4.54).$$

The concentration is controlled by ion flux convergence due to the wind, the electric field, and turbulence, the cosmic ion generation rate (G), ion recombination, and hydrometeor source/sink terms. Ions can interact with the hydrometeors by diffusive and Coulomb forces. In order to remain numerically stable, this equation requires smaller and smaller time steps as the electric field increases (the diffusive time scale of ions is a function of the electric field). Eventually, the time step becomes prohibitively small and the model must be shut down. Usually this occurs before the electric field approaches the dielectric strength of air.

4.4 Representation and Determination of Electricity Fields

The electric field, electric potential, electric energy density, and space charge density are all calculated in this model. The total space charge density is defined by

$$\rho_T = e(n_{+} - n_{-}) + Q_{CW} + Q_R + Q_G + Q_S + Q_{CI} \quad (4.55).$$

Given the total space charge density and appropriate boundary conditions, the electric potential can be determined by inverting the following equation:

$$\nabla^2 \phi_E = -\left(\frac{\rho_T}{\epsilon_0}\right) \quad (4.56).$$

The electric field is proportional to the gradient of the electric potential:

$$\mathbf{E} = -\nabla\phi_E \quad (4.57).$$

In order to invert Poisson's equation (4.56), the boundary conditions need to be prescribed. The lateral boundary conditions are that the horizontal gradient of the electric potential is zero. The potential is forced to zero at the bottom of the model domain. At the top of the model domain, the potential remains a constant which is determined from the initial vertical ion concentration profiles.

CHAPTER V

BREAK PERIOD MODELLING RESULTS

The 0000 UTC sounding taken at Darwin served as the base atmospheric state for initialization of the 19 January storm simulation. A north-south projection of the environmental winds were chosen to represent the two dimensional wind field since this was approximately the direction of storm motion based on radar information. In the lowest levels, a convergence of $2 \times 10^{-4} \text{ s}^{-1}$ was applied, and random perturbations of temperature and water vapor were used to initiate convection. The additional convergence in the low levels was instituted to approximate the effects of the sea breeze front, and the random perturbations were found to give more realistic results than a warm bubble. The initial electric field was determined from a best guess of the vertical profile of ion concentration. The profile was chosen so that the initial vertical electric field at the surface was close to the fair weather electric field. Ion concentration increased exponentially away from the surface as is generally observed (Gish, 1944). The important fields used in the initialization of the model are shown in Fig. 5.1.

The domain is $24 \times 24 \text{ km}$ in the y - z plane with 200 m spacing in the horizontal and vertical. At the top of the domain, vertical velocity, vorticity, and hydrometeor mixing ratios are all set to zero, and entropy, water vapor, and the stream function are held at the initial values. Vertical velocity, vorticity, and the stream function are forced to zero at the lower boundary. The lateral boundary conditions require the horizontal gradient of the stream function to be zero.

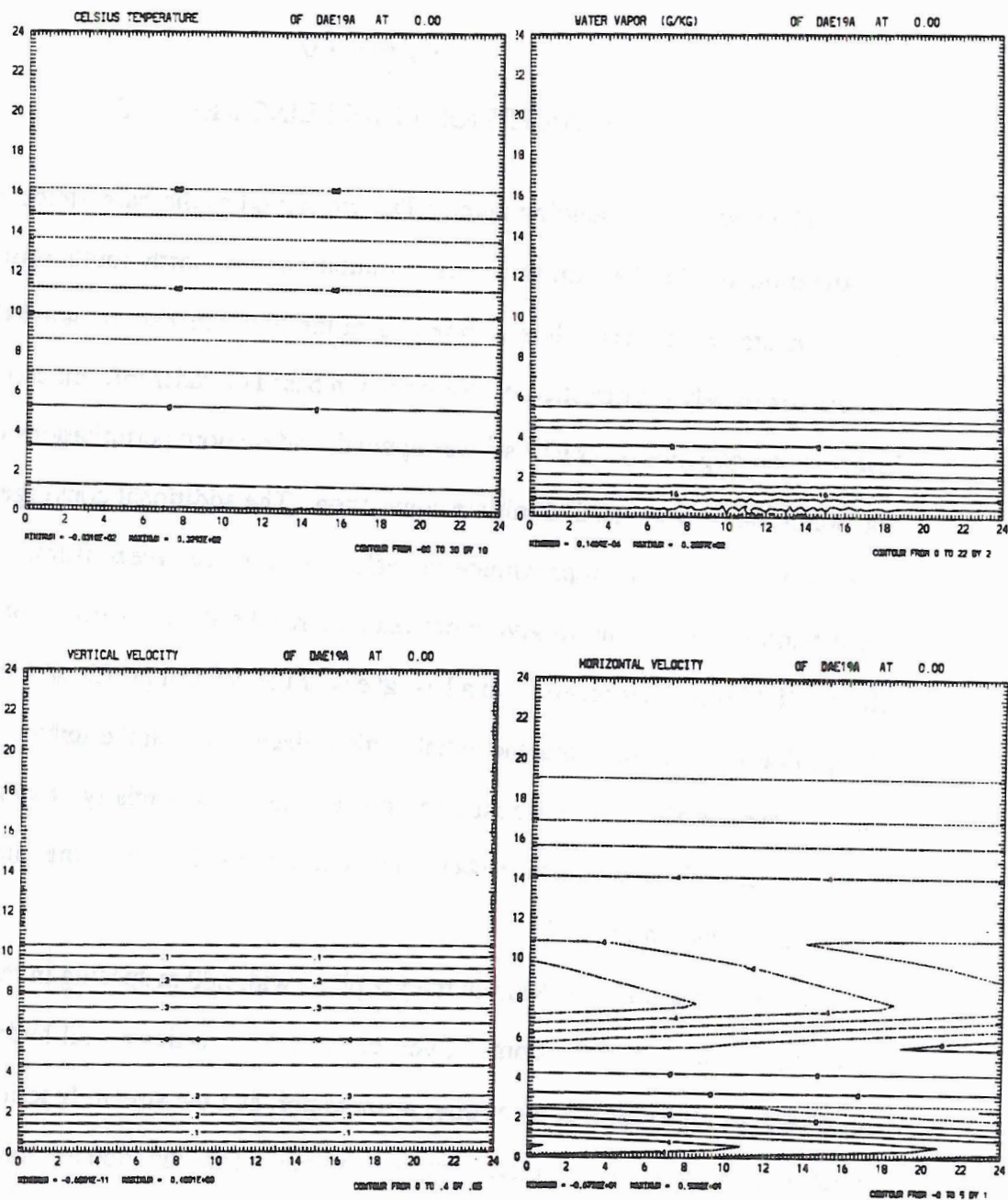


Fig. 5.1a: Thermodynamic and kinematic initialization adapted from the 0000 UTC sounding at Koolpinyah. The north-south component of the horizontal winds are used and modified such that a horizontal convergence of $2 \times 10^{-4} \text{ s}^{-1}$ is applied. Vertical velocity is such that the continuity equation is satisfied. Random perturbations are applied in the lowest levels of the temperature and water vapor field.

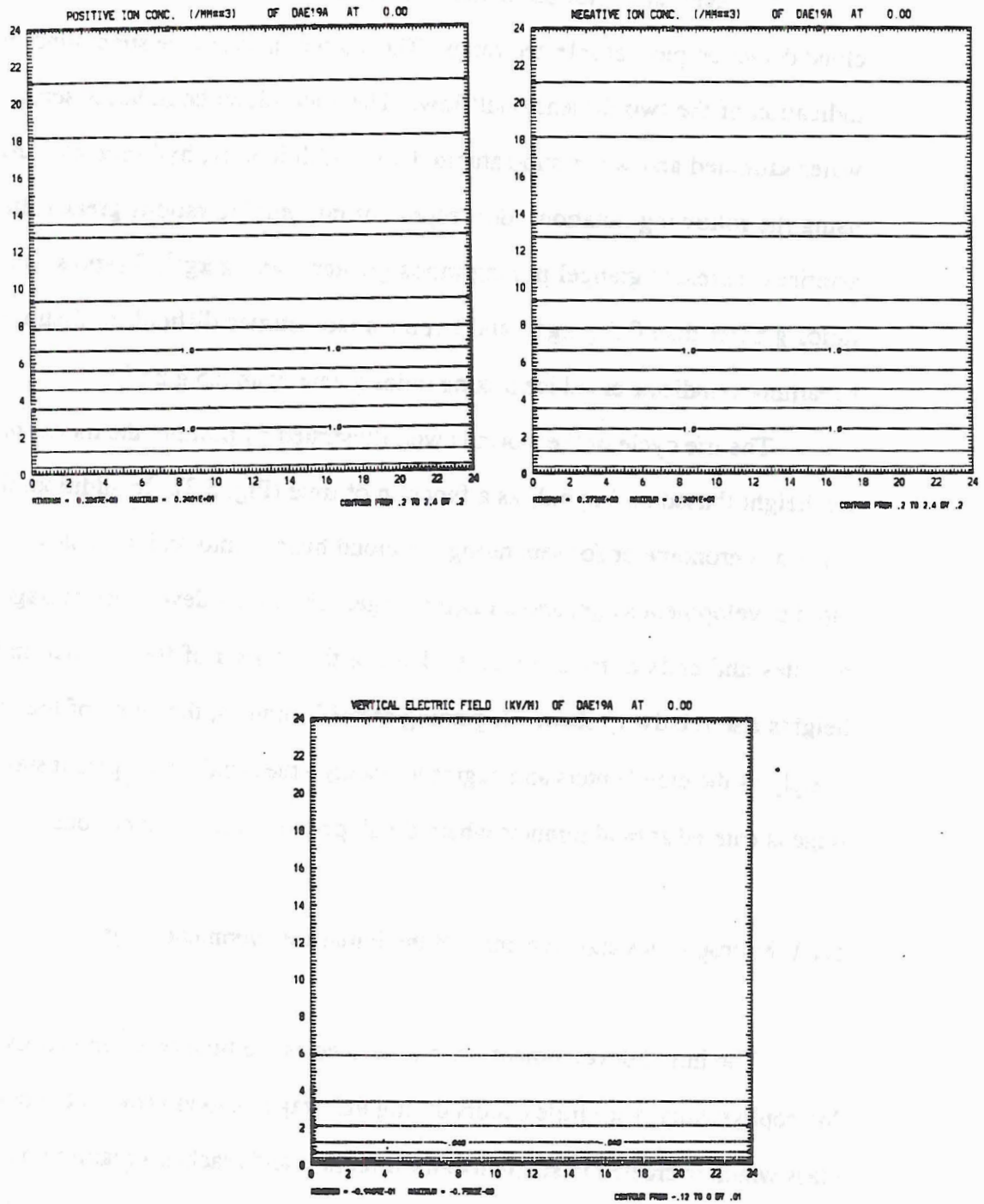


Fig. 5.1b: Electrical initialization. The positive and negative ion concentrations are chosen so that the vertical electric field is close to the value of the fair weather electric field. The ion concentrations increase exponentially away from the surface.

5.1 Non-Electrical Characteristics of the Simulated Cloud

The general evolution of the simulated cloud is shown in Fig. 5.2 as a series of cloud depiction plots at selected times. The dashed lines are the streamlines which give an indication of the two dimensional flow. The solid cloud boundaries separate regions of water saturated and water sub-saturated air. Additionally, hydrometeors are represented using the following notation: dots represent rain mixing ratios greater than 1.0 g kg^{-1} , asterisks represent graupel mixing ratios greater than 1 g kg^{-1} , S represents snow mixing ratios greater than 0.5 g kg^{-1} , and hyphens (sometimes difficult to distinguish from the streamlines) indicate cloud ice mixing ratios greater than 0.5 g kg^{-1} .

The life cycle of the storm is well illustrated by plotting the model predicted cloud top height (based on Fig 5.2) as a function of time (Fig. 5.3). In addition, this figure will serve as chronometer for separating the cloud history into an initial slow growth stage, a rapid development stage, and a mature stage. The initial development stage begins at $t=0$ minutes and ends at $t=18$ minutes. During this period of the simulation the cloud top heights rise relatively slow. Beginning at $t=18$ minutes, the slope of the curve increases sharply as the cloud enters and begins to undergo the rapid development stage. The mature stage is entered at $t=44$ minutes where the slope of the curve flattens out.

5.1.1 Microphysics and Dynamics of the Initial Development Stage

The initial development stage is defined as the time between $t=0$ and $t=18$ minutes. Microphysically, very little occurs during this stage. Cloud water is the only hydrometeor class which is created in small, localized regions and reaches a maximum concentration of near 0.1 g kg^{-1} by $t=15$ minutes (not shown). Dynamically, the vertical velocity is the only field that exhibits appreciable change from the initial conditions (not shown). Several coupled regions of up and down motion, all extending from the ground to slightly over 1.0

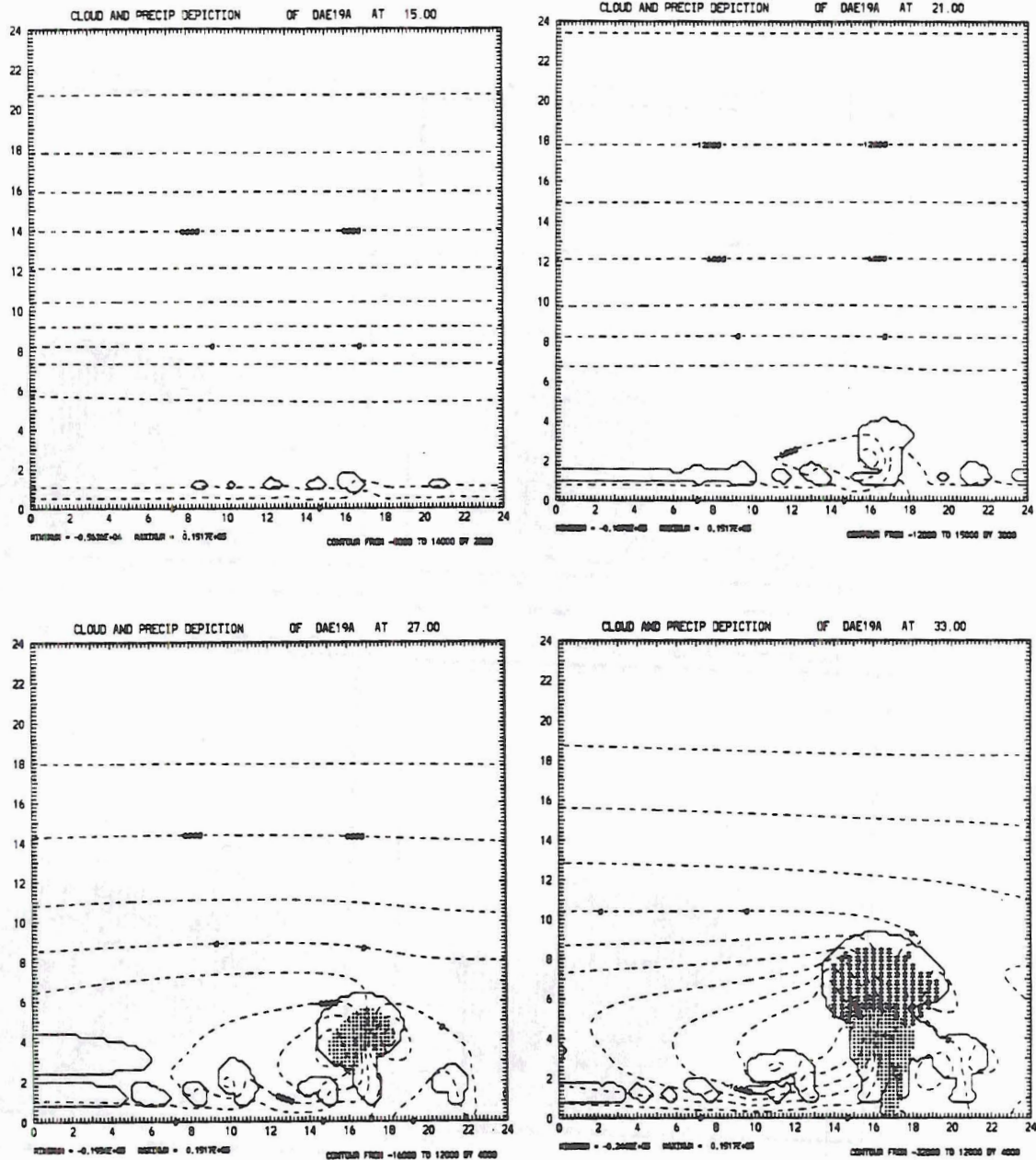


Fig 5.2a: Cloud and precipitation depiction from $t=15$ minutes to $t=33$ minutes. Dashed lines are streamlines, cloud boundaries are defined by the water saturation-water sub-saturation boundary. Asterisks are regions of graupel with mixing ratios greater than 1.0 g kg^{-1} , dots are rain mixing ratios greater than 1.0 g kg^{-1} , S represents snow in mixing ratios greater than 0.5 g kg^{-1} , and underscores are cloud ice mixing ratios greater than 0.5 g kg^{-1} .

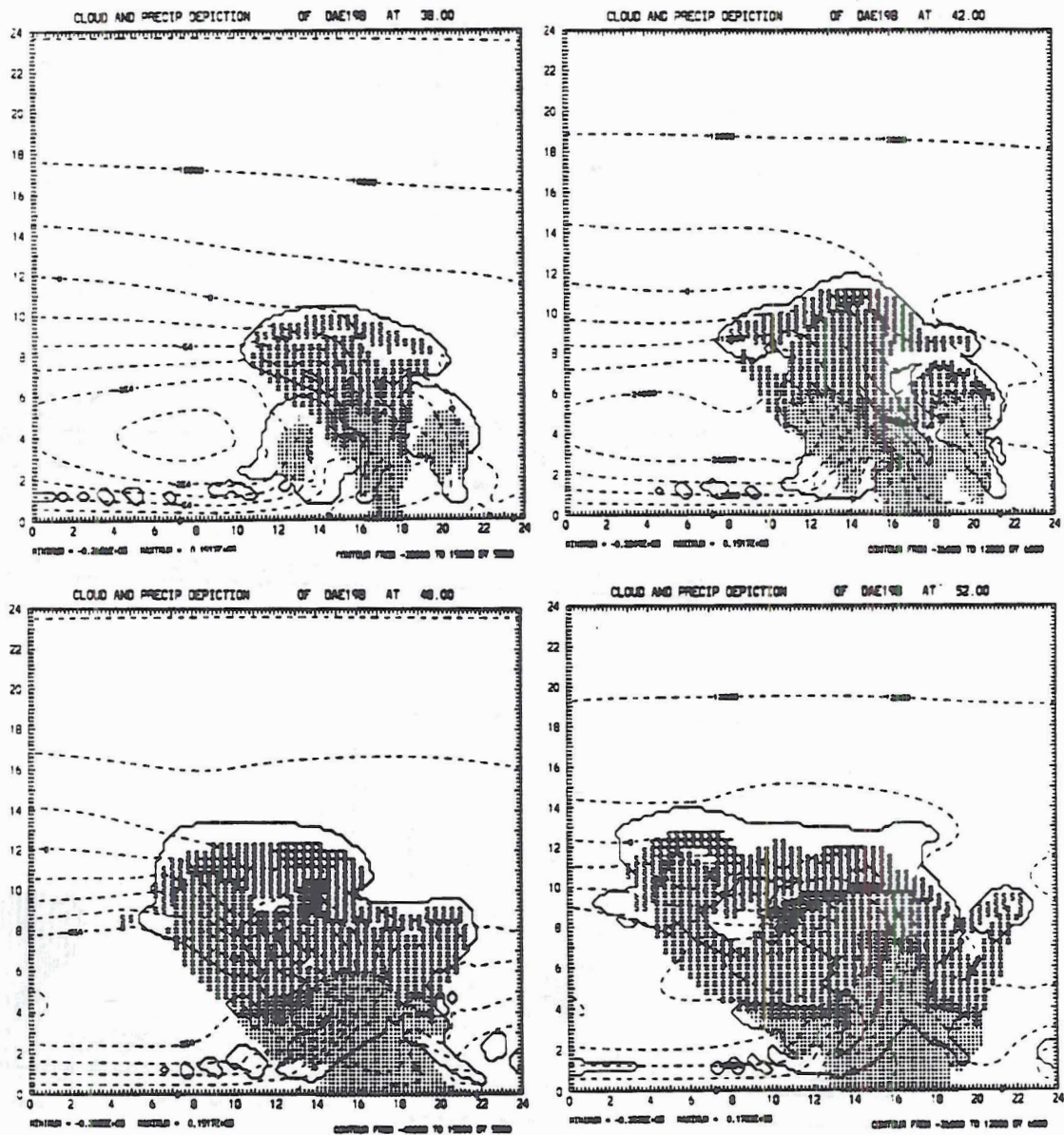


Fig. 5.2b: Same as Fig. 5.2a, but from $t=38$ minutes to $t=52$ minutes.

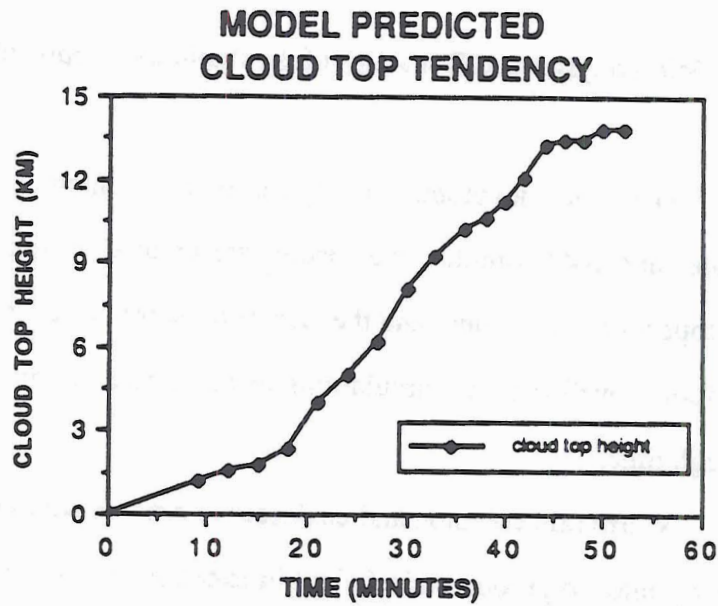


Fig. 5.3: Domain maximum predicted cloud top height in kilometers as a function of time in minutes. The initial development stage (0-18 minutes), the rapid growth stage (18-44) minutes, and the mature stage (44-52 minutes) is evidenced by changes in the slope of the curve.

km are apparent as early as $t=9$ minutes, but are of limited horizontal extent. The highest velocity is 1.0 m s^{-1} . By $t=15$ minutes, the strongest cell contains a maximum updraft of 3.1 m s^{-1} . The cloud water is coincident with the maximum upward velocity, as would be expected. The horizontal velocity fields appear perturbed by $t=15$ minutes, but no well defined circulations are evident (not shown).

5.1.2 Microphysics and Dynamics of the Rapid Development Stage

The rapid development stage is of most interest in this study. Between $t=18$ minutes and $t=44$ minutes, ice species are created, a mixed phase microphysics region develops within the cloud, and the electricity subroutines are activated. From a dynamical standpoint, well defined circulations in the horizontal and vertical evolve and intensify through time.

Warm rain collision and coalescence process begin to operate efficiently enough at $t=18$ minutes to produce rain (albeit in exceptionally small mixing ratios, $4 \times 10^{-7} \text{ g kg}^{-1}$). The mixing ratio of cloud water is 2.1 g kg^{-1} at $t=18$ minutes and increases to 5.3 g kg^{-1} , well above the autoconversion threshold for rain at $t=27$ minutes (Fig. 5.4). Cloud ice and graupel are created at $t=27$ minutes. Snow appears three minutes later at $t=30$ minutes. The mixing ratios of cloud ice, graupel, and snow are initially small, but glaciation of the upper levels of the cloud by cloud ice occurs rapidly. Inspection of the cloud ice production terms indicates that the glaciation is dominated by the contact nucleation of cloud water.

Appreciable concentrations of all the microphysical species exist by $t=33$ minutes (Fig. 5.5, rain not shown). Two distinct maxima in the rain mixing ratios are apparent at $t=36$ minutes (Fig. 5.6). The lowest one is below the melting level and is nearly collocated with the maxima of downward motion and below a region of high graupel mixing ratios. The rain associated with this maxima is reaching the ground and is created by graupel

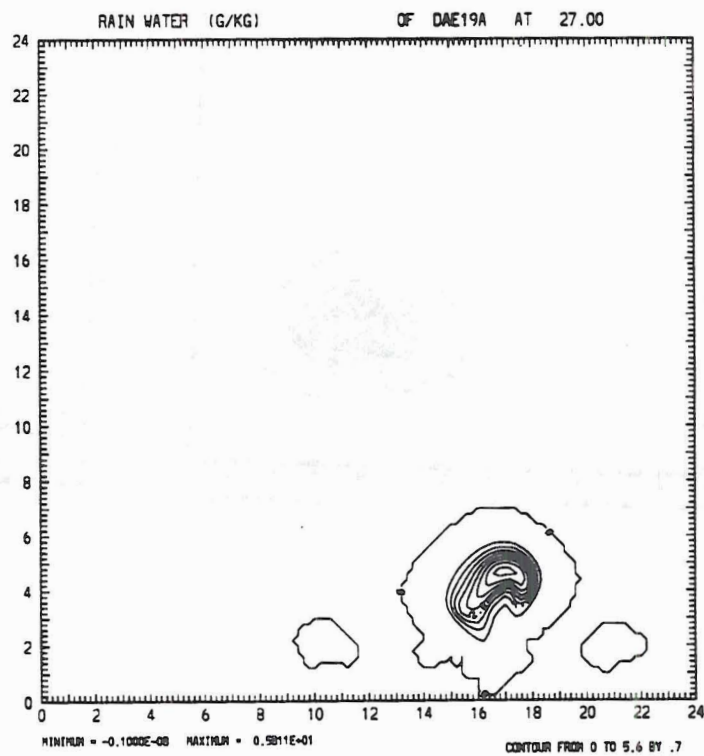
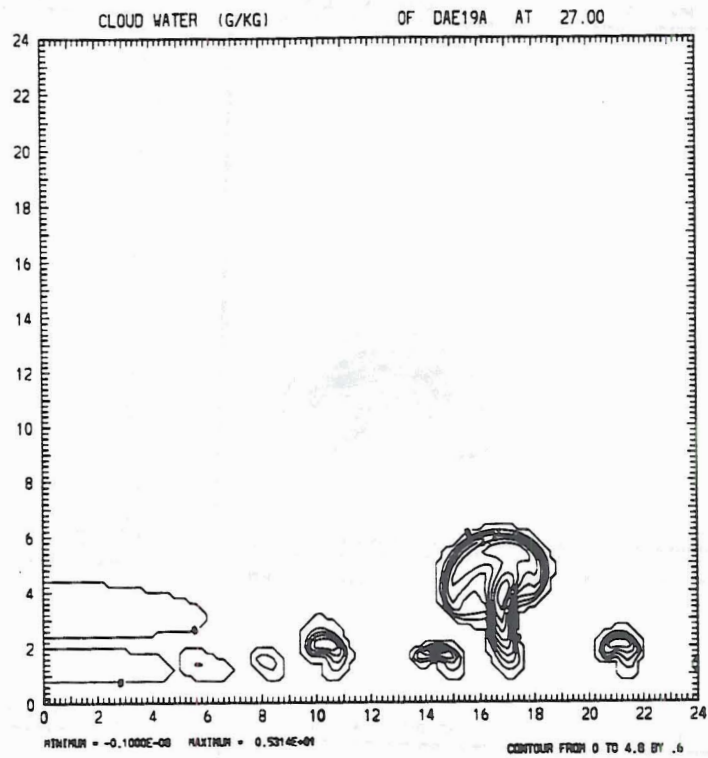


Fig: 5.4: Cloud water and rain fields at t=27 minutes. The rain is formed primarily by the autoconversion of the cloud water.

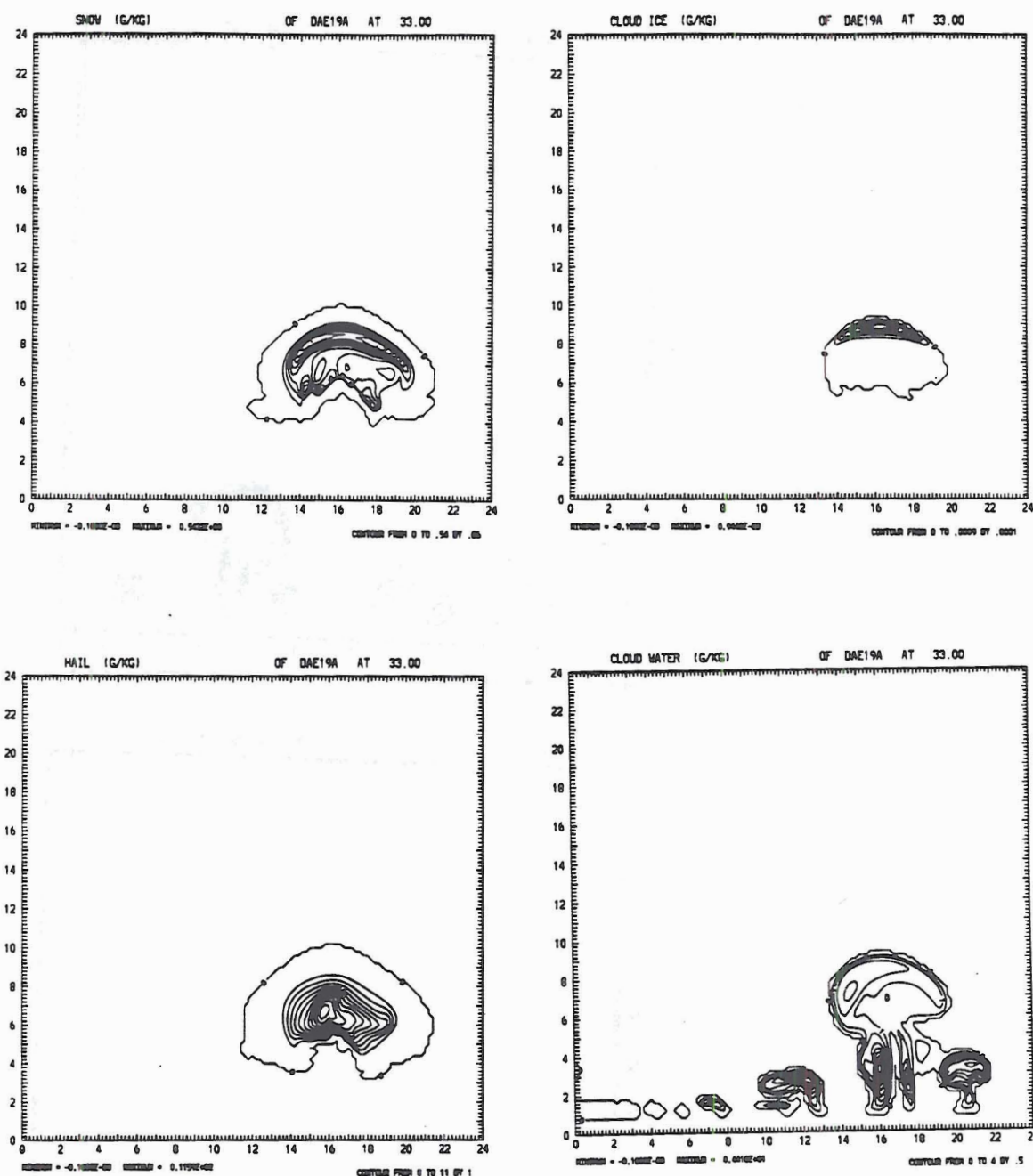


Fig. 5.5: Snow, cloud ice, graupel (hail) and cloud water fields at t=33 minutes. All the microphysical species exist by this time (rain not shown).

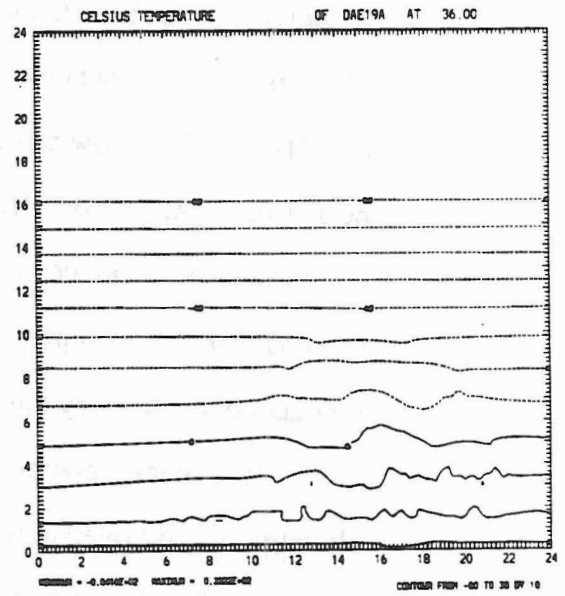
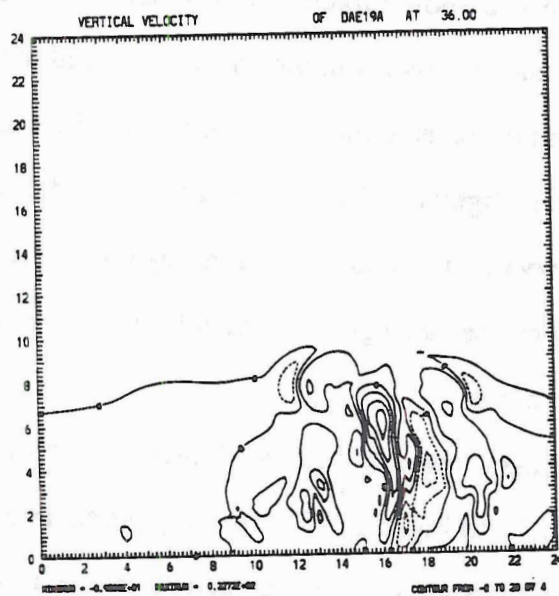
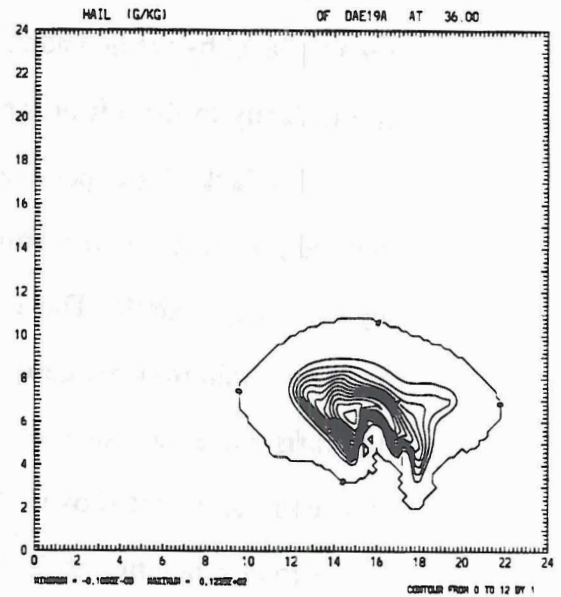
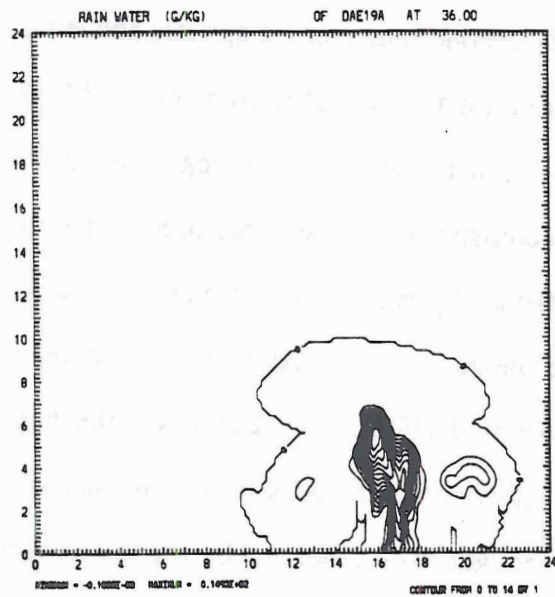


Fig. 5.6: Rain and graupel mixing ratios, vertical velocity, and temperature fields at $t=36$ minutes. Two rain cores are present. The lowest one is produced by graupel melting as it is carried below the melting level by the downdraft. The higher rain maxima is formed by the autoconversion of cloud water in the the updraft and serves as a source for graupel (hail).

melting (determined by examination of the rain production terms) as it is carried below the melting level by the downdraft. The second rain maxima appears above the melting level, immediately to the left of the first rain maxima, and is coincident with the updraft (Fig. 5.6). The lack of graupel overlapping with the rain in this region indicate that the rain is formed primarily by the warm rain collision and coalescence process and then carried aloft by the strong updraft. This is confirmed by evaluation of the rain production terms. Over time both rain maxima descend to the ground while additional rain cores develop in new updrafts on either side of the original (Fig. 5.7). Based on the high cloud water concentrations (not shown), the collocation with updrafts, and the lack of ice, the rain in the second generation updrafts is thought to be generated by warm rain processes as well. Once again, this is confirmed by inspection of the rain production terms.

A time series plot of the domain maximum precipitating hydrometeor mixing ratios is shown in Fig. 5.8. Cloud ice and snow mixing ratios generally increase over time. There is a slight indication that the tendencies in the snow and cloud ice are negatively correlated: when snow mixing ratios increase most rapidly, the cloud ice mixing ratios are nearly constant or even decrease slightly. This information, in addition to the spatial coincidence of cloud ice and snow mixing ratio maxima through the period imply that the snow is being created primarily by the aggregation of cloud ice. The values of the snow production terms verify this hypothesis.

In general, graupel appears lower in the cloud than the snow and cloud ice, although they do overlap (Fig. 5.5 and Fig. 5.9). The primary production of graupel is by the contact freezing of rain water by other ice. The maxima in graupel mixing ratios are in updraft cores and above the rain source. The tendency of the domain maximum graupel and rain mixing ratios further supports this hypothesis (Fig. 5.8). The initial rise is correlated with the increase of rain mixing ratios in the first updraft. As the first updraft collapses and the rain begins to fall the ground, the source of the graupel disappears and the graupel mixing ratios decrease.

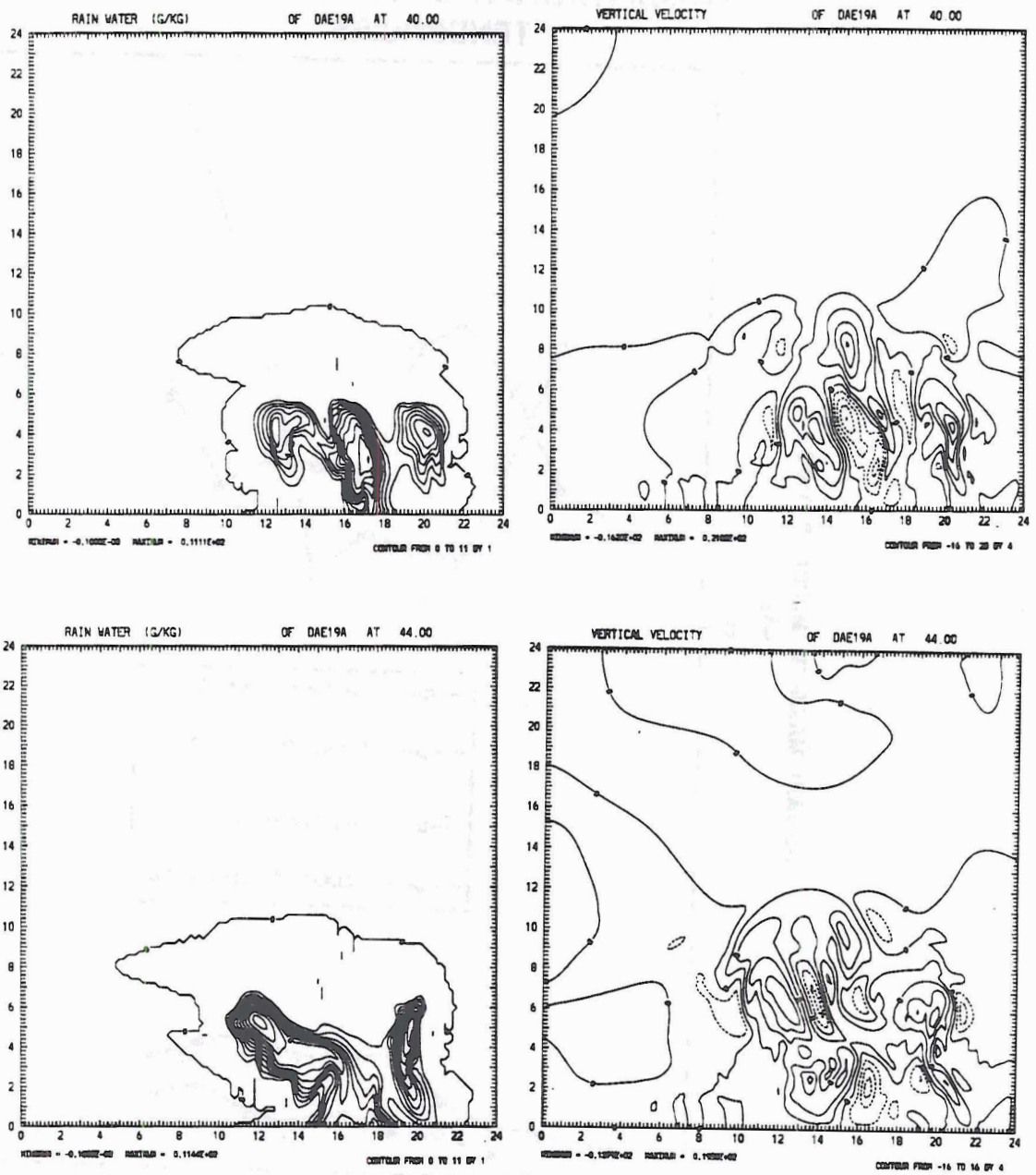


Fig. 5.7: Evolution of the rain and vertical velocity fields during the later stages of the rapid development phase ($t=40$ and $t=44$ minutes). The center rain maxima at $t=40$ minutes descends to the ground by $t=44$ minutes in a strong downdraft. The right most rain core at $t=40$ minutes begins to descend at $t=44$ minutes as a downdraft develops. The left most rain maxima increases over time in a strengthening updraft.

PRECIPITABLE HYDROMETEOR MIXING RATIO TENDENCIES

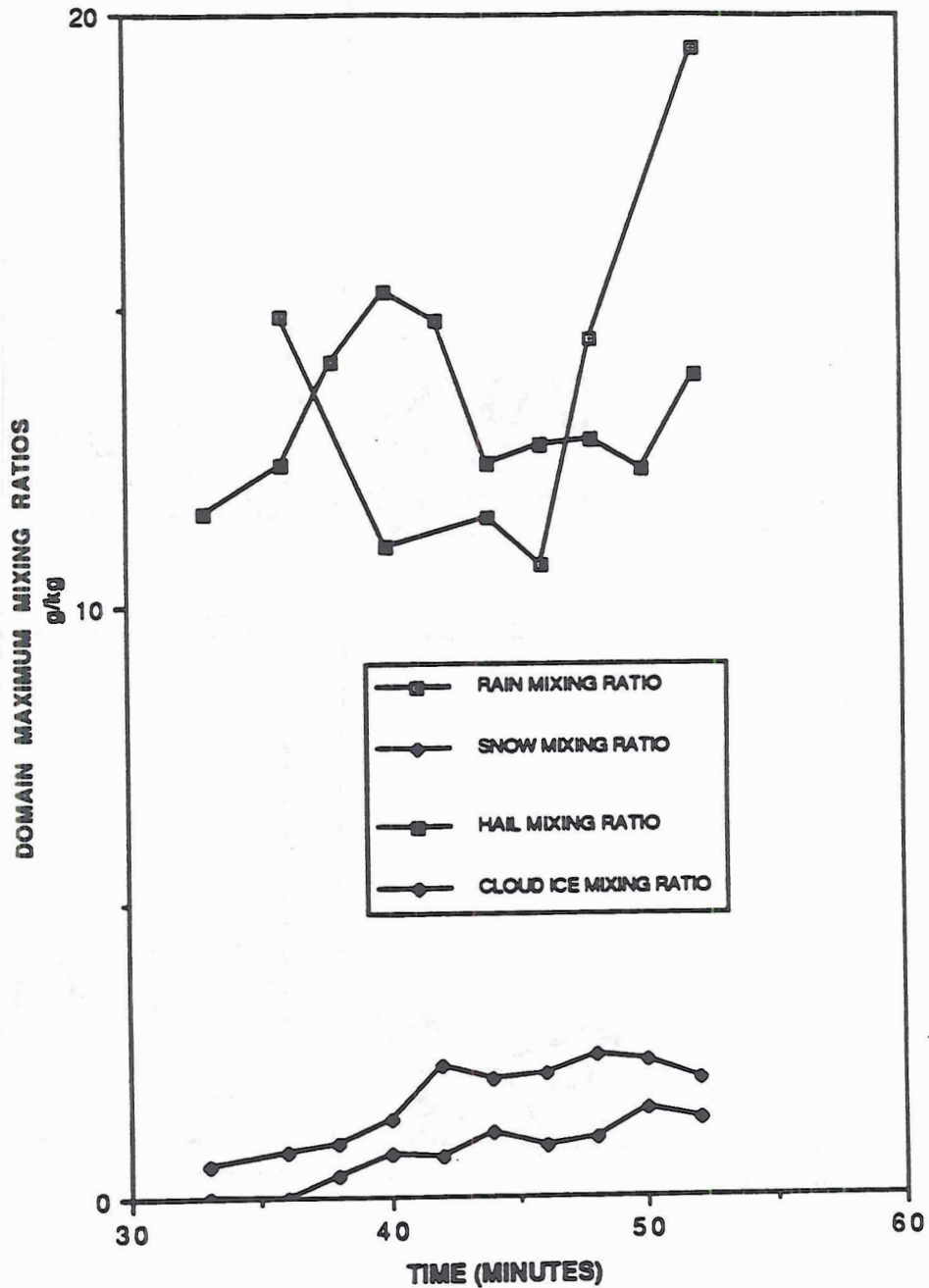


Fig. 5.8: A time series of domain maximum precipitable hydrometeor mixing ratios. The tendency of cloud ice and snow mixing ratios are negatively correlated: snow mixing ratios increase most rapidly when cloud ice mixing ratios decrease. Graupel and rain mixing ratios are negatively correlated: graupel mixing ratios increase when rain decreases.

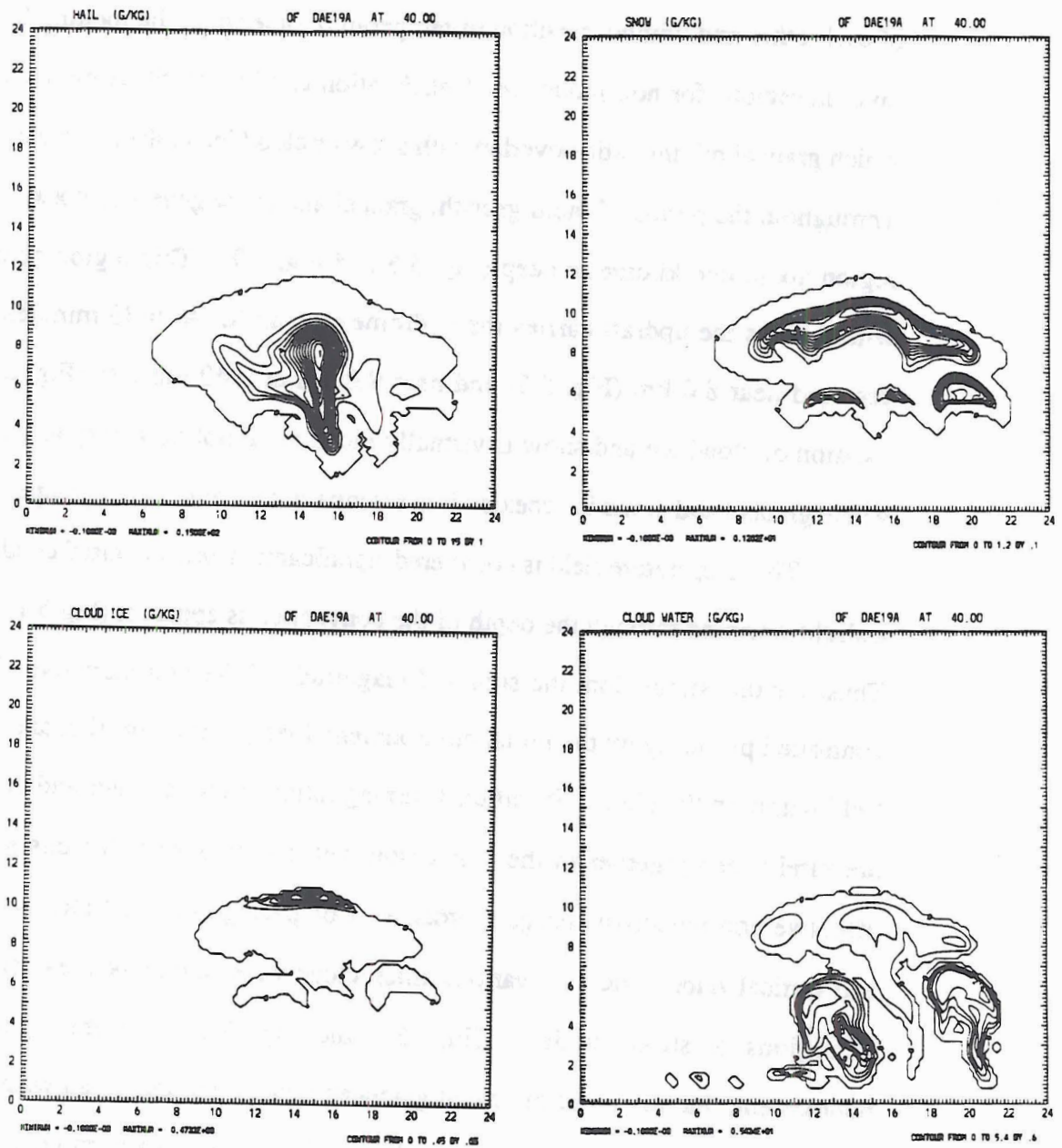


Fig. 5.9: Graupel, snow, cloud ice and cloud water mixing ratios at t=40 minutes. The maximum in the graupel mixing ratio appears lower in the cloud than either the maximum snow or maximum cloud ice mixing ratios, although graupel does overlap with snow in a region about one kilometer centered around 9.0 km.

Up to this point, the microphysical fields have been described almost independently of each other and without mention of temperature other than the melting level. The most favored regions for non-inductive electrification can be identified by locating regions in which graupel mixing ratios overlap with snow or cloud ice in the presence of cloud water. Throughout the period of rapid growth, graupel and snow generally coexist in a boundary region about one kilometer deep (Fig. 5.5 and Fig. 5.9). This region generally ascends with time as the updraft carries the hydrometeors aloft. At $t=33$ minutes the overlap is centered near 8.0 km (Fig. 5.5) and near 9.0 km at $t=40$ minutes (Fig. 5.9). Since the location of cloud ice and snow is virtually identical, it is not necessary to describe in detail where graupel and cloud ice coexist; it is essentially the same as the graupel and snow.

The temperature field is not altered significantly from the initial conditions, although a slight warming through the depth of the convection is apparent (Fig 5.1a and Fig. 5.10). Thus, for this simulation, the sign and magnitude of the non-inductive charging will be controlled primarily by the initial environmental temperature profile, and the cloud water field within in the cloud. Significant mixing ratios of cloud water and cloud ice or snow are rarely seen together in the simulation, yet it is important for this to happen for an effective non-inductive charging process. Comparing the cloud ice, snow, cloud water, and vertical velocity fields at various times, cloud water and cloud ice or snow coexist only in regions of strong updrafts (Fig. 5.9 and Fig. 5.11). If the updraft is weak or nonexistent, that region of the cloud glaciates rapidly and the cloud water is depleted. A strong updraft must be present to supply cloud water at least as rapidly as it is depleted. Based on the model, the strongest electrification should occur in developing portions of the cloud, and virtually no electrification should occur in regions outside the main updraft core.

The final non-electrical fields that need to be addressed during the rapid growth phase of the cloud are the velocity fields. The vertical velocity field has been referenced previously (Fig 5.11e), although not described in detail. The primary information that should be gleaned from these plots is that the storm exhibits multicellular characteristics. A

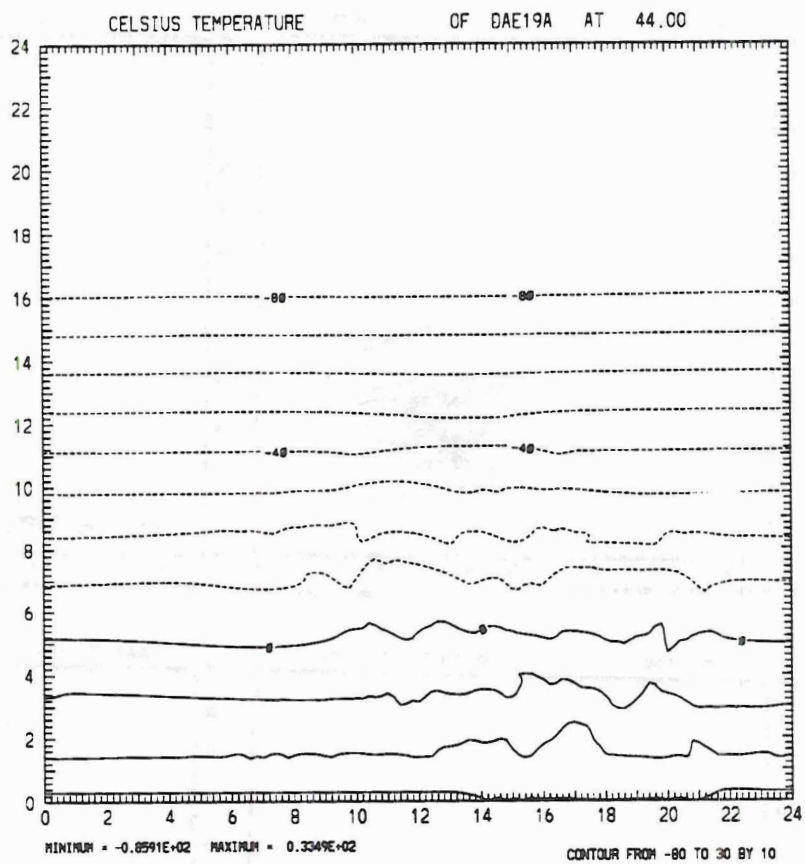


Fig. 5.10: The temperature field at $t=44$ minutes. There is little change from the initial conditions.

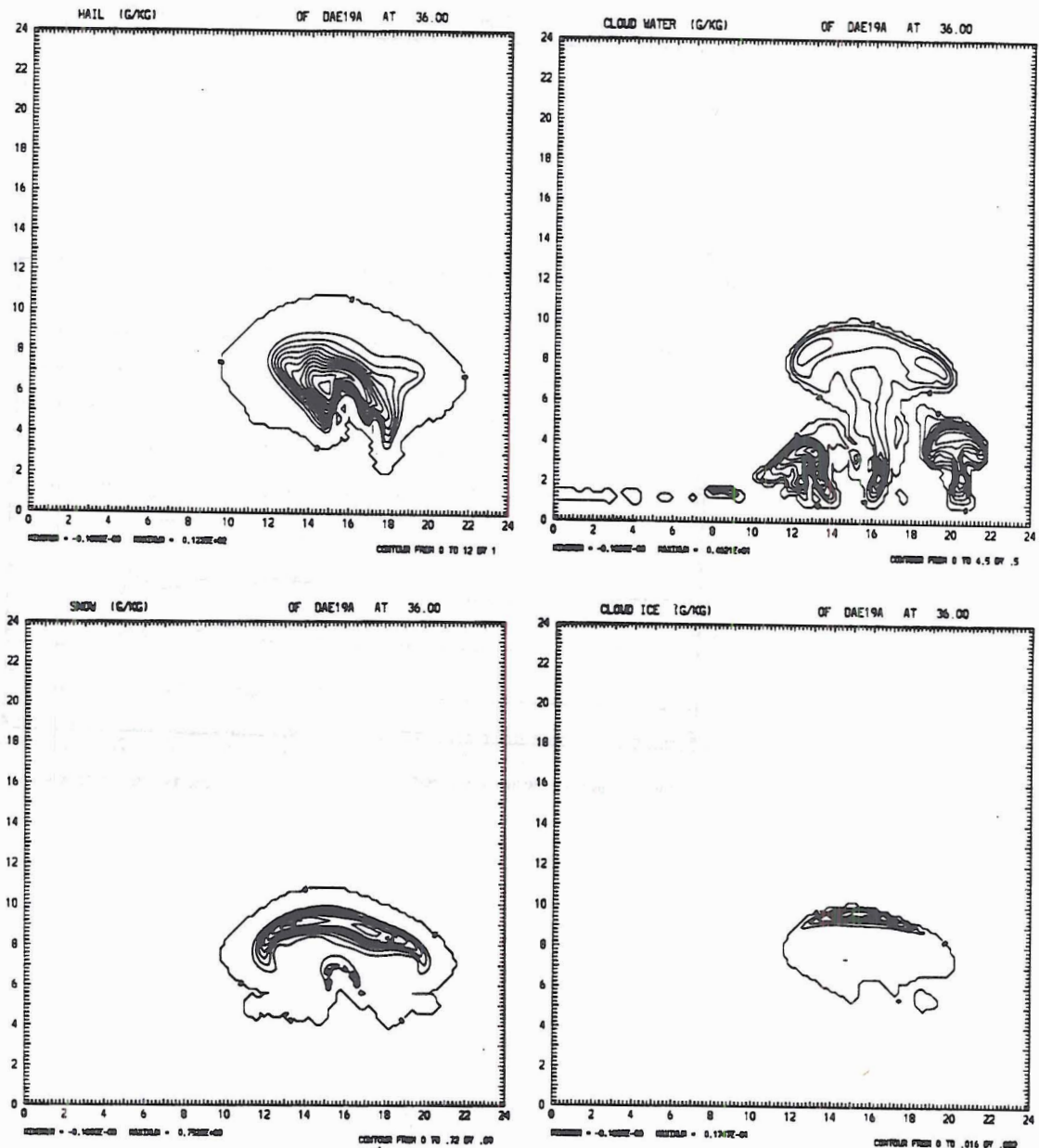


Fig. 5.11a: Graupel, cloud water, snow and cloud ice mixing ratio fields at t=36 minutes. Significant mixing ratios of supercooled cloud water coexists with snow and cloud ice only in regions of strong updrafts.

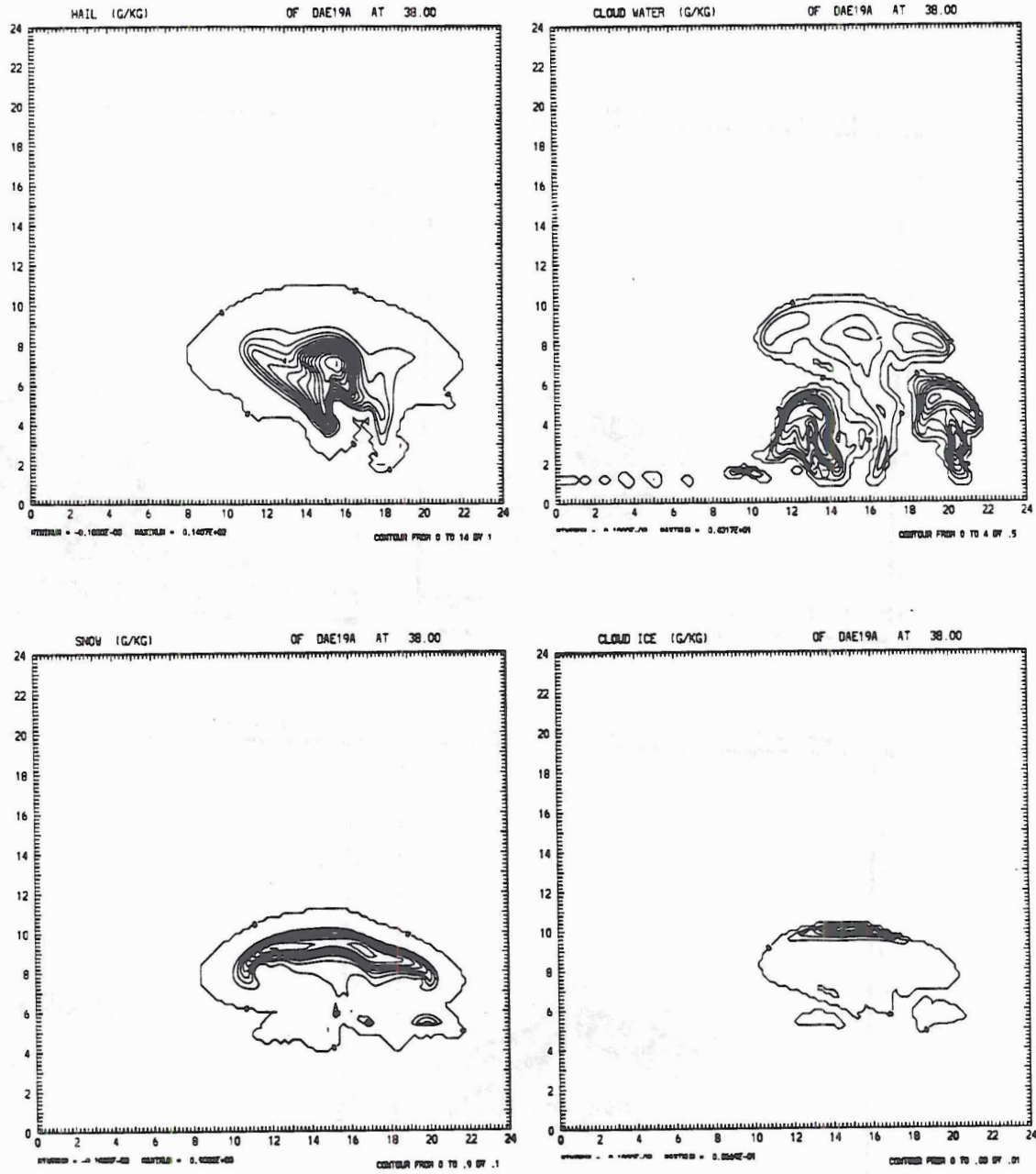


Fig. 5.11b: Same as Fig. 5.11a, but at t=38 minutes

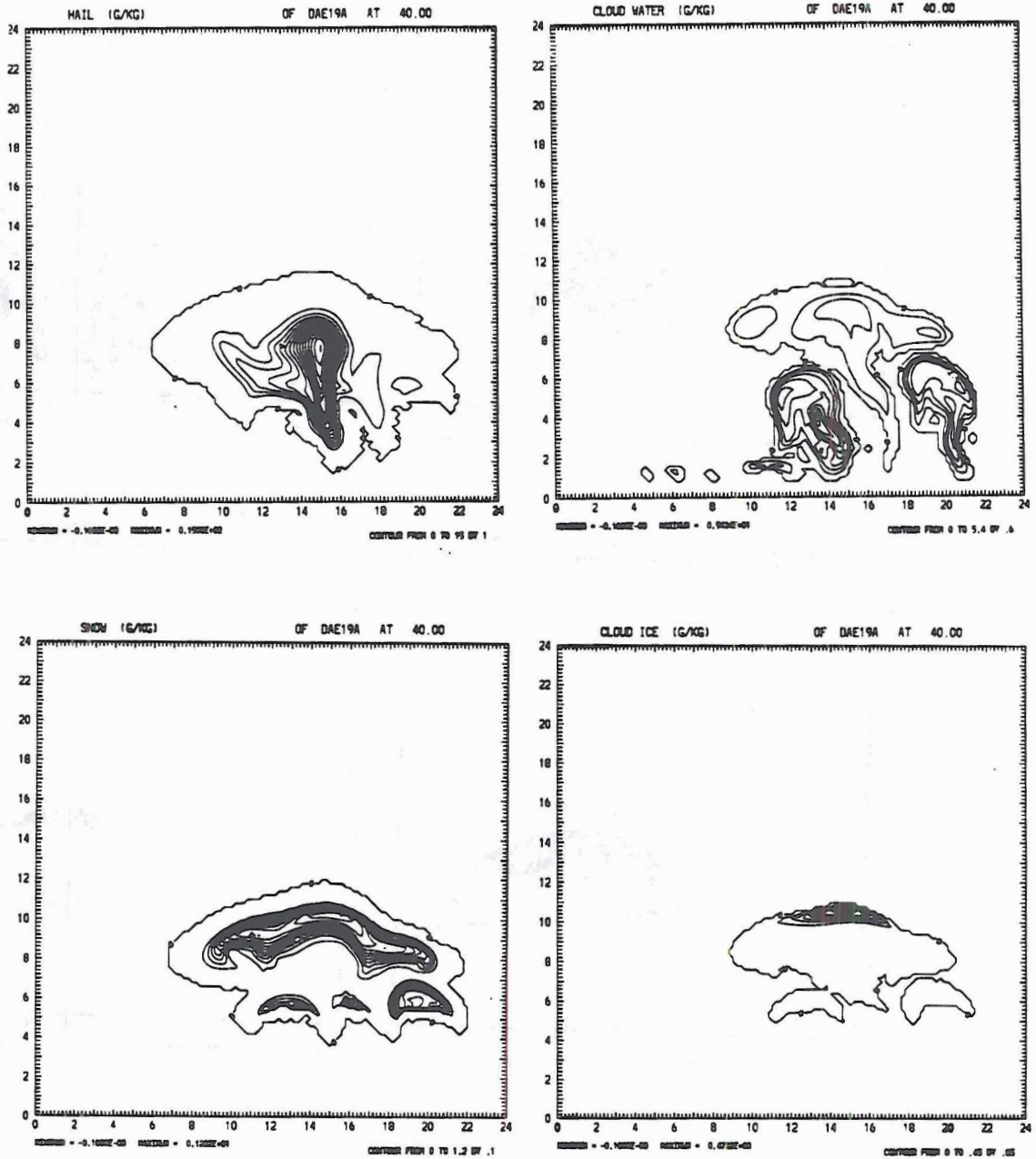


Fig. 5.11c: Same as Fig. 5.11a, but at t=40 minutes.

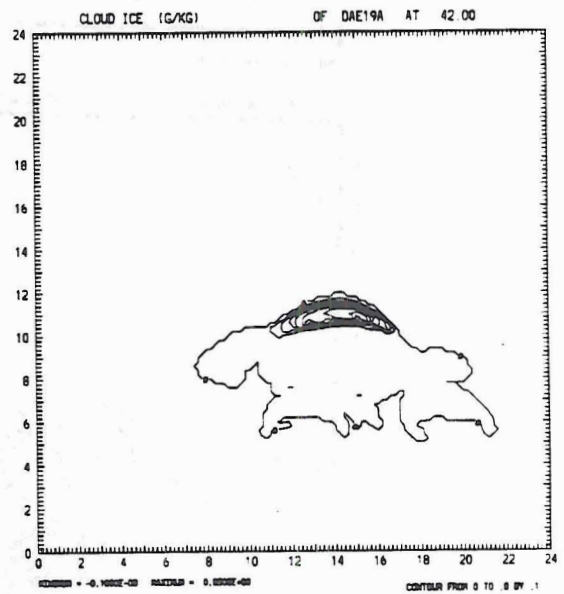
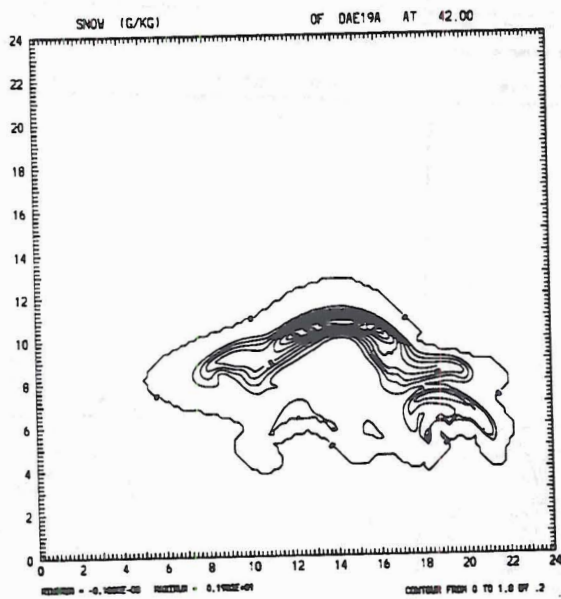
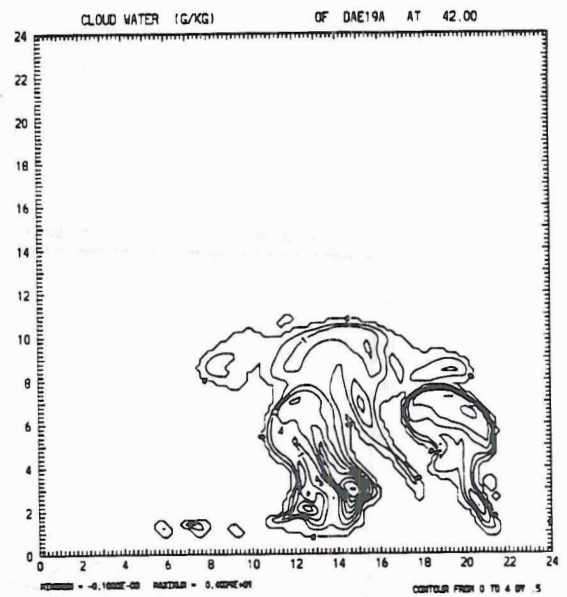
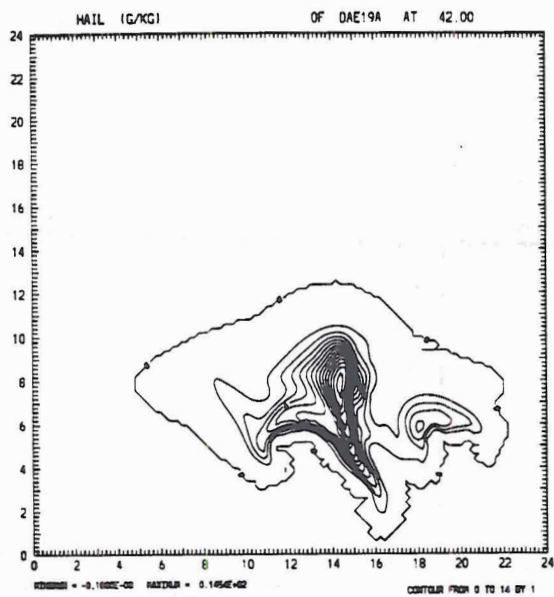


Fig. 5.11d: Same as Fig. 5.11a, but at t=42 minutes.

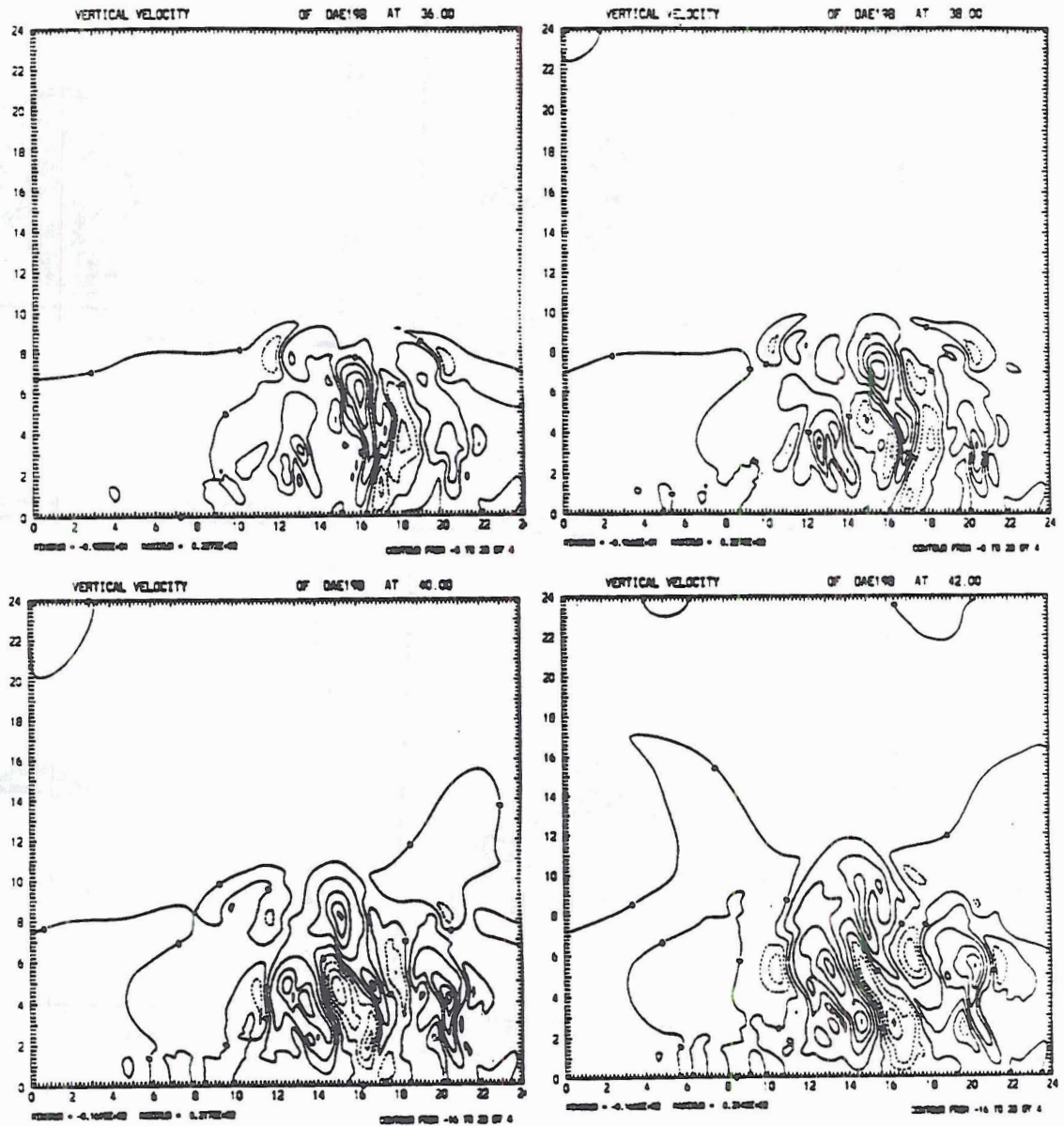


Fig. 5.11e: Vertical velocity at $t=36, 38, 40$ and 42 minutes.

new updraft develops to the left of the main updraft at about $t=36$ minutes. Also roughly at this time, the first cell reaches its maximum vertical speed and then begins to decrease in magnitude. Eventually the second updraft becomes the main updraft ($t=44$ minutes).

The horizontal velocity field reveals a well defined low level convergence and upper level divergence out the upper portions of the cloud through about $t=33$ minutes (not shown). After this time, the field becomes more complicated due to the influence of new cells growing along the outflow boundary. A microburst type structure appears near the ground at $t=38$ minutes and 17 km along the horizontal axis (Fig. 5.12). The strong divergence at the ground is still evident at $t=44$ minutes (Fig. 5.12). It is associated with a downdraft in excess of 12 ms^{-1} centered at about 2 km above the ground, and the 4 ms^{-1} contour is within 200m of the ground (Fig. 5.11e). The gust front is also probably helping to lift air into the new cells on either side of the main updraft.

5.1.3 Microphysics and Dynamics of the Mature Stage

The mature stage of the storm is marked by a cessation of vertical development. The storm reaches its maximum height of about 14.5 km during the period $t=44$ minutes to $t=52$ minutes (Fig. 5.2b). The microphysics in the vigorous convective regions is similar to those in the later stages of the rapid development phase. In the convective updrafts, rain is formed primarily by the collision and coalescence of cloud water. Graupel is created by the freezing of the rain, and snow is created by the aggregation of cloud ice. In the downdrafts, rain is formed by the melting of graupel.

Perhaps the most interesting feature is the development of mixing ratio maxima in the cloud water, cloud ice, snow, and graupel fields within the anvil region (Fig. 5.13 through 5.16). These are associated with a region of positive vertical motion in excess of 12 m s^{-1} (Fig 5.17). Looking at the horizontal velocity fields (Fig. 5.17), the vertical motion seems to be maintained and possibly forced by the deceleration of the divergent

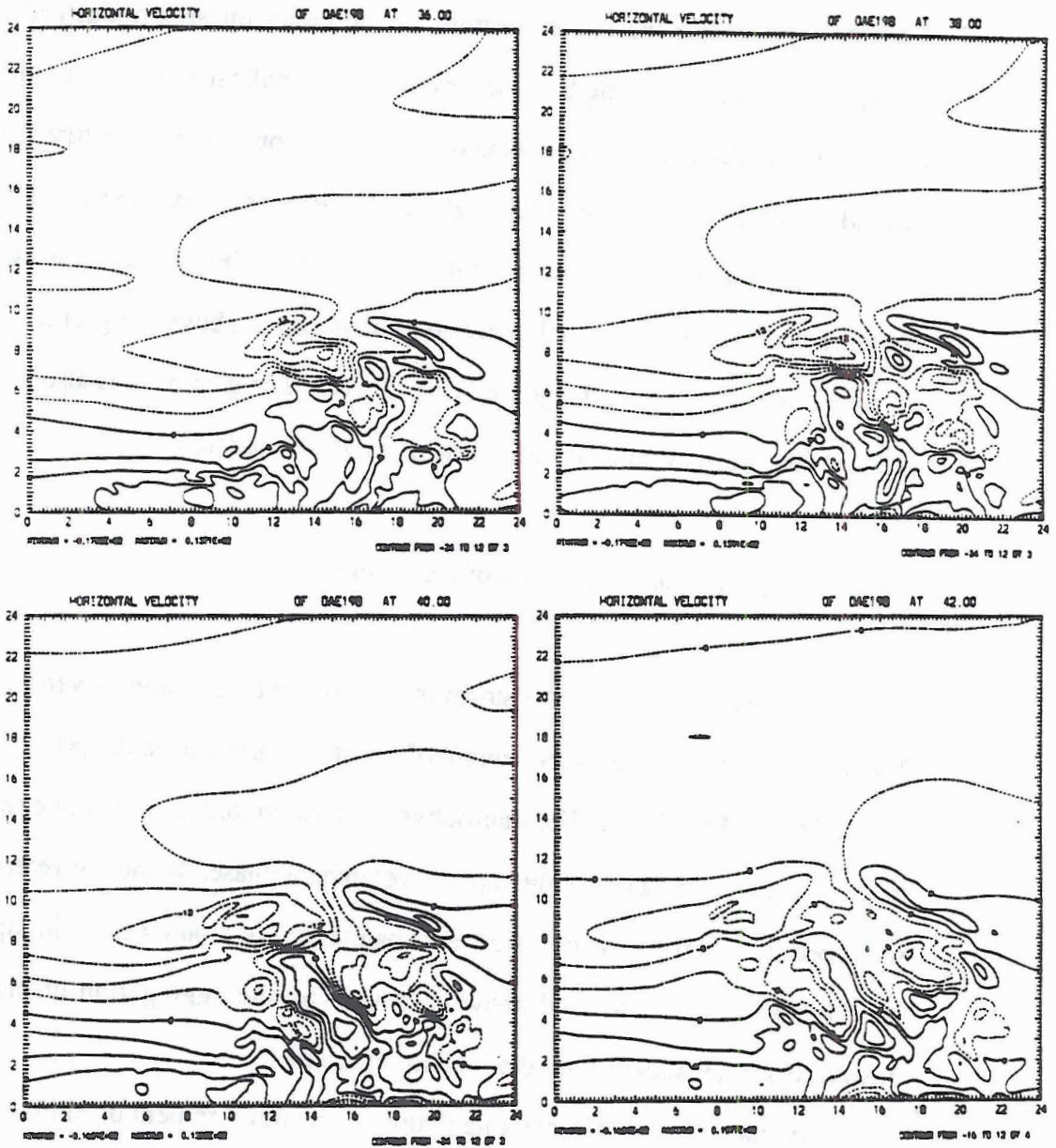


Fig. 5.12: Evolution of the horizontal velocity field from $t=36$ minutes to $t=40$ minutes. Southerly flow (from the left domain boundary) into the storm is simulated at low levels and northerly flow out of the storm is simulated aloft. A microburst type structure appears at $t=38$ minutes near the surface at $y=17$ km.

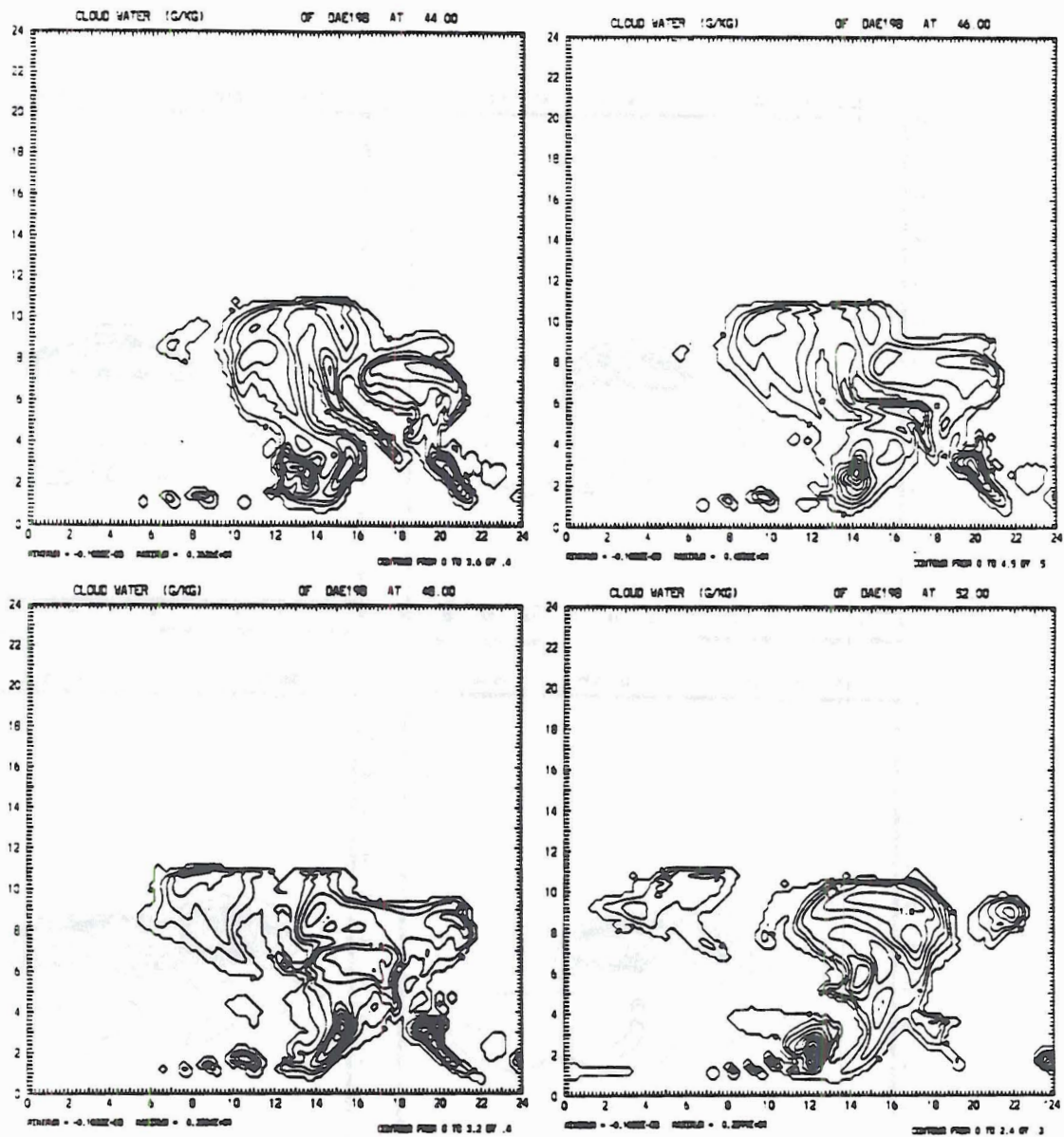


Fig. 5.13: Evolution of the cloud water field during the mature phase of the storm. A maximum in the cloud water field appears in the anvil near $y=11$ km and $z=8$ km at $t=44$ minutes. The maxima rises higher into the cloud and advects downwind through time.

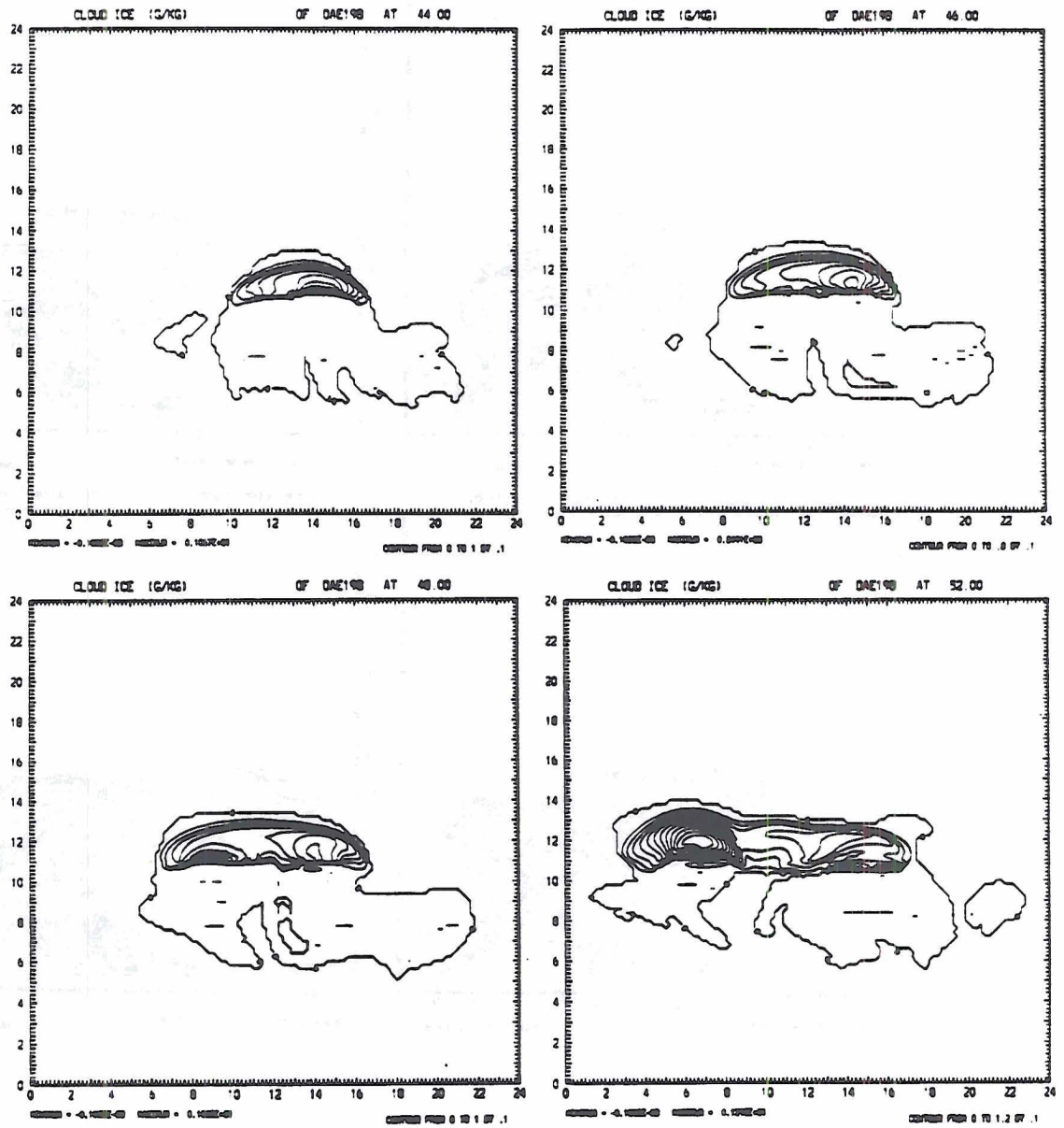


Fig. 5.14: Same as Fig. 5.13, but for cloud ice.

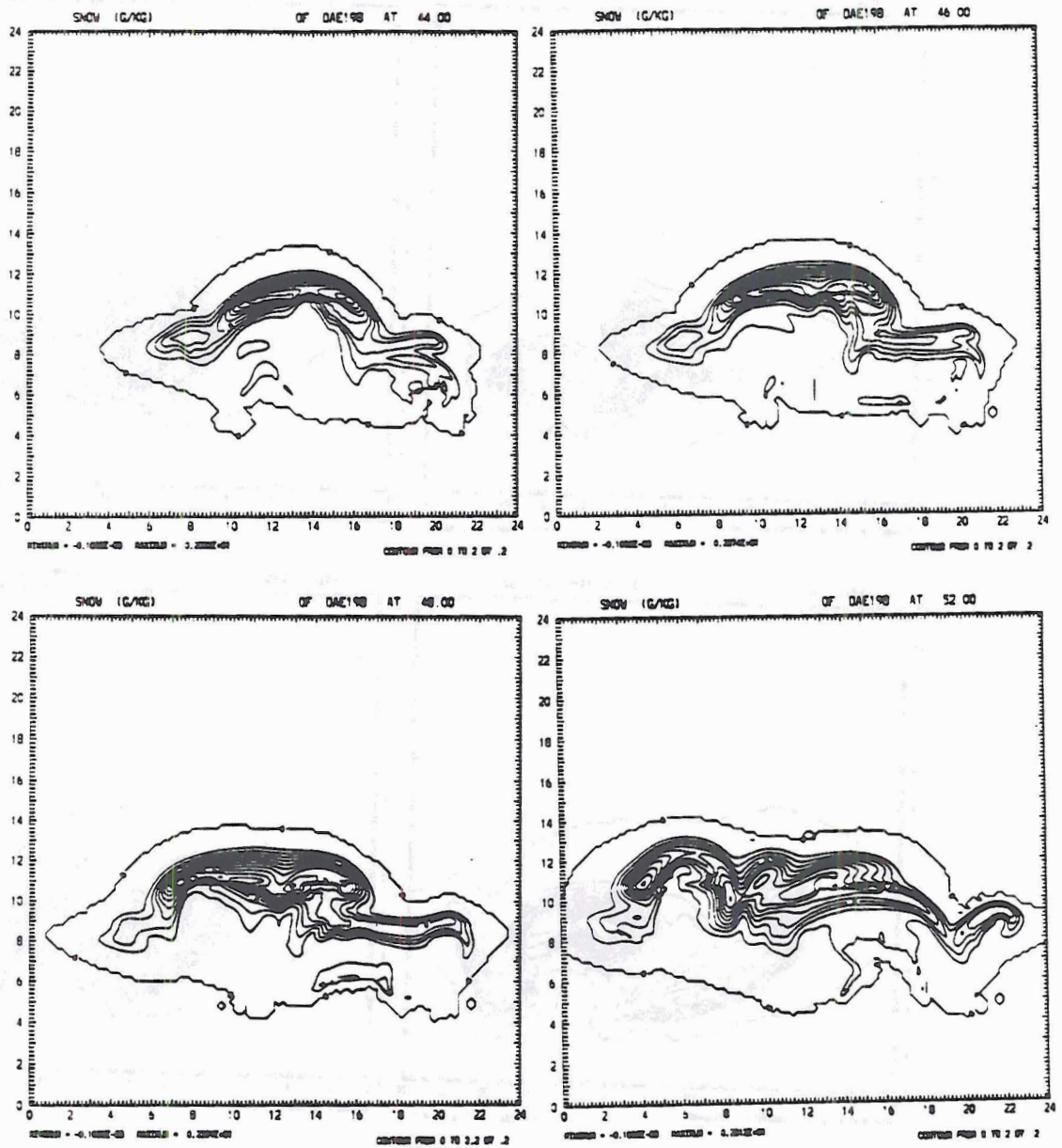


Fig. 5.15: Same as Fig. 5.13, but for snow.

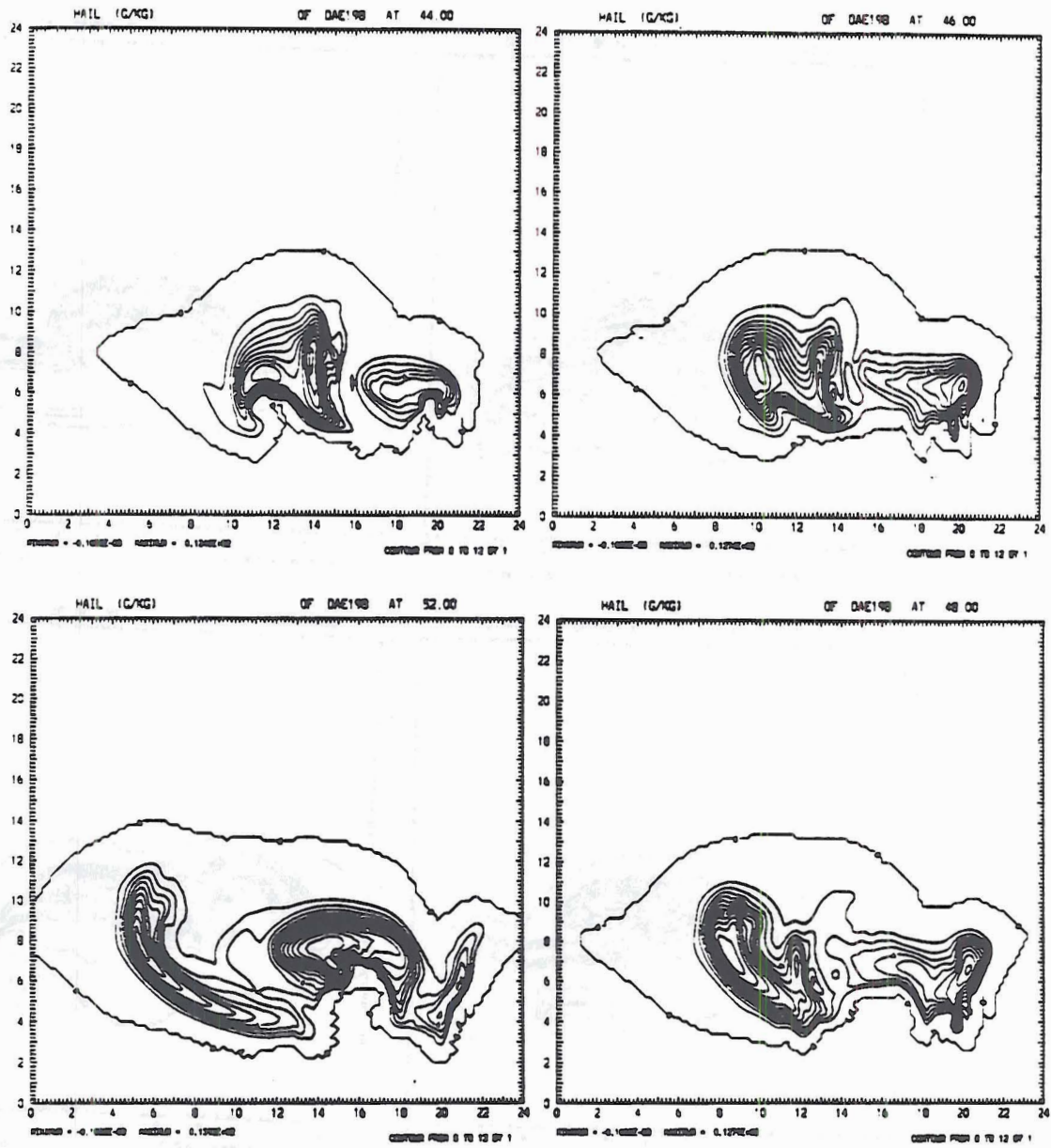


Fig. 5.16: Same as Fig. 5.13, but for graupel (hail).

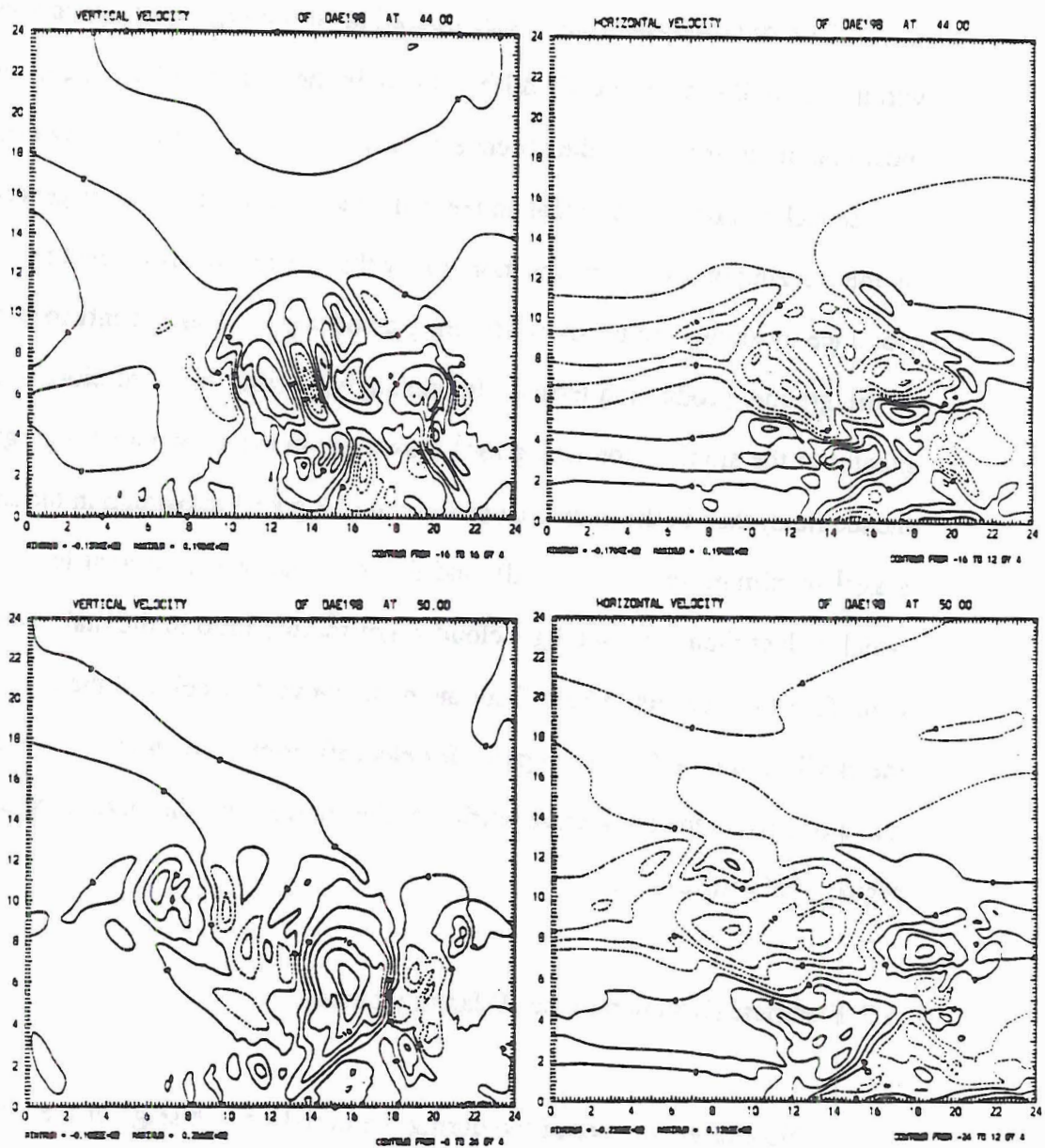


Fig. 5.17: Velocity fields at $t=44$ and $t=50$ minutes. The updraft in the anvil is likely caused by the deceleration of the horizontal wind (continuity equation).

outflow from the top of the main storm: It is coincident with a strong gradient of horizontal wind. It is also possible that the vertical motion is a remnant of a second generation updraft that was cut off by the precipitation shaft emanating from the original convective cell. The main importance of the convection within in the anvil however is not its source, but the microphysics which operate within it.

The microphysical processes operating in the region of upward vertical motion within the anvil is significantly different than in the updrafts of the main convection. The most notable difference is the absence of rain (Fig. 5.18). Graupel however, is abundant, and the lack of rain indicates that unlike in the main convective cell, its generation cannot be by the freezing of rain. It seems more likely that the graupel is formed by the collection of cloud ice by snow, and by snow accreting cloud water. This is confirmed by examination of the graupel production terms. Interestingly, mixing ratios of cloud ice and snow are greater in the anvil region (2.2 g kg⁻¹ maximum in the snow and 1.5 g kg⁻¹ maximum in the ice field) than in the main convective cell (1.8 g kg⁻¹ maximum in the snow field and .8 g kg⁻¹ maximum in the ice field), and the the cloud water content is close to 1.0 g kg⁻¹ which is less than the 2.4 g kg⁻¹ cloud water mixing ratio in the main convective updraft (Fig. 5.13 through Fig. 5.15). Both the main convective cell and the convective region of the anvil should be favored regions for electrification. The higher mixing ratios of snow and cloud ice in the convective portion of the anvil allows the anvil to be the most efficient region of electrification.

5.2 Electrical Evolution of the 19 January Simulation

No charging is permitted during the initial growth stage of the storm since there is no graupel present. Thus the discussion of the electrification results is limited to the rapid development stage and the mature stage of the cloud. The rapid development stage is

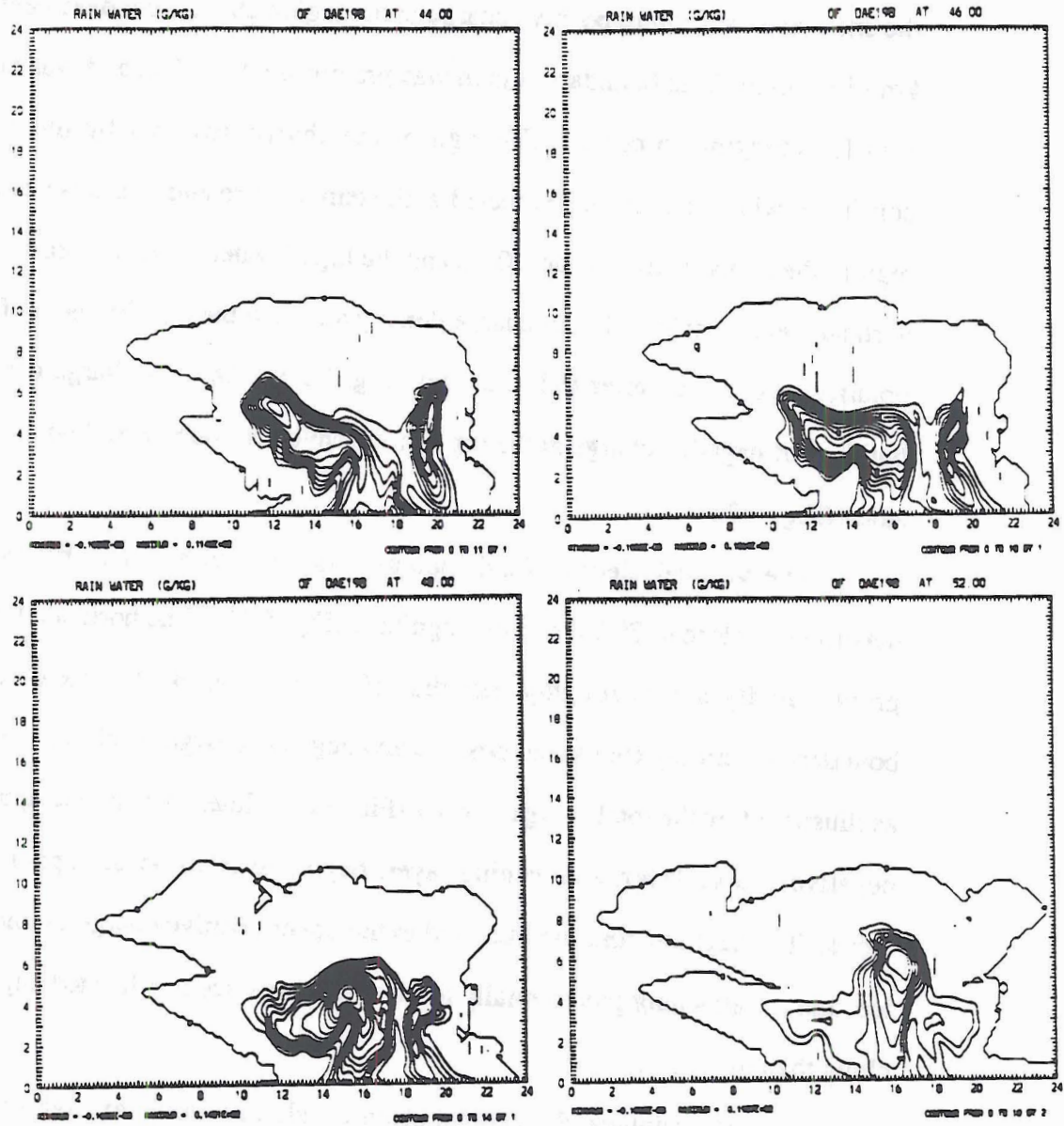


Fig. 5.18: Rain field evolution during the mature stage of the storm. Rain is noticeably absent in the anvil.

characterized by charging in the main convective updraft. In the mature stage, the convective region of the anvil becomes the dominant charge producing region.

When the charging parameterization is initiated at $t=30$ minutes (this is when ice species first appear in the simulation), the graupel begins to acquire negative charge, and the snow and ice acquire positive charge in the region about 1 km deep centered at about 8 km (Fig. 5.19). This boundary region was previously described and was noted as a likely area for charging to occur. The sign of the charge acquired by the hydrometeors is consistent with the charging expected at the temperature and liquid water contents in that region (the temperature is near -20°C and the liquid water content is around 2 g kg^{-1}). The vertical electric field and total charge density all show the development of a weak normal polarity dipole soon after $t=30$ minutes (Fig. 5.20). The ion charge density indicates a build up of negative charge at the top of the convective bubble and positive charge on the sides (Fig. 5.21).

The vertical electric field increases rapidly with time. By $t=38$ minutes the maximum is close to 70 kV m^{-1} in magnitude (Fig. 5.22). The horizontal electric field also grows rapidly and is roughly half that of the vertical electric field (Fig. 5.22). The boundary separating the overall positive and negative charges is closer to 9 km at this time, as illustrated by the total charge density (Fig. 5.23). Interestingly, the appearance of a thin negative charge layer, a screening layer, begins to form on the upper boundary of the cloud. The negative ions are attracted to the upper positive charge on the snow and cloud ice, and are attaching preferentially to the cloud ice since it is located slightly higher in the cloud than the snow.

By $t=42$ minutes, the vertical electric field has grown to slightly over 111 kV m^{-1} and the center of the positive dipole is near 9.5 km (Fig. 5.24). The maximum charge on the snow is centered near 10 km and is 2.1 nC m^{-3} , graupel has a negative charge with a maximum magnitude of 2.4 nC m^{-3} centered at about 9.0 km (Fig. 5.25). The cloud ice is mostly positively charged with a maximum charge of 1 nC m^{-3} , but a substantial negatively

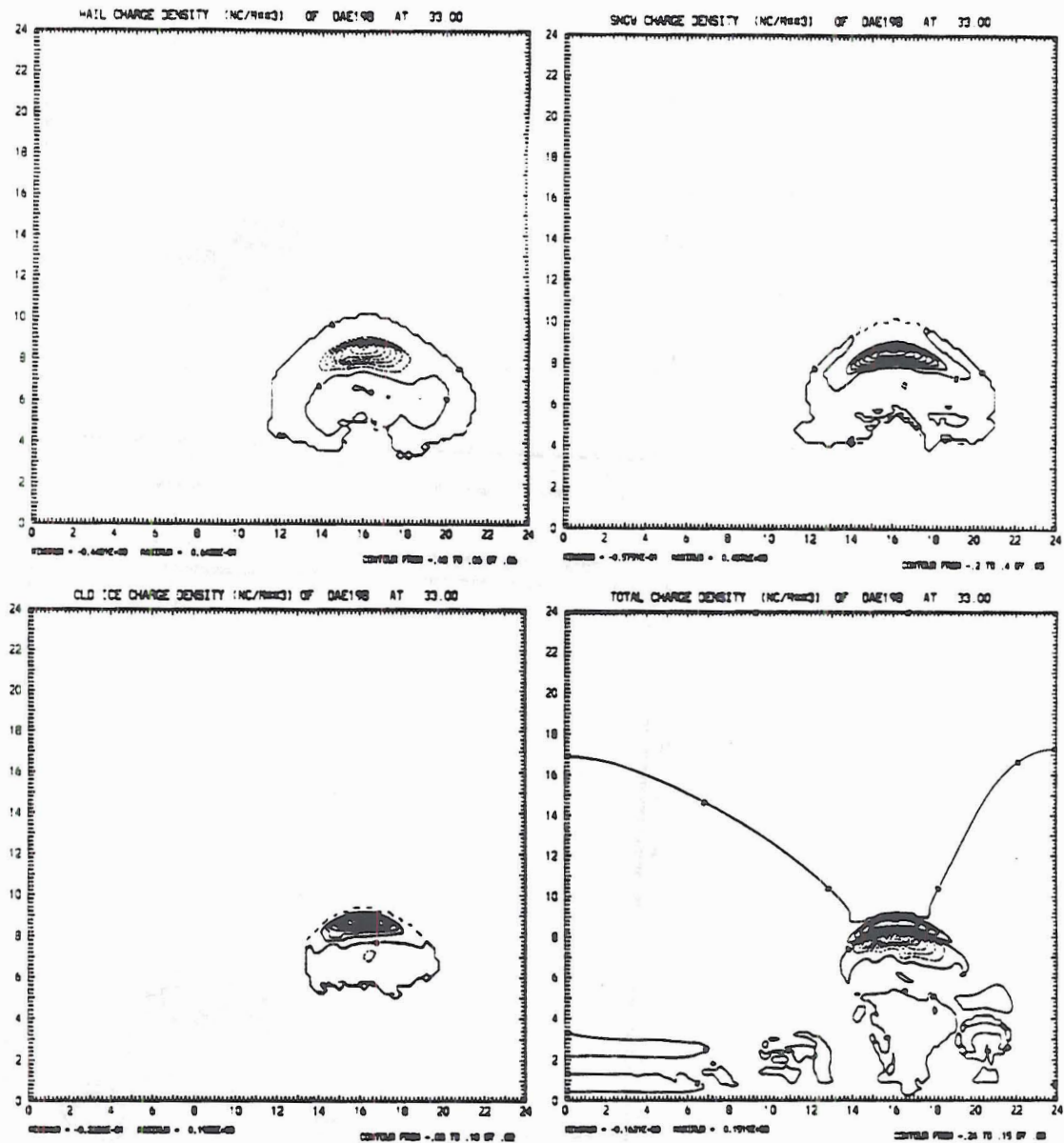


Fig. 5.19: Charge density on ice species and total space charge density at t=30 minutes. The maximum charging occurs in a region about 1 km deep centered at an altitude of near 8 km.

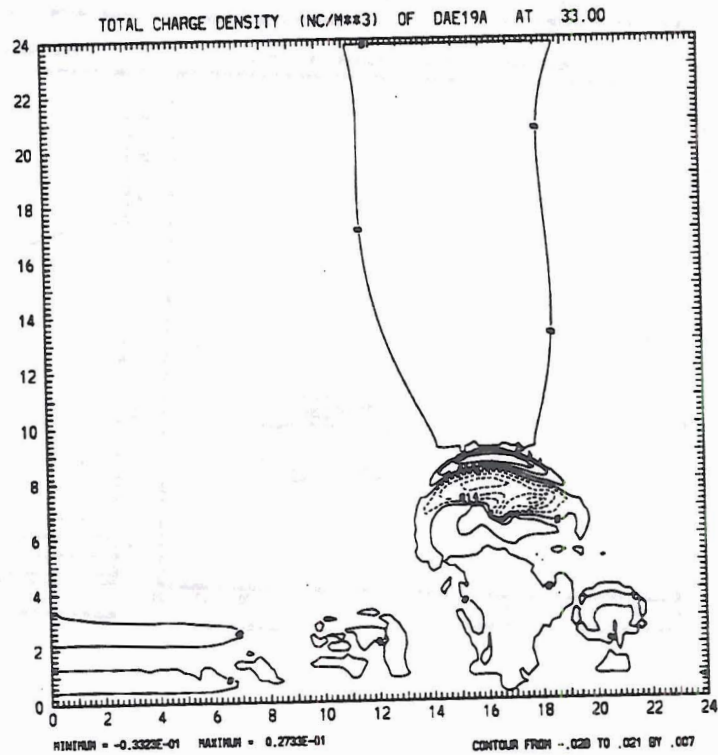
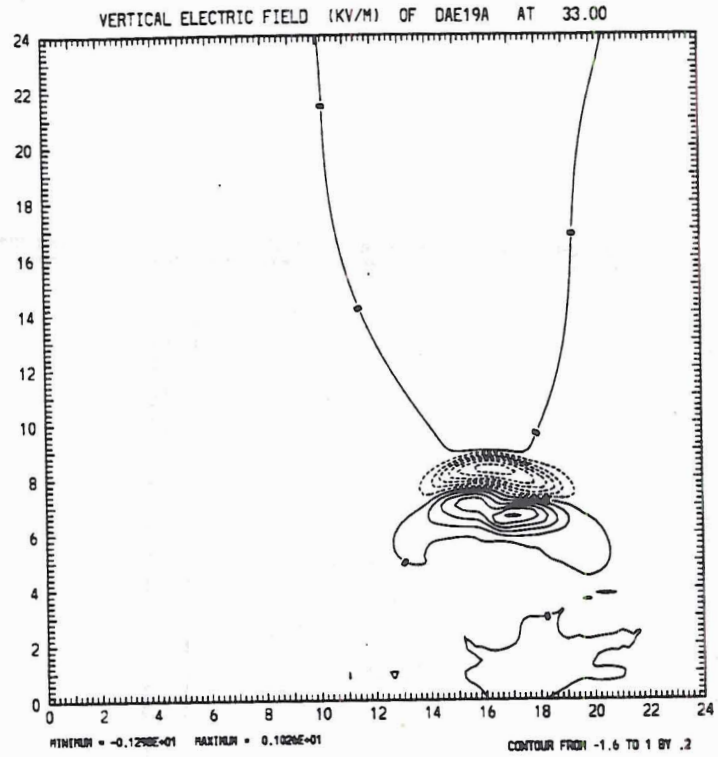


Fig. 5.20: The vertical electric field and total space charge density at $t=33$ minutes. A week normal polarity dipole (negative charge underlying positive charge) is evident.

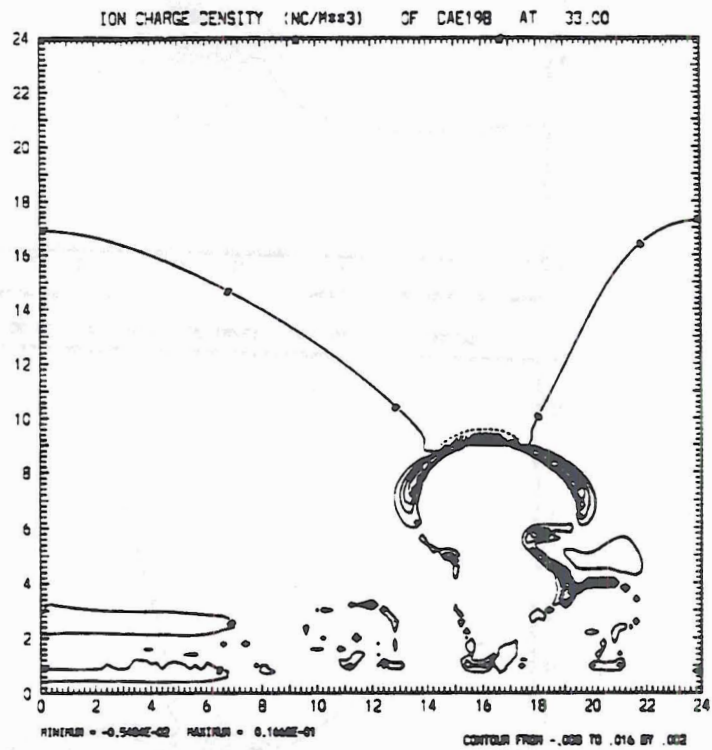


Fig. 5.21: Ion charge density at t=33 minutes. Negative ions are predominant on the top of the cloud and positive ions predominate along the sides.

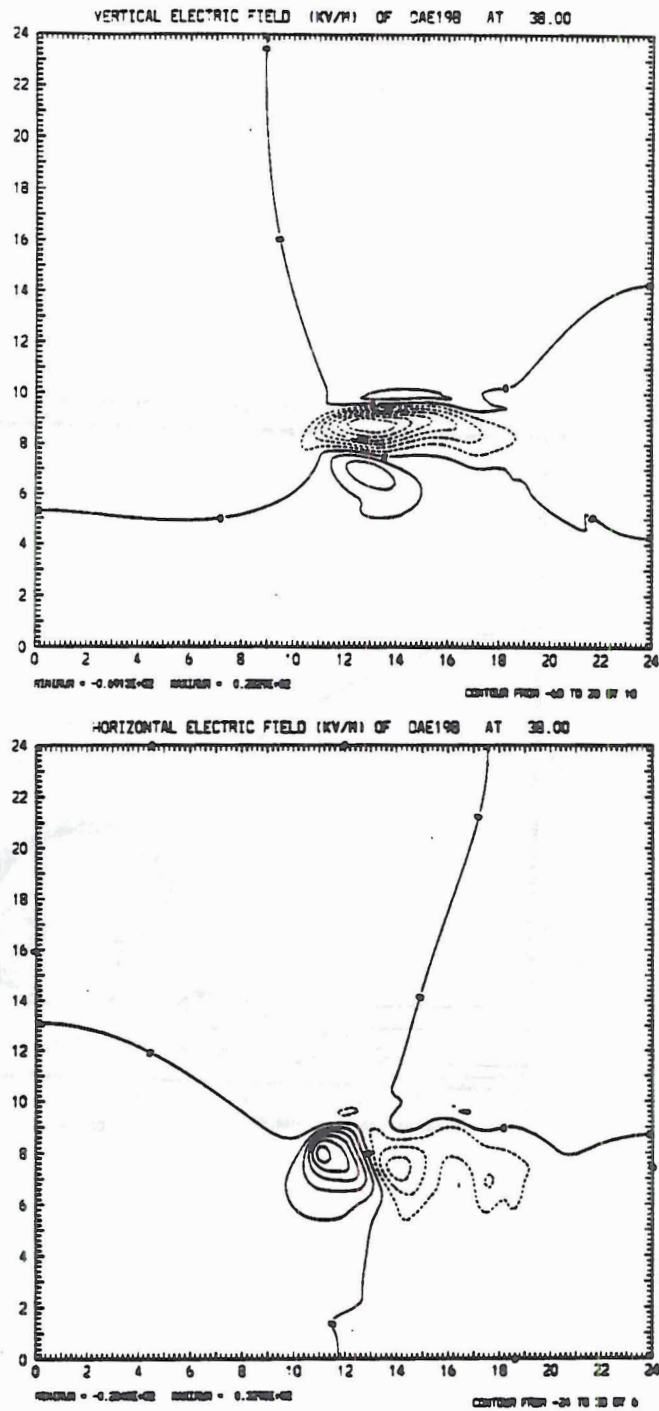


Fig. 5.22: The vertical and horizontal electric field at $t=38$ minutes. The maximum vertical electric field is near 70 kV m^{-1} in magnitude. The maximum magnitude of the horizontal field is roughly half that of the vertical.

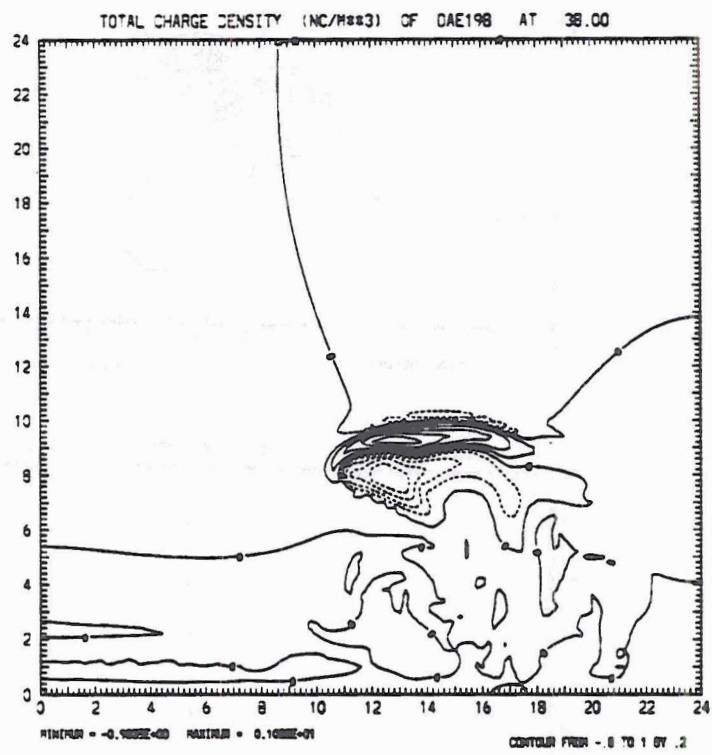


Fig. 5.23: Total space charge density at t=38 minutes. The boundary separating negative and positive charge is near 9.0 km in altitude. A negative charge screening layer is apparent at the top of the cloud.

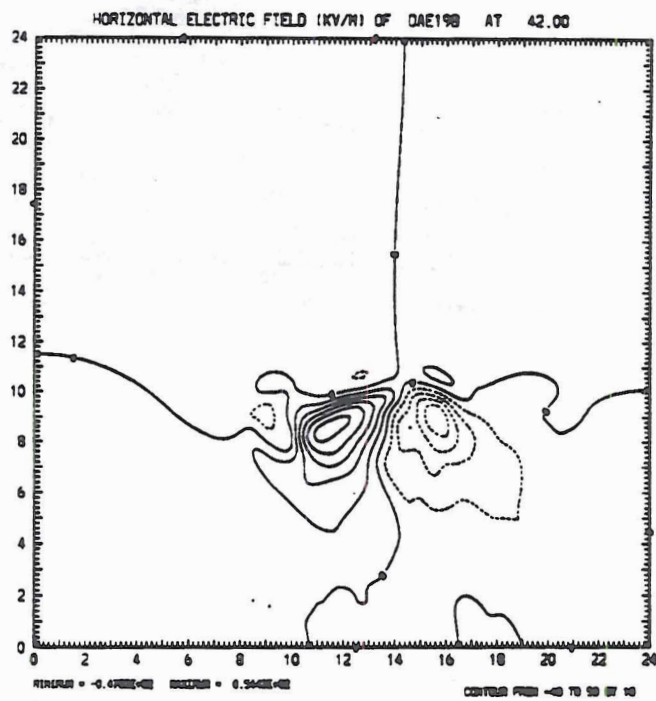
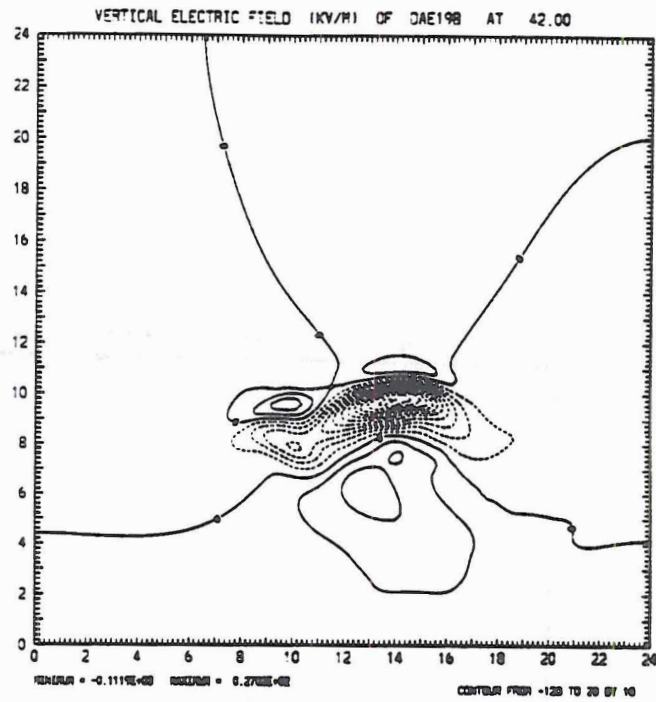


Fig. 5.24: The vertical and horizontal electric field at $t=42$ minutes. The center of the dipole is near 9.5 km in altitude.

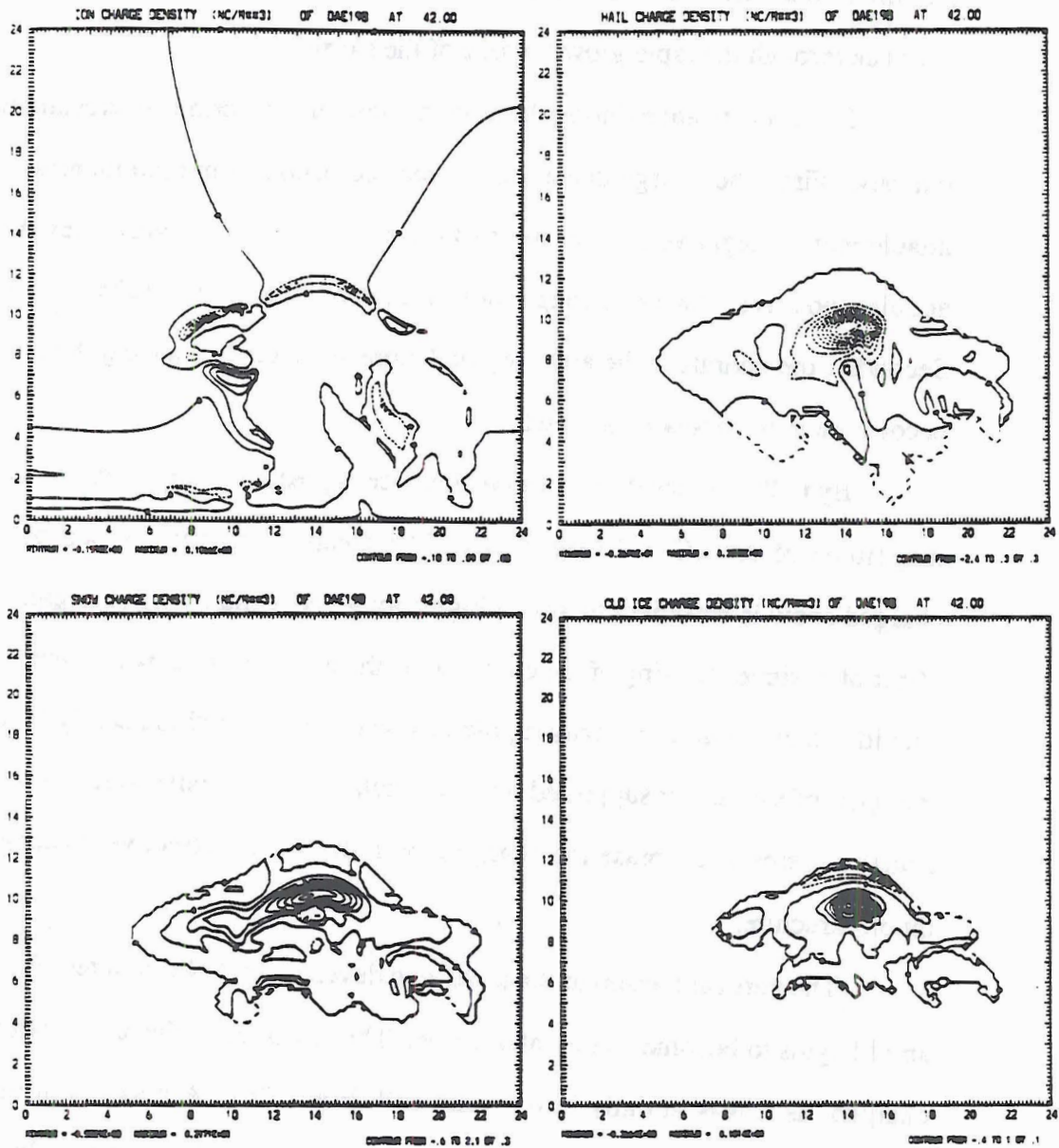


Fig. 5.25: Total ion charge density and the charge density on graupel, snow and cloud ice at $t=42$ minutes. The maximum charge on snow is centered near 10 km in altitude. The maximum charge on graupel is centered near 9 km in altitude. Charge on cloud ice is mostly positive, but a negatively charged region caused by the attachment of ions is evident near cloud top.

charged region caused by the attachment of ions is beginning to form (Fig. 5.25). It has a maximum magnitude of 0.37 nC m^{-3} . The trends in the electrical evolution of the storm continue through the rapid growth phase of the storm.

The electrification during the mature phase of the storm is interesting for a couple of reasons. First, the charge density on cloud ice becomes predominantly negative. The attachment of negative ions to the surface of the cloud ice overcomes the tendency to acquire positive charge through non-inductive charging mechanism with graupel. Secondly, the updraft in the anvil region begins to electrify, causing the electric dipole to become more horizontally oriented.

By $t=48$ minutes the charge on cloud ice is predominantly negative with a maximum magnitude of 2.6 nC m^{-3} (Fig. 5.26). The electric potential caused by the positively charged snow is sufficient to attract high enough concentrations of negative ions that the effect of positive charging of the cloud ice by the non-inductive mechanism is counteracted. The idea that a normal polarity dipole can be created in a cloud solely by the convective transport of ions is not supported by this simulation. The convective charging mechanism actually seems to decrease the charging by reducing the effective positive charge in the dipole structure.

The vertical motion in the anvil also develops by $t=48$ minutes (Fig. 5.17), and the anvil begins to become electrically active. The cloud ice in the anvil updraft is positively charged, as it was initially in the main cell (Fig. 5.26). A maxima in the snow charge density is also evident at this time (Fig. 5.26). It is nearly comparable in magnitude, around 2.5 nC m^{-3} , to the maxima associated with the main updraft..

As the convective anvil region becomes more active, the simple dipole structure of the storm begins to break down. This is most readily seen in the evolution of the electric potential (Fig. 5.27). At $t=48$ minutes the electric potential indicates a roughly vertical dipole. At $t=50$ minutes the charge production in the anvil region becomes more evident as a lobe of negative electric potential. At $t=52$ minutes a closed contour region develops, and

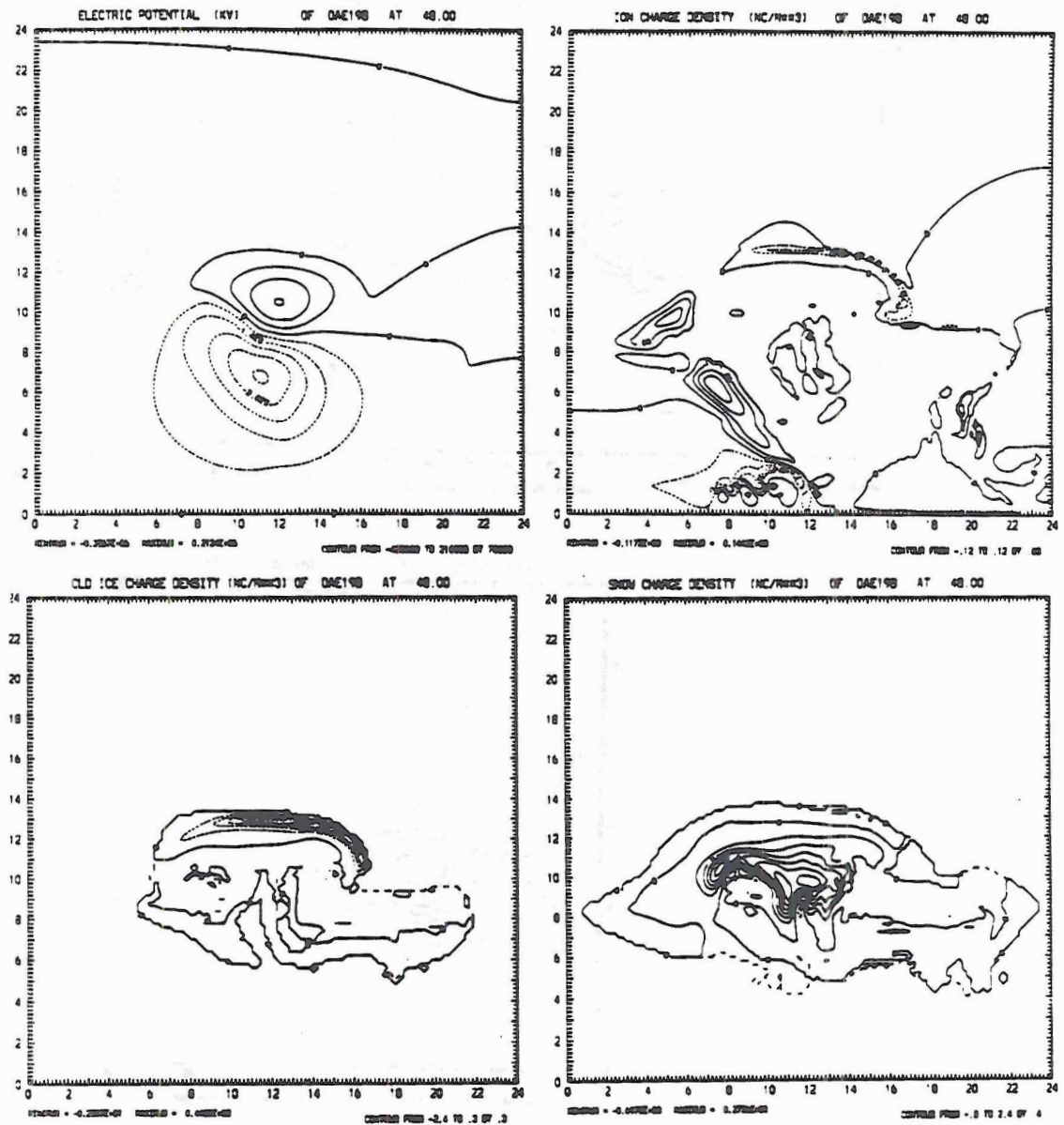


Fig. 5.26: Electric potential, ion charge density and charge density on cloud ice and snow at t=48 minutes. The charge on cloud ice is predominantly negative due to the attachment of negative ions. The anvil region also begins to become electrically active at this time.

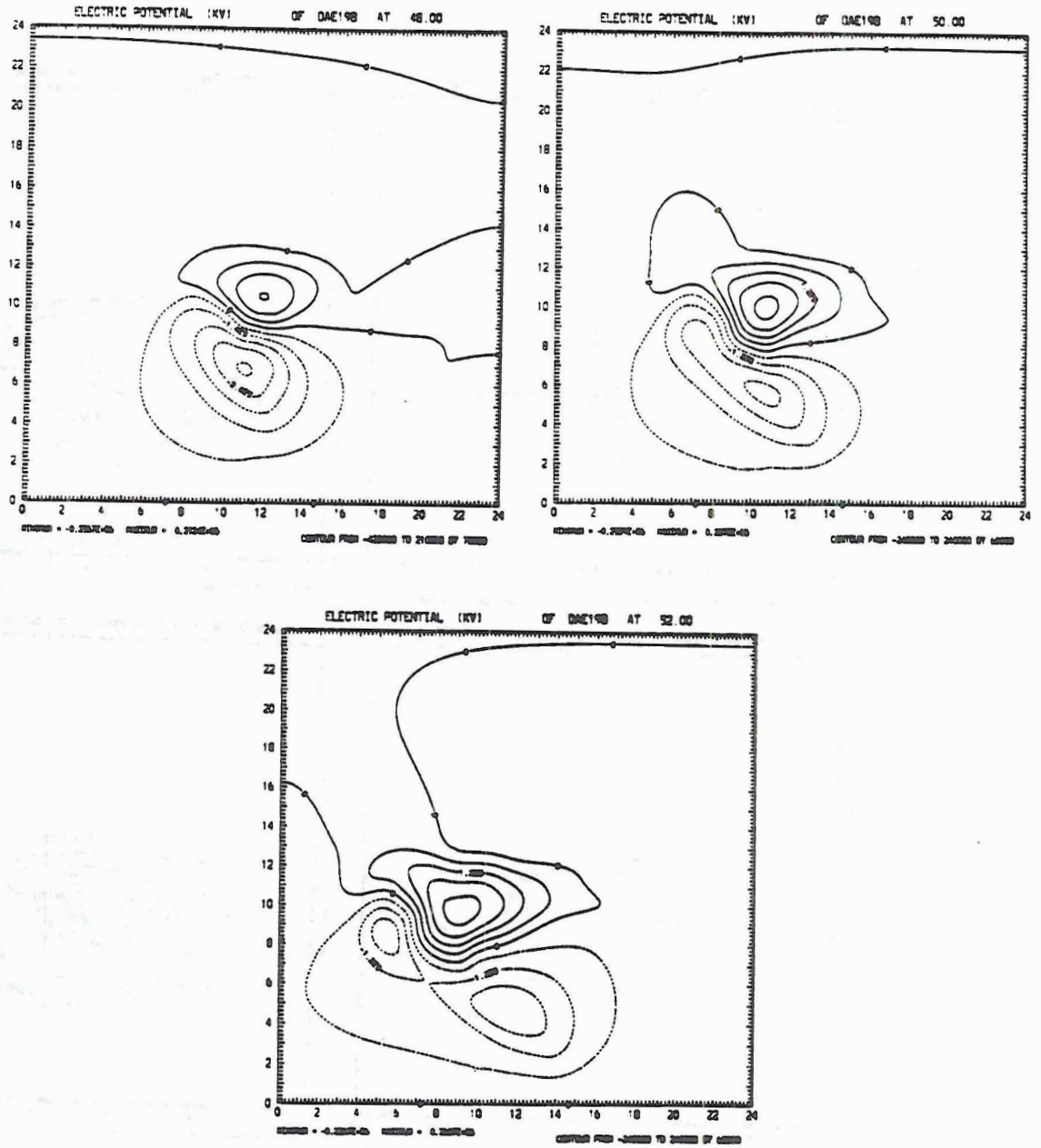


Fig. 5.27: Evolution of the electric potential during the mature phase of the storm. The simple dipole structure of the storm breaks down as the anvil begins to electrify.

the horizontal and vertical electric fields become roughly equal in magnitude by this time (on the order of 150 kV m^{-1} , Fig. 5.28). The maximum charge of graupel and snow are found in the anvil convective region at the end of the model run (Fig. 5.29). The maximum magnitude of cloud ice charge is found in the negative screening layer associated with the main updraft.

A summary of the electrical evolution of the storm are captured in Fig 5.30, and Fig. 5.31. The domain maximum charge densities on the ice species are displayed in Fig. 5.30. There is a correlation between the charge density of graupel and snow: the rate of increase of negative charge on the graupel is nearly the same as the rate of increase of positive charge on the snow. The charge density on ice is initially correlated with the charge density of the graupel, but then becomes dominated by the attachment of negative ions at around $t=44$ minutes. The effect of the negative ions attaching to cloud ice on the vertical electric field is evident in Fig. 5.31. While the cloud ice has positive charge, the vertical electric field increases rapidly. When the cloud ice begins to collect negative ions, the rate of increase of the electric field slows and eventually reverses. Ion conduction currents counteract the non-inductive charging process.

5.3 Comparison of Model Predicted Radar Reflectivity with Observation

Model results can only be considered representative of reality if they compare favorably with observations. A model is used to understand processes and phenomena that are usually too complex, detailed, or ephemeral in nature to be observed. This makes comparison of specific details difficult or impossible. Nonetheless, the gross features of a phenomena, such as those of a thunderstorm, is observable and should be reproduced adequately. A model that fails to reproduce the overall structure of a system can not be relied upon to understand its details.

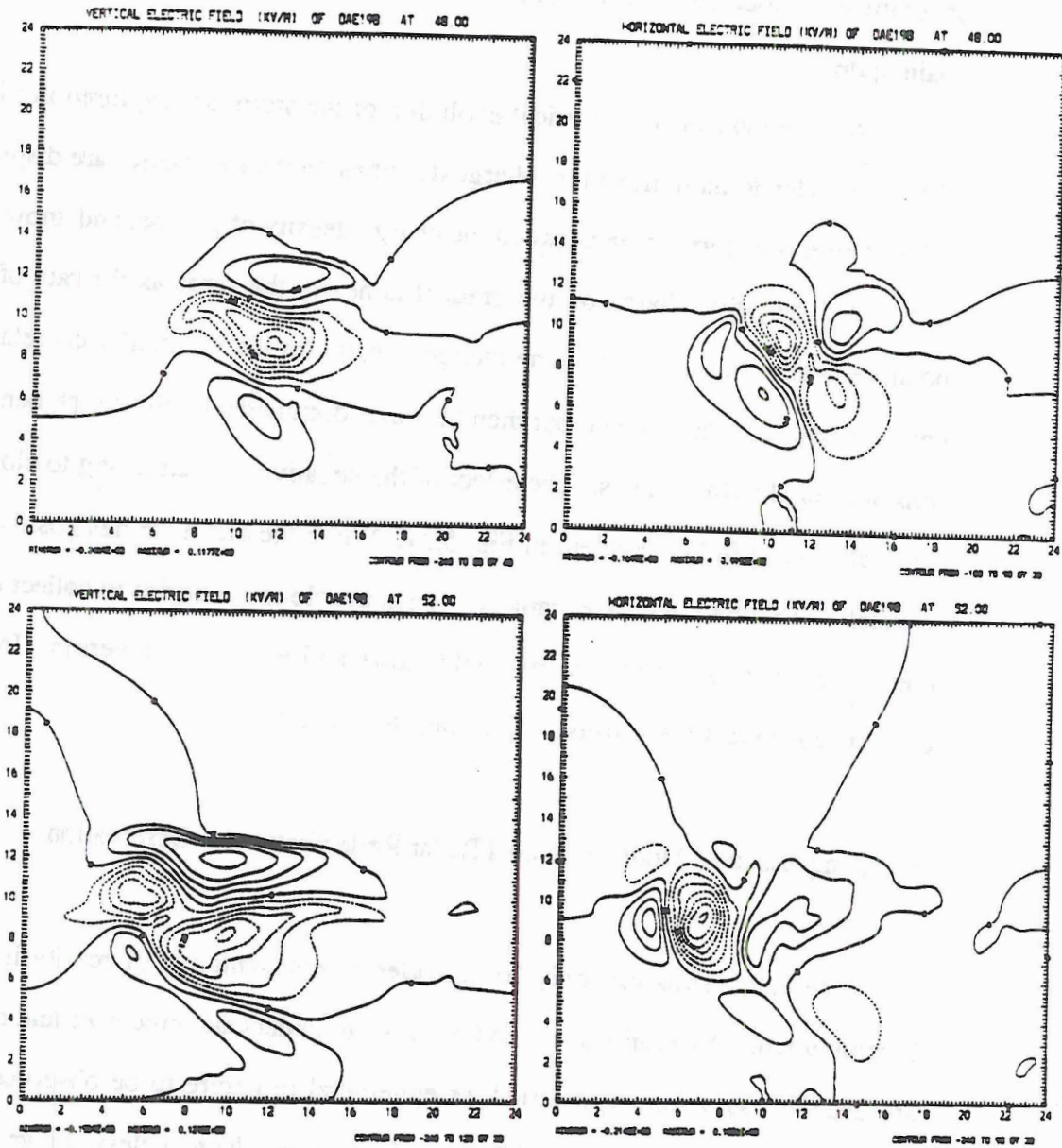


Fig. 5.28: Vertical and horizontal electric fields at $t=48$ and 52 minutes. The horizontal and vertical electric fields become roughly equal in magnitude by $t=52$ minutes.

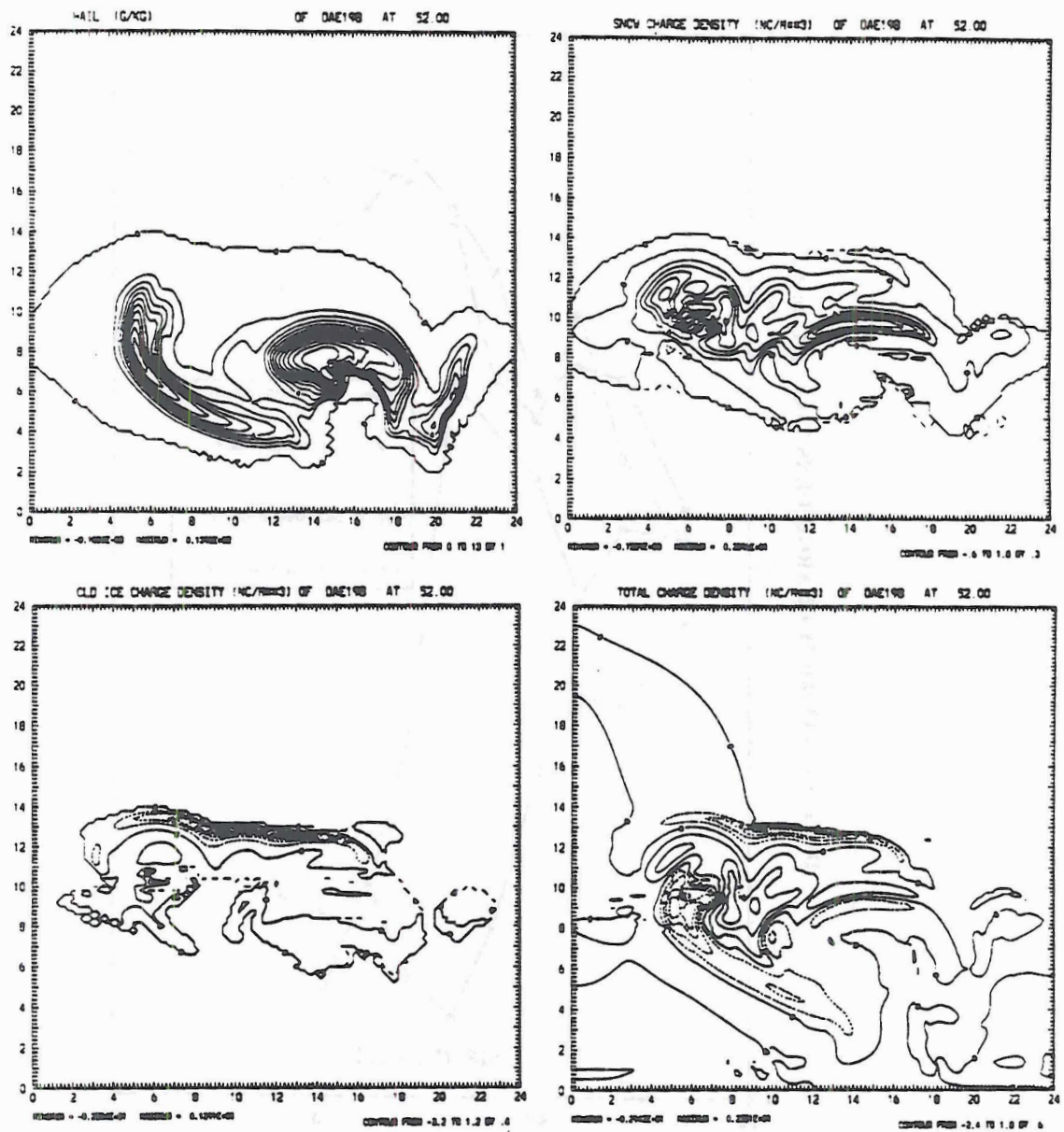


Fig. 5.29: Charge density on the ice species and the total space charge density at $t=52$ minutes. The maximum charge on graupel and snow are found in the anvil and not in the convective updraft. The maximum charge on cloud ice is found in the negative screening layer at the top of the convective updraft.

CHARGE DENSITY TENDENCIES

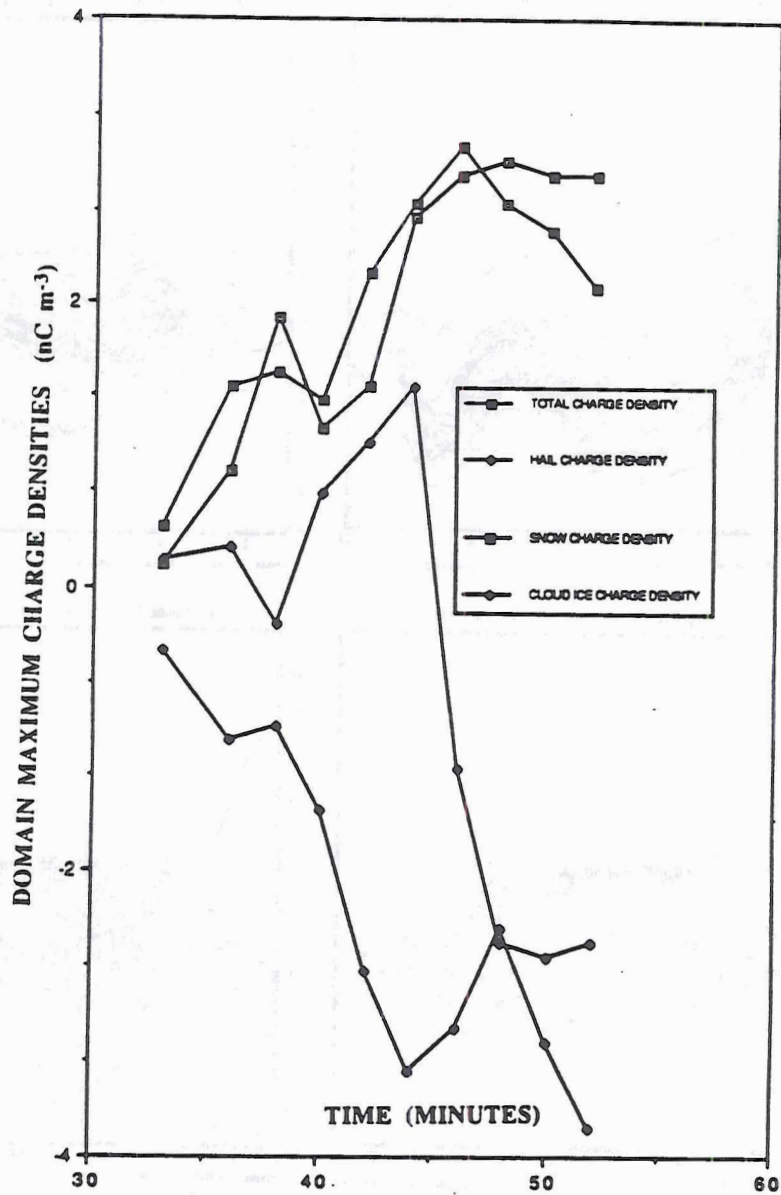


Fig. 5.30: Domain maximum charge density on ice species as a function of time.

**VERTICAL ELECTRIC FIELD AND
CLOUD ICE CHARGE DENSITY TENDENCIES**

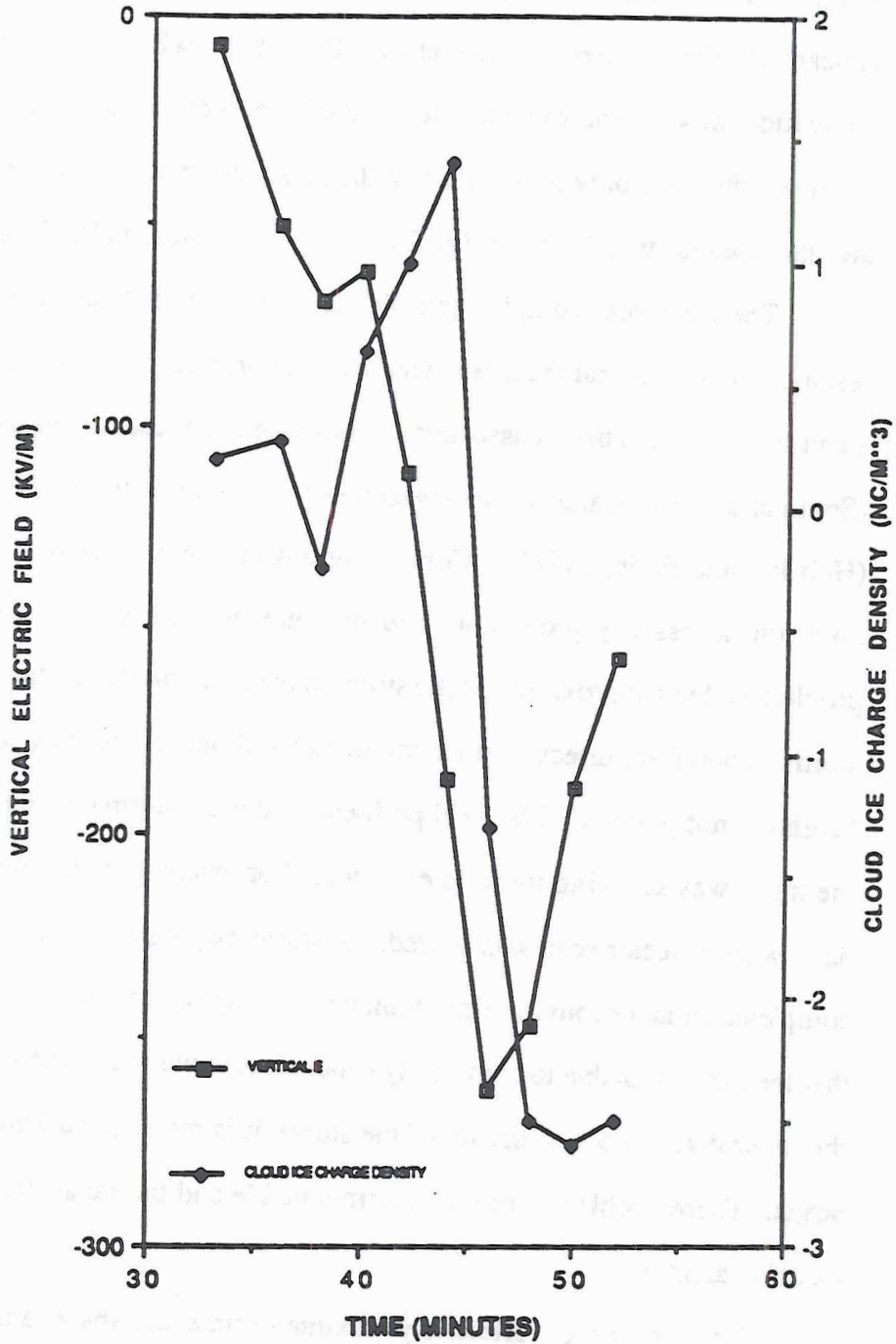


Fig. 5.31: Domain maximum vertical electric field and cloud ice charge density.

The primary verification for the model results is from radar information. In order to compare the model results with the radar observations, the two must be correlated in time. The first low level radar echoes appear at 0552 UTC. The first radar echo in the simulation appears at $t=21$ minutes. Based on this, 0552 UTC will correspond to $t=21$ minutes of simulation time in the model. Because of the short model simulation time (only 52 minutes), there are only two times that the radar observations can be compared directly to the simulated radar reflectivity: 0612 UTC ($t=41$ minutes) and 0620 UTC ($t=49$ minutes).

There are three complications that arise when comparing the radar data to the model results. The first is that the model tends to over predict the reflectivity by 10-20%. This is a common problem that is associated with models that use a Marshall-Palmer distribution (Smith *et al.*, 1975), and has also been noted in previous studies that have used this model (Helsdon and Farley, 1987). Comparing absolute values of radar reflectivity therefore does not necessarily provide a good measure of the model performance. The second problem is that the proximity of the storm to the radar prevented the radar from topping the storm. Therefore, direct comparison of radar cloud top heights and predicted cloud top heights is not possible. The final problem is that the storm develops faster vertically than the radar was scanning towards echo top. For example, if the storm was initially 3 km deep when a sector scan was started, the storm may be 8 km deep by the time the scan is completed (it takes roughly eight minutes to complete a volume scan). The result of this is that the radar is unable to completely capture the evolution of the storm, or, in other words, the radar data is not a snapshot of the storm, it is more like a long exposure of a moving target. These problems are not insurmountable and the radar data is still valuable in the model evaluation.

The location of reflectivity maxima in time and space, and the extent of the main convective updraft should be comparable in structure even if the magnitudes of the reflectivity are not the same. These ideas and others will be explored in turn in an attempt to instill a reasonable level of confidence in the reality of the model simulation

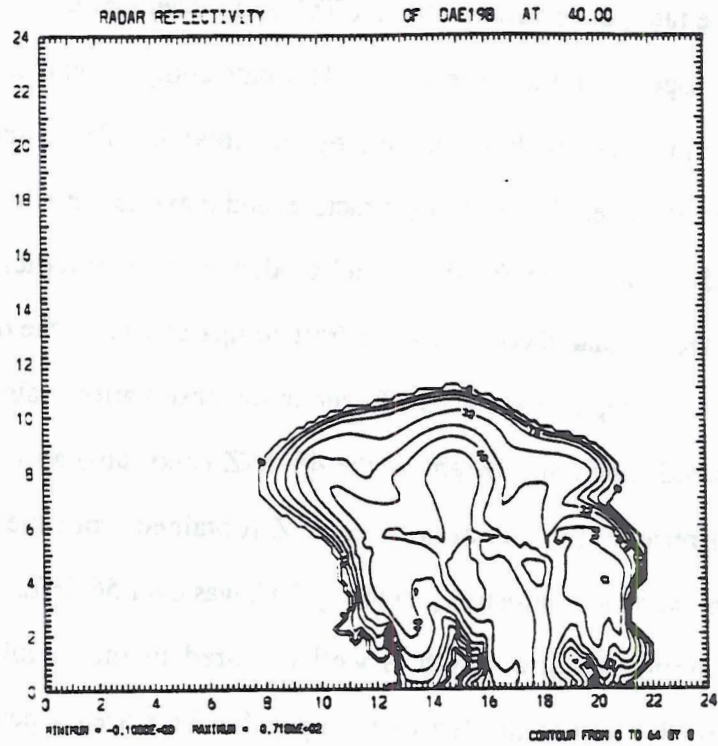
The radar observations (0612 UTC) and model predicted reflectivity (t=40 minutes) are shown together at the same scale to facilitate comparison (Fig. 5.32). There are several features which are well simulated by the model. These include the height of the convection, the overall reflectivity structure, and maximum predicted reflectivity.

After correcting for the model tendency to overpredict reflectivity by 15%, the height of the simulated convective updraft compares well to the observation. For example, the maximum height of the 40 dBZ echo in the observations (almost 8 km) is very close to the predicted maximum height of the 48 dBZ echo (also almost 8 km). The maximum observed reflectivity was almost 50 dBZ (obtained from the raw radar data), and the maximum predicted reflectivity in the updraft was over 56 dBZ.

Another feature which is well captured in the simulation is the minimum in reflectivity located to the left of the updraft. This area separates the updraft from the downdraft. In the observations, the region is about 2 km wide at the ground and extends to an altitude near 3 km. The simulation also shows a region about 2 km wide and near 3 km in altitude.

The simulation at t=50 minutes compares even more favorably than at t=40 minutes (Fig. 5.33). In the simulation there is a broad region of high reflectivity (above 40 dBZ) in the updraft, and above 8 km there is a tight reflectivity gradient. The model predicted values are higher, as expected, but compare very well after about a 15% percent correction. The reflectivity gradient the model is near 9 km in altitude instead of the observed height of 8 km. To the left of the updraft the model predicts an intense (in excess of 64 dBZ) brightband in the anvil. A bright band can be seen in the observation, but it is not near 64 dBZ.

With the limited amount of radar information that is available, an attempt has been made to justify the validity of the model simulation of 19 January, 1990. The overall reflectivity structure resembles the structure observed by the MIT radar. The predicted height of the maximum reflectivity was shown to be consistent with the observations.



19 JAN 90 0612 UTC VERTICAL SLICE X=30 DBZ

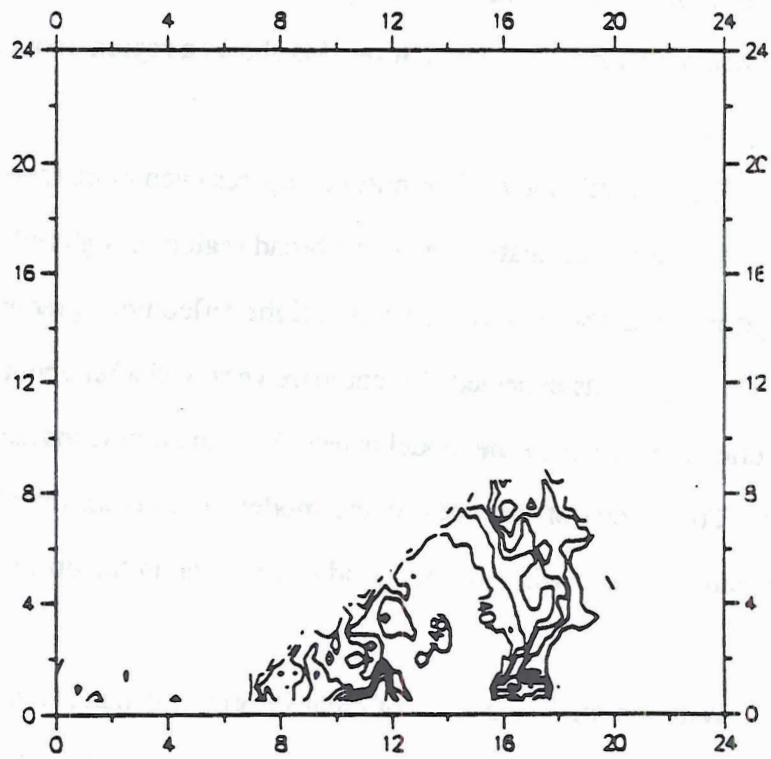


Fig. 5.32: Comparison of model predicted radar reflectivity with observation.

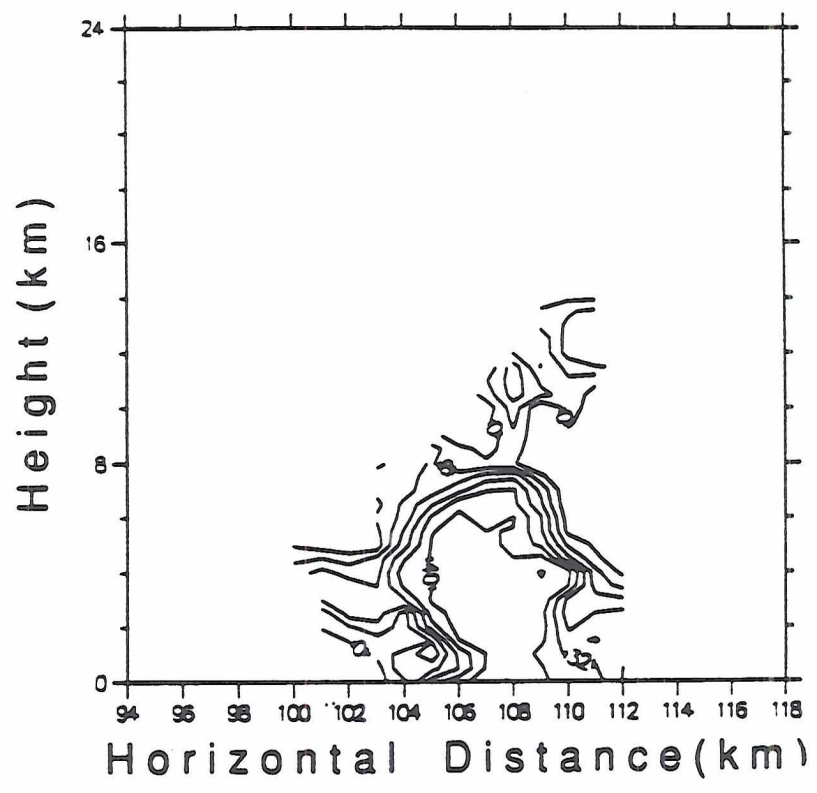
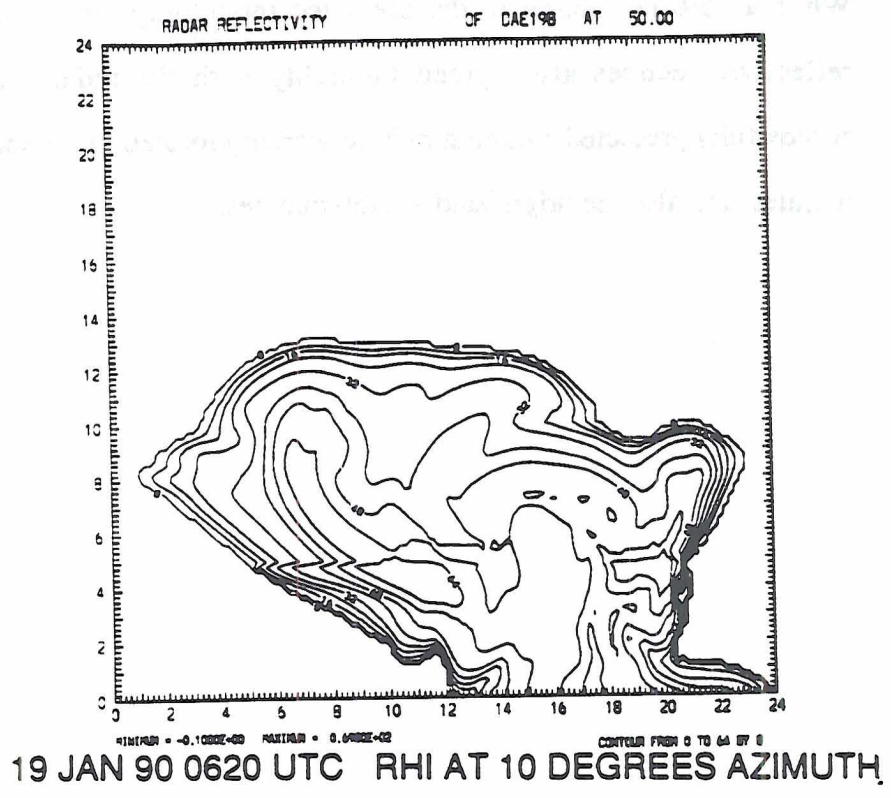


Fig. 5.33: Comparison of model predicted radar reflectivity with observation.

When a 15% correction in the predicted reflectivity was used, the height of various reflectivity echoes also agreed favorably with the radar information. The model successfully predicted a minimum in reflectivity located to the south of the updraft at $t=40$ minutes, and also the brightband at $t=50$ minutes.

CHAPTER VI

MONSOON MODELLING RESULTS

The 0000 UTC sounding taken at Darwin served as the base atmospheric state for initialization of the 12 January monsoon simulation. A northwest-southeast projection of the environmental winds were chosen to represent the two dimensional wind field since this was approximately the direction of storm motion based on radar information. In the lowest levels, a convergence of $1.5 \times 10^{-4} \text{ s}^{-1}$ was applied, and random perturbations of temperature and water vapor were used to initiate convection. The additional convergence in the low levels was instituted to approximate the effects of the ITCZ. The initial conditions are shown in Fig. 6.1.

6.1 Non-Electrical Characteristics of the Simulation

The general evolution of the convection is shown in Fig 6.2 as a series of cloud depiction plots at selected times. Similar to the break period model output, the dashed lines are the streamlines and the cloud boundaries are solid lines which divide water saturated and water sub-saturated air. Dots and asterisks represent rain and graupel mixing ratios greater than 1.0 g kg^{-1} , respectively, and hyphens and S represent cloud ice and snow mixing ratios greater than 0.5 g kg^{-1} , respectively.

Unlike the break period, the monsoon simulation does not have well defined growth stages. Beginning at $t=9$ minutes (Fig. 6.2), only a water saturated stratiform cloud layer is present as result of the imposed large-scale convergence and vertical motion of order $10\text{-}50 \text{ cm s}^{-1}$. The cloud base is at 3.2 km and extends to a height of 7.6 km. The cloud deck increases in thickness through time ($t=15$ minutes (Fig. 6.2), for

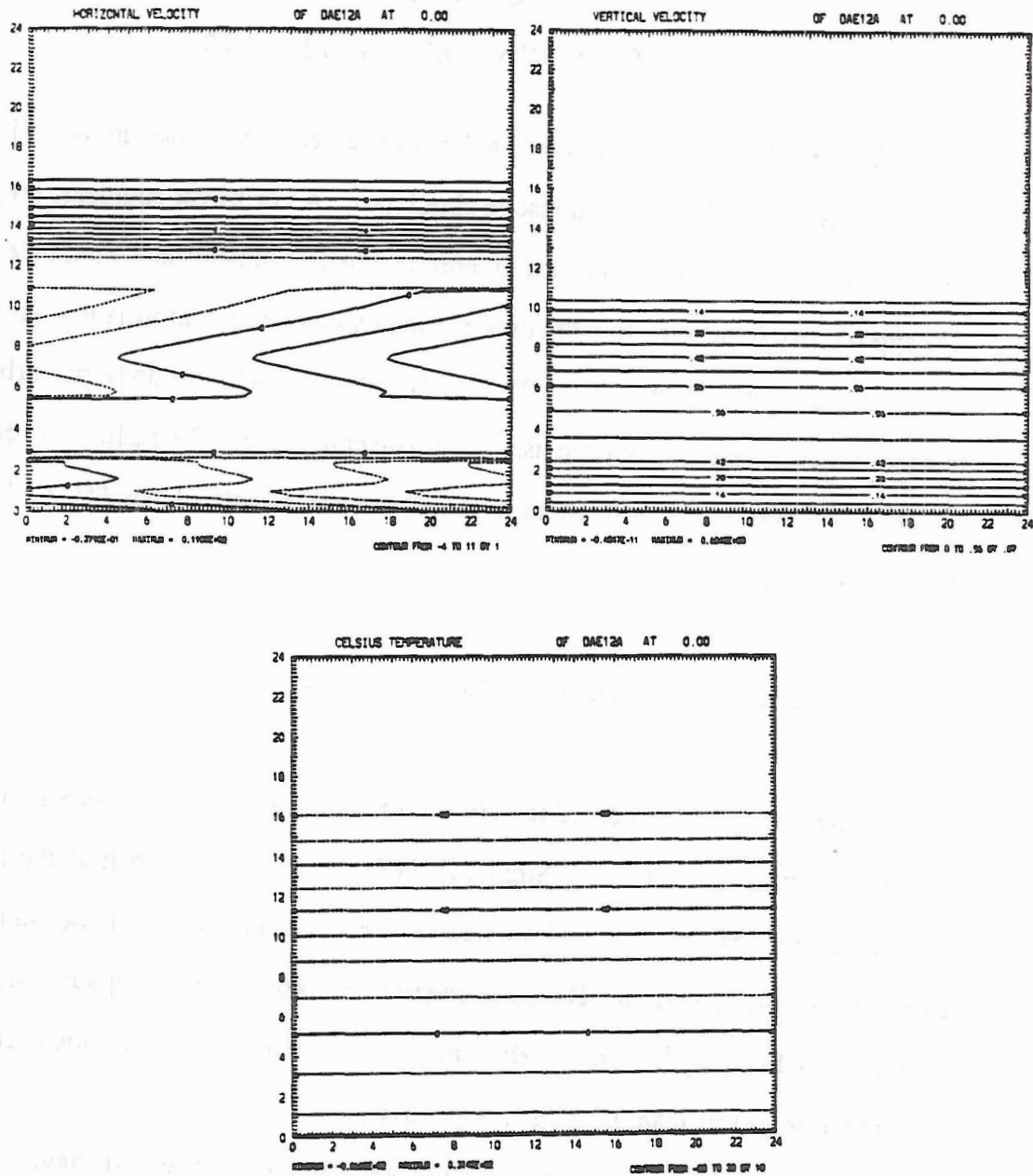


Fig. 6.1a: Thermodynamic and kinematic initialization adapted from the 0000 UTC sounding at Darwin. A northwest-southeast component of the horizontal winds are used and modified such that a convergence of $1.0 \times 10^{-4} \text{ s}^{-1}$ is applied. Vertical velocity is such that the continuity equation is satisfied. Random perturbations are applied in the lowest levels of the temperature and water vapor fields.

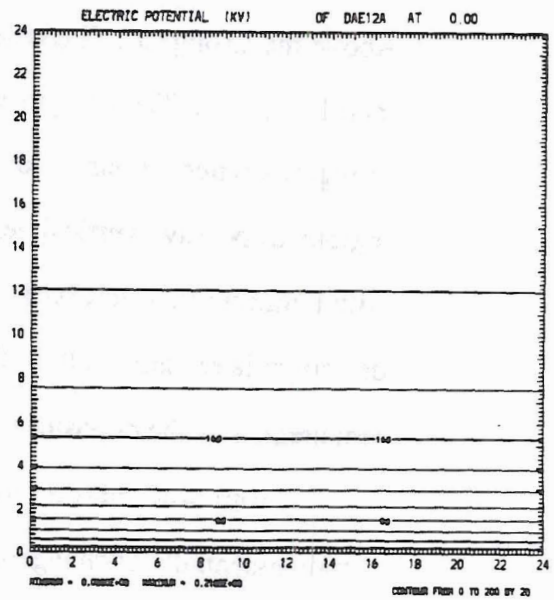
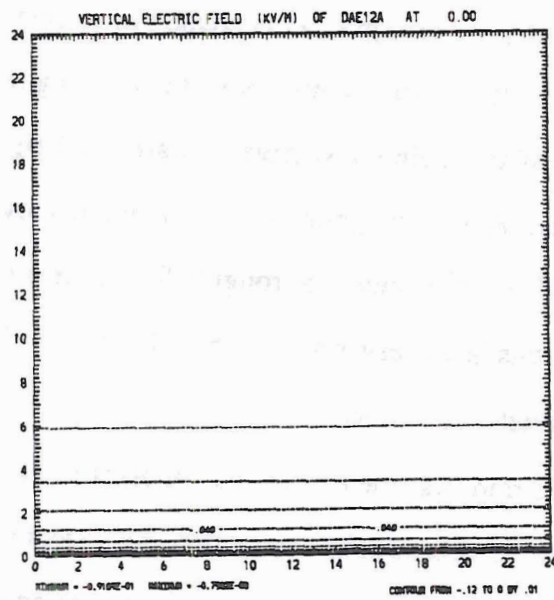
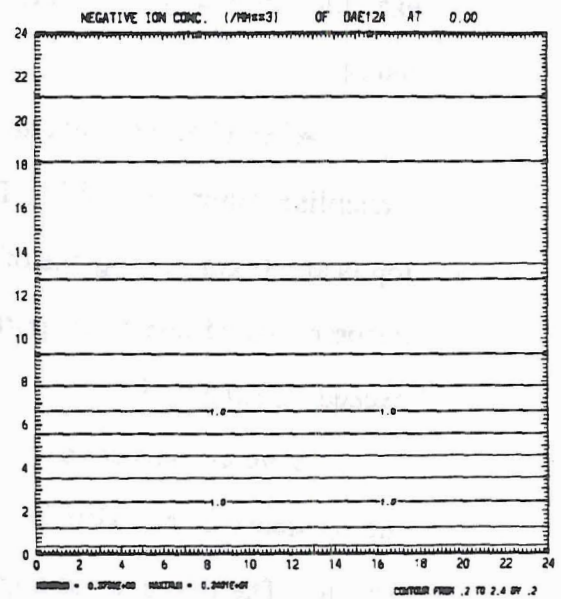
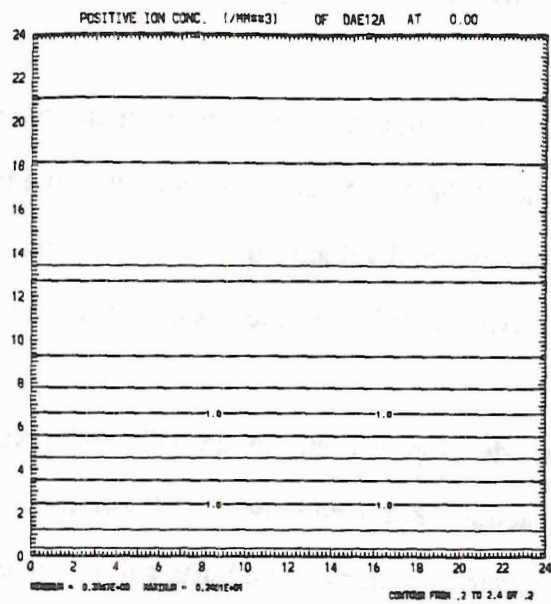


Fig 6.1b: Electrical initialization. The positive and negative ion concentrations are chosen so that the vertical electric field is close to the value of the fair weather electric field. The ion concentrations increase exponentially away from the surface.

example), primarily due to the base of the cloud lowering and less from the cloud height rising.

After a half hour of simulation time convective circulations begin to appear in the streamline pattern (Fig. 6.2). The base of the cloud deck lowers to 800 m and the cloud top is at 9.0 km. In regions of negative vertical velocity the base of the cloud begins to become ragged due to evaporation. Also at $t=30$ minutes rain reaches a mixing ratio exceeding 1.0 g kg^{-1} .

Several convective circulations develop by $t=40$ minutes (Fig. 6.2). Rain becomes more extensive and exists in a layer about 2 km deep between 2.0 km and 4.0 km above ground. The rain extends slightly higher in regions of updrafts and lower in regions of downdrafts. The rain is reaching the ground in the strongest downdraft around $y=12$ km. Above the strongest cell (centered at $y=13$ km) graupel is created in mixing ratios greater than 1.0 g kg^{-1} . The graupel extends from just slightly below the freezing level (Fig. 6.3) in regions where it has fallen out of the main convective updraft to a height of 7 km in regions of positive vertical velocity. Above the graupel, a thin band of snow 400 m thick with a mixing ratio in excess of 0.5 g kg^{-1} centered at roughly 8.0 km is present. As will be shown later, snow falling from this layer serves as a source of graupel. The snow is in turn created by the depositional growth of cloud ice.

From $t=40$ minutes to $t=80$ minutes (the end of the simulation) the microphysics remain essentially unchanged. The cloud base continues to descend so that at $t=50$ minutes a large percentage of the troposphere below 10 km is completely saturated with respect to water (Fig 6.2). By $t=60$ minutes, the cloud top has reached 12 km, although pockets of unsaturated air are present above about 9.0 km. The thin band of high snow mixing ratios are present until the end of the simulation and extends across most of the domain between approximately 7.0 km and 9.5 km. Below the snow and in regions of moderate convective activity graupel is present in a layer about 3 km deep that begins about 1 km below the melting level (5 km) (Fig. 6.3) and extends up to about 7 km. Dynamically, the convection

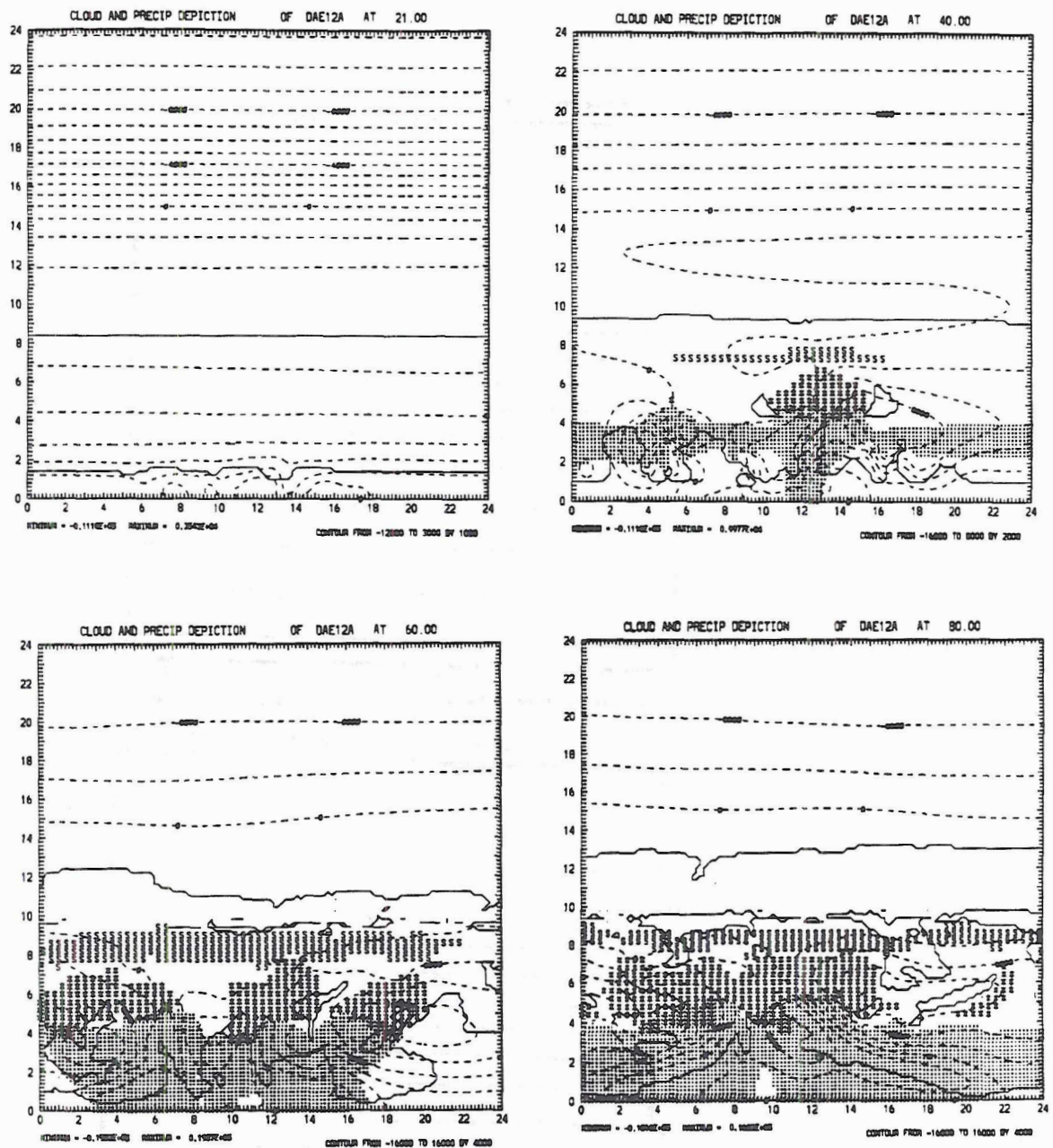
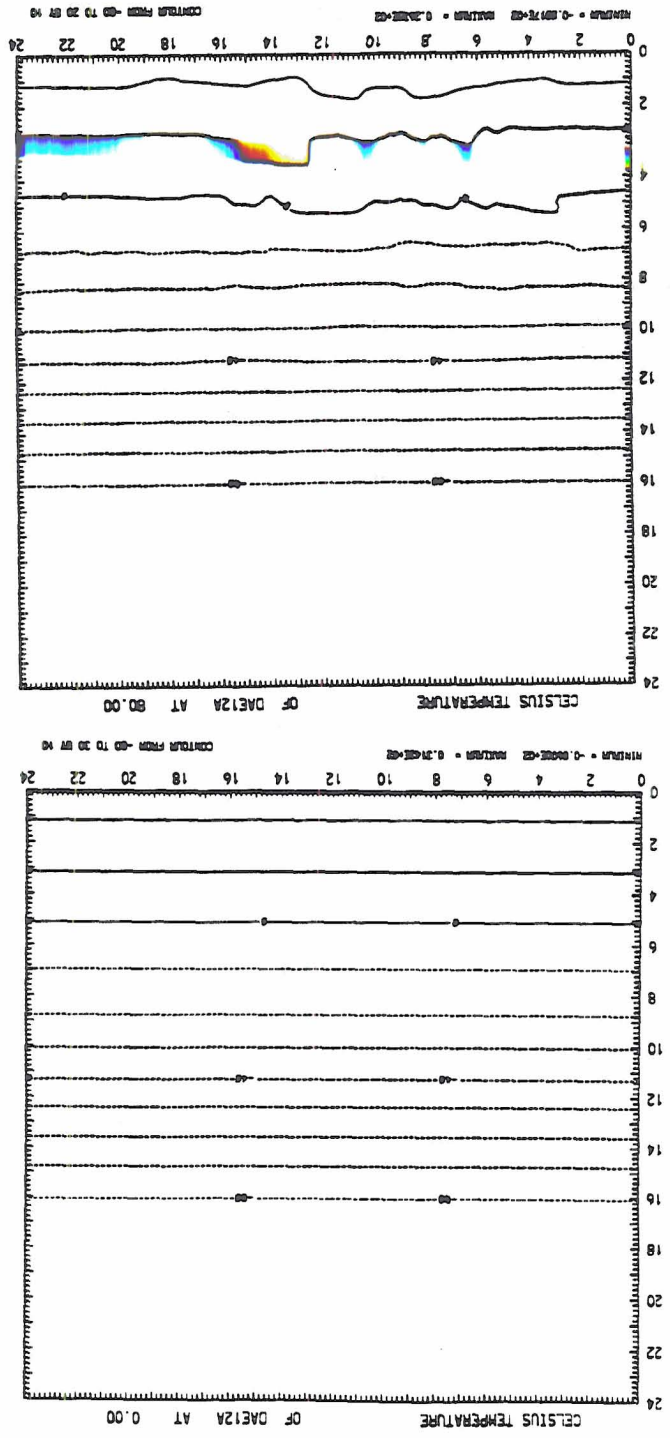


Fig. 6.2: Cloud and precipitation depiction from $t=21$ minutes to $t=80$ minutes. Dashed lines are streamlines, cloud boundaries are defined by the water saturation-water-subsaturation boundary. Asterisks are regions of graupel with mixing ratios greater than 1.0 g kg^{-1} , dots are rain mixing ratios greater than 1.0 g kg^{-1} , S represents snow in mixing ratios greater than 0.5 g kg^{-1} , and underscores are cloud ice mixing ratios greater than 0.5 g kg^{-1} .

Fig. 6.3: Temperature field in degrees Celsius at t=0 minutes and t=80 minutes of simulation time.



becomes more organized by $t=80$ minutes (Fig. 6.2), but it still appears stratiform in nature with regions of embedded convection.

The cloud and precipitation fields (Fig 6.2) provide a general description of the microphysical and dynamical evolution of the monsoon simulation. However, the specific details such as the exact mixing ratios of microphysical species are not resolvable. Thus the evolution of the microphysical species will now be described in detail, and to a lesser degree the dynamical evolution will also be discussed.

The evolution of the snow field is the simplest and easiest to describe. From $t=30$ minutes to $t=80$ minutes the snow mixing ratio is nearly horizontally homogeneous (Fig. 6.4). The maximum in the snow mixing ratio is centered at about 6 km at $t=30$ minutes and rises through time to a height of about 8.5 km at $t=80$ minutes. The lower boundary of the snow remains nearly constant at 4.0 km in altitude, but the upper boundary rises through time from 9.5 km at $t=30$ minutes to over 12.0 km by $t=80$ minutes. Although snow is present in a deep layer, most of the snow is concentrated in layer about 3 km deep which rises through time with the maximum mixing ratio. The snow is created primarily through depositional growth of cloud ice.

It should be mentioned that there are a few regions below the main stratiform snow field where snow reaches appreciable mixing ratios which are associated with regions of convective updrafts. The snow in the convective updrafts serve as graupel nuclei and also play an important role in the electrification since they represent a relative maximum in the graupel-snow collision frequency.

Cloud ice also evolves in a fairly simple manner. At $t=30$ minutes, the field is horizontally homogeneous and only small cloud ice mixing ratios are present (Fig. 6.5). The cloud ice is in a layer about 1.0 km deep centered around 8.2 km. The cloud ice layer rises through time along with the cloud top boundary and generally exists in the top 1.0 to 2.0 km of the cloud. At $t=60$ minutes, the cloud ice field appears less homogeneous and contains many isolated regions of relative mixing ratio maximums and minimums. At $t=80$

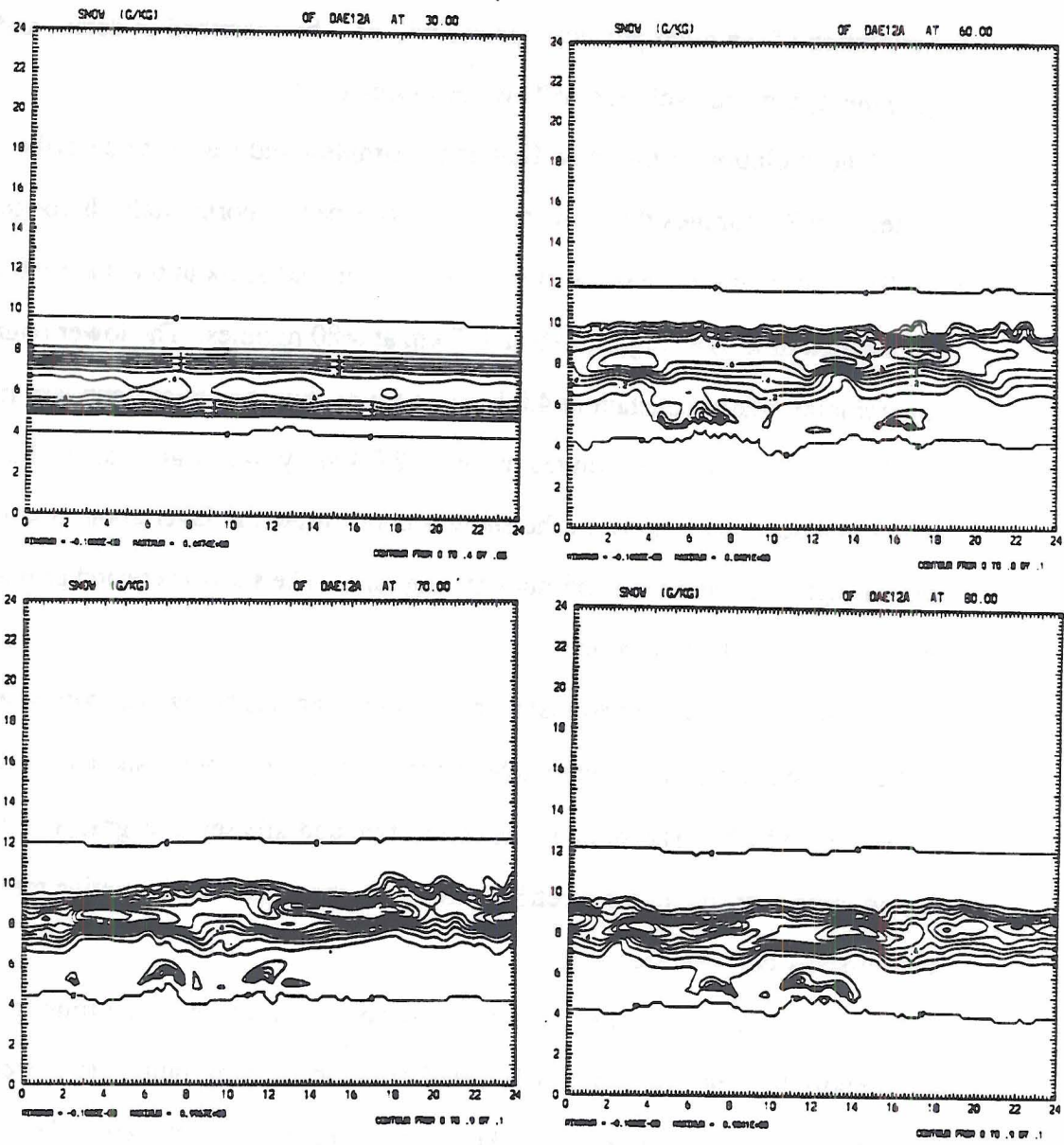


Fig. 6.4: Evolution of the snow field.

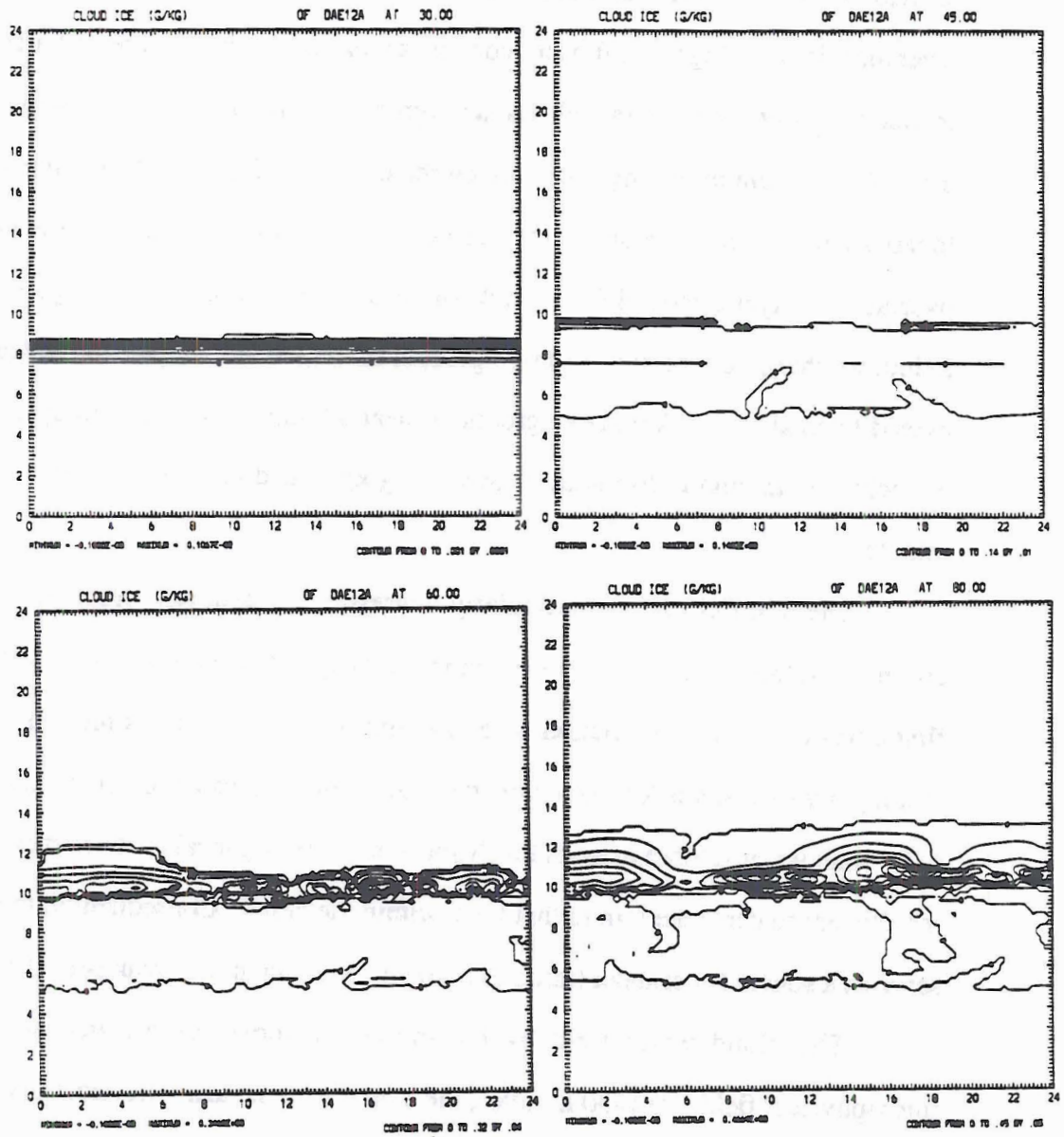


Fig. 6.5: Evolution of the cloud ice field.

minutes, the cloud ice is concentrated near 10.0 km with a maximum mixing ratio over $.46 \text{ g kg}^{-1}$, although much smaller mixing ratios are present as low as 5.5 km.

The graupel field is much more complicated than the snow or cloud ice field because it is formed in the convection embedded in the stratiform cloud. The graupel is created primarily by the accretional growth of snow that has fallen from the extensive snow layer aloft into the high liquid water content regions of the convective updrafts (similar to a seeder-feeder process). Graupel reaches significant mixing ratios near $t=45$ minutes (Fig. 6.6). The maximum mixing ratios are on the order of 3.0 g kg^{-1} . The graupel maxima are located between relative snow mixing ratio maximums (Fig. 6.3). Graupel and snow overlap in a layer almost 4.0 km thick and provide the potential for large values of non-inductive charging. Regions of large graupel mixing ratios are present in deep layers that extend from about 4.0 km above ground to near 8.0 km. Maximum graupel mixing ratios are achieved around $t=70$ minutes (over 7.5 g kg^{-1}) and then begin to stabilize near $t=80$ minutes.

The rain field is not particularly interesting. Warm rain processes (collision and coalescence through the autoconversion process) operate exclusively for approximately the first thirty minutes of simulation time. Beyond a half hour, rain is formed primarily from melting graupel, and is located below the regions of the greatest graupel mixing ratios (Fig. 6.7). Rain water seldom extends much above the freezing level as the vertical velocities are insufficient to carry the rain to that level within the cloud. Consequently, the rain does not serve as a source for graupel (through freezing) as it did in the break period simulation.

The cloud water field by far shows the most complicated structure of any microphysical field. At $t=30$ minutes, the cloud water is nearly horizontally homogeneous except for a maximum associated with the initiation of the convection (Fig 6.8). By $t=45$ minutes, the field has become much more complicated. Any indication of horizontal homogeneity is lost and regions of local minimum and maximum mixing ratios are evident. Mixing ratios are as large as 1.0 g kg^{-1} , at altitudes near 7 km. The field continues to

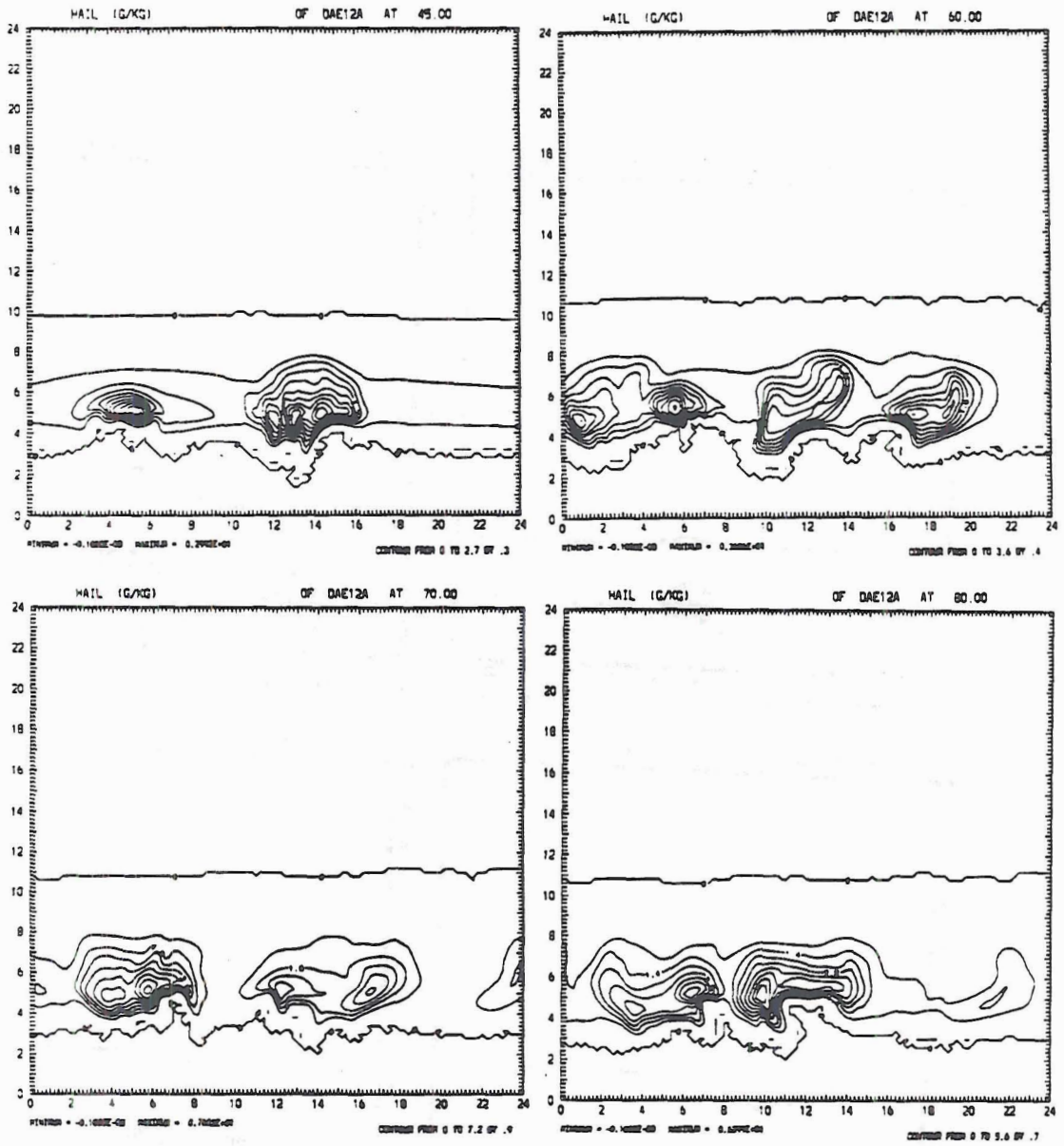


Fig. 6.6: Evolution of the graupel field

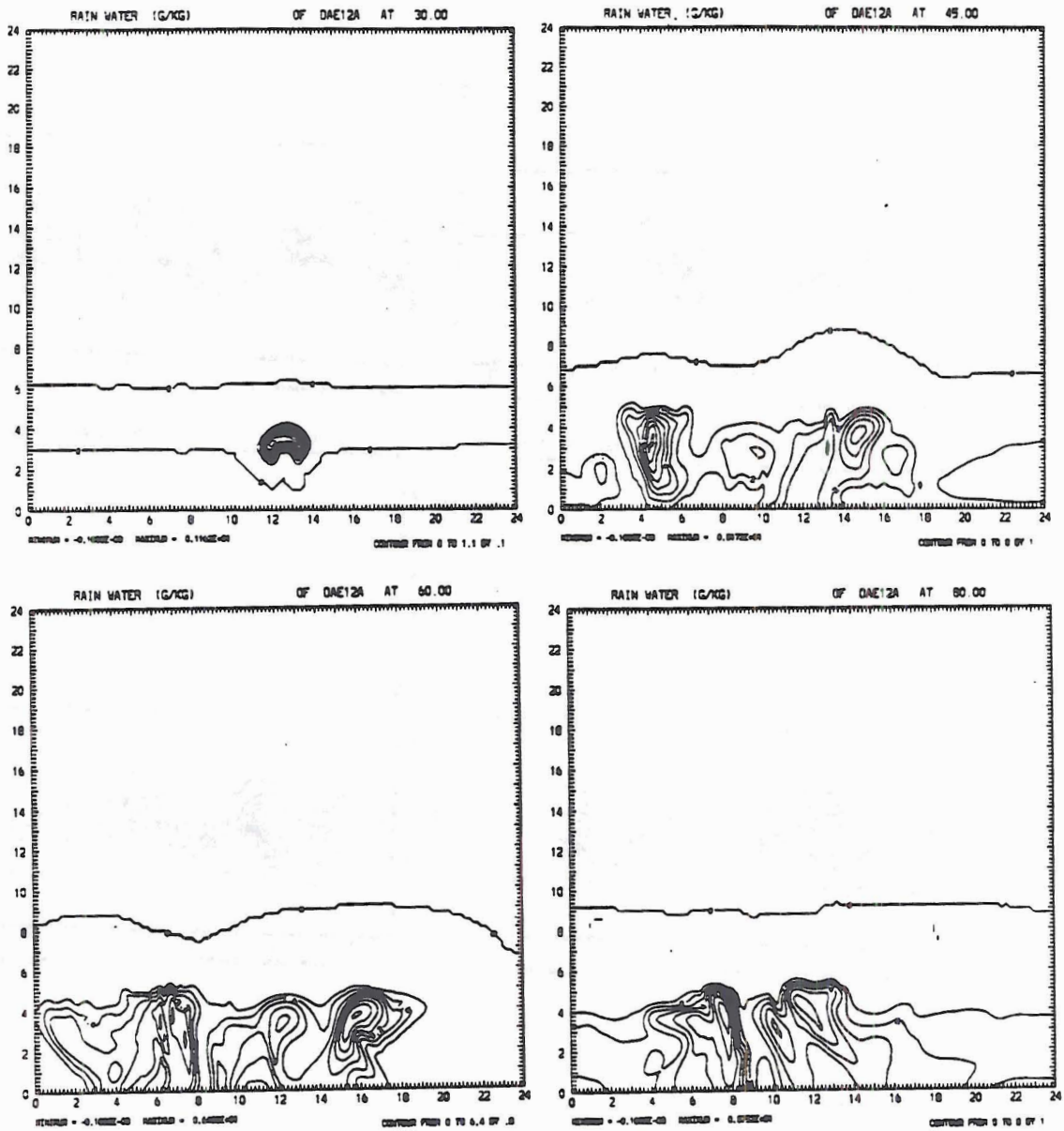


Fig. 6.7: Evolution of the rain water field.

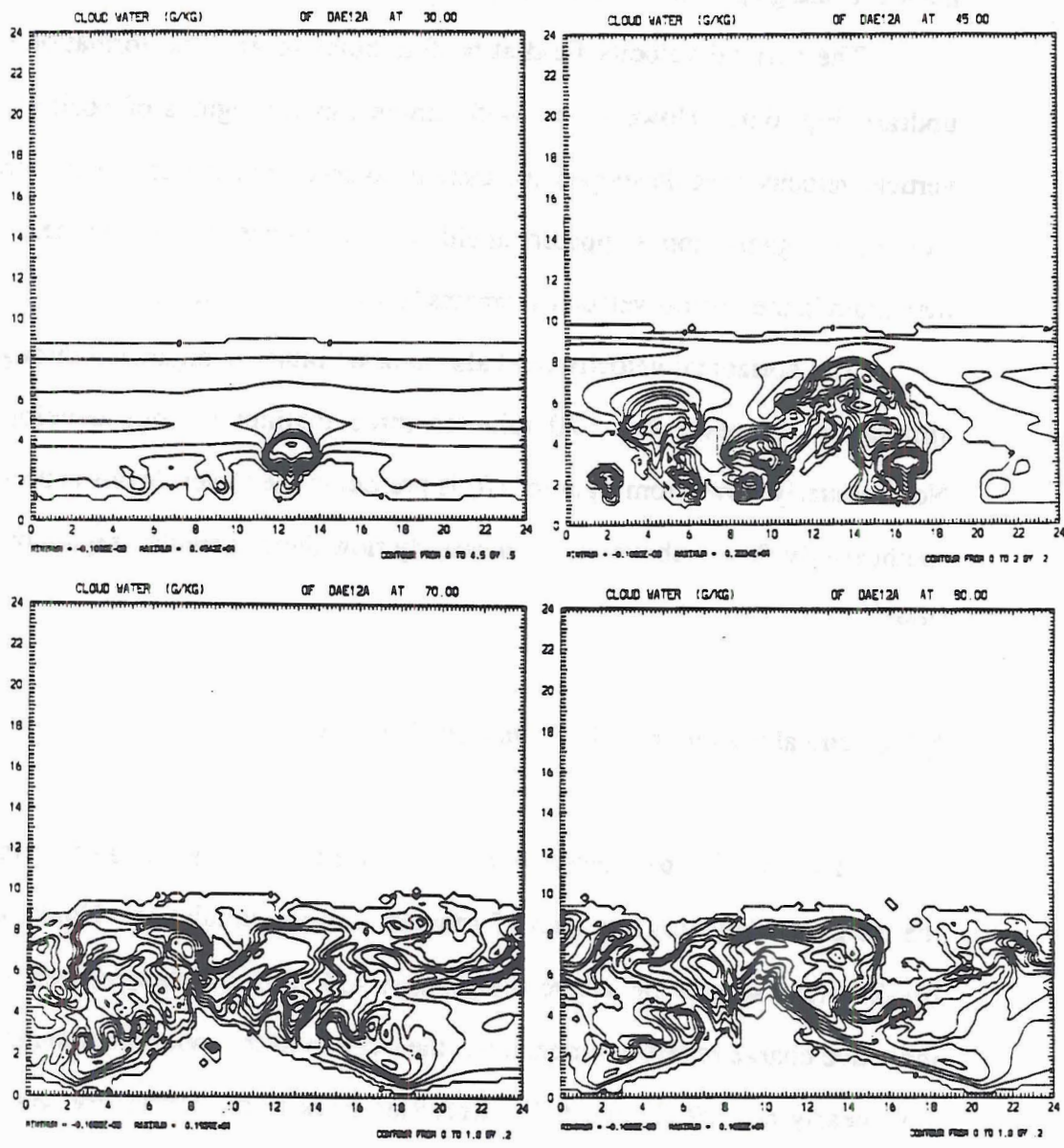


Fig. 6.8: Evolution of the cloud water field.

become more convoluted at $t=70$ minutes. Large mixing ratios of cloud water are present up to 8.0 km. Keeping in mind that there is a deep region of the cloud that contains both snow and graupel, the high cloud water contents would seemingly indicate that non-inductive charging would be extremely active and efficient.

The vertical velocity field at $t=30$ minutes reveals the formation of an isolated updraft (Fig. 6.9). However by $t=45$ minutes, many regions of positive and negative vertical velocity have developed and there is no organized pattern of convection (Fig. 6.9). Very little organization is apparent at either $t=60$ minutes or $t=80$ minutes. In general the maximum in the vertical velocities remains below 5.0 km in altitude.

The horizontal velocity field also appears rather unorganized through most of the simulation, however by $t=70$ minutes three distinct regions develop (Fig. 6.10). Northwesterly flow (from right to left) is present in the lowest levels capped by a level of southeasterly flow. Above the southeasterly flow there is another region of northwesterly flow.

6.2 Electrical Evolution of the 12 January Simulation

The charging parameterization is activated at the beginning of the model run since the ice phase develops less than 15 minutes into the simulation. Unlike the 19 January break period simulation where the graupel and snow overlapped well above the non-inductive charge reversal temperature, the overlap in the monsoon simulation is centered very nearly at -10° C (Fig. 6.3). Referring back to the laboratory work of Takahashi (1978), the charge reversal temperature is near -10° C when the liquid water content is around 1.0 g m^{-3} (Fig. 6.11). Also the sign (and magnitude) of the charge transferred between graupel and snow is highly dependent on the cloud water mixing ratio.

The effect of the the cloud water content on the charging is best illustrated at $t=45$ minutes when the cloud water field is still relatively simple (Fig. 6.8). The charge density

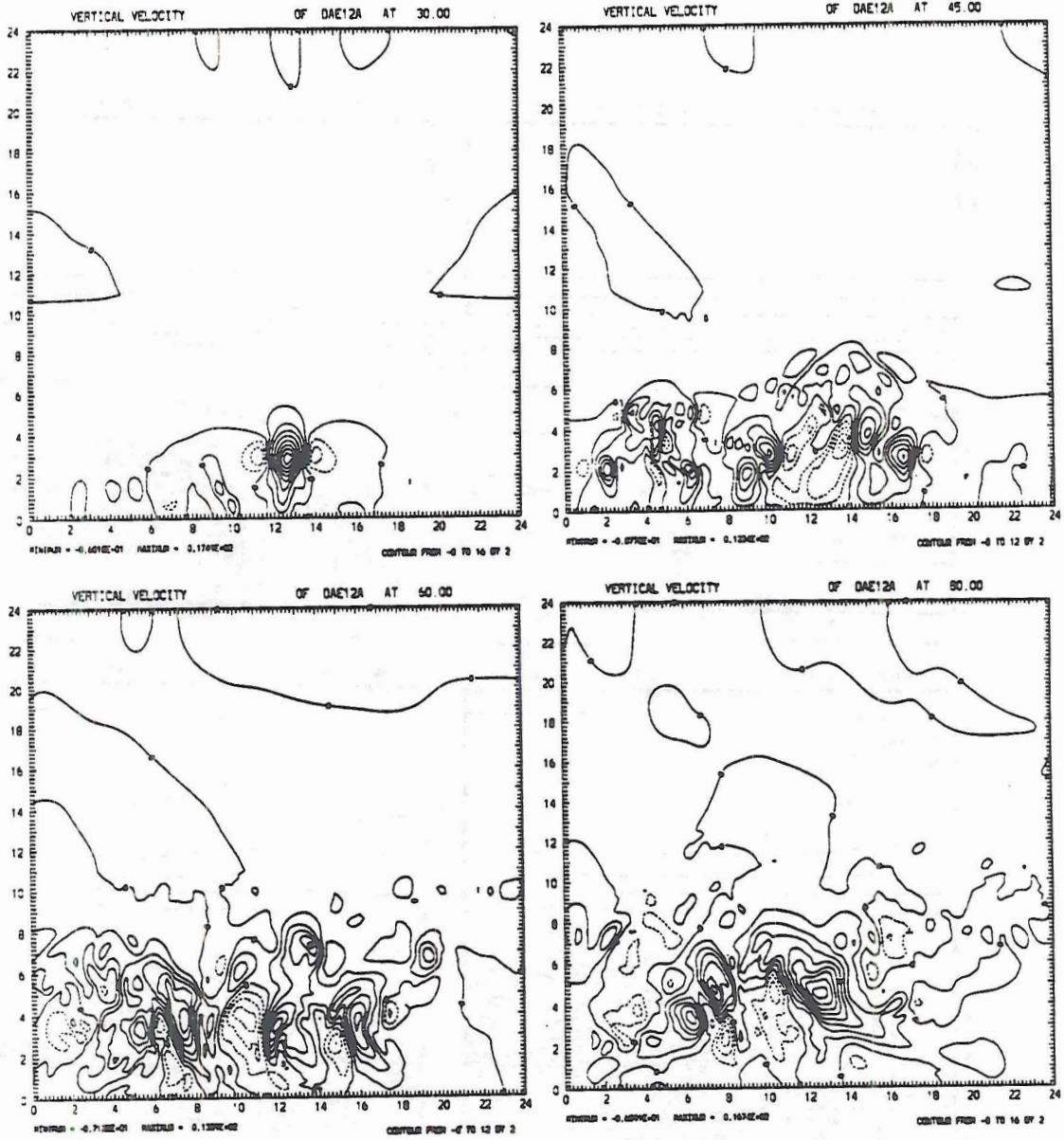


Fig. 6.9: Evolution of the vertical velocity field.

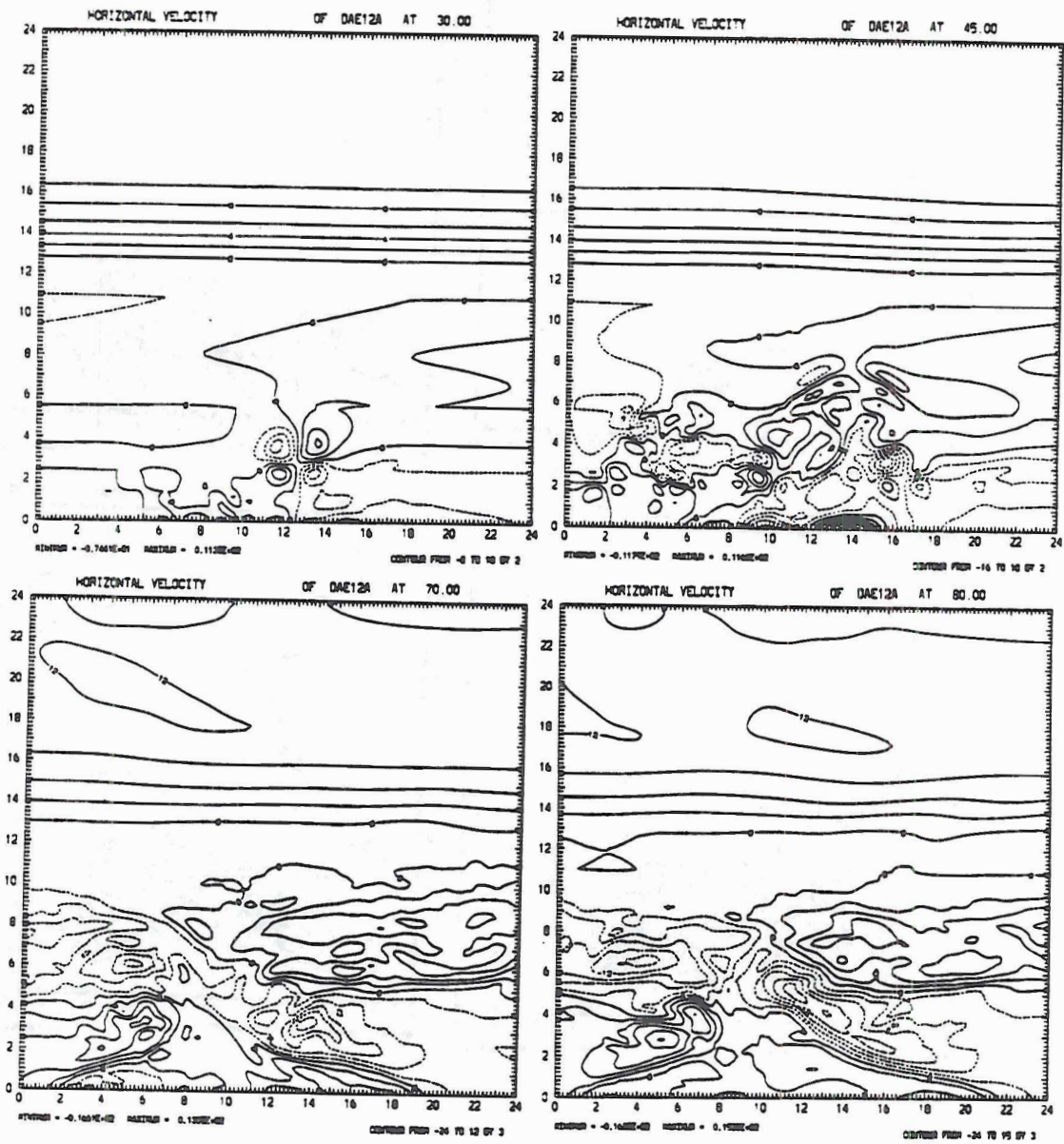


Fig. 6.10: Evolution of the horizontal velocity field.

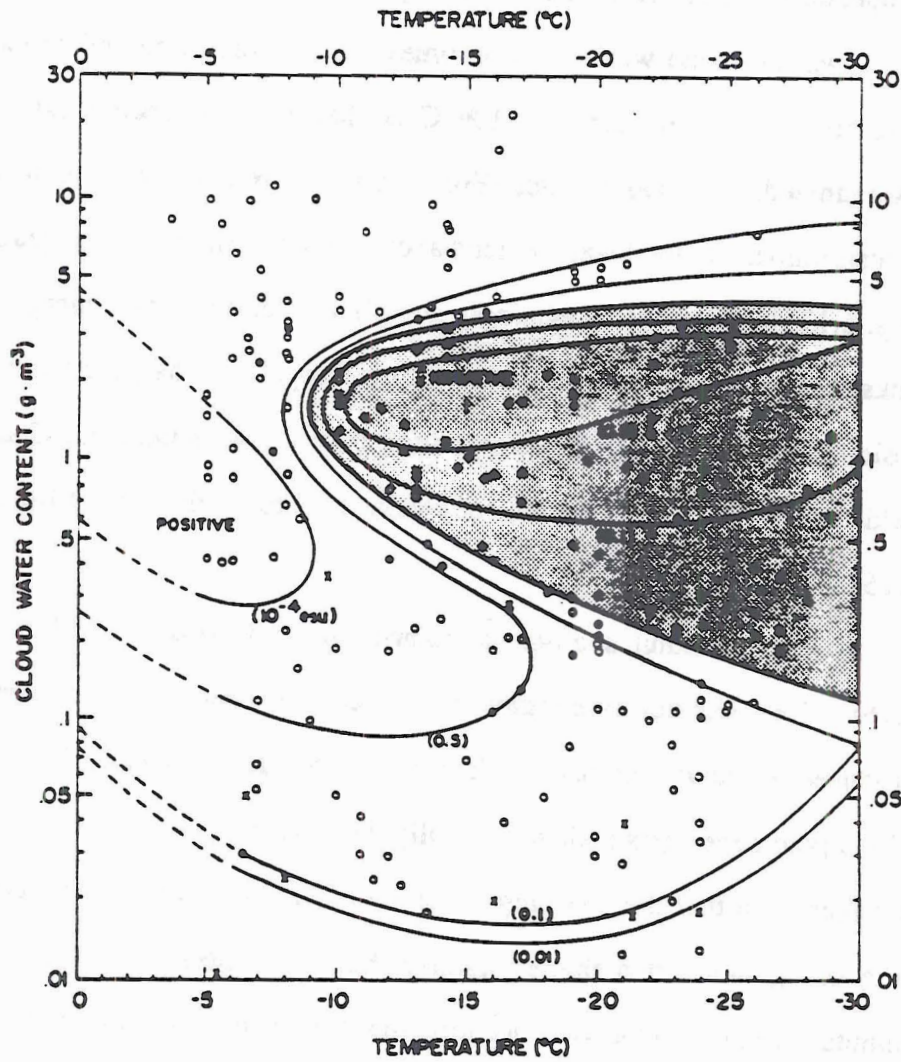


Fig. 6.11: Electrification of the riming rod. Open circles show positive charge, solid circles negative charge and crosses represent uncharged cases. The electric charge of the riming rod per ice crystal collision is shown in units of 10^{-4} esu (After Takahashi, 1978).

on graupel and snow is shown in Fig. 6.12. In general, the graupel acquires positive charge with a maximum near a height 7.0 km, and snow acquires negative charge near a height of 7.5 km. The exception to this is in the region of the strongest updraft ($y=14$ km), where high cloud water mixing ratios have penetrated above 7.0 km. In this region the graupel charges negatively and the snow positively.

As the cloud water field becomes more complicated and as more cloud water is advected or created near the -10° C isotherm, the charging pattern becomes more disorganized. At $t=60$ minutes (Fig. 6.8) there are many regions in which appreciable concentrations of cloud water extend above 7.0 km. The snow and graupel charge density (Fig. 6.13) become correspondingly complicated and the total charge density (Fig. 6.14) lacks organization. There are local regions of separated charge, either negative underlying positive or visa versa, but the effect on the electric field is minimal. The sum of the electric fields from all the small regions of charge tend to produce a net field close to zero (Fig 6.15).

At $t=70$ minutes, a normal polarity dipole begins to develop near $y=17$ km (Fig. 6.16). The lower negative region is produced by graupel and the upper positive region is produced by snow (Fig. 6.17). The center of the dipole is located at a height near 7.0 km. The dipole never gets a chance to fully develop because the cloud water field (Fig. 6.8) changes such that the charging tendency of graupel and snow reverse by $t=80$ minutes (Fig. 6.18); an inverted dipole (negative charge over positive charge) has developed at $t=80$ minutes virtually in the same location that the normal polarity dipole was at $t=70$ minutes (Fig. 6.19).

The electric charge density on cloud ice has been virtually ignored. This is primarily because it is much higher in the cloud than graupel and also because it exists at temperatures much less than the charge reversal temperature. Consequently, the charge on cloud ice is predominantly positive, but due to a small number of graupel-cloud ice

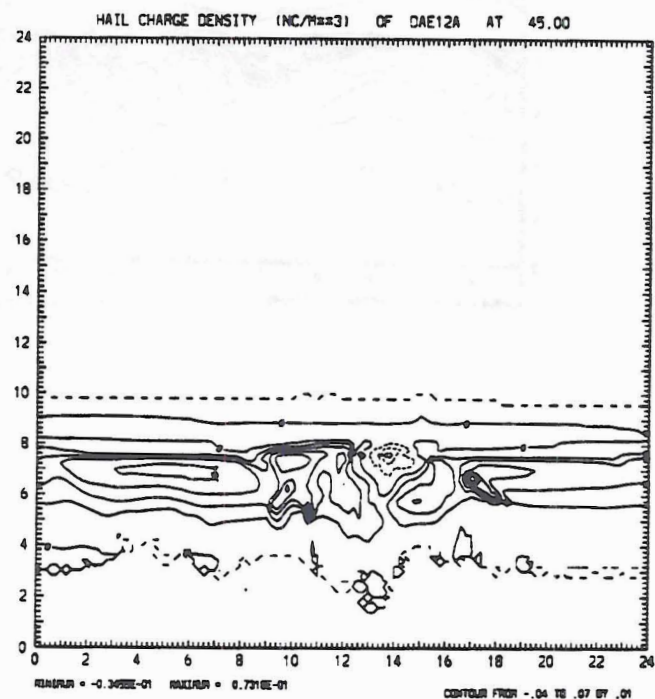
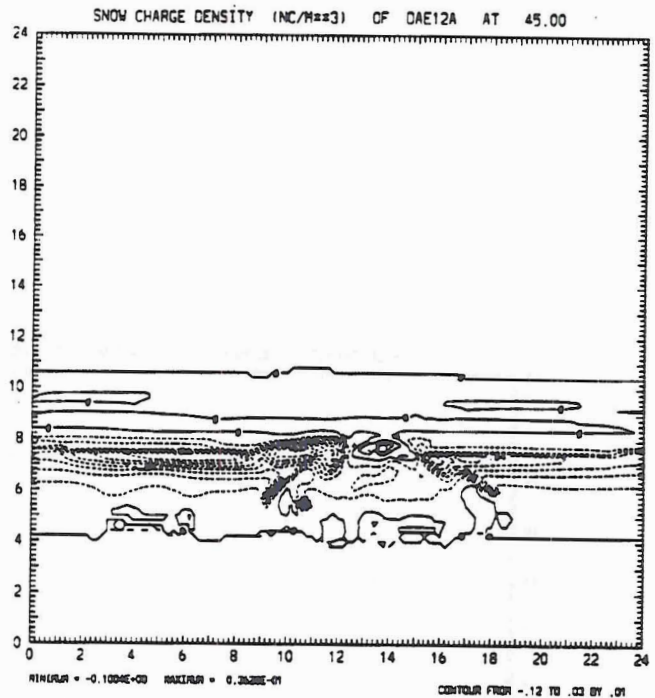


Fig. 6.12: Charge density on snow and graupel at t=45 minutes.

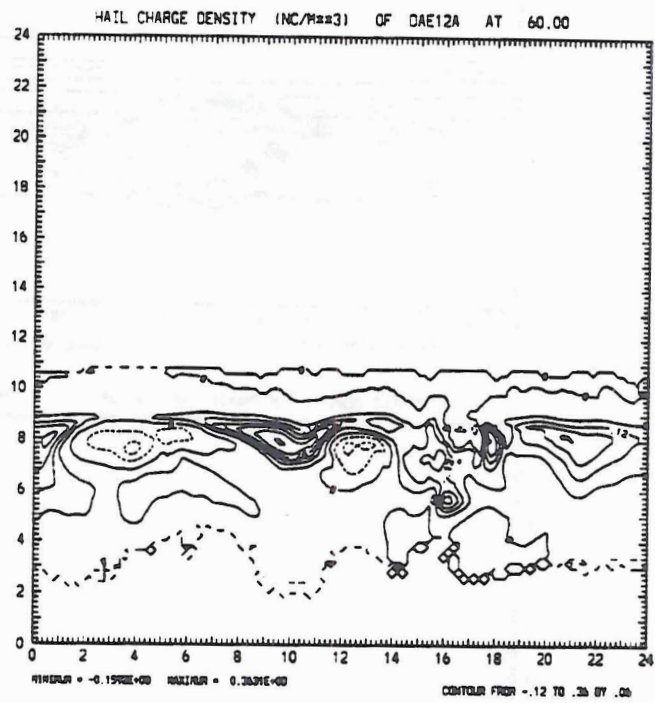


Fig. 6.13: Charge density on snow and graupel at t=60 minutes.

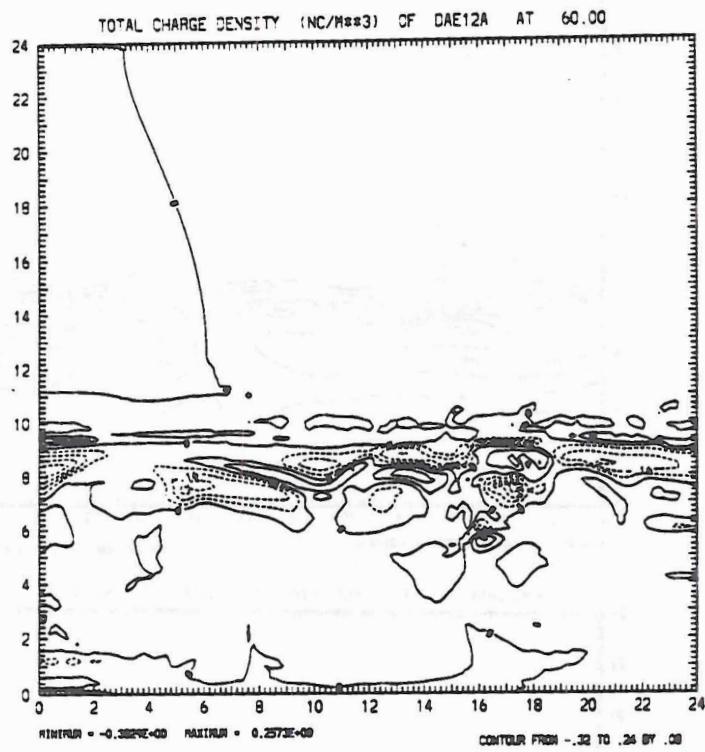


Fig. 6.14: Total space charge density at t=60 minutes.

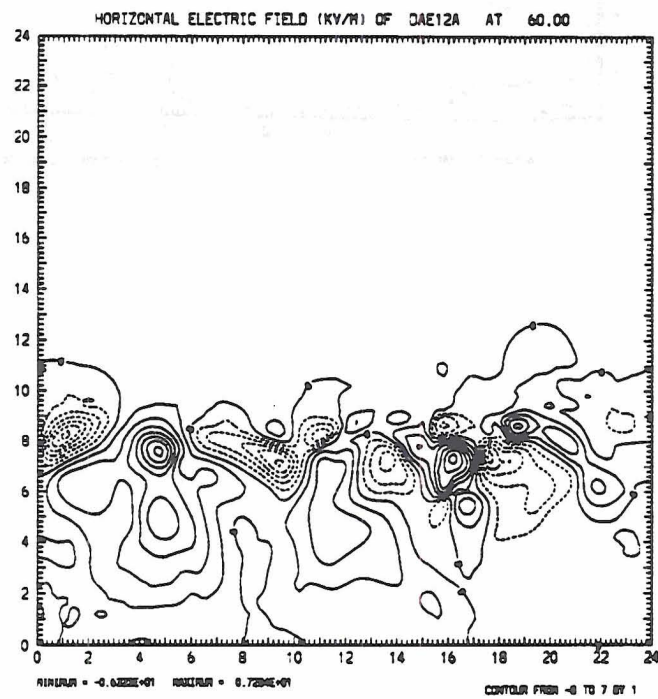
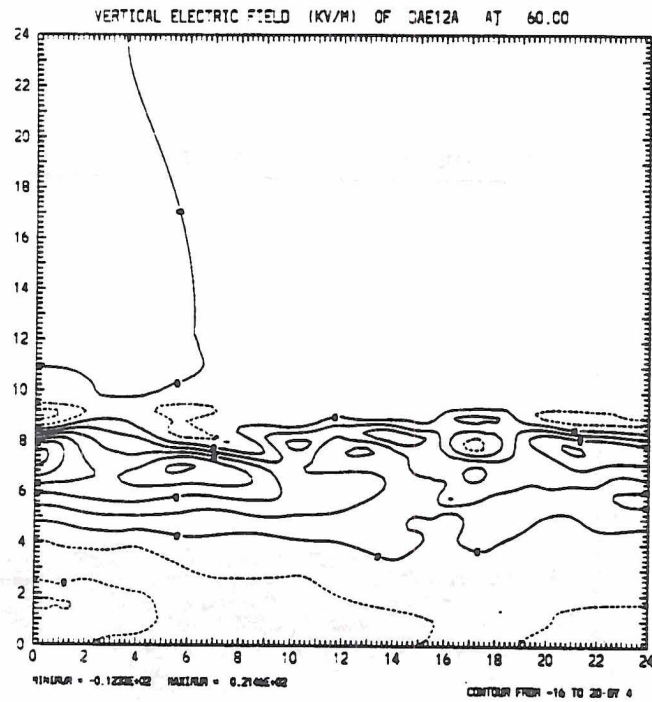


Fig. 6.15: Vertical and horizontal electric field at t=60 minutes.

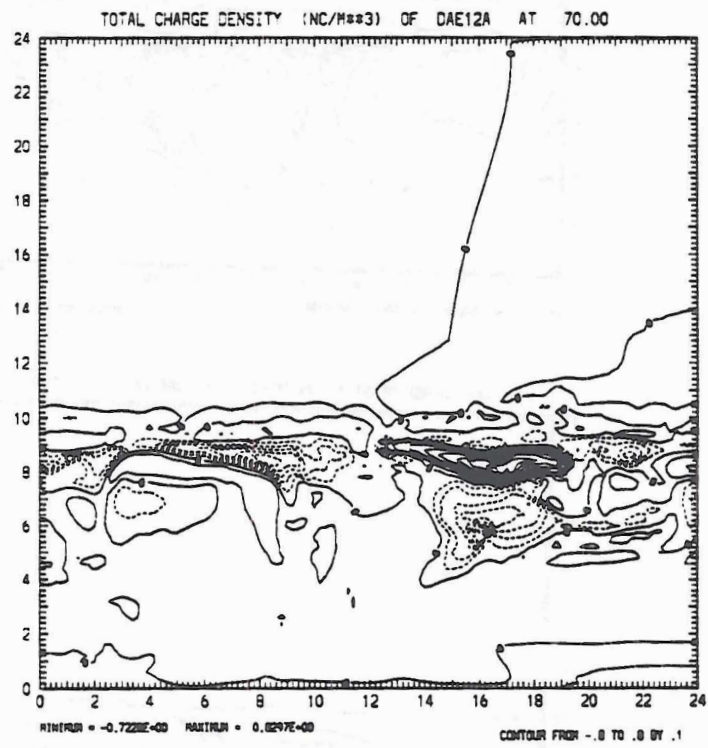


Fig. 6.16: Total space charge density at t=70 minutes.

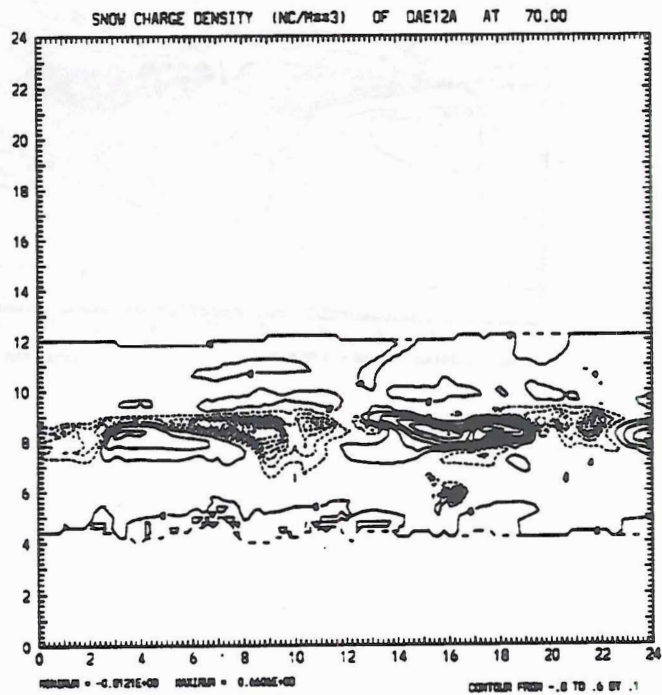
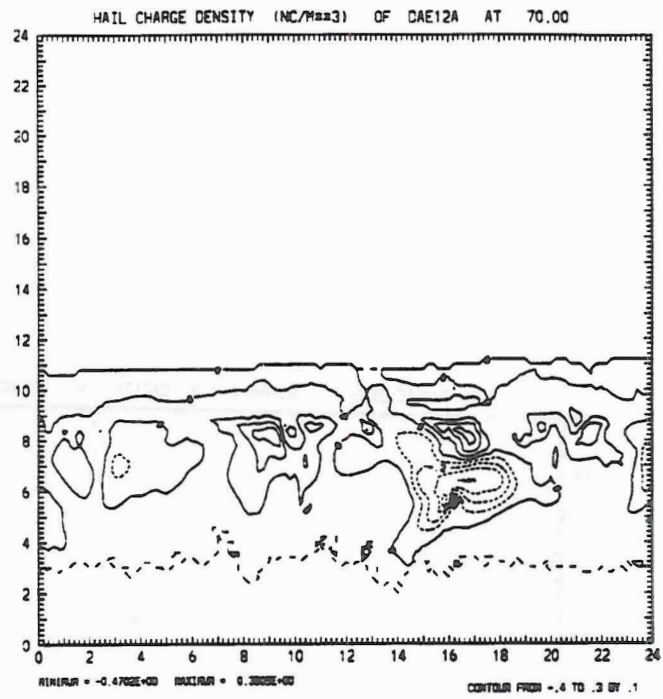


Fig. 6.17: Charge density on snow and graupel at t=70 minutes.

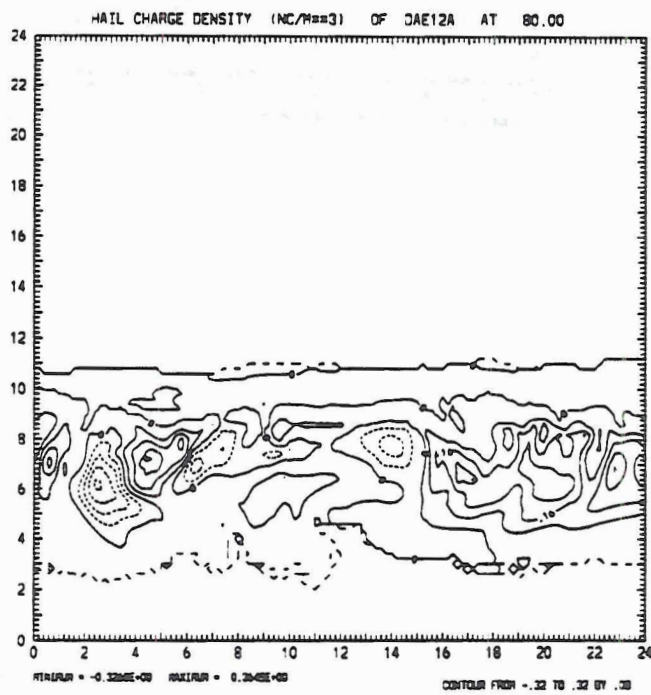
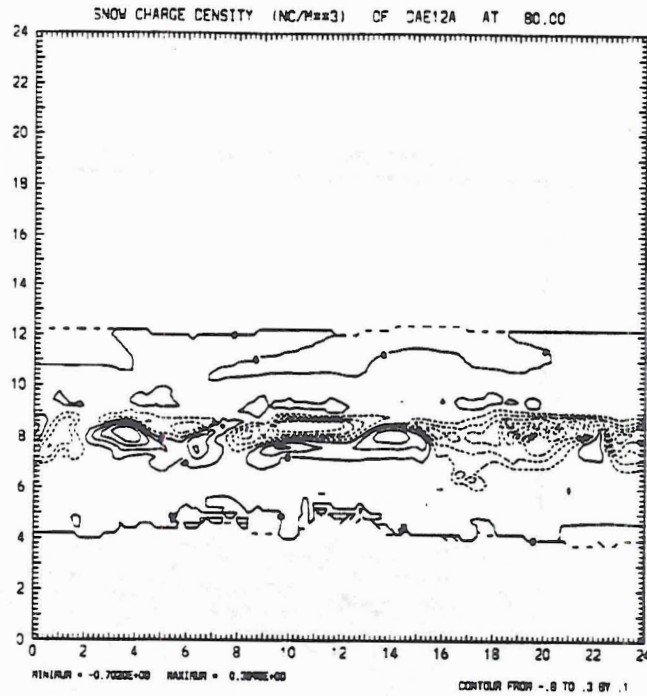


Fig. 6.18: Charge density on snow and graupel at t=80 minutes.

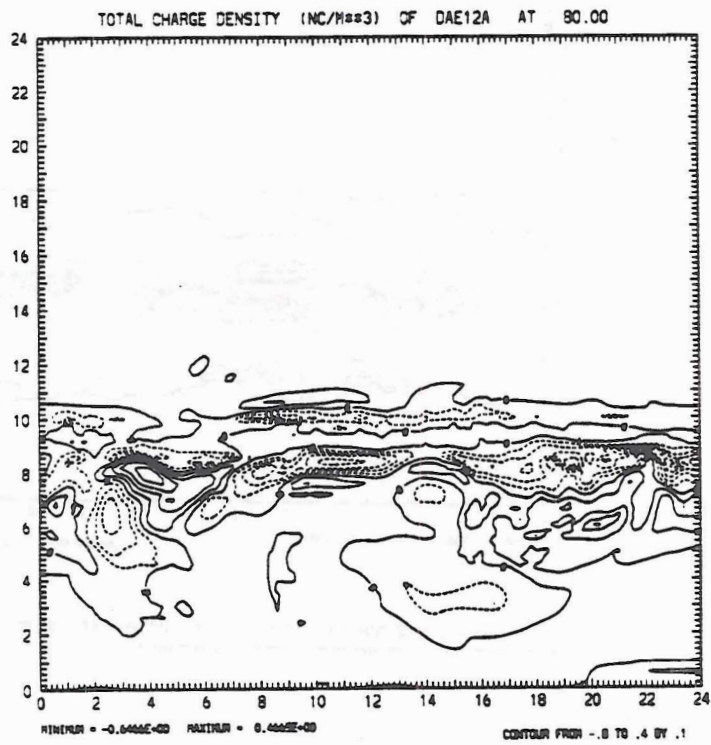


Fig. 6.19: Total space charge density at t=80 minutes.

interactions, the charge density is small. Nonetheless, the cloud ice charge density is shown at selected times for completeness (Fig. 6.20)

The ion fields have also been virtually ignored. The reason for this is that the electric fields never become strong to attract significant concentrations of ions. Furthermore, because of the ephemeral nature of the charge pockets (the normal polarity dipole at $t=70$ minutes becoming an inverted dipole at $t=80$ minutes for example) ions that are attracted at one time may find themselves being repelled away a short time later. The charge density from the ions is however also shown for completeness (Fig. 6.21)

In general, the monsoon simulation does not predict the development of a persistent dipole or any other well defined electric structure. There are several reasons for this behavior. The most important reason is that the graupel-snow interactions occur very near to the charge reversal temperature. As the cloud water content changes near the charge reversal temperature, the graupel (or snow) charging tendency continually changes. This prevents pockets of charge from accumulating. Even if the cloud water content does not change significantly over time at a particular location, the vertical transport of the graupel or snow by convective motions or gravitational settling across the charge reversal temperature will cause the species to begin neutralizing thereby reducing the effective charge at that level. This process is shown schematically in Fig. 6.22.

6.3 Comparison of Model Predicted Reflectivity with Observation

Unlike the 19 January break period case, no attempt was made to simulate a specific event of the monsoon on 12 January. The monsoon convection is too disorganized to expect a model to simulate the details. Rather, an attempt was made to simulate the general characteristics of the monsoon. These include widespread stratiform cloudiness with embedded convection, a well defined radar bright band, and extensive precipitation.

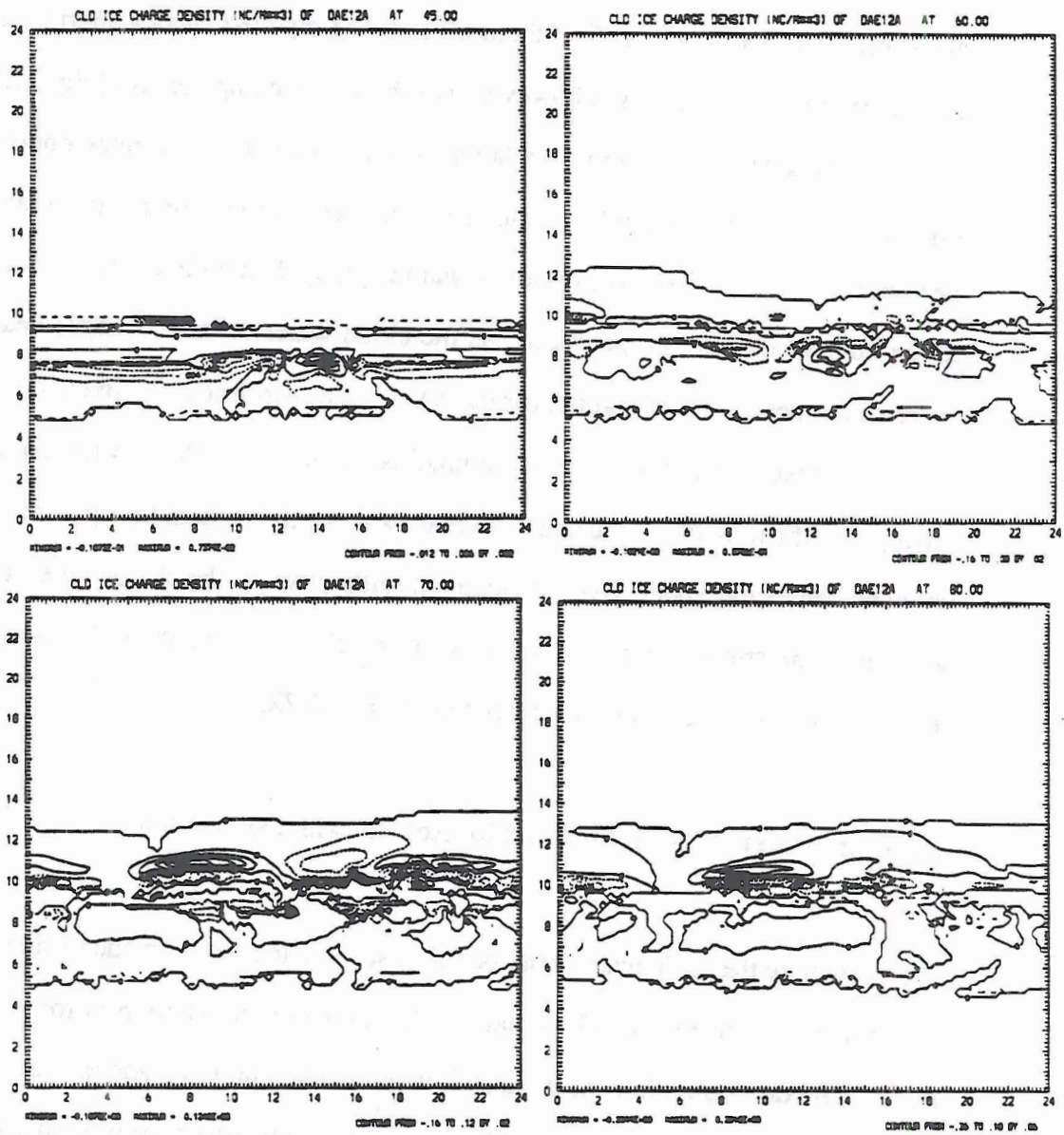


Fig. 6.20: Evolution of the cloud ice charge density field.

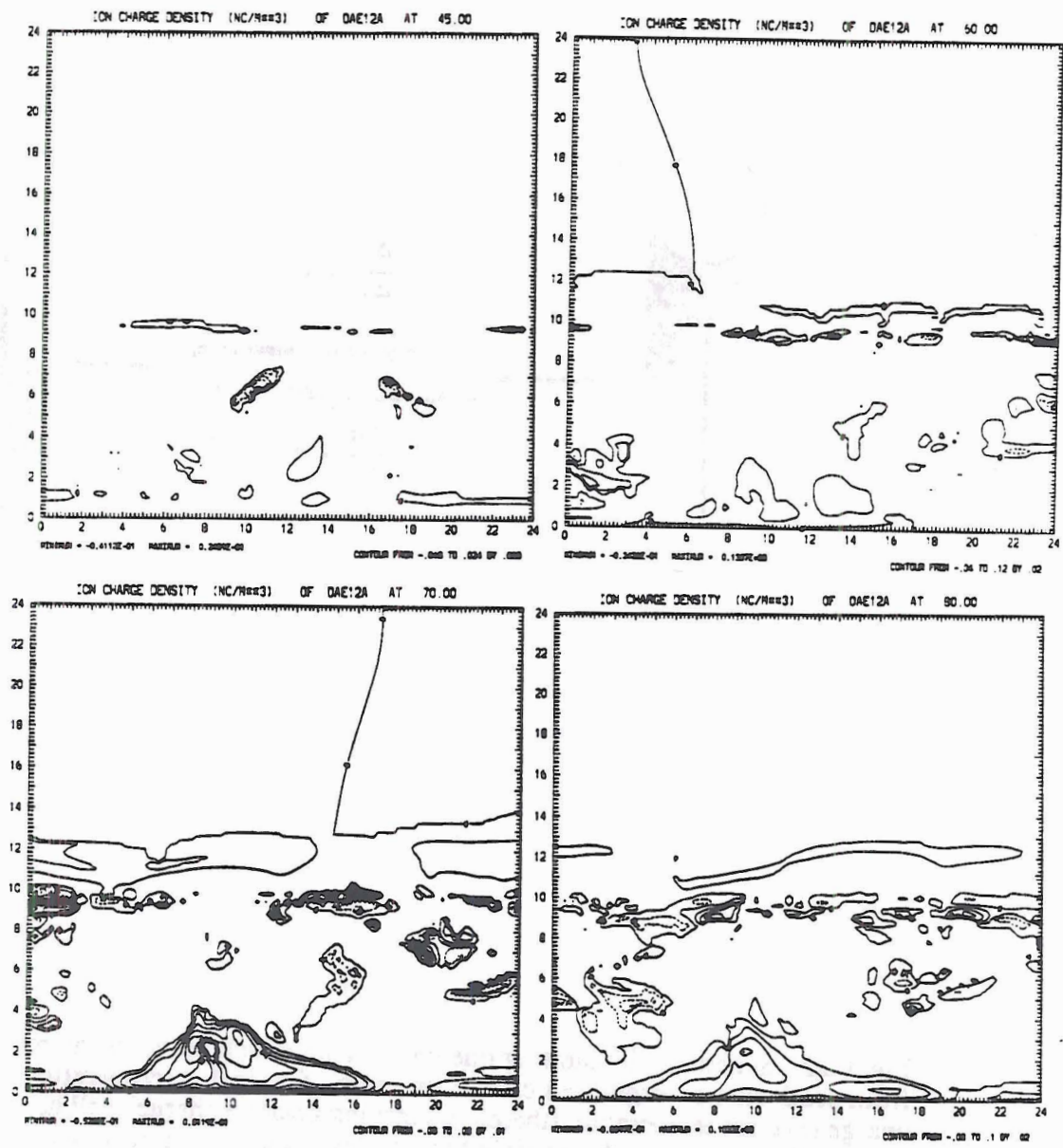


Fig. 6.21: Evolution of the ion charge density field.

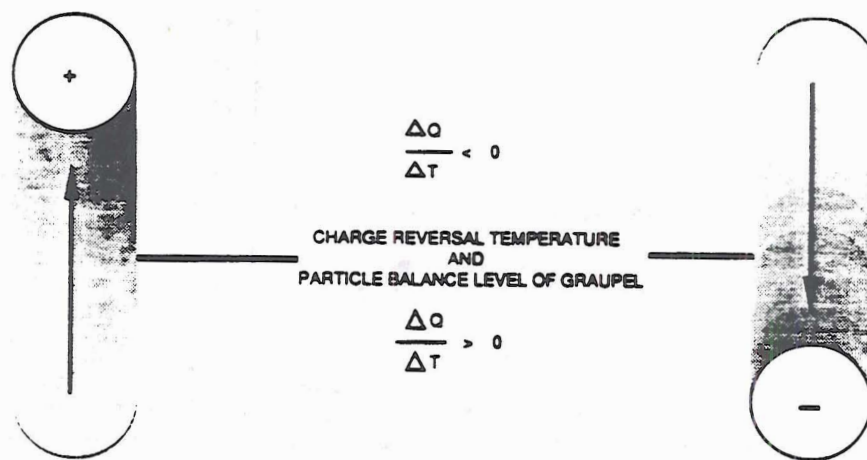


Fig. 6.22: Schematic illustrating one mechanism which prevents the monsoon simulation from producing an organized charge structure. Graupel at temperatures warmer than the charge reversal temperature (therefore carrying positive charge) will have a tendency to be carried higher, toward the particle balance level and charge reversal temperature. Some graupel will cross the charge reversal temperature and begin acquiring negative charge, thus becoming electrically neutral. The graupel can also neutralize by colliding with other negatively charged graupel species. The opposite occurs for graupel at temperatures colder than the charge reversal temperature.

Widespread stratiform cloudiness with *embedded convection and extensive precipitation* have already been shown to exist based on the previous figures (Fig. 6.2 for example). To investigate the existence of a bright band the predicted radar reflectivity at various times are shown in Fig. 6.23. Fig. 6.23 should be compared to the previously presented radar observations on 12 January which have been reproduced in this chapter to facilitate the comparison (Fig. 6.24).

Beginning at $t=30$ minutes, the model reflectivity structure is nearly horizontally homogeneous except for the echo surrounding developing convection. The largest reflectivities in the stratiform portion of the cloud, approximately 30 dBZ, are found near the 0° C (radar bright band) and are associated with melting ice species (mostly graupel). At $t=45$ minutes, convective cores are apparent with reflectivities in excess of 60 dBZ. The pockets of high reflectivity, however, do not extend much above the freezing level, similar to the reflectivity structures observed in monsoon cases by Rutledge *et al.* (1991). Above the freezing level, the echoes are stratiform in nature. There is little change in the model predicted reflectivity structure at $t=60$ minutes and $t=80$ minutes. Convective cores again do not extend much above the freezing level, and the radar bright band is well defined at the 0° C. The reflectivity structure is essentially horizontally homogeneous and stratiform in nature above the bright band. These features are nearly identical to those observed by the MIT radar (Fig. 3.16-3.18). The cloud top heights are also comparable. Thus, based at least on the predicted reflectivity, the simulation seems to be realistic.

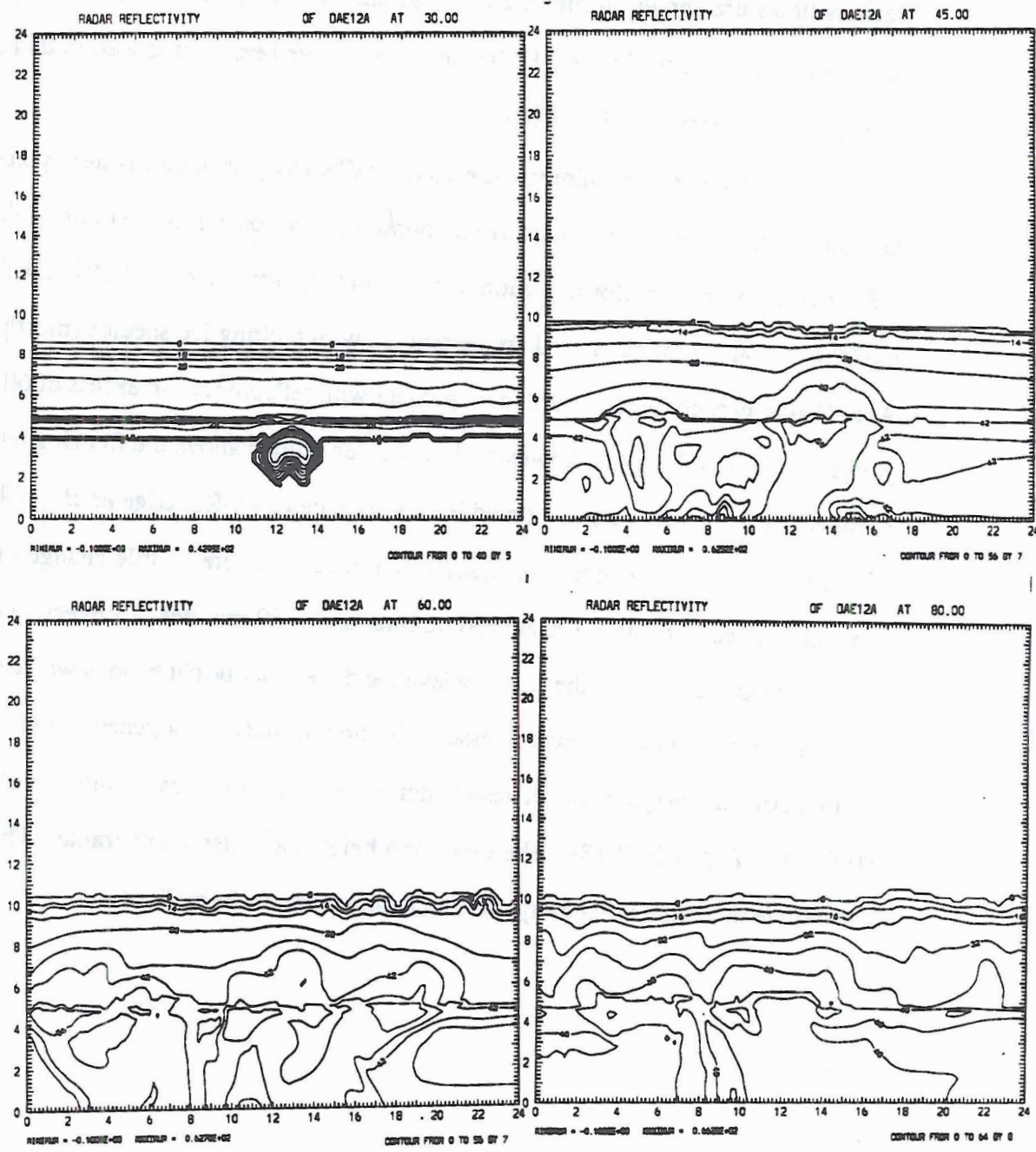


Fig. 6.23: Evolution of model predicted radar reflectivity.

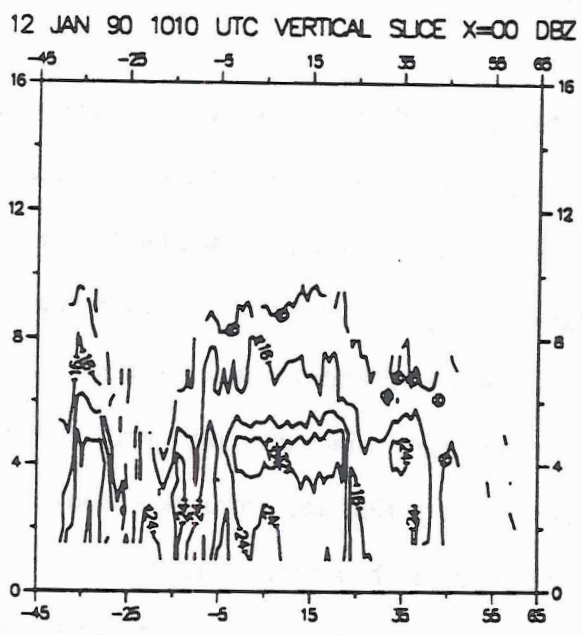
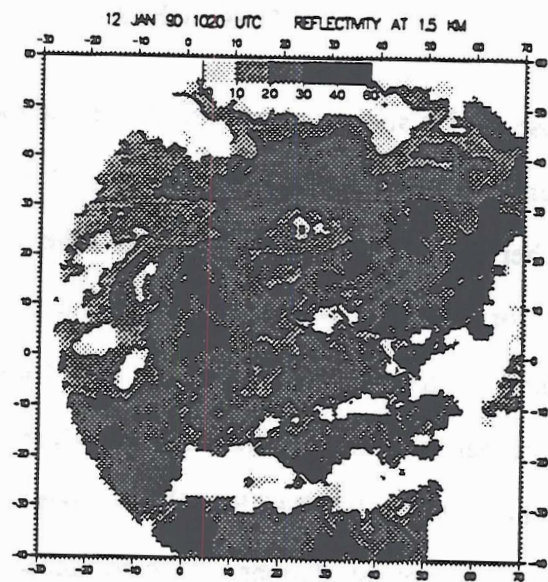


Fig. 6.24: Radar observations of the monsoon convection 12 January 1990.

CHAPTER VII

CONCLUSION

The purpose of this study was to investigate and explain the dissimilar lightning flash rates between monsoon and break period convection that were observed during the DUNDEE. Another goal of this thesis was to test the validity of the CAPE--ice mass scaling argument forwarded by Williams and Rutledge (1990), also described in chapter III, and to test the effectiveness of the non-inductive charging mechanism in tropical convection. The numerical modelling results of break period convection (CHAPTER V) and the monsoonal convection (CHAPTER VI) have been described independently. In this chapter the results of the two simulations will be combined to address the above goals.

7.1 Relationship Between CAPE and the Level of Storm Electrification

The model simulated drastically different levels of electrification between the break period and the monsoon. Time series of the domain maximum values of the vertical and horizontal electric field, the electric potential, total space charge density, and electric energy density are shown in Fig 7.1. In all cases the the break period simulation reveals more intense electrical activity. Based on the tendencies of the electrical parameters, the break period also electrifies faster. Since the model simulated the general differences of electrical activity between break period and monsoonal convection, it is reasonable to question whether the differences can be attributed in any way to the amount of ice mass (graupel) at the particle balance level and the CAPE as suggested by the scaling argument of Williams and Rutledge (1990). Before this question is answered, however, it is useful to review the assumptions and conclusions of the argument.

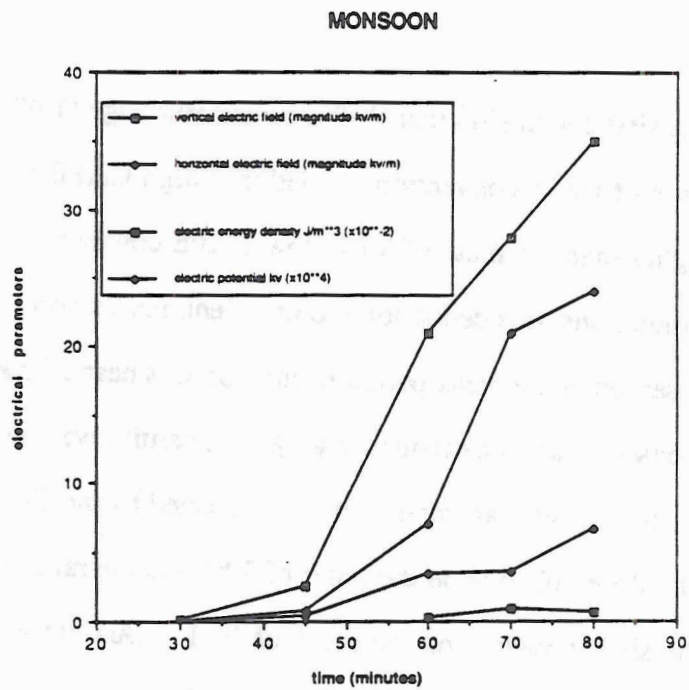
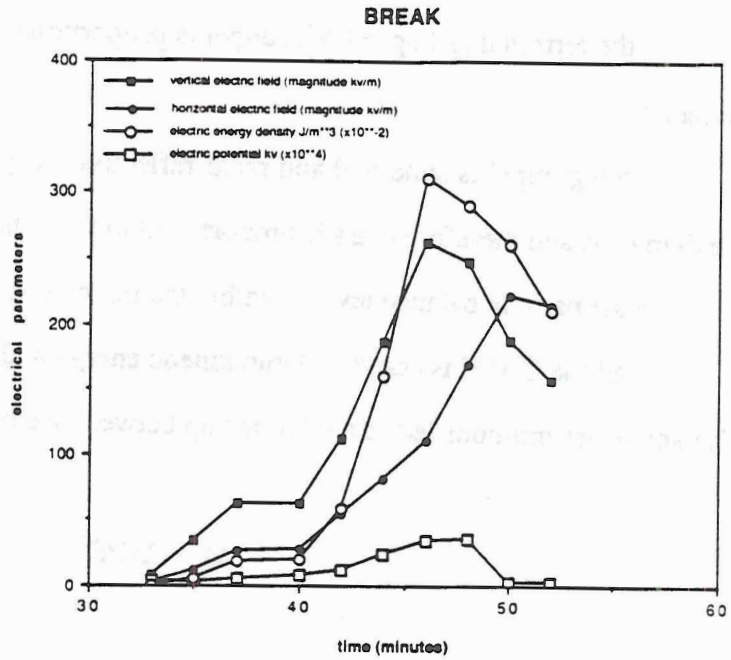


Fig. 7.1: Time series of the domain maximum values of the vertical and horizontal electric field, the electric potential, total space charge density, and electric energy density for the break period and monsoon period simulations.

The assumptions are:

- graupel is the dominant precipitation type in the cold part of the cloud.
- the terminal fall speed of graupel is proportional to the square root of the particle diameter.
- the graupel is spherical and radar reflectivity is proportional to the sixth power of the diameter, and therefore mass is proportional to the cube of the diameter.
- the particle balance level is within the mixed phase region of the cloud.
- all the CAPE is converted into kinetic energy and all motion is vertical.

The above assumptions led to a relationship between ice mass and CAPE:

$$M \sim \text{CAPE}^3 \tag{7.1}$$

$$M \sim W^6$$

The first conclusion that Williams and Rutledge (1990) drew from this result was that the mass of ice in convection formed in a high CAPE environments should be considerably higher than the mass of ice in low CAPE convection (*i.e.*, monsoons). Based on the two simulations, this deduction seems essentially correct. The maximum graupel mixing ratio observed in the break period simulation was near 15 g kg^{-1} while the maximum value in the monsoon case was around 5 g kg^{-1} . Quantitatively speaking the ratio of ice mass, 3:1, is much smaller than what would be expected by the CAPE or the vertical velocity. The ratio of CAPE cubed is on the order of 30:1 and the ratio of the maximum vertical velocities to the sixth power is on the order of 10:1. Qualitatively, the scaling analysis successfully captured the gross difference, and furthermore the above figures of ice mass and vertical velocity are not necessarily values taken at the particle balance level which is difficult to determine.

The next step in the scaling argument is to link the mass of ice to the degree of cloud electrification. Assuming that in both high and low CAPE environments the graupel is of roughly the same density and size, then an increase in mass (per unit volume) translates into a larger particle concentrations. This has actually already been assumed by scaling the mass to the cube of the diameter. An increased number of particles implies an increased number of particle interactions and thus more effective non-inductive charging, provided that it occurs in a mixed phase environment.

The true effectiveness of the non-inductive charging mechanism is not, however, purely a function of the number of particle interactions. The effect of the temperature and cloud water content also controls the degree of non-inductive charging. The omission of the temperature and cloud water field from the scaling argument has little consequence in the break period simulation, but has significant impact on the simulation of the monsoon electrification. The reason for this is that the particle balance level is near the charge reversal temperature (T_r) in the monsoon simulation.

Conceptually it is not hard to understand why having the particle balance level at or near T_r should be so critical. Basically, half the graupel will charge positively (the half at temperatures warmer than T_r) while the other half charges negatively. The net sum of the charge on the graupel is at or close to zero. This is assuming that roughly half the graupel mass resides below the particle balance level and half above.

The scaling argument of Williams and Rutledge (1990) can be strengthened through the addition of one more assumption. The additional assumption that needs to be stated explicitly is that the particle balance level be in a region of temperature and cloud water conducive to charging of one sign. In other words, the particle balance level and the level of charge reversal must be sufficiently separated so that the graupel will acquire charge predominantly of one sign.

The validity of the assumption that the particle balance is sufficiently separated from the charge reversal temperature is related to the CAPE. As CAPE increases, to a first

approximation, so should the vertical velocities, resulting in greater cloud water contents and higher (colder) particle balance levels. Since the charge reversal temperature decreases as the cloud water content decreases (Fig. 6.11), the vertical separation between the charge reversal temperature and the particle balance level should increase as CAPE increases. Thus the assumption becomes more reasonable for large values of CAPE.

The scaling argument as modified above is now sufficient to explain the differences in electrical activity between the break period and the monsoon. In the case of the break period, the large values of CAPE produce deep and strong updrafts which result in the region of maximum graupel/snow mixing ratio overlap (where a maximum of non-inductive charging will occur provided that cloud water is present) at temperatures at or colder than -20°C . Based on the charging parameterization, graupel will charge negatively in this region if the cloud water content is roughly between 0.1 g m^{-3} and 4.0 g m^{-3} . Because of the large vertical velocities, the cloud water content was between these bounds and the assumption that the charge reversal temperature be far from the particle balance level, (the particle balance level can be taken either as the level of maximum graupel/snow mixing ratio overlap or the as the center of the maximum graupel mixing ratio) was therefore valid. The CAPE in the monsoon simulation was such that the graupel/snow overlap occurred at or near -10°C . Furthermore, the cloud water content slightly exceeded about 1.0 g m^{-3} in the strongest convective regions, but remained less than this value in the less vigorous portions of the storm. A temperature of -10°C places the graupel/snow overlap directly at the charge reversal temperature. As the cloud water field changed, the charge reversal temperature at a particular place changed, and the sign of the charge acquired by the graupel (or snow) continually reversed.

It is possible to hypothesize what would happen with a moderate CAPE environment; say an environment that is an average of the break period and monsoon soundings. In this case, the overlap in the graupel and snow fields would be at a temperature colder than -10°C . Also, the vertical velocity at the particle balance level

would be somewhere between that of the break period and monsoon, as would the cloud water mixing ratio. For the sake of argument suppose the overlap was at -15° C. The cloud water content associated with $T_r = -15^{\circ}$ C is close to 0.4 g m^{-3} . However, the cloud water content in this hypothetical example should be at least above the average monsoon cloud water mixing ratio (about 1.0 g m^{-3}). Thus the level of the charge reversal temperature and the particle balance level are farther apart than in the case of the monsoon simulation, but still not as far apart as in the break period simulation.

For environments CAPEs lower than the monsoon (*i.e.*, stable ascent), the scaling argument is almost a moot point. Presumably, there would be so little ice mass generated, and the mixed phase region would be so limited that virtually no charging would occur anyway. It is interesting though that Rutledge *et al* (1990) simulated a inverted dipole in the modeling study of the stratiform region of a mesoscale convective system. The environment in the stratiform region was stable with updrafts of only centimeters per second and correspondingly low liquid water contents. It is possible that this would place the particle balance level at temperatures much warmer than the charge reversal temperature allowing the graupel to almost exclusively acquire positive charge, consistent with the observed preference for positive cloud-to-ground flashes in these regions.

A schematic of the expected charging as a function of the CAPE is illustrated in Fig. 7.2. All the possibilities that have been discussed are indicated. For very low CAPE (in the stratiform region of a mesoscale convective system for example), an inverted dipole might be expected over time. For low CAPE (in the monsoon for example) very little organized charge structure would be produced. For moderate values of CAPE (perhaps some middle latitude storms) a moderately strong normal polarity dipole might result. Finally, in the case of high CAPE environments (the break period) strong charging would be possible.

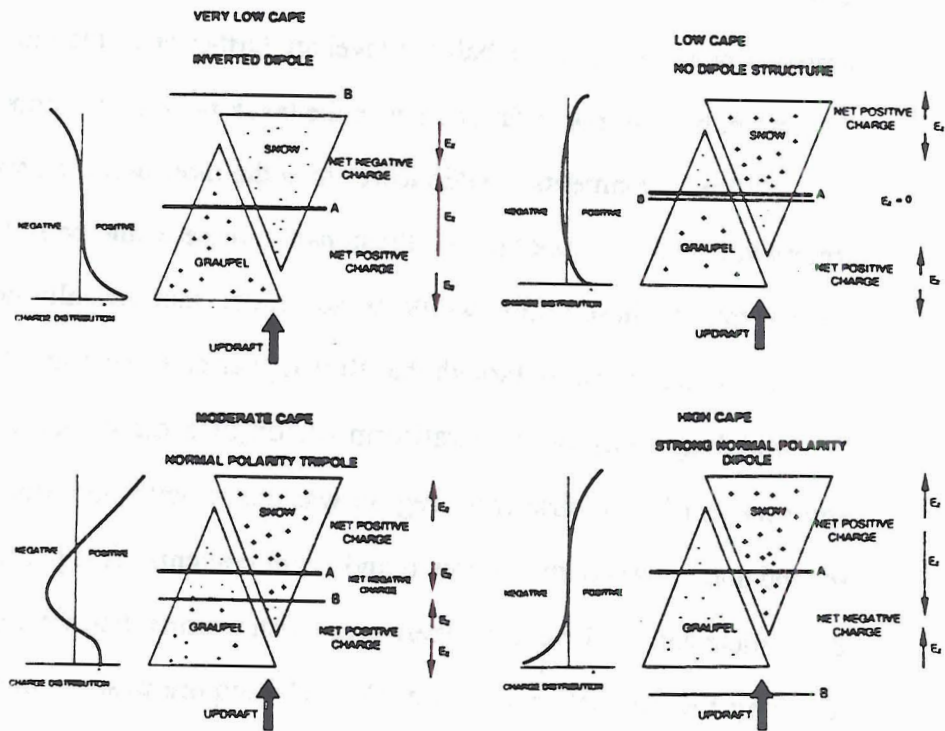


Fig. 7.2: A schematic of the expected charging that results from various levels of CAPE. The charge structure depends on the spatial separation of the level of charge reversal (line B) and the particle interaction region (centered on line A)

7.2 Effectiveness of the Non-inductive Charging Mechanism

The non-inductive charging mechanism operates very efficiently in the break period simulation. At the end of the rapid growth phase, the maximum charge density is on the order of 2 C km^{-3} . If this charge density is spread over about 10 km then this value becomes close to the typical value observed in a dipole (about 40 C). On average the center of the negative charge was at about -12° C isotherm, and the positive charge was near the -25° C isotherm. Once again, this is consistent with observation (Simpson and Scrase, 1937; Reynolds, 1954; Takahashi, 1965; Magono, 1977; Byrne *et al.*, 1987).

The non-inductive charging mechanism was also very active in the monsoon simulation: there were large mixing ratios of graupel, snow, and cloud water in coexistence. However, the microphysical conditions, specifically the cloud water field, did not allow the potential of the non-inductive charging to be realized. There were numerous graupel-snow interactions and correspondingly large amounts of charge being separated, but the graupel and snow were continually acquiring different polarity charges.

In summary, the non-inductive charging mechanism was operating in both the break period and the monsoon simulation. In the break period simulation, the mechanism effectively separated charge because the environmental temperature was much colder than the charge reversal temperature at the particle balance level. This allowed the graupel (or snow) to acquire and accumulate charge of one sign over time. In the monsoon simulation, the non-inductive mechanism was active, but ineffective in producing a well defined charge structure. The reason for this is that the graupel (or snow) was not able to acquire or accumulate charge on one sign over time because of the collocation of the charge reversal temperature with the overlapping region of graupel and snow mixing ratios.

7.3 Lightning and the Degree of Storm Electrification

Based on the simulations, it seems reasonable to expect that the break period convection would produce lightning much more easily and frequently than the monsoon. In the monsoon simulation, the electric field never acquired significant magnitude due to the lack of an organized charge structure. If the monsoon simulation is representative of monsoon convection in general, then it is really pointless to discuss lightning for this type of convection. In the break period, the electric field reached over 300 kv m^{-1} in magnitude by the end of the rapid growth stage. This is approaching the values observed before lightning is initiated (Gunn, 1954).

The electrical structure in the break period simulation also provides some possible insight into the types of lightning that are observed. During the rapid growth phase, the electrical structure was that of a normal polarity dipole. In the mature phase, the anvil became electrically active and created a horizontal electrical field that was roughly the same strength as the dipole in the convective updraft. Assuming that lightning propagates along the direction of the maximum electric field, vertically propagating flashes might be more common in the growing stages of the convection. In the mature stage, there might be more of a tendency to produce horizontally propagating lightning in the anvil. Horizontal lightning in the anvil was observed propagating away from the convective updraft during DUNDEE (personal communication, S. Rutledge and E. Rasmussen).

7.4 Future Studies

The deep mixed phase microphysics in the monsoon simulation was perhaps one of the biggest surprises to come out of this study. Before the simulation, the expectations were that the monsoon did not charge because it was almost completely glaciated above the freezing level (Churchill and Houze, 1984; Gamache, 1990). This turned out not to be

true, at least for the case modelled in the thesis. More simulations of the monsoon need to be conducted to determine: 1) if a deep mixed phase region is simulated; 2) if the region of overlapping graupel and snow generally occurs near the charge reversal temperature. One modelling study does not prove anything, but additional studies, coupled with observation, will provide further support for the hypothesis. Another monsoon modelling study will most likely be undertaken in the near future.

Another potential improvement in the simulations would be to activate more charging mechanisms. The current model is already capable of calculating charging due to inductive mechanisms. These should be included in future studies to assess the roles of conductive, non-inductive, and inductive charging.

Improvements can be made in the non-inductive charging parameterization. The impact velocity between graupel and ice crystals, and the diameter of the ice crystals has been shown to have effects on the magnitude of the non-inductive charge transfer (Gaskell and Illingworth, 1980). These effects should be included in future modelling work.

Finally, the electrical feedbacks on the microphysics should be addressed. Electric fields and charges on hydrometeors may have effects on collection efficiencies and growth rates, as well as habits of ice species (Abbas and Latham, 1968; Ochs *et al.*, 19??; Weinheimer and Few, 1987). This might perhaps be better addressed with an explicit microphysical model.

REFERENCES

- Anderson, B. J., and J. Hallet, 1979: Influence of environmental saturation and electric field on growth and evaporation of ice crystals. *J. Crystal Growth*, **46**, 427-444.
- Aufdermaur, A. N., and D. A. Johnson, 1972: Charge separation due to riming in an electric field. *Quart. J. Roy. Meteor. Soc.*, **98**, 369-382.
- Avila, E. E., G. M. Caranti, and M. Lanfri, 1988: Charge reversal in individual ice-ice collisions. *Proceedings of the International Conference on Atmospheric Electricity*. 245-250.
- Baker, B., M. B. Baker, E. R. Jayaratne, J. Latham, and C. P. R. Saunders, 1987: The influence of diffusional growth rates on the charge transfer accompanying rebounding collisions between ice crystals and soft hailstones. *Quart. J. Roy. Meteor. Soc.*, **113**, 1193-1215.
- Barnard, V., 1951: The approximate mean height of the thundercloud charges taking part in a flash to ground. *J. Geophys. Res.*, **56**, 33-35.
- Battan, L. J., 1973, *Radar Observations of the Atmosphere*, University of Chicago Press, 324 pp.
- Bennetts, D. A., and F. Rawlings, 1981: Parameterization of the ice-phase in a model of mid-latitude cumulonimbus convection and its influence on the simulation of cloud development. *Quart. J. Roy. Meteor. Soc.*, **107**, 477-502.
- Blakeslee, R. J., Christian, H. J., and Vonnegut, B., 1989: Electrical measurements over thunderstorms. *J. Geophys. Res.*, **94**, 13,135.
- Brode, R. W., and Mak, M. K., 1982: On the monsoonal midtropospheric cyclogenesis over western India. *Proceedings of the International Symposium on Monsoon Dynamics, New Delhi, 1977*.
- Brown, K. A., P. R. Krehbiel, C. B. Moore, and G. N. Sargent, 1971: Electrical screening layers around charged clouds. *J. Geophys. Res.*, **76**, 2825.
- Byers, H. R., 1965: Elements of Cloud Physics, University of Chicago Press.
- Byrne, G. J., A. A. Few, and M. F. Stewart, 1989: Electric field measurements within a severe thunderstorm anvil.
- Byrne, G. J., _____, _____, A. C. Conrad, and R. L. Torczon, 1987: In situ measurements and radar observations of a severe storm: Electricity, kinematics, and precipitation. *J. Geophys. Res.*, **92**, 9911-9920.

- _____, _____, and M. E. Weber, 1983: Altitude, thickness and charge concentrations of charged regions of four thunderstorms during TRIP 1981 based upon in situ balloon electric field measurements. *Geophys. Res. Lett.*, **10**, 39-42.
- Caranti, J. M., and A. J. Illingworth, 1980: Surface potentials of ice and thunderstorm charge separation, *Nature*, **284**, 44-46.
- Chang, C. H., 1977: Ice generation in clouds. *M. S. Thesis, South Dakota School of Mines and Technology*, 128 pp.
- Chauzy, S., and P. Raisonville, 1983: Electrostatical screening below thunderstorms due to coronae at ground level. *Proceedings in Atmospheric Electricity*. 184-187.
- Chen, C., and H. D. Orville, 1980: Effects of mesoscale convergence on cloud convection. *J. Appl. Meteor.*, **19**, 256-274.
- Cheng, C.P., 1981: Numerical simulation of the dynamics, cloud microphysics and radar echo structure of tropical and mid-latitude convection. *Ph.D. Thesis, University of Washington*, 217 pp.
- Chiu, C., 1978: Numerical study of cloud electrification in an axisymmetric, time-dependent cloud model. *J. Geophys. Res.*, **83**, 5025-5048.
- Chong, M., P. Anayenc, G. Scialom, and J. Testud, 1987: A tropical squall line observed during COPT '81 experiment in West Africa. Part I: Kinematic structure inferred from dual-doppler radar data. *Mon. Wea. Rev.*, **115**, 670-694.
- Colgate, S. A., and J. M. Romero, 1970: *J. Geophys. Res.*, **75**, 5873.
- Danielson, E. F., R. Bleck, and D. A. Morris, 1972: Hail growth by stochastic collection in a cumulus model. *J. Atmos. Sci.*, **29**, 135-155.
- Dye, J. E., J. J. Jones, A. J. Weinheimer, and W. P. Winn, 1988: Observations within two regions of charge during initial thunderstorm electrification. *Quart. J. R. Met. Soc.*, **114**, 1271-1290.
- Emanuel, K., 1988: Toward a general theory for hurricanes. *Am. Scientist*, **76**, 370-379.
- Ette, A. I. I., J. I. Aina, and E. U. Utah, 1977: Point discharge characteristics and charge configuration in thunderclouds. *Electrical Processes in Atmospheres*.
- Farley, R. D., and H. D. Orville, 1986: Numerical modeling of hailstorms and hailstone growth: Part I: Preliminary model verification and sensitivity tests. *J. Clim. Appl. Met.*, **25**, 2014-2035.
- Ferrier, B. S., and R. A. Houze, Jr., 1989: One-dimensional time-dependent modeling of GATE cumulonimbus convection. *J. Atmos. Sci.*, **46**, 330-352.
- Fujita, T. T., 1955: Results of detailed synoptic studies of squall lines. *Tellus*, **7**, 405-436.
- Gamache, J. F., and R. A. Houze, Jr., 1982: Mesoscale air motions associated with a tropical squall line. *Mon. Wea. Rev.*, **110**, 118-135.

- _____, and R. A. Houze, Jr., 1983: Water budget of a mesoscale convective system associated with a tropical squall line. *J. Atmos. Sci.*, **70**, 1835-1850.
- Gaskell, W. A., and J. Illingworth, 1980: Charge transfer accompanying individual collisions between ice particles and its role in thunderstorm electrification. *Quart. J. Roy. Meteor. Soc.*, **106**, 841-854.
- Gaskell, W. A., J. Illingworth, J. Latham, and C. B. Moore, 1978: Airborne studies of electric fields and the charge and size of precipitation elements in thunderstorms. *Quart. J. R. Met. Soc.*, **104**, 447-460.
- Goodman, S. J. and D. E. Buechler, 1988: Convective tendency images derived from a combination of lightning and satellite data. *Wea. and For.*, **3**, 173-188.
- _____, and D. R. MacGorman, 1986: Cloud-to-Ground Lightning Activity in Mesoscale Convective Complexes. *Mon. Wea. Rev.*, **114**, 2320-2328.
- Grenet, G., 1947: Essay d'explication de la charge electrique de nuage d'orages. *Ann. Geophys.*, **3**, 306-307.
- Griffiths, R. F., J. Latham, and V. Meyers, 1974: The ionic conductivity of electrified clouds. *Quart. J. R. Met. Soc.*, **100**, 181-190.
- Gunn, R., 1948: Electric field intensity inside of natural clouds. *J. Appl. Phys.*, **19**, 481-484.
- _____, 1956: Diffusion charging of atmospheric droplets by ions and the resulting combination coefficients, *J. Meteor.*, **11**, 339.
- Hacking, C. A., 1954: Observation on the negatively charged column in thunderclouds. *J. Geophys. Res.*, **59**, 449-453.
- Hall, W. D., 1980: A detailed microphysical model with a two-dimensional dynamic framework: model description and preliminary results. *J. Atmos. Sci.*, **37**, 2486-2507.
- Hallet, J., and Saunders, C. P. R., 1979: Charge separation associated with secondary ice crystal production, *J. Atmos. Sci.*, **36**, 2230-2235.
- Haltiner, G. J., and R. T. Williams, 1980: *Numerical Prediction and Dynamic Meteorology*. John Wiley and Sons, 477 pp.
- Helsdon, J. H., and R. D. Farley, 1987a: A numerical modeling study of a Montana thunderstorm: 1. Model results versus observations involving nonelectrical aspects. *J. Geophys. Res.*, **92**, 5645-5659.
- _____. and _____, 1987b: A numerical modeling study of a Montana thunderstorm: 2. Model results versus observations involving electrical aspects. *J. Geophys. Res.*, **92**, 5661-5675.
- Hendon, H. H., and Liebmann, 1990: A composite study of onset of the Australian summer Monsoon. *J. Atmos. Sci.*, **47**, 2227-2240.

- Heymsfield, G. M., and S. Schotz, 1985: Structure and evolution of a severe squall line over Oklahoma. *Mon. Wea. Rev.*, **113**, 1563-1589.
- Heymsfield, A. J., and M. R. Hjermfelt, 1984: Processes of hydrometeor development in Oklahoma convective clouds. *J. Atmos. Sci.*, **41**, 2811-2835.
- Hosler, C. L., D. C. Jensen, and P. L. Golshlak, 1957: On the aggregation of ice crystals to form snow. *J. Meteor.*, **14**, 415-420.
- Houze, R.A., Jr., S. A. Rutledge, M. I. Biggerstaff, and B. F. Smull, 1989: Interpretation of doppler weather radar displays of midlatitude mesoscale convective systems. *Bull. Amer. Meteor. Soc.*, **70**, 608-619.
- _____, 1981: Structure of atmospheric precipitation systems -- A global survey. *Radio Sci.*, **16**, 671-689.
- _____, 1977: Structure and dynamics of a tropical squall-line system. *Mon. Wea. Rev.*, **105**, 1540-1567.
- Illingworth, A. J., 1985: Charge separation in thunderstorms: Small scale processes. *J. Geophys. Res.*, **90**, 6026-6032.
- _____, and J. Latham, 1977: Calculations of electric field growth, field structure and charge distribution in thunderstorms. *Quart. J. Roy. Meteor. Soc.*, **103**, 281-295.
- Jacobson, E. A., and E. P. Krider, 1976: Electrostatic field changes produced by Florida lightning. *J. Atmos. Sci.*, **33**, 103-117.
- Jayarathne, E. R., and C. P. R. Saunders, 1985: Thunderstorm electrification: The effect of cloud droplets. *J. Geophys. Res.*, **90**, 13,063-13,066.
- _____, _____, and J. Hallet, 1983: Laboratory studies of the charging of soft-hail during ice crystal interactions. *Quart. J. Roy. Meteor. Soc.*, **109**, 609-630.
- Johnson, R. H., 1980: Diagnosis of convective and mesoscale motions during Phase III of GATE. *J. Atmos. Sci.*, **37**, 733-753.
- Keenan, T. D., and S. A. Rutledge, 1991: Mesoscale characteristics of a monsoon rainband. *Mon. Wea. Rev.*
- Keenan, T. D., and R. E. Carbone, 1989: A preliminary morphology of convective systems in tropical northern Australia. *Proceedings of the 24th American Meteorological Society Conference on Radar Meteorology*. 640-644.
- _____, and L. R. Brody, 1988: Synoptic-scale modulation of convection during the Australian summer monsoon. *Mon. Wea. Rev.*, **116**, 71-85.
- Keith, W.D., and C.P.R. Saunders, 1989a: The collection efficiency of a cylindrical target for ice crystals. *Atmospheric Research*, **23**, 83-95.
- _____, and _____, 1989b: Charge transfer during multiple large ice crystal interactions with a riming target. *J. Geophys. Res.*, **94**, 13,103-13,106.

- _____, and _____, 1990: Further laboratory studies of the charging of graupel during ice crystal interactions. *Atmos. Res.*, 25, 445-464.
- Kessinger, C. J., P. S. Ray, and C. E. Hane, 1987: The 19 May 1977 Oklahoma squall line. Part I: A multiple doppler analysis of convective and stratiform structure. *J. Atmos. Sci.*, 44, 2840-2864.
- Kessler, E., 1969: On the distribution and continuity of water substance in atmospheric circulation. *Meteor. Monogr.*, 32, 84 pp.
- Krasnogorskaya, N. V., and A. I. Neizvestnyy, 1973: *Atmos. Ocean Phys.*, 9, 220.
- Krehbiel, P. R., M. Brook, R. Lhermitte, and C. Lennon, 1983: Lightning charge structure in thunderstorms. *Proceedings in Atmospheric Electricity*, 408-460.
- _____, _____, and R. A. McCrory, 1979: An analysis of the charge structure of lightning discharges to ground. *J. Geophys. Res.*, 84, 2432-2456.
- Krider, E. P., 1989: Electric field changes and cloud electrical structure. *J. Geophys. Res.*, 94, 13,145.
- Kumar, P. P., and C. P. R. Saunders, 1988: Charge transfer during single crystal interaction with a rimed target: *1988 Proceedings of the International Conference on Atmospheric Electricity*.
- Kuettner, J. P., Z. Levin, and J. D. Sartor, 1981: Thunderstorm electrification--inductive or non-inductive?, *J. Atmos. Sci.*, 38, 2470-2484.
- _____, 1950: The electrical meteorological conditions inside thunderstorms. *J. Meteor.*, 7, 322-332.
- Lafore, J. P., and M. W. Moncrieff, 1989: A numerical investigation of the organization and interaction of the convective and stratiform regions of tropical squall lines. *J. Atmos. Sci.*, 46, 521-544.
- Latham, J., and J. E. Dye, 1989: Calculations on the electrical development of a small thunderstorm. *J. Geophys. Res.*, 94, 13,141.
- Latham, J. and C. D. Stow, 1969: Airborne studies of the electrical properties of large convective clouds. *Quart. J. Roy. Meteor. Soc.*, 95, 486-500.
- _____, and B. J. Mason, 1962: Electrical charging of hail pellets in a polarizing electric field. *Proc. Roy. Soc. London*, A266, 387-401.
- _____, and _____, 1961a: Electric charge transfer associated with temperature gradients in ice, *Proc. Roy. Soc. London*, A260, 523-536.
- _____, and _____, 1961b: Generation of electric charge associated with the formation of soft hail in thunderclouds. *Proc. Roy. Soc. London*, A260, 537-549.
- Leary, C. A., and R. A. Houze, Jr., 1979: Melting and evaporation of hydrometeors in precipitation from anvil clouds of deep tropical convection. *J. Atmos. Sci.*, 36, 689-679.

- Lhermitte, R. M., and D. Atlas, 1961: Precipitation motion by pulse Doppler. *Proc. Ninth Weather Radar Conf.*, Amer. Meteor. Soc., Boston, Mass., 218-223.
- _____, and P. R. Krehbiel, 1979: doppler radar and radio observations of thunderstorms, *IEEE Trans. Geosci. Electron.*, 17, 162-171.
- Lin Y., R. D. Farley, and H. D. Orville, 1983: Bulk parameterization of the snow field in a cloud model. *J. Climate Appl. Meteor.*, 22, 1065-1092.
- Liu, J. Y., and H. D. Orville, 1969: Numerical modelling of precipitation and cloud shadow effects on mountain-induced cumuli. *J. Atmos. Sci.*, 26, 1283-1298.
- Livingston J. M., and E. P. Krider, 1978: Electric fields produced by Florida thunderstorms. *J. Geophys. Res.*, 83, 385-401.
- Maddox, R. A., 1980: Mesoscale convective complexes. *Bull. Amer. Met. Soc.*, 61, 1374-1387.
- Magono, C., 1977: Precipitation electricity of thunderclouds and shower clouds. *Electrical Processes in Atmospheres*, 368-378.
- Magono, C., and T. Takahashi, 1963a: On the electrical phenomena during riming and glazing in natural supercooled droplets, *J. Meteor. Soc. Japan*, 41, 71-81.
- _____, 1963b: Experimental studies on the mechanisms of electrification of graupel pellets. *J. Meteor. Soc. Japan*, 41, 197-210.
- Malan, D. J., and B. F. J. Schonland, F. R. S., 1951: The distribution of electricity in thunderclouds. *Proc. Roy. Soc. London*, A209, 158-177.
- Marshall, B. J. P., J. Latham, and C. P. R. Saunders, 1978: A laboratory study of charge transfer accompanying the collision of ice crystals with a simulated hailstone. *Quart. J. Roy. Meteor. Soc.*, 104, 163-178.
- Marshall, J. S., and W. Palmer, 1948: The distribution of raindrops with size. *J. Meteor.*, 5, 165-166.
- Marshall, T. C., W. D. Rust, W. P. Winn, and K. E. Gilbert, 1989: Electrical structure in two thunderstorm anvil clouds. *J. Geophys Res*, 94, 2171-2181.
- McBride, J. L., 1987: The Australian summer monsoon. *Review of Monsoon Meteorology*, Oxford Univ. Press, 203-231.
- _____, 1983: Satellite observations of the Southern Hemisphere monsoon during winter MONEX. *Tell.*, 35A, 189-197.
- Moore, C. B., Vonnegut, B., and Holden, D., 1989: Anomalous electric fields associated with clouds growing over a source of negative space charge. *J. Geophys. Res.*, 94, 13,127.
- Moore, C. B., B. Vonnegut, T. D. Rolan, J. W. Cobb, D. N. Holden, R. T. Hignight, S. M. McWilliams, and G. W. Cadwell, 1986: Abnormal polarity of thunderclouds grown from negatively charge air, *Science*, 233, 1414-1416.

- Mossop, S. C., 1968: Comparison between concentration of ice crystals in cloud and the concentration of ice nuclei. *J. Rech. Atmos.*, **3**, 119-124.
- Ogawa, T., and F. Sakaguchi, 1983: Electrification of winter minor showerclouds. *J. Meteor. Soc. Jap.*, **61**, 313-324.
- Ogura, Y., and M. T. Liou, 1980: The structure of a midlatitude squall line: A case study. *J. Atmos. Sci.*, **37**, 553-567.
- _____, and T. Takahashi, 1973: The development of warm rain in a cumulus model. *J. Atmos. Sci.*, **30**, 262-277.
- Orville, H. D., and F. I. Kopp, 1977: Numerical simulation of the life history of a hailstorm. *J. Atmos. Sci.*, **34**, 1596-1618.
- _____, 1965: A numerical study of the initiation of cumulus clouds over mountainous terrain. *J. Atmos. Sci.*, **22**, 684-699.
- Orville, R. E., and R. W. Henderson, 1986: Global distribution of midnight lightning: September 1977 to August 1978. *Mon. Wea. Rev.*, **114**, 2640-2653.
- Orville, R. E., and D. W. Spencer, 1979: Global lightning flash frequency. *Mon. Wea. Rev.*, **107**, 934-943.
- Pruppacher, H. R., and J. D. Klett, 1980: *Microphysics of Clouds and Precipitation*. D. Reidel Publishing Company.
- Rawlins, F. A., 1982: A numerical study of thunderstorm electrification using a three-dimensional model incorporation the ice phase. *Quart. J. Roy. Meteor. Soc.*, **108**, 779-800.
- Reynolds, S. E., M. Brook, and M. F. Gourley, 1957: Thunderstorm charge separation, *J. Meteor.*, **14**, 426-436.
- _____, 1954: Thunderstorm-precipitation growth and electrical-charge generation. *Bull. Amer. Met. Soc.*, **34**, 117-123.
- Ruhnke, L. H., 1972: *Meteor. Res.*, **25**, 38.
- Ruhnke, L. H., 1970: *J. Appl. Meteor.*, **9**, 947.
- Rust, W. D., W. L. Taylor, D. R. MacGorman, E. Brandes, V. Mazur, R. Arnold, T. Marshall, H. Christian, and S. J. Goodman, 1985: Lightning and related phenomena in isolated thunderstorms and squall line systems. *J. Aircraft*, **22**, 449-454.
- _____, and D. R. MacGorman, 1981: Positive cloud-to-ground lightning flashes in severe storms. *Geophys. Res. Lett.*, **8**, 791-794.
- Rutledge, S. A., E. W. Williams, and T. D. Keenan, 1991: The Down Under Doppler and Electricity Experiment (DUNDEE): overview and preliminary results. *Bull. Amer. Met. Soc.*

- _____, 1990: Middle latitude tropical mesoscale convective systems. Submitted to *Rev. of Geophys.*
- _____, 1990: Mesoscale convective systems and lightning. *1990 Proceedings of the Conference on Atmospheric Electricity.*
- _____, C. Lu, and D. R. MacGorman, 1990: Positive cloud-to-ground lightning in mesoscale convective systems, *J. Atmos. Sci.*
- _____, and D. R. MacGorman, 1988: Cloud-to-ground lightning activity in the 10-11 June 1985 mesoscale convective system observed during the Oklahoma-Kansas PRE-STORM project. *Mon. Wea. Rev.*, 116, 1393-1408.
- _____, 1986: A diagnostic numerical study of the stratiform region associated with a tropical squall line. *J. Atmos. Sci.*, 43, 1337-1358.
- Saunders, C. P. R., 1977: Review Article: Thunderstorm electrification.
- Scott, B. C., and P. V. Hobbs, 1977: A theoretical study of the evolution of mixed phase cumulus clouds. *J. Atmos. Sci.*, 34, 812-826.
- Scott, W. D., and Z. Levin, 1970: The effect of potential gradient on the charge separation during interactions of snow crystals with an ice sphere. *J. Atmos. Sci.*, 27, 463-473.
- Shewchuk, S. R., and J. V. Irbarne, 1974: Electrification associated with droplet accretion on ice. *J. Atmos. Sci.*, 31, 777-786.
- Simpson, G. C., and F. J. Scrase, 1937: The distribution of electricity in thunderclouds, *Proc. Roy. Soc. London*, A161, 309-353.
- _____, and G. D. Robinson, 1941: The distribution of electricity in thunderclouds II. *Proc. Roy. Soc. London*, A177, 281-329.
- Simpson, J., and V. Wiggert, 1969: Models of precipitating cumulus towers. *Mon. Wea. Rev.*, 97, 471-489.
- Smith, P. L., Jr., C. G. Meyers, and H. D. Orville, 1975: Radar reflectivity calculations in numerical cloud models using bulk parameterizations of precipitation. *J. Appl. Met.*, 14, 1156-1165.
- Smull, B. F., and R. A. Houze, Jr., 1985: A midlatitude squall line with a trailing region of stratiform rain: Radar and satellite observations. *Mon. Wea. Rev.*, 113, 117-133.
- _____, and _____, 1987a: Dual-Doppler radar analysis of a midlatitude squall line with a trailing region of stratiform rain. *J. Atmos. Sci.*, 44, 2128-2148.
- Sommeria, G., and J. Testud, 1984: COPT '81: A field experiment designed for the study of dynamics and electrical activity of deep convection in continental tropical regions. *Bull. Amer. Meteor. Soc.*, 65, 4-10.
- Soong, S. T., 1974: Numerical simulation of warm rain development in an axisymmetric cloud model. *J. Atmos. Sci.*, 31, 1262-1285.

- Takahashi, T., 1984: Thunderstorm electrification--A numerical study. *J. Atmos. Sci.*, 41, 2541-2558.
- _____, 1979: Warm cloud electricity in a shallow axisymmetric cloud model. *J. Atmos. Sci.*, 36, 2236-2258.
- _____, 1978: Riming electrification as a charge generation mechanism in thunderstorms, *J. Atmos. Sci.*, 35, 1536-1548.
- _____, 1976: Hail in an axisymmetric cloud model. *J. Atmos. Sci.*, 33, 1579-1601.
- _____, 1975: Electric charge life cycle in warm clouds. *J. Atmos. Sci.*, 32, 123-142.
- _____, 1972: Electric charge of small particles (1μ - 40μ). *J. Atmos. Sci.*, 29, 921-928.
- _____, 1965: Measurement of electric charge in thunderclouds by means of radiosonde. *J. Meteor. Soc. Japan.*, 43, 206-217.
- _____, 1969: Electric charge generation by the breaking of frost under a temperature gradient. *J. Meteor. Soc. Japan.*, 47, 22-28.
- _____, 1969: Electric potential of liquid water on an ice surface. *J. Atmos. Sci.*, 26, 1253-1258.
- _____, 1969: Electric potential of a rubbed ice surface. *J. Atmos. Sci.*, 26, 1259-1265.
- _____, 1962: Electric charge generation by the breaking of an ice piece. *J. Meteor. Soc. Japan.*, 40, 277-286.
- Takeuti, T., M. Nakano, M. Brook, D. J. Raymond, and P. Krehbiel, 1977: The anomalous winter thunderstorms of the Hokuriku Coast. *J. Geophys. Res.*, 83, 2385-2394.
- Teer, T. L., and A. A. Few, 1974: Horizontal lightning. *J. Geophys. Res.*, 79, 3436-3441.
- Turman, B. N., and B. C. Edgar, 1982: Global lightning distributions at dawn and dusk. *J. Geophys. Res.*, 87, 1191-1206.
- Tzur, I., and Z. Levin, 1981: Ions and precipitation charging in warm and cold clouds as simulated in one-dimensional time-dependent models. *J. Atmos. Sci.*, 38, 2444-2461.
- Vardiman, L., 1978: The generation of secondary ice particles in clouds by crystal-crystal collision. *J. Atmos. Sci.*, 35, 2168-2180.
- Vonnegut, B., 1982: The physics of thunderclouds. *CRC Handbook in Atmospheric*, 1, 1-22.
- _____, C. B. Moore, G. E. Stoud, D. W. Staggs, J. W. Bullock, and W. E. Bradley, 1962a: Artificial modification of atmospheric space charge, *J. Geophys. Res.*, 67, 1073-1083.

- _____, _____, R. G. Semonin, J. W. Bullock, D. W. Staggs, and W. E. Bradley, 1962b: Effect of atmospheric space charge on initial electrification of cumulus clouds. *J. Geophys. Res.*, **67**, 3909-3922.
- _____, 1953: Possible mechanism for the formation of thunderstorm electricity. *Bull. Amer. Met. Soc.*, **34**, 378-381.
- Weber, M. E., H. J. Christian, A. A. Few, and M. F. Stewart, 1982: A thundercloud electric field sounding: Charge distribution and lightning. *J. Geophys. Res.*, **87**, 7158-7169.
- Weickmann, H. K., and J. J. aufm Kampe, 1950: Preliminary experimental results concerning charge generation in thunderstorms concurrent with the formation of hailstones. *J. Meteor.*, **7**, 404-405.
- Weinheimer, A. J., and A. A. Few, 1987: The electric field alignment of ice particles in thunderstorms. *Quart. J. Roy. Meteor. Soc.*, **107**, 477-502.
- William, J. K., and Krider, E. P., 1989: Analysis of lightning field changes during active Florida thunderstorms. *J. Geophys. Res.*, **94**, 1165-1186.
- Williams, E. R., S. G. Geotis, N. Renno, S. A. Rutledge, E. Rasmussen, and T. Rickenback, 1990: *Hot towers in the tropics, Preprints of the AMS Conference on Atmospheric Electricity, 1990.*
- _____, 1990: The role of ice in the electrification and dynamics of thunderstorms. *Preprints of the Conference of Cloud Physics*, 282-289.
- _____, and S. A. Rutledge, 1990: Studies of electrification and lightning in deep tropical precipitation systems. *Preprints Cloud Physics Conf., Amer. Meteor. Soc.*, San Francisco. 290-294.
- _____, R. Zhang, and J. Rydock, 1990: Mixed phase microphysics and cloud electrification. *Preprints Cloud Physics Conf., Amer. Meteor. Soc.*, San Francisco. 295-301
- _____, 1989: The tripole structure of thunderstorms. *J. Geophys. Res.*, **94**, 13,151.
- _____, M. E. Weber, and R. E. Orville, 1989: The relationship between lightning type and convective state of thunderclouds. *J. Geophys. Res.*, **94**, 13213-13220.
- _____, C. M. Cooke, and K. A. Wright, 1985: Electrical discharge propagation in and around space charge clouds. *J. Geophys. Res.*, **94**, 1165-1186.
- _____, 1985: Large scale charge separation in thunderclouds. *J. Geophys. Res.*, **90**, 6013-6025.
- Willis, P. T., 1984: Functional fits to some observed drop size distributions and parameterization of rain. *J. Atmos. Sci.*, **41**, 1648-1661.
- Wisner, C. E., H. D. Orville, and C. G. Myers, 1972: A numerical model of a hail bearing cloud. *J. Atmos. Sci.*, **29**, 1160-1181.
- Workman, E. J., and S. E. Reynolds, 1949: Electrical activity as related to thunderstorm cell growth. *Bull. Amer. Meteor. Soc.*, **30**, 142-144.

_____, and _____, 1950: Electrical phenomena occurring during the freezing of dilute aqueous solutions and their possible relationship to thunderstorm electricity. *Phys. Rev.*, **78**, 254-259.

Workman, E. J., and Reynolds S. E., 1954: Thunderstorm research program at the New Mexico School of Mines. *Thunderstorm Electricity*, University of Chicago Press.

Yau, M. K., and P. M. Austin, 1979: A model for hydrometeor growth and evolution of raindrop size spectra in cumulus cells. *J. Atmos. Sci.*, **36**, 655-668.

APPENDIX A
LIST OF SYMBOLS

<u>Notation</u>	<u>Description</u>
a	constant in empirical formula for particle velocity
a ₁	parameter in Beregeron process
a ₂	parameter in Beregeron process
A	constant in the charge transfer equation
A'	constant in Bigg freezing
A''	coefficient in the diffusion equation for an ice particle
b	constant in empirical formula for particle velocity
B'	constant in raindrop freezing equation
B''	coefficient in the diffusion equation for an ice particle
c	constant in empirical equation for particle velocity
C _D	drag coefficient for graupel
C _i	specific heat of ice
C _p	specific heat of air at constant pressure
C _w	specific heat of water
d	constant in empirical formula for particle velocity
D ₀	dispersion of cloud droplet distribution
D _G	diameter of hailstone
D _R	diameter of a raindrop
D _S	diameter of snow crystal
e	elementary electric charge
E	electric field
E _f	separation efficiency of small and large particle
E _{IW}	collection efficiency of cloud ice for cloud water
E _{GW}	collection efficiency of graupel for cloud ice
E _{GR}	collection efficiency of graupel for rain
E _{GS}	collection efficiency of graupel for snow
E _{GW}	collection efficiency of graupel for water
E _{RI}	collection efficiency of rain for cloud ice
E _{SI}	collection efficiency of snow for cloud ice
E _{SR}	collection efficiency of snow for rain
E _{SW}	collection efficiency of snow for water
F _x	horizontal friction force
F _Z	vertical friction force
g	gravitational acceleration
G	generation of ions through cosmic rays
K _a	thermal conductivity of air
K _h	heat eddy coefficient
K _m	momentum eddy coefficient
L	precipitation loading

L_v	latent heat of vaporization
L_f	latent heat of fusion
L_s	latent heat of sublimation
m_{I50}	mass of a 50 μm size ice crystal
M_i	mass of one cloud ice crystal
n_o	parameter in Fletcher's equation
n_+	number concentration of positive (negative) ions
N_{oG}	intercept of graupel size distribution
N_{oS}	intercept of snow size distribution
N_{oR}	intercept of rain size distribution
NG	spectral density of graupel
NS	spectral density of snow
NR	spectral density of rain
N_I	number concentration of cloud droplets
N_{I50}	number concentration of 50 μm size ice crystals
N_n	number of active natural ice nuclei
N_{SMALL}	number of small particles
\hat{p}	perturbation pressure
PG	total production rate for graupel
PS	total production rate for snow
PR	total production rate for rain
P_{IMLT}	production rate for melting of cloud ice to form cloud water
P_{IDW}	production rate for depositional growth of cloud ice at expense of cloud water
P_{IHOM}	production rate for homogeneous freezing of cloud water to form cloud ice
P_{IACR}	production rate for accretion of rain by cloud ice
P_{RACI}	production rate for accretion of cloud ice by rain
P_{RAUT}	production rate for autoconversion of cloud water to form rain
P_{RACW}	production rate for accretion of cloud water by rain
P_{REVP}	production rate for rain evaporation
P_{RACS}	production rate for accretion of snow by rain
P_{SACW}	production rate for accretion of cloud water by snow
P_{SACR}	production rate for accretion of rain by snow
P_{SACI}	production rate for accretion of cloud ice by snow
P_{SAUT}	production rate for autoconversion of cloud ice to form snow
P_{SFW}	production rate for Bergeron process (cloud water to snow)
P_{SFI}	production rate for Bergeron process (cloud ice embryos used to calculate transfer rate of cloud ice to snow)
P_{SDEP}	production rate for depositional growth of snow
P_{SSUB}	production rate for sublimation of snow
P_{SMLT}	production rate for snow melting to form rain
P_{GAUT}	production rate for autoconversion of snow to form graupel
P_{GFR}	probalistic freezing of rain to form graupel
P_{GACW}	production rate for accretion of cloud water by graupel
P_{GACI}	production rate for accretion of cloud ice by graupel
P_{GACR}	production rate for accretion of rain by graupel
P_{GACS}	production rate for accretion fo snow by graupel
P_{GSUB}	production rate for graupel sublimation

PGMLT	production rate for graupel melting to form rain
PGWET	wet growth rate of graupel
PGDRY	dry growth rate of graupel
q	mixing ratio of water vapor, cloud water, and cloud ice
q _{CI}	mixing ratio of cloud ice
q _{CI} *	cloud ice autoconversion mixing ratio threshold
q _{CW}	mixing ratio of cloud water
q _{CW} *	cloud water autoconversion mixing ratio threshold
q _G	mixing ratio of graupel
q _R	mixing ratio of rain
q _S	mixing ratio of snow
q _S *	mixing ratio threshold for snow aggregation
$\Delta\hat{q}$	charge transferred during particle interaction
Q	total charge on a hydrometeor
ΔQ	charge transferred between two particles due to non-inductive charging
\hat{q}_{LARGE}	charge on the large particle
\hat{q}_{SMALL}	charge on the small particle
r _{LARGE}	radius of large particle
r	mixing ratio of water vapor
r _s	saturation mixing ratio of water vapor with respect to water
r _{so}	saturation mixing ratio of water vapor at surface of graupel
r _{si}	saturation mixing ratio for water vapor with respect to ice
Δr_s	r _{so} -r
RI50	radius of ice crystal (50 μm)
R _w	specific gas constant for water vapor
S	saturation ratio
S _c	collision angle dependent function used in determining charge transfer
S _i	Schmidt number
t	saturation ratio over ice
Δt_1	time
T	temperature dependent time scale
T _O	temperature in cloud environment
T _{OO}	melting temperature
T _C	reference temperature
T _{v0}	temperature in degrees Celsius
\hat{T}_v	reference virtual temperature
u	perturbation virtual temperature
V _G	horizontal component of velocity vector
V _R	mass weighted terminal velocity of graupel
V _S	mass weighted terminal velocity of rain
V _{DG}	mass weighted terminal velocity of snow
V _{DR}	terminal velocity for graupel of diameter DG
V _{DS}	terminal velocity for rain of diameter DR
V _{SL}	terminal velocity for snow of diameter DS
V	differential velocity between large and small particles
	velocity vector

w	vertical component of velocity vector
x	horizontal coordinate
z	vertical coordinate
α	angle of contact between small and large particle ion recombination rate
α_1	autoconversion rate coefficient for PSAUT
α_2	autoconversion rate coefficient for PGAUT
β	parameter in Fletchers equation
δ_1	indicator for condensation (deposition) and evaporation (sublimation)
δ_2	indicator of PRACS and PSACR
δ_3	indicator of PIACR and PRACI
ϵ_0	permativity of free space
μ_{\pm}	postive (negative) ion mobility
θ	potential temperature
θ'	potential temperature deviation
Θ	reference potential temperature
Λ_R	slope in Marshall-Palmer rain distribution
Λ_S	slope in Marshall-Palmer snow distribution
Λ_G	slope in Marshall-Palmer graupel distribution
ρ_0	density of air at the surface
ρ	density of air
ρ_G	density of graupel
ρ_S	density of snow
ρ_w	density of water
ρ_T	total space charge density
ν	kinematic viscosity of air
ψ	diffusivity of water vapor in air density weighted stream function
ϕ'	normalized potential temperature including latent heat effects
ϕ_E	electric potential
η	density weighted vorticity